MICROCOPY RESOLUTION TEST CHART
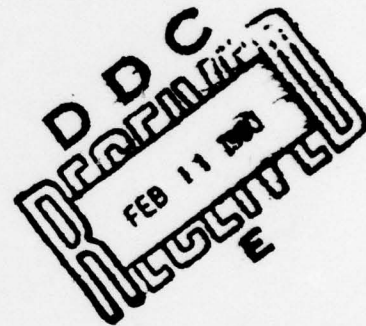
NATIONAL BUREAU OF STANDARDS-1963-A

LEVEL

AN INVESTIGATION OF THE LOW FREQUENCY SOUND
FIELD OF A REVERBERANT ENCLOSURE AND THE
EFFECTS OF DIGITAL ELECTRONIC FEEDBACK

John Baptist Ochs

DDC
FEB 11
E

The Pennsylvania State University
Institute for Science and Engineering
APPLIED RESEARCH LABORATORY
Post Office Box 30
State College, PA 16801

NAVY DEPARTMENT

NAVAL SEA SYSTEMS COMMAND

REPORT DOCUMENTATION PAGE		READ INSTRUCTIONS BEFORE COMPLETING FORM
1. REPORT NUMBER ARL/PSU TM-79-192	2. GOVT ACCESSION NO.	3. RECIPIENT'S CATALOG NUMBER
4. TITLE (and Subtitle) AN INVESTIGATION OF THE LOW FREQUENCY SOUND FIELD OF A REVERBERANT ENCLOSURE AND THE EFFECTS OF DIGITAL ELECTRONIC FEEDBACK		5. TYPE OF REPORT & PERIOD COVERED Ph.D. Thesis, February 1980
		6. PERFORMING ORG. REPORT NUMBER TM 79-192
7. AUTHOR(s) John Baptist Ochs		8. CONTRACT OR GRANT NUMBER(s) N00024-79-C-6043
9. PERFORMING ORGANIZATION NAME AND ADDRESS The Pennsylvania State University Applied Research Laboratory P. O. Box 30, State College, PA 16801		10. PROGRAM ELEMENT, PROJECT, TASK AREA & WORK UNIT NUMBERS 221
11. CONTROLLING OFFICE NAME AND ADDRESS Naval Sea Systems Command Department of the Navy Washington, D. C. 20362		12. REPORT DATE Oct 79
		13. NUMBER OF PAGES 220 pages & figures
14. MONITORING AGENCY NAME & ADDRESS(if different from Controlling Office) Doctoral thesis,		15. SECURITY CLASS. (of this report) Unclassified, Unlimited
		15a. DECLASSIFICATION/DOWNGRADING SCHEDULE

16. DISTRIBUTION STATEMENT (of this Report)

Approved for public release, distribution unlimited,
per NSSC (Naval Sea Systems Command), 12/3/79

17. DISTRIBUTION STATEMENT (of the abstract entered in Block 20, if different from Report)

18. SUPPLEMENTARY NOTES

19. KEY WORDS (Continue on reverse side if necessary and identify by block number)

low frequency, sound, reverberation, enclosures, feedback, filter, diffusion, models

20. ABSTRACT (Continue on reverse side if necessary and identify by block number)

The use of reverberant enclosures for the measurement of sound power of a small source is based on the assumption that the sound is diffuse. In reverberant enclosures, there exists a frequency range above which the characteristics that define a diffuse sound field approach well-defined statistical properties. The goals of this research have been to investigate the low frequency fluctuation of the characteristics of the sound field in comparison to those characteristics at high frequency and to implement —over page

DD FORM 1473 EDITION OF 1 NOV 65 IS OBSOLETE 391 007 UNCLASSIFIED

20. ABSTRACT (Continued)

electronic feedback, using a single Finite Impulse Response (FIR) filter, to beneficially change the degree of diffusion to increase the useful frequency range of reverberant enclosures for sound power measurements. This investigation included a computer model study and an experimental study in a model $(6.82\ m^3)$ enclosure of the frequency-by-frequency fluctuation of the time-averaged spatial mean squared pressure as it relates to sound power measurements; the normalized spatial variance, the probability density function and the cumulative distribution function of time-averaged squared pressure normalized to the spatial mean; the spatially averaged cross correlation coefficient; and the vector intensity.

The model studies were extended to investigate the effectiveness and the stability properties of digital electronic feedback as characterized by a FIR filter. In this study, the open loop response and the fluctuations of the enclosure transfer function with source and receiver positions, wall absorption, and temperature have been investigated. The data from both the computer model and the experimental model showed that the feedback implemented in this study did not significantly affect the diffusion of the sound field.

For the sound field sampled at 120 spatial points from 0 to 1000 Hz at 1 Hz increments, an adequate degree of diffusion is apparent at much lower frequencies than previously predicted, particularly if 1/3-octave averages are considered.

Accession For

NTIS GRA&I

DDC TAB

Unannounced

Justification_____

By_____

Distribution/

Availability Codes

Dist	Avail and/or special
A	

ABSTRACT

The use of reverberant enclosures for the measurement of sound power of a small source is based on the assumption that the sound is diffuse. In reverberant enclosures there exists a frequency range above which the characteristics that define a diffuse sound field approach well-defined statistical properties. The goals of this research have been to investigate the low frequency fluctuation of the characteristics of the sound field in comparison to those characteristics at high frequency and to implement electronic feedback, using a single Finite Impulse Response (FIR) filter, to beneficially change the degree of diffusion to increase the useful frequency range of reverberant enclosures for sound power measurements. This investigation included a computer model study and an experimental study in a model (6.82 m^3) enclosure of the frequency-by-frequency fluctuation of the time-averaged spatial mean squared pressure as it relates to sound power measurements; the normalized spatial variance, the probability density function and the cumulative distribution function of time-averaged squared pressure normalized to the spatial mean; the spatially averaged cross correlation coefficient; and the vector intensity.

The model studies were extended to investigate the effectiveness and the stability properties of digital electronic feedback as characterized by a FIR filter. In this study the open loop response and the fluctuations of the enclosure transfer function with source and receiver positions, wall absorption, and temperature have been investigated. The data from both the computer model and the experimental

model showed that the feedback implemented in this study did not signifi-
cantly affect the diffusion of the sound field.

For the sound field sampled at 120 spatial points from 0 to 1000 Hz
at 1 Hz increments, an adequate degree of diffusion is apparent at much
lower frequencies than previously predicted, particularly if 1/3-octave
averages are considered.

TABLE OF CONTENTS

ABSTRACT iii

LIST OF TABLES vii

LIST OF FIGURES viii

LIST OF SYMBOLS xix

ACKNOWLEDGEMENTS xxiv

I.   INTRODUCTION   1

     1.1 Background and Statement of the Problem   1
     1.2 Objectives and Organization of Presentation 4

II. REVERBERANT ENCLOSURES: FREE-WAVE, RAY-ACOUSTIC MODEL . . . 5

     2.1 Ray-Acoustic Model: Diffusion   5
     2.2 Sound Power Measurement: Ray-Acoustic Model 6
     2.3 Spatial Distribution of Squared Pressure in a
          Diffuse Field   9
     2.4 Estimation of Spatial Mean in a Diffuse Field 10
     2.5 Cross Spectral Density Function in a Diffuse Sound
          Field - Cross Correlation Coefficient 15
     2.6 Summary   19

III. REVERBERANT ENCLOSURES: NORMAL MODE MODEL 21

     3.1 Computer Implementation of the Normal Mode Model . . . 21
     3.2 Sound Power Measurement - Normal Mode Model 30
     3.3 Spatial Pressure Distribution in a Non-Diffuse
          Field   35
     3.4 Estimate of Spatial Mean of Squared Pressure in a
          Non-Diffuse Field   51
     3.5 Normalized Spatial Variance of Squared Pressure in
          a Non-Diffuse Field   57
     3.6 Cross Correlation Coefficient in a Non-Diffuse
          Field   59
     3.7 Energy Flow - Vector Intensity in a Non-Diffuse
          Field   68
     3.8 Summary   70

IV. REVERBERANT SOUND FIELD WITH FEEDBACK 74

     4.1 Introduction 74
     4.2 Theoretical Model   75

LIST OF TABLES

LIST OF FIGURES

LIST OF SYMBOLS

Symbol	Definition
a	radius of finite size source
a/d	analog to digital
c	speed of sound in air
$CDF(x)$	cumulative distribution function of x
$CLR(\omega)$	closed loop response of the feedback loop (Equation (4.7))
ΔdB_{max}	maximum allowable change in dB to avoid the Gibbs phenomenon
DFT	discrete Fourier transform
DHT	discrete Hilbert transform
E_N	product of $\varepsilon_\ell \varepsilon_m \varepsilon_n$ for a given mode number N
f, f_0	frequency, frequency in model enclosure
f_i, i = 1, 2, 3 . . .	frequency for the location of peak amplitude in the design of a FIR filter
f_{BL}	band limiting frequency for the design of a FIR filter
f_c	Schroeder cutoff frequency (Equation (1.1))
f_{c_i}, i = 1, 2, 3 . . .	critical frequency where the phase of the open loop response is 0°
f_{max}	maximum frequency of interest in the design of a FIR filter
f_N	N resonance frequencies for a given rectangular enclosure (Equation (3.6))
f_{N_i}, $f_{N_i + 1}$, $f_{N_i - 50}$	i^{th}, $i^{th} + 1$, and $i^{th} - 50$ resonance frequencies for a rectangular enclosure (see discussion of the computer implementation of the normal mode model in Section 3.2)

Symbol	Definition
f_s	sampling rate of the a/d converters in the FIR filter
Δf	frequency resolution of the FIR filter (Equation (3.2))
FFT	fast Fourier transform
FIR	finite impulse response
g	gain in the open loop response
G_i, $i = 1, 2, 3, 4$	four transfer functions in an enclosure with feedback
G_{21}	cross spectral density function
$Im(G_{21})$	imaginary part of G_{21}
$h(n)$	impulse response of a FIR filter
$H(\omega)$	the Fourier transform of the impulse response of a FIR filter
$\vert H(\omega)\vert$	the magnitude of $H(\omega)$
i	square root of -1
$\vec{I}_r$, $\vec{I}_x$, $\vec{I}_y$, $\vec{I}_z$	vector intensity (Equation (3.)) in the r, x, y, and z direction
k	wave number for the drive frequency f
k_N	wave number for the resonance frequency f_N
K^*	coupling parameter for feedback implementation (Equation (4.3))
ℓ, m, n	quantum mode numbers for a given enclosure resonance frequency
$\ell n \vert H \vert$	natural logarithm (to the base e) of the magnitude of H
L	length of the edges in a rectangular enclosure
$L(\omega)$	open loop response for the feedback loop (Equation (4.8))

Symbol	Definition
M, N	summation index for the modal summation
N_{eq}	the equivalent number of uncorrelated points in a spatial sample
N_t	number of sample points of the impulse response of the FIR filter
p, $p(r_1, t)$	pressure, pressure at position r_1 and time t (Equation (3.1))
$\overline{p^2}$	time-averaged square pressure
$\langle \overline{p^2} \rangle$, $\langle \overline{p^2} \rangle_N$	spatial mean of the time-averaged square pressure based on a spatial sample of N position
$\langle \overline{p^2} \rangle_V$	spatial mean of the time-averaged square pressure based on a volume integral (Equation (3.14))
p^*	complex conjugate of pressure
pT	total pressure with feedback (Equation (4.5))
PDF(x)	probability density function of x
Q_0	source strength
Q_0^f	modified source strength of the feedback loop (Equation (4.6))
r	separation between microphones
$r_{0, 1, 2 \ldots}$	position variables
R	position vector
R(kr)	cross correlation coefficient
$R(kr)_{avg}$	spatially averaged cross correlation coefficient
$R(kr)_T$	theoretical cross correlation coefficient for diffuse sound field (sin(kr)/kr)
S	surface area of the rectangular enclosure

Symbol	Definition
t	time
T_{60}	reverberation time
u	particle velocity
v	velocity of the speaker cone
V, V_0	volume of the rectangular enclosure and model enclosure
w_d	direct field energy density (Equation (2.8))
w_r	reverberant field energy density (Equation (3.10))
w_t	total energy density
$w_{kinetic}$	kinetic energy density (Equation (2.2))
$w_{potential}$	potential energy density (Equation (2.3))
W	sound power
W_0	sound power radiated in free space (Equation (3.10))
W_N	sound power based on the spatial mean of $\overline{p^2}$ sampled at N positions (Equation (3.17))
W_S	sound power based on surface integration (Equation (3.9))
W_V	sound power based on volume mean of $\overline{p^2}$ (Equation (3.15))
x, y, z	positions or directions in the enclosure
α	spatially averaged absorption
β	specific normal admittance
δ_N	modal damping factor (Equation (3.4))
θ_{ap}	phase of the FIR filter in the all pass mode ($|H| = 0$ dB)

Symbol	Definition
θ_{G_i}, $i = 1, 2, 3 \ldots$	phase of the enclosure transfer function
θ_H	phase of the FIR filter
θ_L	phase of the open loop response
λ	wavelength
ϵ_r^2	standard error of estimate for the variation of $R(kr)_{avg}$ from $\sin(kr)/kr$ behavior
ϵ_s^2	standard error of estimate for the variation of a CDF from the exponential CDF
π	3.14159
ρ_o	density of air
$\rho_o c$	characteristic impedance of air
σ^2	spatial variance
$\sigma^2 / \overline{\langle p^2 \rangle}$	spatial variance normalized to spatial mean
ϕ	space angle
$\psi_N(r)$, $\psi_M(r_0)$	eigen function for the Nth or M^{th} modal evaluated at r or r_2
ω	angular frequency

ACKNOWLEDGEMENTS

The author gratefully acknowledges the many people associated with the Applied Research Laboratory at The Pennsylvania State University who have contributed time, effort, experience, and equipment to insure the success of this study. In particular, sincere thanks are extended to Professor Jiri Tichy, thesis advisor, for his guidance and helpful discussion throughout the course of this study and to Professors William Thompson, Jr., James Lawther, and Eugen Skudrzyk for their instruction and participation in the author's doctoral committee.

The author wishes to thank fellow students Messrs. John Bullock, Paul Kitek, Marc Warshowsky, and Gary Elko for their assistance and encouragement. The author wishes to extend his deepest gratitude to Mr. Jack Sharer for his invaluable help with the electronics and programming associated with the microprocessor controls.

CHAPTER I

INTRODUCTION

1.1 Background and Statement of the Problem

Due to the recent public awareness of noise pollution and litigations based on job-related hearing loss, industry and government are concerned with the measurement of the noise radiated from various sources. The basic quantity of interest is the sound power radiated by a source as averaged over 1/3-octave frequency bands within the audible frequency range.

The sound power can be accurately measured for small sources radiating broadband noise above 150 Hz in a large reverberant enclosure as described by the American National Standards Institute Standard ANSI S1.21-1972 (1) (also see Reference (2)). This standard describes the method and qualification procedures for the use of reverberant enclosures for sound power measurement, which is based on the assumption that, within the frequency range of interest, the acoustic energy density is randomly distributed and therefore proportional to the spatial mean of the time-averaged squared pressure $\overline{<p^2>}$.

This assumption gives rise to two fundamental questions: (1) how to determine the diffusion or, more practically, the degree of diffusion necessary for the spatial mean of the time-averaged squared pressure to be proportional to the sound power and (2) how to accurately determine the spatial average of squared pressure. From the many studies of the properties of reverberant enclosures (6, 9, 24, 45, 49, 71, 92, 93) and

spatial averaging techniques (11, 47, 48, 49, 50, 51, 70), it is gener-
ally accepted that a reverberant sound field excited by nonpure-tone
sources is considered to be diffuse at high frequencies in large enclo-
sures where the eigen frequencies of the enclosure are sufficiently close
and the modal overlap is high. At low frequencies, typically below 150
Hz in a 200 m^3 enclosure, the sound field is not considered diffuse, and
the accuracy of measuring sound power via the spatial mean of square
pressure has been shown to be low (34, 67, 82, 84). This is particularly
true for sources that radiate discrete or pure tones (17, 50, 54, 55, 76,
91).

The transition region of the sound field from low modal overlap to
high modal overlap has never been clearly defined. One generally
accepted criterion has been developed by Schroeder (69) which requires
that the normal or eigen modes of an enclosure overlap each other in a
ratio of 3:1, that is, the average spacing of the resonance frequencies
is smaller than one-third of their 3 dB down bandwidth. Based on this
criterion, the lowest frequency, f_c, which defines the useful frequency
range of an enclosure is given by

$$f_c = 2000 (T_{60}/V)^{1/2} , \qquad (1.1)$$

where V is the volume (m^3) and T_{60} is the reverberation time (sec) of
the enclosure. Thus, below f_c, the sound field would lack sufficient
diffusion for accurate measurement of sound power.

One of the main areas of interest in this study will be to investi-
gate the characteristics of the sound field from low to high frequency
in an attempt to quantify the concept of diffusion. To aid in this

investigation, an experimental model enclosure will be used. The char-
acteristics of the model enclosure can be related to a full-size enclo-
sure as recommended by ANSI S1.21-1972 by the frequency transform

$$f_0 = f(V/V_0)^{1/3} \quad , \tag{1.2}$$

where f_0 and V_0 are the frequency and volume of the full-size (200 m^3)
enclosure and f and V are the frequency and volume of the model enclosure
(f = 0.324 f_0 for 200 m^3 enclosure as compared to the 6.82 m^3 model
enclosure described in Chapter V with f_c = 760 Hz for no added absorp-
tion.

In order to improve the diffusion of the sound field at low
frequencies, researchers have employed various methods to modify the
resonance frequency spacing of an enclosure. The use of rotating vanes
(28, 66, 75, 78, 80, 81, 85), static panels, alteration of the enclosure
boundaries (11, 24, 67, 77, 36), or the addition of feedback (22, 23,
27, 32, 37, 43, 69, 89) all attempt to redistribute the energy clustered
at the eigen frequencies of the enclosure. Based on some promising
results predicted in a computer model studied by Lilly (43), the
addition of digital electronic feedback to the enclosure has been shown
to beneficially affect the diffusion of the sound field as indicated by
lowering the normalized spatial variance. A second consideration of
this study will be to investigate theoretically and experimentally the
implementation of digital electronic feedback and its effect on the
diffusion of the sound field.

1.2 Objectives and Organization of Presentation

As stated in the title, the general objective of the study is to investigate the characteristics of the low frequency sound field in a reverberant enclosure and to investigate the effects of implementation of digital electronic feedback. Toward these goals, Chapter II describes the ray-acoustic model for a diffuse sound field and the various statistical quantities that reflect the relative degree of diffusion. In addition, the various assumptions for sound power measurement are outlined. These considerations reflect the properties of the sound field at high frequencies where "high" is relative to the size of the enclosure.

In Chapter III the computer implementation of the normal mode model is described. The various quantities that were described in Chapter II for a diffuse field at high frequency are calculated over the frequency range from below the first enclosure resonance to above f_c for the model enclosure considered. A theoretical study of the sound power radiated in an enclosure to that radiated in free space quantifies the level of diffusion and the accuracy of estimating the spatial mean of squared pressure. In addition, two indicators of the degree of diffusion of the sound field are introduced.

In Chapter IV the sound field with feedback is described using the normal mode model, and the defining characteristics of a programmable digital filter are studied.

Finally, Chapter V describes the experimental investigation, and Chapter VI states the summary and conclusions.

REVERBERANT ENCLOSURES:
FREE-WAVE, RAY-ACOUSTIC MODEL

2.1 Ray-Acoustic Model: Diffusion

As stated in the introduction, the interest in the transition from
the low modal overlap to the high modal overlap frequency region in a
reverberant sound field is based on determining the usable frequency
range for the measurement of sound power. In the frequency range of high
modal overlap, the sound field is considered to be diffuse and the field
exhibits measurable characteristics that are indicative of diffusion.

The concept of a diffuse sound field is based on the ray-acoustic
model which assumes that the reverberant sound field consists of equal
amplitude plane waves traveling with equal probability in all directions.
These plane waves are the result of multiple reflections of sound waves
off the boundaries of the enclosure. At high frequencies (where high is
related to the size of the enclosure), the source excites many enclosure
resonances, each of which exhibit a preferred direction of propagation.
As more modes are excited, the number of directions of wave propagation
increases until the sound field exhibits characteristics which are sta-
tistical in nature. In terms of total acoustic energy, a diffuse sound
field is said to have a uniform distribution of energy density, and, in
relation to the flow of acoustic energy or acoustic intensity, a diffuse
sound field exhibits equal intensity in all directions at all points in
the field. Thus, although there is no known way to measure diffusion

directly, at high frequencies, certain measurable quantities of the sound field in a reverberant enclosure exhibit well-defined statistical properties. In the following sections, the theoretical bases for sound power measurements will be considered along with examining the measurable quantities that are indicative of diffuse sound fields.

2.2 Sound Power Measurement: Ray-Acoustic Model

For a typical reverberant enclosure used for sound power measurements, there exists a frequency region above which the sound field will be considered diffuse and satisfy the qualification criterion set forth by the American National Standards Institute, ANSI SI.21-1972 document (1) (see (65), (82), and (84) for a synopsis and assessment of the qualification procedure). The theoretical basis for the qualification is the assumption that the sound field is diffuse and, by definition, exhibits a uniform distribution of energy density at all points in the enclosure. In general, the total energy density w_t is given by (38)

$$w_t = w_{kinetic} + w_{potential} \quad , \tag{2.1}$$

where the kinetic energy density $w_{kinetic}$ is given by

$$w_{kinetic} = 1/2 \; \rho_o u^2 \tag{2.2}$$

and the potential energy density $w_{potential}$ is given by

$$w_{potential} = 1/2 \; \rho_o (p^2/\rho_o^2 c^2) \quad . \tag{2.3}$$

In these equations p^2 and u^2 are the amplitude of the instantaneous pressure and particle velocity squared, and $\rho_o c$ is the characteristic

impedance of air in MKS rayls. Thus, the total energy density in joules per cubic meter is given by

$$w_t = 1/2 \, \rho_o(u^2 + p^2/\rho_o^2 c^2) \quad . \tag{2.4}$$

For a plane wave, the particle velocity u can be replaced by $p/\rho_o c$ and, finally,

$$w_t = p^2/\rho_o c^2 \quad . \tag{2.5}$$

For the ray-acoustic model of a reverberant enclosure, the total pressure at any point in a diffuse field is the sum of plane waves incident for all directions, and the total energy density is proportional to the spatial average of the squared pressure. Thus,

$$w_t = <\overline{p^2}>/\rho_o c^2 \quad , \tag{2.6}$$

where $\overline{p^2}$ is the time-averaged squared pressure and the <> designates spatial mean.

The problems of adequate averaging in time for continuous or discrete spatial sampling of the sound field are described by Bolt (13), Maling (54), Warshowsky (85), and others (82, 84). Recommended procedures are followed in this study, and the designation of time-averaged will only be used for emphasis.

The relationship between sound power W and energy density w_t was first put forth by Sabine and is based again on classical ray-acoustic model. The total energy density in a reverberant enclosure can be

expressed as the sum of the direct field energy density w_d and the rever-
berant field energy density w_r as

$$w_t = w_d + w_r \quad , \tag{2.7}$$

where

$$w_d = \frac{W}{4\pi r^2 c} \tag{2.8}$$

and

$$w_r = \frac{4W}{c\alpha S} \quad . \tag{2.9}$$

In the preceding equations, r is the distance from the source to the
receiver in meters, α is the average absorption in sabines, and S is the
chamber surface area. These relations were derived assuming a uniform
distribution of absorption over the enclosure surface area and assuming
that the acoustic energy density is uniformly distributed throughout the
enclosure volume (i.e., the sound field is diffuse). Thus, Equation
(2.7) can be written as

$$w_t = \frac{W}{4\pi r^2 c} + \frac{4W}{c\alpha S} \quad . \tag{2.10}$$

Combining Equations (2.10) and (2.6) yields

$$\overline{\langle p^2 \rangle} = \frac{W\rho_o c}{4\pi r^2} + \frac{4W\rho_o c}{\alpha S} \quad . \tag{2.11}$$

By specifying that the measuring points be sufficiently distant from the
source, the direct field contribution can be neglected and the sound

power W can be calculated from the spatial mean of the time-averaged
squared pressure as

$$W = \frac{\overline{<p^2>}\alpha S}{4\rho_o c} \quad , \tag{2.12}$$

where $\overline{<p^2>}$ is typically calculated from the pressure sampled at uncor-
related spatial positions. Finally, in terms of the reverberation time,
T_{60}(sec), and enclosure volume, $V(m^3)$,

$$W = \frac{13.9\overline{<p^2>}V}{\rho_o c^2 T_{60}} \quad . \tag{2.13}$$

Thus, Equations (2.12) and (2.13) form the theoretical basis for
the use of reverberant enclosures for the measurement of sound power.
In practice, two major factors affect the accuracy of measuring the sound
power: (1) determining under what conditions the sound field is diffuse
and (2) determining the criterion for sampling the sound field for an
accurate estimation of the true spatial mean of squared pressure. The
spatial distribution of squared pressure at high frequencies has been
shown to be an important statistical quantity that can be related to both
of the above factors.

2.3 Spatial Distribution of Squared Pressure in a Diffuse Field

Waterhouse (90), Lubman (46), and Schroeder (68) have shown that
the squared pressure in a diffuse sound field has an exponential spatial
distribution. The probability density function PDF(x) of the squared
pressure normalized to the spatial mean $(x = \overline{p^2}/\overline{<p^2>})$ is given by

$$PDF(x) = e^{-x} \quad , \tag{2.14}$$

which has the so-called "saturation" cumulative distribution function CDF(x),

$$CDF(x) = 1 - e^{-x} \quad . \tag{2.15}$$

Equations (2.14) and (2.15) are plotted in Figure 2.1 along with experimental data taken for a pure-tone source excitation in the high frequency region (1000 Hz) and in the low frequency region (200 Hz) of the experimental enclosure (see Chapter V for details of the experimental setup). The variation of the measured CDF from that expected for a diffuse sound field can be considered an indication of diffusion since, as seen in Figure 2.1, the CDF at 1000 Hz follows that for a diffuse sound field more closely than the CDF at 200 Hz. This variation of CDF's will be considered in Section 3.4.

2.4 Estimation of Spatial Mean in a Diffuse Field

The error in estimating the spatial mean for a diffuse sound field excited by a pure-tone source depends on the underlying exponential distribution function $(x = \overline{p^2}/\overline{<p^2>})$ and is given by the variance (46) as

$$\sigma_x^2 = 1/N_{eq} \quad , \tag{2.16}$$

where N_{eq} is the equivalent number of uncorrelated spatial samples. Cook et al. (20) have derived the point-to-point correlation coefficient for a diffuse sound field based on the ray-acoustic free wave model as

$$R(kr) = \sin(kr)/kr \quad , \tag{2.17}$$

where $k = \omega/c$ is the wave number at angular frequency ω for speed of sound in air, c (meters/sec), and r is the distance in meters between
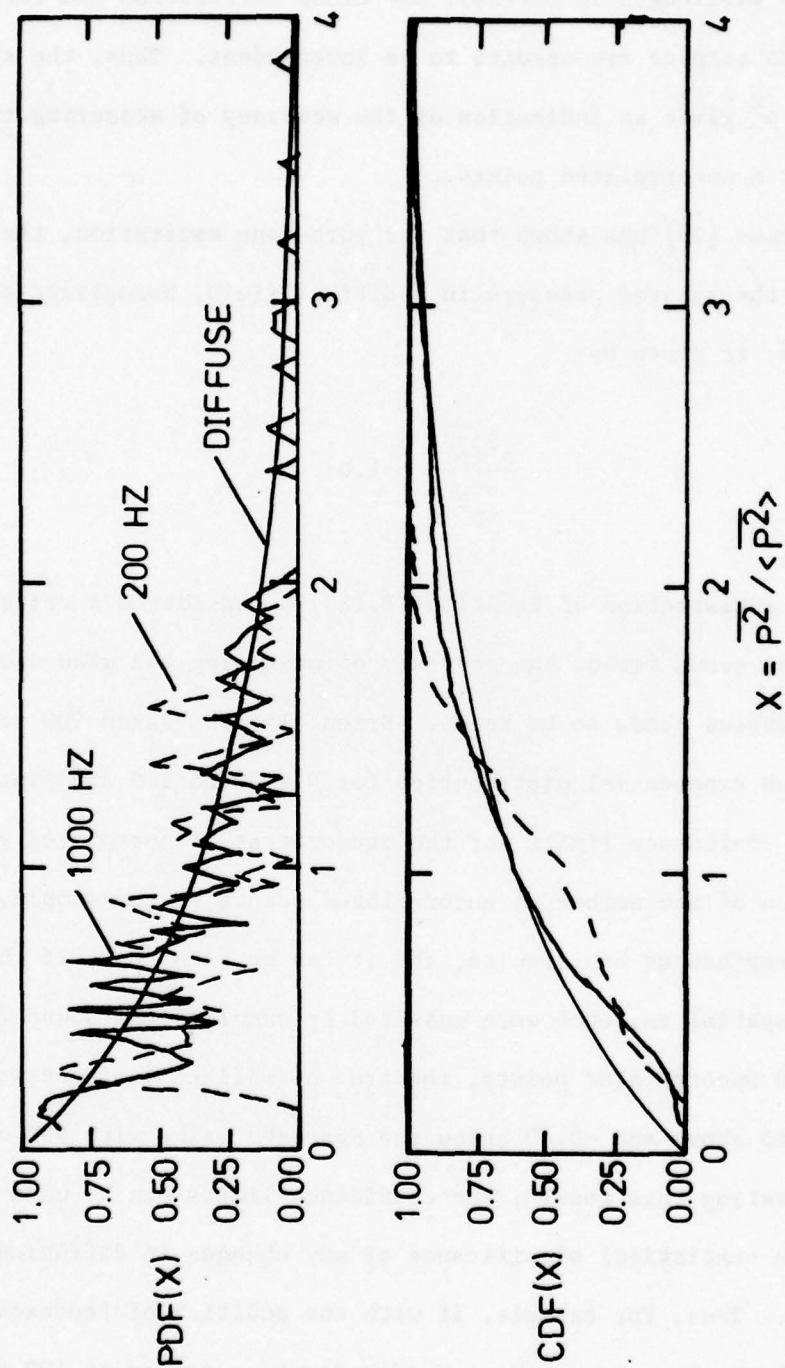
Figure 2.1. Probability density function $PDF(x)$ and cumulative distribution function $CDF(x)$ for $x = \overline{p^2}/\langle \overline{p^2} \rangle$ for a diffuse field, which has an exponential distribution, and $CDF(x)$ calculated from experimental data for the model enclosure (6.82 m^3) at 1000 Hz and 200 Hz.

the two points. From Figure 2.2, which shows a plot of this function, one can observe that, for spatial samples greater than $\lambda/2$ apart ($kr = \pi$ and λ is the wavelength in meters), the cross correlation coefficient is small and the samples are assumed to be independent. Thus, the spatial variance of $\overline{p^2}$ gives an indication of the accuracy of measuring the spatial mean at N uncorrelated points.

Waterhouse (90) has shown that for pure-tone excitation, the spatial variance of the squared pressure in a diffuse field, normalized to the spatial mean, is given by

$$\frac{\sigma^2(\overline{p^2})}{\overline{\langle p^2 \rangle}} = 1.0 \quad . \tag{2.18}$$

If the satisfaction of Equation (2.18) is considered a criterion for a diffuse sound field, the accuracy of measuring the mean and variance at N samples needs to be known. Brien (15) has taken 200 sets of N samples of an exponential distribution for N = 20 to 100 and plotted the 90% and 95% confidence limits for the measurement of normalized variance as a function of the number of uncorrelated points in the sample. Figure 2.3 reproduces his results, and it can be seen that, if the normalized spatial variance were measured by sampling the sound field at, say, 100 uncorrelated points, the true normalized variance would lie between +0.45 above and -0.40 below the measured value with 95% confidence. Restating this result, the confidence limits can be used to indicate the statistical significance of any changes in diffusion of the sound field. Thus, for example, if with the addition of feedback the normalized spatial variance of squared pressure measured at 100 points were to decrease from 1.5 to 1.4 at a particular frequency, the 95%
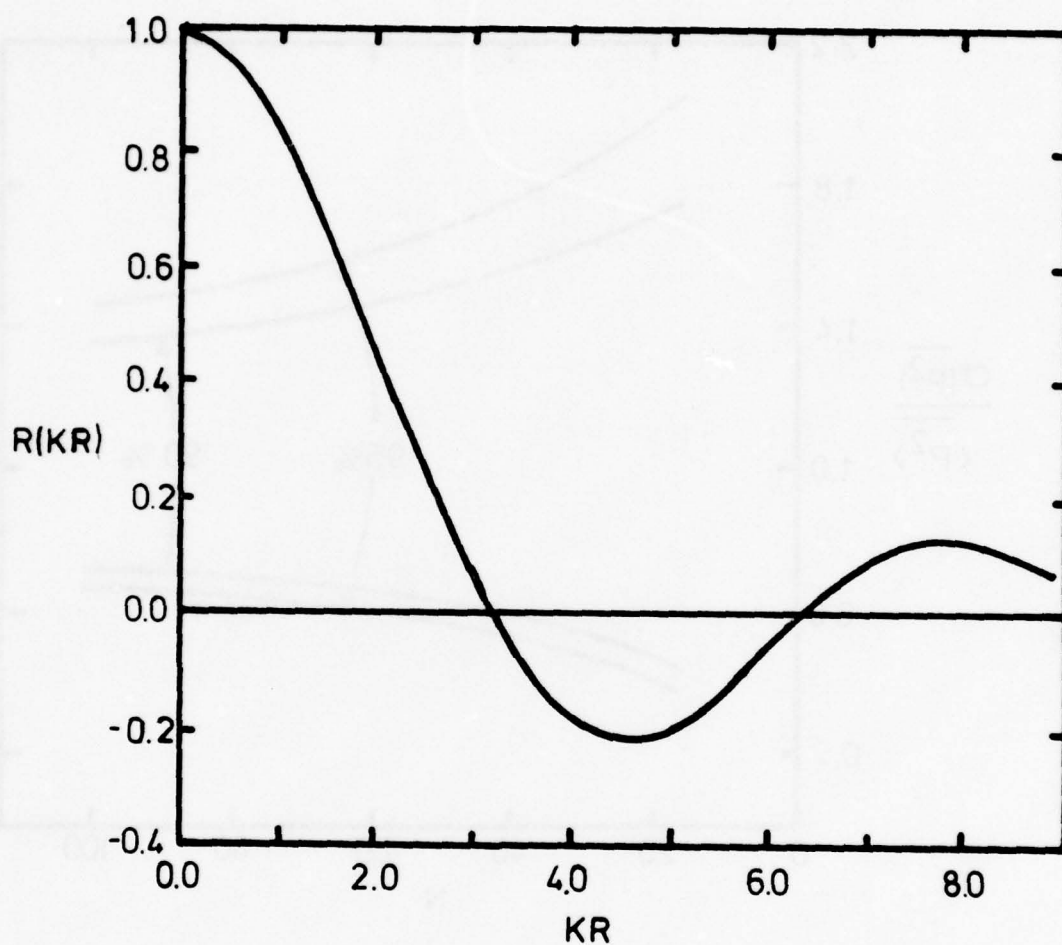
Figure 2.2. Theoretical cross correlation coefficient R(kr) for squared pressure normalized to the spatial mean for diffuse sound field for narrowband excitation, where k is the wave number and r is the microphone separation.
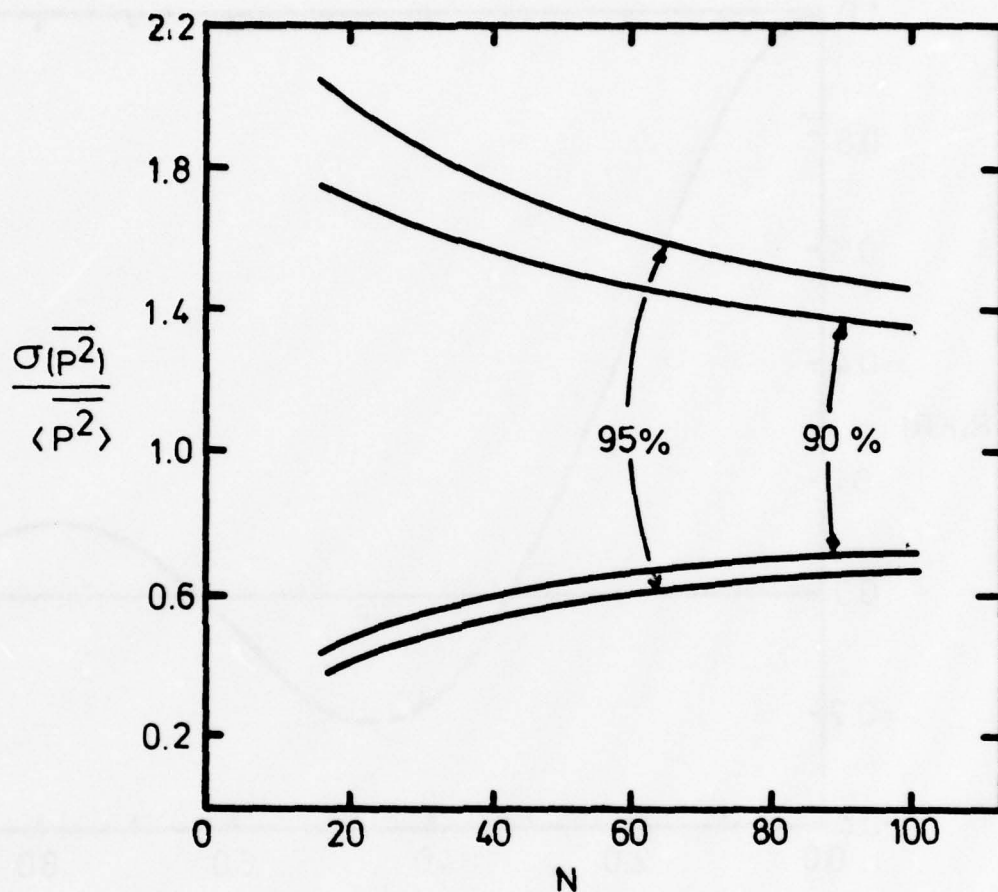
Figure 2.3. Confidence limits of 90% and 95% for the measurements of spatial variance of squared pressure normalized to the spatial mean as a function of the number of uncorrelated samples for an exponential distribution.

confidence limits for the measurement of normalized variance of an expo-
nential distribution at 100 points would indicate that the change is not
statistically significant since it falls within +0.45 or -0.40 from the
previously measured value.

Nevertheless, from Equation (2.18), if the measured normalized vari-
ance (plus and minus the 95% confidence limits) approaches unity with
increasing frequency, it would indicate that the sound field is approach-
ing the diffuse condition.

2.5 Cross Spectral Density Function in a Diffuse Sound Field - Cross Correlation Coefficient

Figure 2.4 illustrates a model of the sound field for the
calculation of the cross spectral density function for two closely spaced
microphones at positions 1 and 2 separated by r meters and R meters from
the source at angle ϕ. The time-averaged cross spectral density function
is of particular importance since the real part normalized to the
magnitude yields the cross correlation coefficient R(kr) (8) and the
imaginary part is proportional to the vector intensity $\vec{I}$ or power flow
in the direction of the microphone axis (31). For a diffuse field
consisting of equal amplitude plane waves traveling with equal
probability in all directions, it has been suggested that a necessary
criterion for diffusion is that R(kr) follow the sin(kr)/kr behavior in
all radial directions from any given reference point (17, 20, 40). This
criterion for diffusion has been shown to be valid by several
investigators using narrowband noise (40), variable tones (20, 93), or
pure-tone sources with rotating diffusion (85).

Piersol (62) and Cross and Sherman (21) have considered the spatial
correlation for various noise models. In particular, for the case
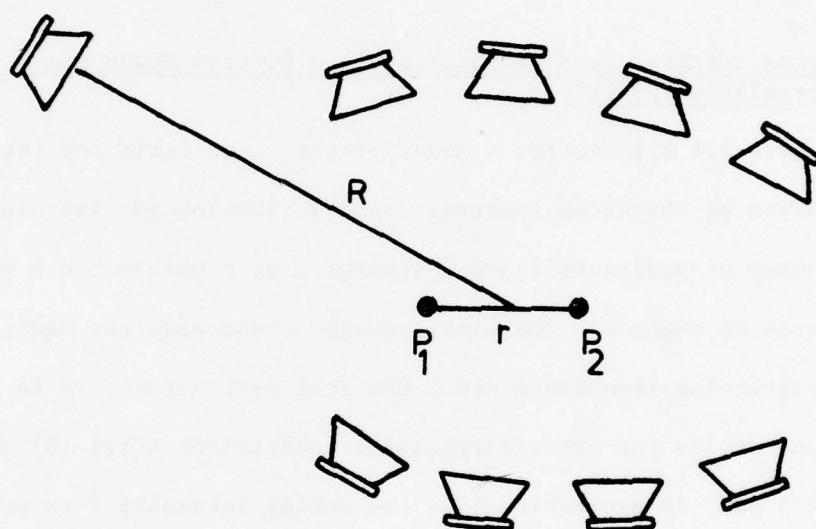
Figure 2.4. Illustration of the ray-acoustic model for measurement of
the cross spectral density function in a diffuse field.

illustrated in Figure 2.4, it is assumed that the total cross spectrum is given as the sum of a diffuse field component (multiple sources) and the progressive wave contribution directly from the source. For a noise model with few sources, as in a semireverberant environment, the effects of the reverberant enclosure can be measured for narrowband sources.

The characteristics of a highly reverberant sound field are somewhat different, particularly when it is excited by a pure-tone source. It can be easily shown that for pure-tone excitation, the cross correlation coefficient is given by

$$R(kr) = \cos(\theta_2 - \theta_1) \quad , \tag{2.19}$$

where $\theta_2 - \theta_1$ is the phase difference between the two measuring points.

Since for pure-tone excitation the phase distribution of a sound field in an enclosure is fixed by the standing wave pattern, the phase difference between any two points in the enclosure could be any value between $\pm 180^\circ$. Large variations from the $\sin(kr)/kr$ behavior for a given direction in a reverberant enclosure excited by a pure tone have been reported in leterature (17, 18) and verified in this study. For example, Figure 2.5 shows the cross correlation coefficient given by the cosine of the measured phase difference in the model enclosure between a fixed microphone and a microphone moving in a straight line away from the fixed reference microphone at 1000 Hz, which is well above f_c. For comparison, the cross correlation coefficient for a diffuse field (expected in any direction) is plotted with a dashed line. The noticeable difference between the two plots is an indication of the special nature of the standing wave field. Pure-tone excitation of the sound field has been experimentally and analytically verified as the worst case condition for
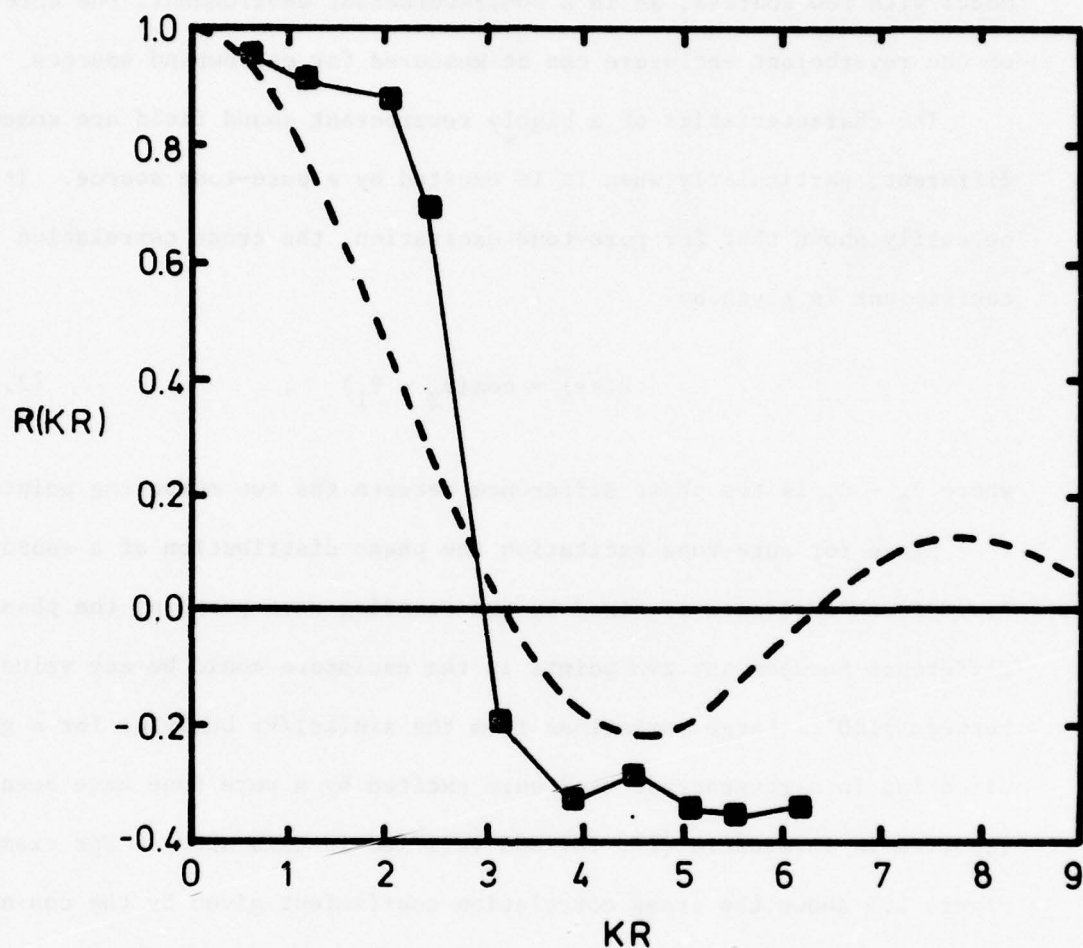
Figure 2.5. Sin(kr)/kr (---) and measured (——) cross correlation coefficient as a function of kr for pure-tone excitation at 1000 Hz in an arbitrary direction from the reference position at (0.841 m, 0.841 m, 0.841 m) in the model enclosure (6.82 m^3).

the measurement of sound power (11, 50, 53, 54, 55, 79, 91). In the next chapter the various indicators of diffusion will be investigated for pure-tone excitation using the normal mode model, which can be used to investigate both the high and low frequency regions of an enclosure.

2.6 Summary

The diffuse sound field, which is assumed to exist in the frequency region of high modal overlap in a reverberant enclosure, can be described in several equivalent ways. Two such common definitions of a diffuse field are:

(1) A diffuse field consists of plane waves traveling with equal probability in all directions about all points in the field.

(2) In a diffuse field there exists equal energy flow in all directions at all points in the field.

The free-wave, ray-acoustic model has been shown to be an effective tool in describing the characteristics of a diffuse sound field. These characteristics, which are necessary but not sufficient for a diffuse field, are:

(1) The spatial mean of the square pressure is proportional to the sound power.

(2) The spatial distribution of square pressure normalized to the spatial mean is an exponential distribution.

(3) The spatial variance of squared pressure normalized to the spatial mean approaches unity for pure-tone excitation.

(4) For narrowband excitation, the cross correlation coef-
ficient for a pair of microphones separated by a dis-
tance, r, is given by sin(kr)/kr.

For pure-tone excitation, the sound field in a reverberant enclosure
consists of a fixed pressure amplitude and phase distribution, and the
cross correlation coefficient even at high frequencies does not follow
the sin(kr)/kr behavior.

CHAPTER III

REVERBERANT ENCLOSURES:
NORMAL MODE MODEL

3.1 Computer Implementation of the Normal Mode Model

Morse (59) has shown that the pressure at any point within the boundaries of a rectangular enclosure, excited by a pure tone from a point source, is given by the solution of the forced wave equation expressed as a sum of the eigen functions for the enclosure. Thus,

$$p(r_1,t) = \left(\frac{i\omega Q_0}{V}\right) \sum_N \frac{E_N \psi_N(r_1) \psi_N(r_0)}{k^2 - k_N^2 + 2ik\delta_N} e^{-i\omega t} \quad , \tag{3.1}$$

where $p(r_1,t)$ is the pressure; r_1 is the microphone position (x, y, z); r_0 is the source position; t is time; $i = \sqrt{-1}$; ω is the angular frequency of excitation; Q_0 is the source strength (mass flow/sec); V is the volume of the enclosure with sides L_x, L_y, and L_z; $k = \omega/c$ is the wave number; and c is the speed of sound in air. For a rectangular enclosure with small and uniform wall absorption α, the specific normal admittance β is approximately 8α and is assumed to be real. Based on the assumption that $\beta \ll 1$,

$$\psi_N(r_1) \simeq \cos\left(\frac{\ell\pi x}{L_x}\right)\cos\left(\frac{m\pi y}{L_y}\right)\cos\left(\frac{n\pi z}{L_z}\right) \quad , \tag{3.2}$$

$$k_N^2 \simeq \left(\frac{\ell\pi}{L_x}\right)^2 + \left(\frac{m\pi}{L_y}\right)^2 + \left(\frac{n\pi}{L_z}\right)^2 \quad , \qquad (3.3)$$

and

$$\delta_N \simeq (\varepsilon_\ell/L_x + \varepsilon_m/L_y + \varepsilon_n/L_z)\beta \quad . \qquad (3.4)$$

In these equations, $E_N = \varepsilon_\ell \varepsilon_m \varepsilon_n$, where $\varepsilon = 1$ for ℓ, m, or n equal to 0, $\varepsilon = 2$ otherwise, and ℓ, m, n are the real positive integer quantum numbers corresponding to the ith of N modes included in the summation.

Equation (3.1) describes the pressure at a point in an enclosure as the sum of the contributions of all the normal modes excited at frequency ω. Figure 3.1 shows the computer generated magnitude and phase (relative to the source) of the time-averaged pressure in dB (ref 20 µPa) as a function of the drive frequency $f = \frac{\omega}{2\pi}$ for $\beta = 0.005$, the source in a corner of the enclosure and the receiver 1 meter away.

Figure 3.2 shows the magnitude and phase (relative to the source) of the pressure as a function of distance as the receiver is moved through the enclosure in a straight line for 400 Hz excitation, $\beta = 0.005$, and the source in a corner of the enclosure. Note that in both Figure 3.1 and Figure 3.2 the phase exhibits an overall negative slope (phase lag) and appears to be discontinuous due to the normalization of the phase to be between $\pm 180^o$. This normalization of the phase appears throughout this paper.

Thus, Equation (3.1) can be used to investigate both the spatial and frequency fluctuations of the amplitude and phase for pure-tone excitation. The implementation of Equation (3.1) on a high speed, large memory minicomputer makes this study possible. In order to decrease the

23
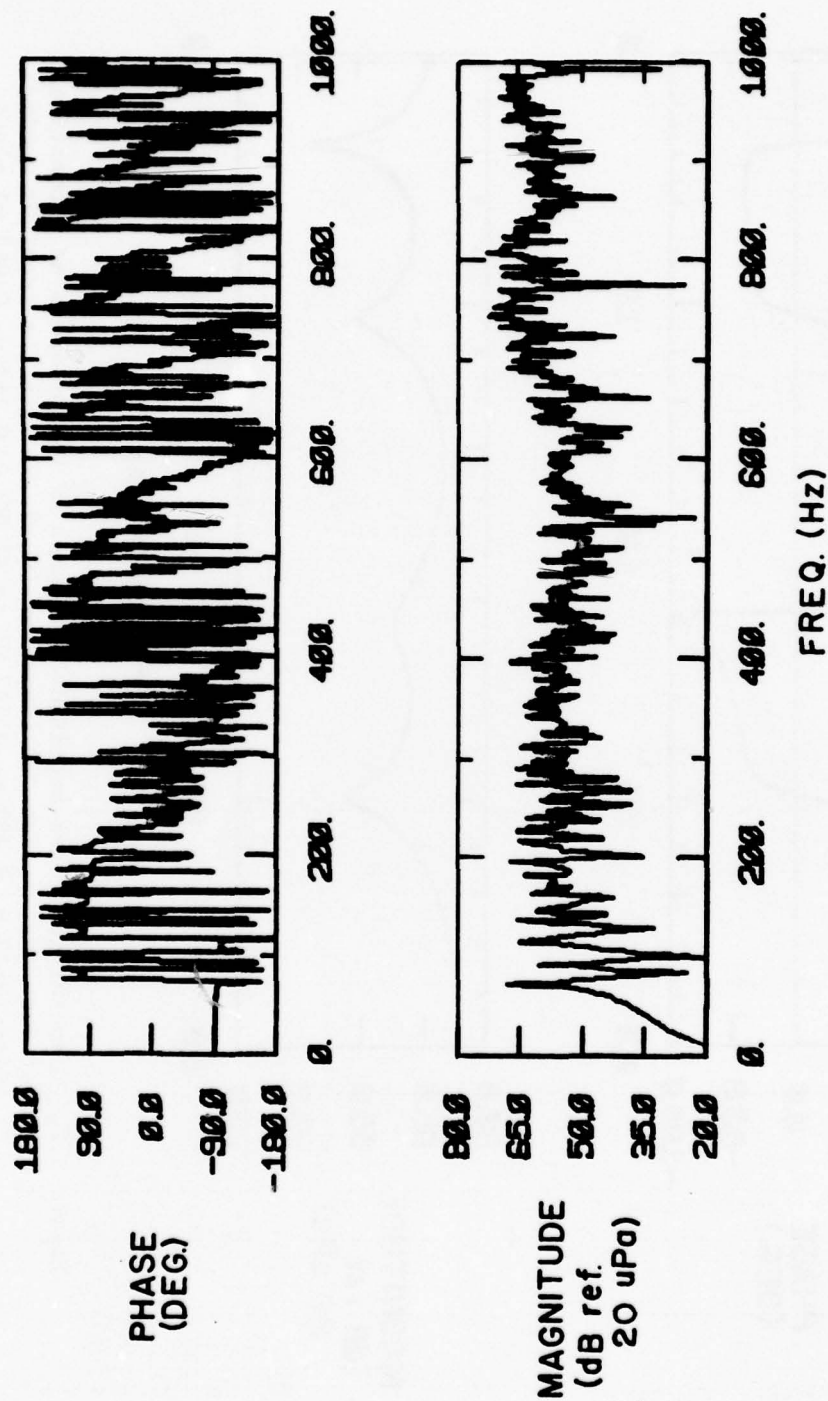
Figure 3.1. Computer generated magnitude and phase of the pressure as a function of frequency for the model enclosure (6.82 m^3) with the source in a corner and a receiver 1 meter away. β = 0.005.
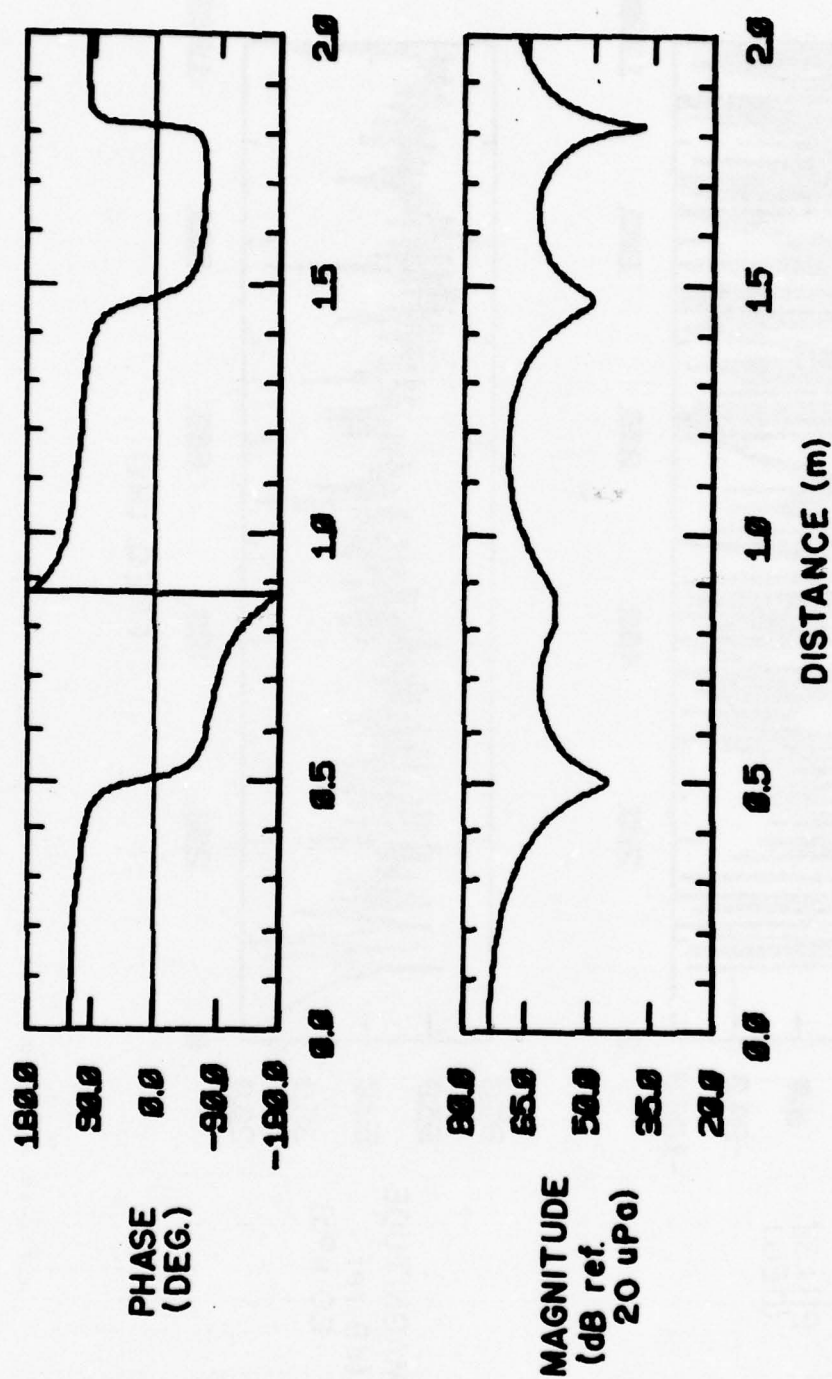
Figure 3.2. Computer generated magnitude and phase of the pressure as a function of distance, r, for the source at (0, 0, 0) with the receiver moving from (0.10 m, 0.753 m, 0.947 m) to (2.00 m, 0.753 m, 0.947 m) along a straight line at 400 Hz. β = 0.005.

amount of time to calculate the pressure as the sum of the contributions of <u>all</u> the eigen modes, the number of modes that contributed significantly to the magnitude and phase as a function of frequency and for a given β has been calculated for the source in the reverberant field. The total number of modes with resonance frequencies less than the drive frequency f can be approximated by

$$N = \frac{4}{3}\frac{\pi V}{c^3} f^3 + \frac{\pi S}{4c^2} f^2 + \frac{L}{8c} f \quad , \tag{3.5}$$

where $V = L_x L_y L_z$, $S = 2(L_x L_y + L_y L_z + L_x L_z)$, and $L = 4(L_x + L_y + L_z)$. Based on this equation approximately 900 modes would be summed for each frequency increment up to 1000 Hz. By solving Equation (3.3) for f_N given by

$$f_N = \frac{c}{2\pi}\left[\left(\frac{\ell\pi}{L_x}\right)^2 + \left(\frac{m\pi}{L_y}\right)^2 + \left(\frac{n\pi}{L_z}\right)^2\right]^{1/2} \tag{3.6}$$

and ordering the modes in sequence from low to high frequency, the total number of modes N less than a given frequency can be plotted as a function of frequency as in Figure 3.3.

As a matter of practical implementation only the modes in the vicinity of the driving frequencies contribute significantly to the total pressure when the source and receiver are well separated. By experimenting with various criteria for "significant" contribution, the criterion of $\pm 1.0^\circ$ phase stability for the addition of 20 modes in the summation was chosen. Figure 3.4 plots the number of modes as a function of frequency for the source and receiver positions as in Figure 3.1 and with $\beta = 0.005$. It should be noted that the frequency regions
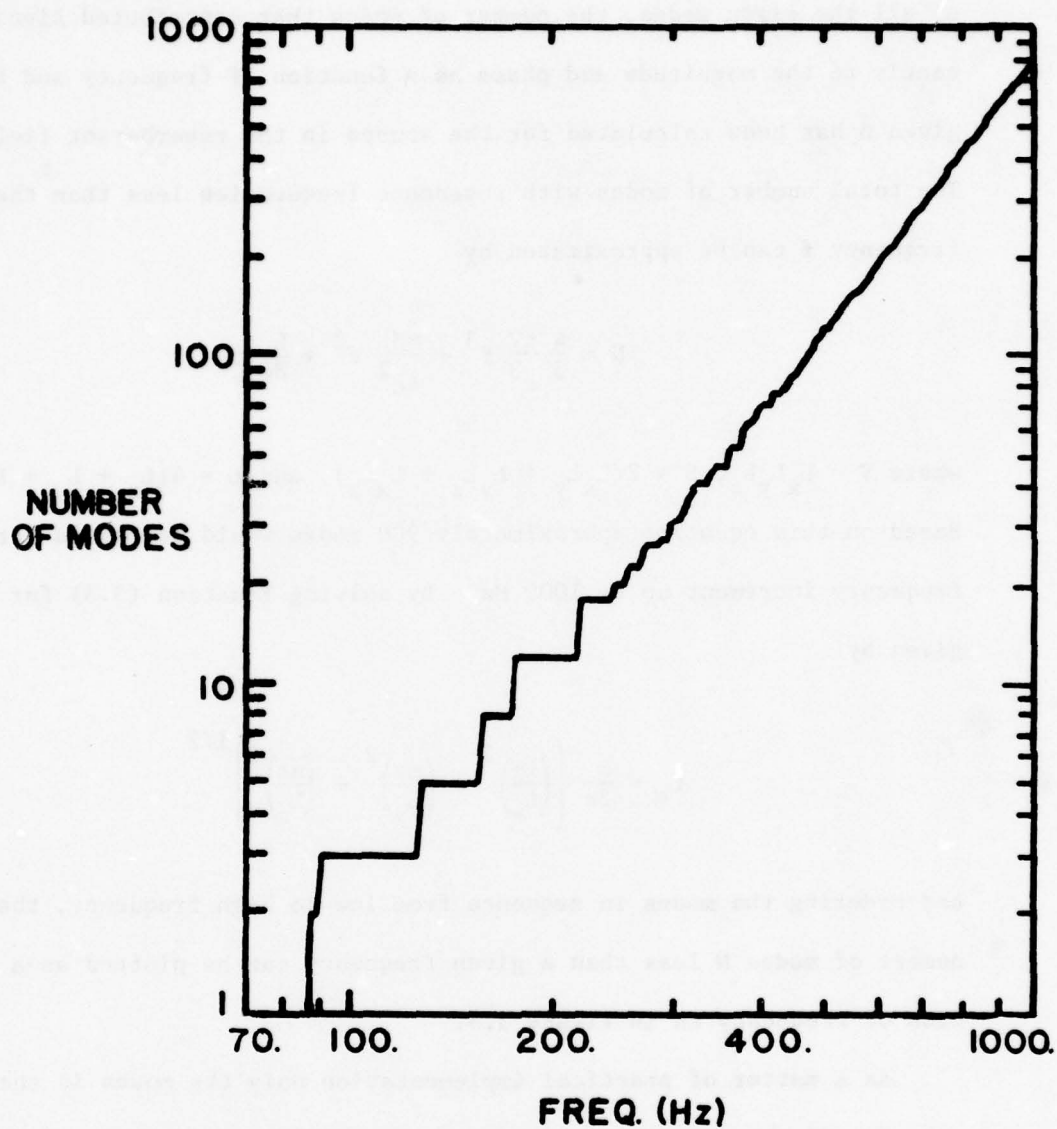
Figure 3.3. Total number of modes with resonance frequencies less than
the drive frequency f for the model enclosure (6.82 m^3)
based on Equation (3.3).
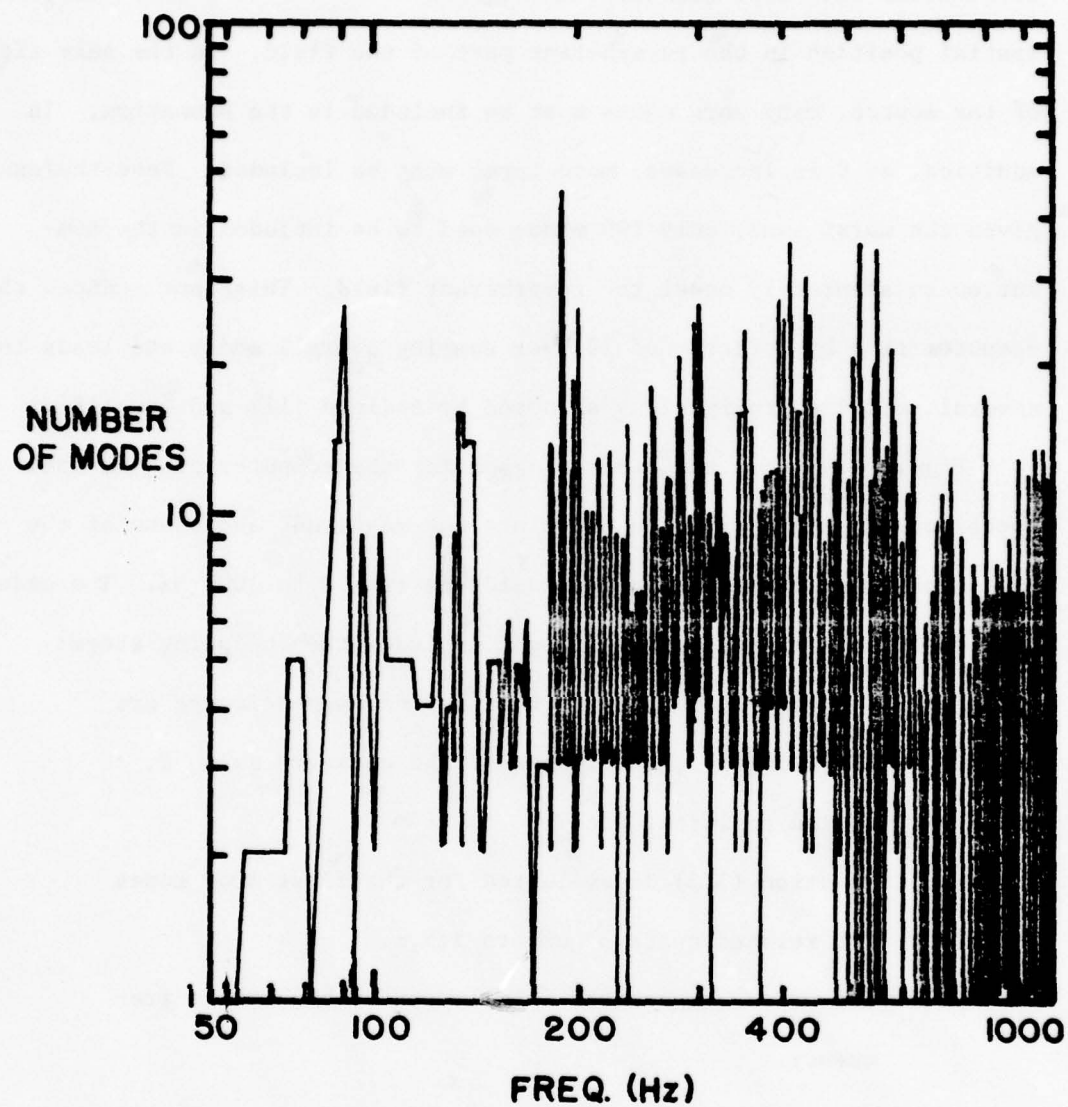
Figure 3.4. The number of modes in summation of Equation (3.1) for ±1° phase accuracy as a function of frequency for the model enclosure. β = 0.005.

between resonances require the greatest number of terms in the summation, and the center of the enclosure, which exhibits peaks only at resonance frequencies with even quantum numbers, proved to be the most sensitive spatial position in the reverberant part of the field. In the near field of the source, many more modes must be included in the summation. In addition, as β is increased, more terms must be included. Nevertheless, given the worst case, only 100 modes need to be included in the summation to accurately model the reverberant field. This fact reduced the computer time by a factor of 10 over summing overall modes and leads to several useful approximations as noted by Bodlund (11) and Chu (18).

Figure 3.5 shows the block diagram for the computer program that implements Equation (3.1) to calculate the magnitude and phase of the pressure at 120 positions in the enclosure from 0 to 1000 Hz. The order of sequences in the programming logic includes the following steps:

(1) The various parameters that define the enclosure are entered (i.e., the length of the chambers axis, β, source position, etc.).

(2) Equation (3.3) is evaluated for the first 1000 modes and related quantum numbers ℓ, m, n.

(3) The modes are ordered from lowest to highest in frequency.

(4) The receiver positions are determined.

(5) Each driving frequency f is located between two resonance frequencies f_{N_i} and $f_{N_i + 2}$.

(6) The receiver position is set.

(7) The real part and the imaginary part of Equation (3.1) are calculated starting 50 modes less than f_{N_i} and

```
┌─────────────────────────────┐
│   SET CONSTANT PARAMETERS    │
│  (Lₓ, L_Y, L_Z, β, c, ETC.) │
└─────────────────────────────┘
              │
┌─────────────────────────────┐
│  CALCULATE 1200 EIGEN MODES  │
│  BY INCREASING ℓ,m,n INDICES │
└─────────────────────────────┘
              │
┌─────────────────────────────┐
│    ORDER THE 1ST 1000        │
│     EIGEN FREQUENCIES        │
└─────────────────────────────┘
              │
┌─────────────────────────────┐
│  CALCULATE THE DESIRED ARRAY │
│   OF 120 RECEIVER POSITIONS  │
└─────────────────────────────┘
              │
┌──────────────────────────────────┐
│ SET MAXIMUM AND MINIMUM FREQUENCY │
│     AND FREQUENCY RESOLUTION      │
└──────────────────────────────────┘
              │
┌──────────────────────────────────────┐
│ POSITION THE DRIVING FREQUENCY f BETWEEN │
│    TWO CONSECUTIVE EIGEN FREQUENCIES     │
└──────────────────────────────────────┘
              │
┌─────────────────────────────┐
│      SELECT ONE OF THE       │
│     RECEIVER POSITIONS       │
└─────────────────────────────┘
              │
┌───────────────────────────────────────────────┐
│     CALCULATE THE PRESSURE AT FREQUENCY f       │
│ AND GIVEN POSITION AS THE SUM OF CONTRIBUTION   │
│ OF 100 MODES, 50 LESS THAN f 50 GREATER THAN f  │
└───────────────────────────────────────────────┘
              │
┌─────────────────────────────┐
│    STORE DATA IN AN ARRAY    │
│    RETURN FOR NEXT POSITION  │
└─────────────────────────────┘
              │
┌─────────────────────────────┐
│     WRITE DATA TO TAPE       │
│   RETURN FOR NEXT FREQUENCY  │
└─────────────────────────────┘
              │
         ┌─────────┐
         │  STOP   │
         └─────────┘
```

Figure 3.5. Block diagram of the computer program logic for the implementation of Equation (3.1).

summing over 100 modes (if $f_{N_i} - 50$ is less than the first mode, the summation starts at the first mode).

(8) The magnitude and phase are calculated for each receiver position and each frequency and stored in magnetic tape.

(9) The process returns to Step (6) and is repeated for each receiver position.

(10) The process returns to Step (5) and is repeated for each frequency.

To calculate the magnitude and phase of the pressure at 120 spatial positions from 1 to 1000 Hz takes approximately three hours on a System 85 computer with 128 K bytes memory. The computer program implementation of the normal mode model can be used to study the fluctuation of pressure as a function of frequency for various values of β, source positions, receiver positions, temperature changes, for a variety of chamber volumes and length-to-width-to-height ratio. In addition, the spatial characteristics of the sound field that are indicative of diffusion, such as the cross correlation coefficient, the cross spectral density function, the vector intensity, etc., can be investigated as a function of frequency for the transition from non-diffuse to diffuse conditions. With an appropriate high speed, large memory computer, both the low and high frequency regions of the sound field can be examined.

3.2 Sound Power Measurement - Normal Mode Model

Maling (53) and Bodlund (11) have shown that the total sound power output W can be found by integrating the time-averaged sound intensity

over the surface area of the enclosure assuming the particle velocity $u = \frac{p\beta}{\rho_o c}$. Thus, W is given by

$$W = \int \int_S \frac{1}{2}(pp*)\beta/\rho_o c \; dB \quad , \tag{3.7}$$

where p* is the complex conjugate of p. It can be easily shown that $\frac{1}{2}(pp*)$ can be expressed in terms of Equation (3.2) as

$$\overline{p^2} = \frac{1}{2}(pp*) = \frac{\omega^2 Q_0^2}{2V^2} *$$

$$\sum_N \sum_M \frac{E_N E_M \psi_N(r) \psi_N(r_0) \psi_M(r) \psi_M(r_0) \left((k^2 - k_N^2)(k^2 - k_M^2) + 4k^2 \delta_N \delta_M \right)}{\left((k^2 - k_N^2)^2 + (2k\delta_N)^2 \right) \left((k^2 - k_M^2)^2 + (2k\delta_M)^2 \right)} \; .$$

$$\tag{3.8}$$

By evaluating the surface integral of Equation (3.8), Bodlund has shown that Equation (3.7) can be expressed as follows:

$$W_S = \frac{\omega^2 Q_0^2}{\pi c V} \sum_N \frac{E_N \psi_N^2(r_0) \delta_N}{(k^2 - k_N^2)^2 + (2k\delta_N)^2} \quad . \tag{3.9}$$

Normalizing Equation (3.9) to the free-field power output W_0 given by

$$W_0 = \omega^2 Q_0^2 / 8\pi \ell c \quad , \tag{3.10}$$

Equation (3.12) becomes

$$\frac{W_S}{W_0} = \frac{8\pi}{V} \sum_N \frac{E_N \psi_N^2(r_0) \delta_N}{(k^2 - k_N^2)^2 + (2k\delta_N)^2} \quad . \tag{3.11}$$

Figure 3.6 shows the fluctuation of the ratio of sound power radiated in a reverberant enclosure to that in free space as a function of frequency for the model chamber with $\beta = 0.01$ for the source near a corner (Figure 3.6a) and in a random spatial position (Figure 3.6b). For comparison, the 1/3-octave average of the curves in Figure 3.6 are plotted in Figure 3.7. Note that, for the sound source near the corner of the enclosure, the sound power ratio fluctuates from +9.0 dB at low frequency to -9.0 dB near 500 Hz and 0 dB above 800 Hz. This fluctuation illustrates the problems associated with the effects of the impedance near an enclosure boundary. Note also that the sound power ratio for the source in a typical spatial position approaches 0 dB on the average at 400 Hz, which is well below the critical frequency $f_c \simeq 760$ Hz given by Schroeder as the low frequency limit for adequate diffusion.

Based on Equation (3.11), Bodlund [11] has investigated the variance of W/W_0 about the mean of W/W_0 for different source positions and found that it is approximately 1.5 dB at low frequencies, reducing to 1.0 dB at high frequencies. Maling [53] has reported similar results at high frequency, and it has been noted that, for the dominance of oblique
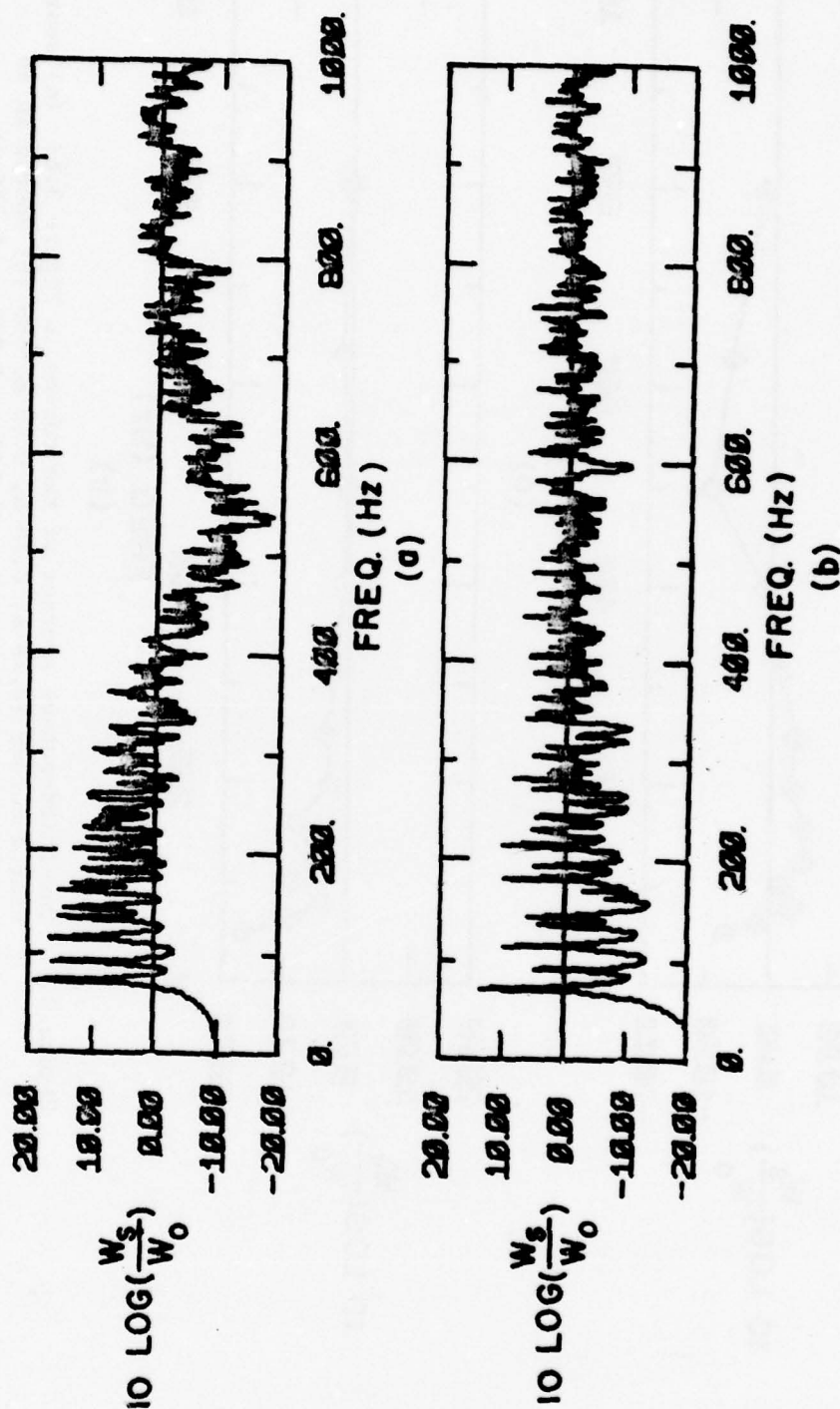
Figure 3.6. Ratio of sound power radiated in a reverberant enclosure to that radiated in a free field in dB as a function of frequency for the model enclosure (6.82 m^3) with β = 0.005 and (a) the source near the corner (0.18 m, 0.18 m, 0.18 m) and (b) the source in an arbitrary spatial position (1.596 m, 1.005 m, 0.785 m).
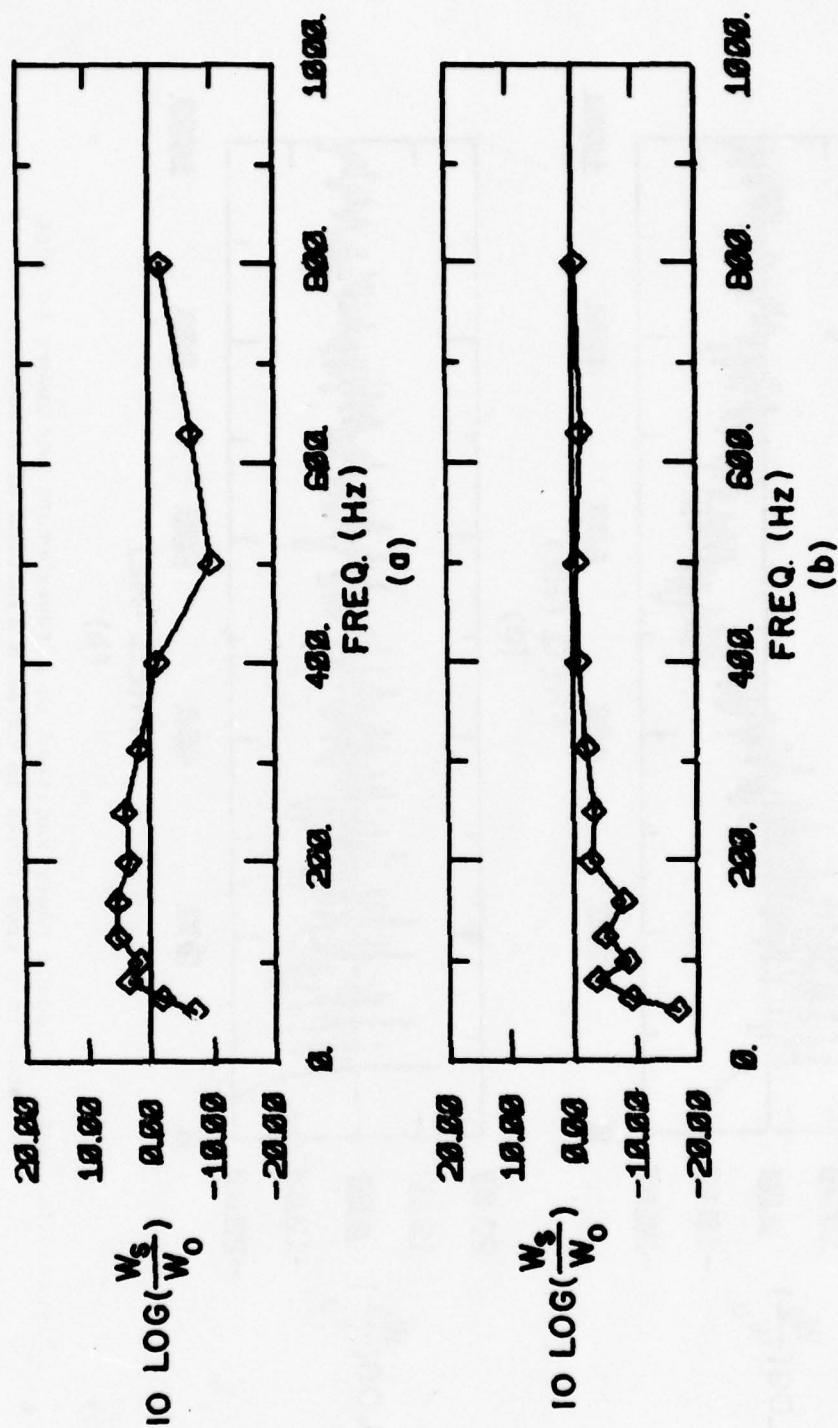
Figure 3.7.   One-third-octave average of the curves in Figure 3.6:   (a) source near a corner (0.18 m, 0.18 m, 0.18 m) and (b) source in an arbitrary spatial position (1.596 m, 1.005 m, 0.785 m).

modes, δ_N, as given by Equation (3.4), reduces to S/V. Thus, Equation (3.11) can be rewritten as

$$W_S/W_0 = \frac{64\beta S}{V^2} \sum_N \frac{\psi_N^2(r_0)}{(k^2 - k_N^2) + \frac{(2k\beta S)^2}{V}} \quad . \tag{3.12}$$

3.3 Spatial Pressure Distribution in a Non-Diffuse Field

In the low modal overlap regions, well separated eigen frequencies result in large variations in the frequency and spatial responses of the pressure field. Waterhouse (91) has derived the theoretical spatial cumulative distribution functions for the excitation of a single axial, tangential, and oblique mode, and these are reproduced for reference in Figure 3.8. Due to the specification of the ratio of L_y to L_x, L_z to L_x for sound power measurements (typically, $1:\sqrt{2}:\sqrt[3]{2}$ (44, 72)), a single natural mode shape is typically not encountered. Even at low frequency when pure-tone excitation is tuned to a resonance frequency, the pressure in the nodal planes is determined by adjacent mode shapes (74).

In order to investigate the variation of the probability density function (PDF) and the cumulative distribution function (CDF) for the low frequency region of the model enclosure, Equation (3.1) was used to generate the pressure at 120 positions in the enclosure in a rectangular grid of points 0.152, 0.203, and 0.305 meters apart from 50 to 1000 Hz at 10 Hz increments. Because of the number of spatial samples per wavelength, very little difference was noted between the data generated for the three different separations. At each frequency, the PDF and CDF for the spatial data normalized to the spatial means were calculated. Figures 3.9 and 3.10 show the PDF and CDF for the model enclosure
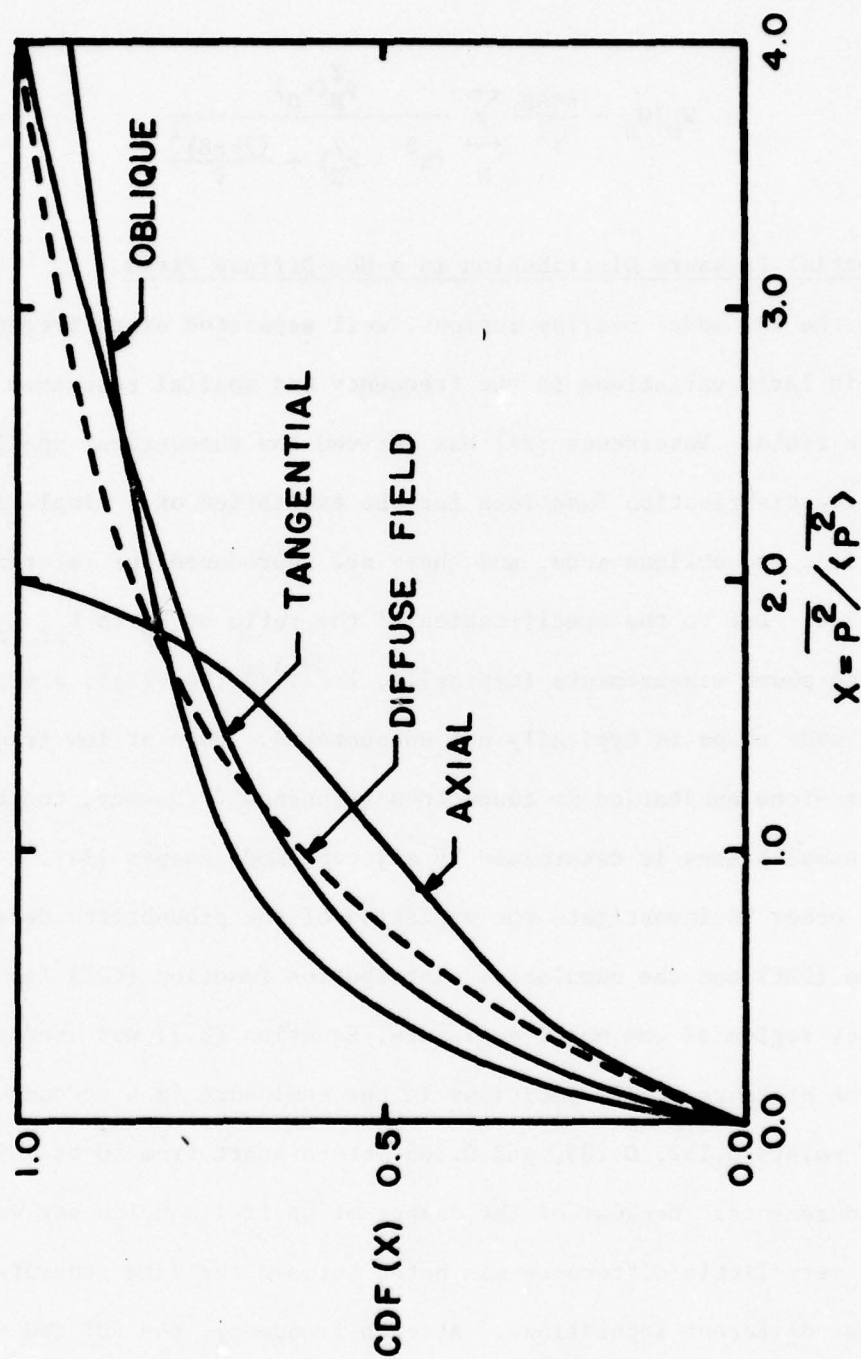
Figure 3.8. Theoretical spatial cumulative distribution functions for the excitation of a single axial, tangential, and oblique mode along with the exponential distribution for a diffuse field.
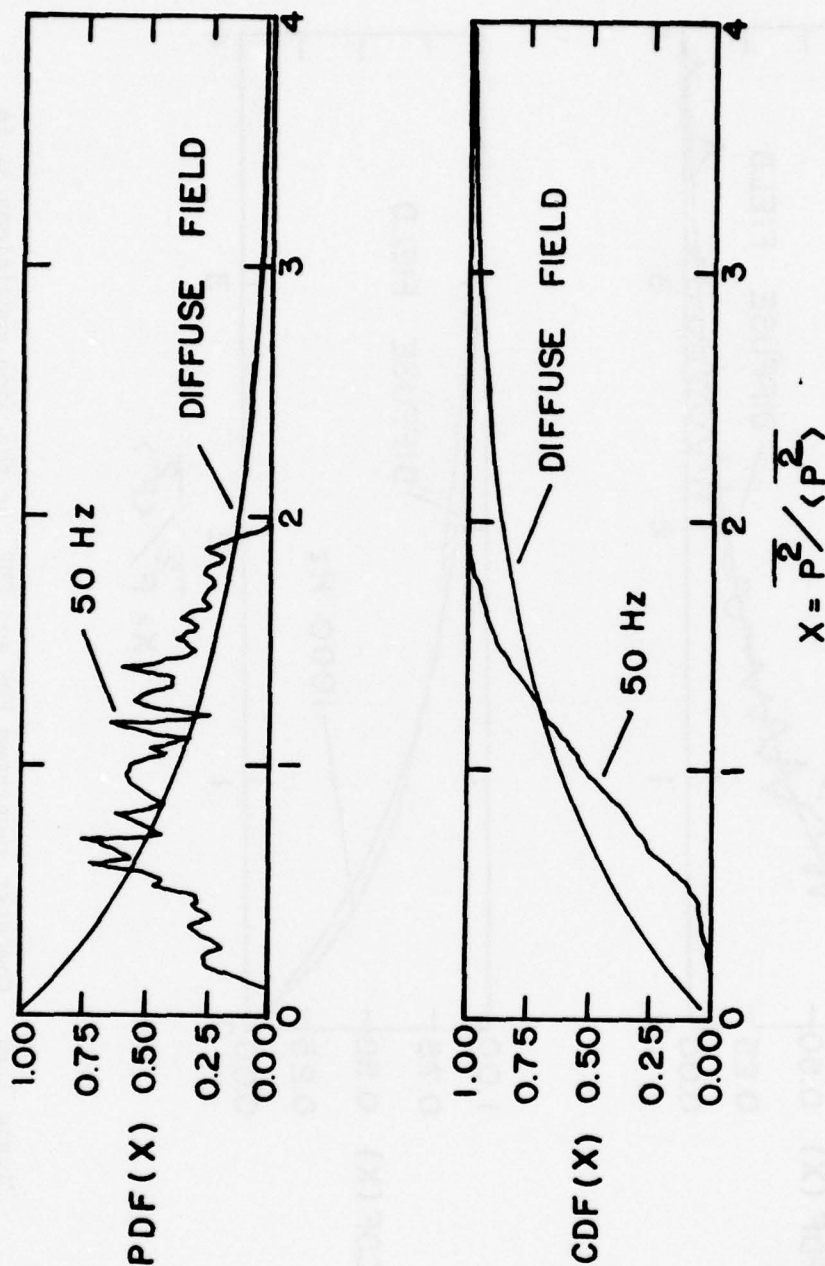
Figure 3.9. Probability Density Function (PDF) and Cumulative Distribution Function (CDF) of the normalized pressure at 120 positions in a rectangular grid with 0.152 m separation at 50 Hz in the model enclosure (6.82 m^3) with the source in a typical spatial position and $\beta = 0.005$ (computer generated).
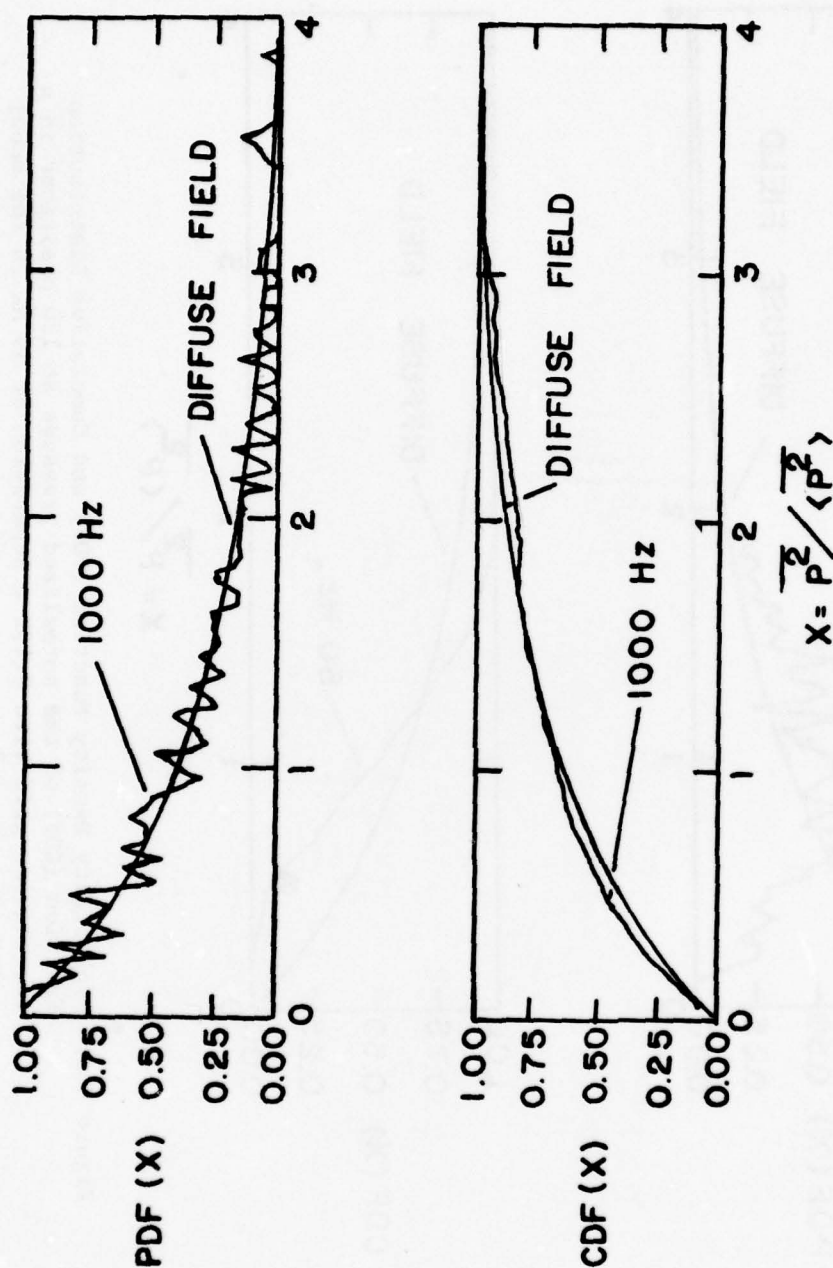
Figure 3.10. Computer generated PDF and CDF for the same conditions as in Figure 3.9 but at 1000 Hz.

($6.83 \ m^3$) at 250 Hz and 1000 Hz (below and above $f_c \simeq 760$ Hz for $\beta =$ 0.005) for a source in a typical spatial position and $\beta = 0.005$. In these figures, the theoretical CDF_T for a diffuse field is also plotted. A measurement of the difference between the ideal case and the computer generated data is given by the Standard Estimate of Error ε_s^2 given by

$$\varepsilon_s^2 = \frac{1}{N} \sum_N \left(CDF_T(x) - CDF(x) \right)^2 \quad . \tag{3.13}$$

In each case, the x axis is divided into 100 sections so that N in Equation (3.13) is 100. Note that for 250 Hz and 1000 Hz the values of ε_s^2 are 6.31 and 3.07 respectively.

In order to investigate the changes in the sound field as reflected in the PDF and CDF as the sound field goes from the low to high modal overlap conditions, the PDF and CDF are plotted as a function of frequency in Figures 3.11 through 3.20. For each plot, the CDF and PDF are plotted side by side with frequency increasing from front to back at 1 Hz increments, 100 Hz increments per plot. Both the PDF and CDF reflect the effects of strong well-separated modes in the low frequency region with fewer anomalies as frequency increases until at high frequencies the CDF, for example, fluctuates little from frequency to frequency and approaches the exponential CDF_T. Figure 3.21a quantifies the change of the CDF relative to the CDF_T by plotting the fluctuation of ε_s^2 as a function of frequency for the CDF's in Figures 3.11 through 3.20. The general trend can be emphasized if 1/3-octave averages are taken of the data in Figure 3.21a which are plotted in Figure 3.21b. Note that, as the frequency increases, the values of ε_s^2 decrease to a level of less than 5.
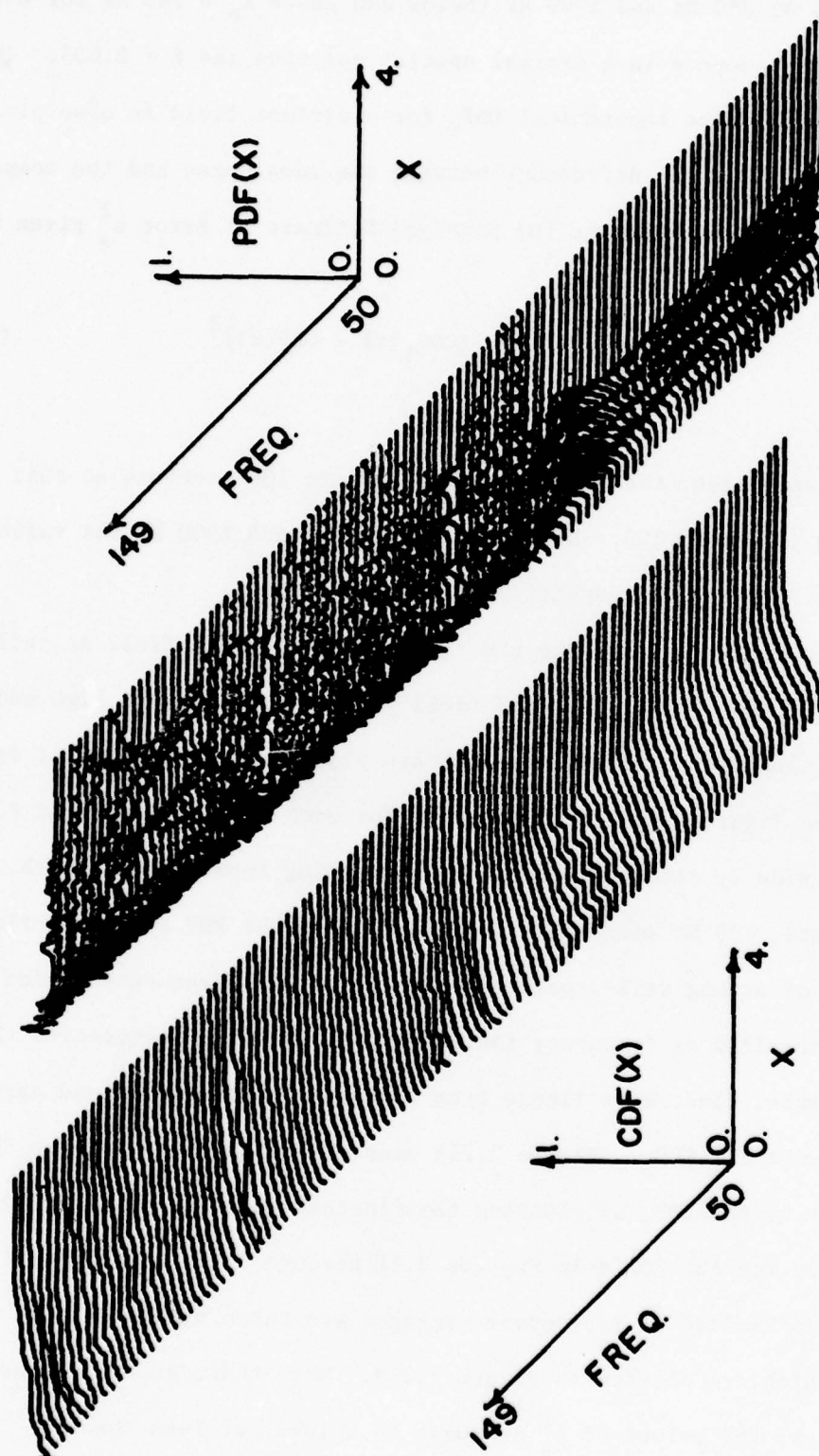
Figure 3.11. Probability Density Function (PDF) and Cumulative Distribution Function (CDF) of the normalized computer generated spatial pressure at 120 positions with 0.152 m separation in the model enclosure as a function of frequency for the source in a typical position (1.546 m, 1.005 m, 0.785 m) and β = 0.005 for the frequency range from 50 – 149 Hz.
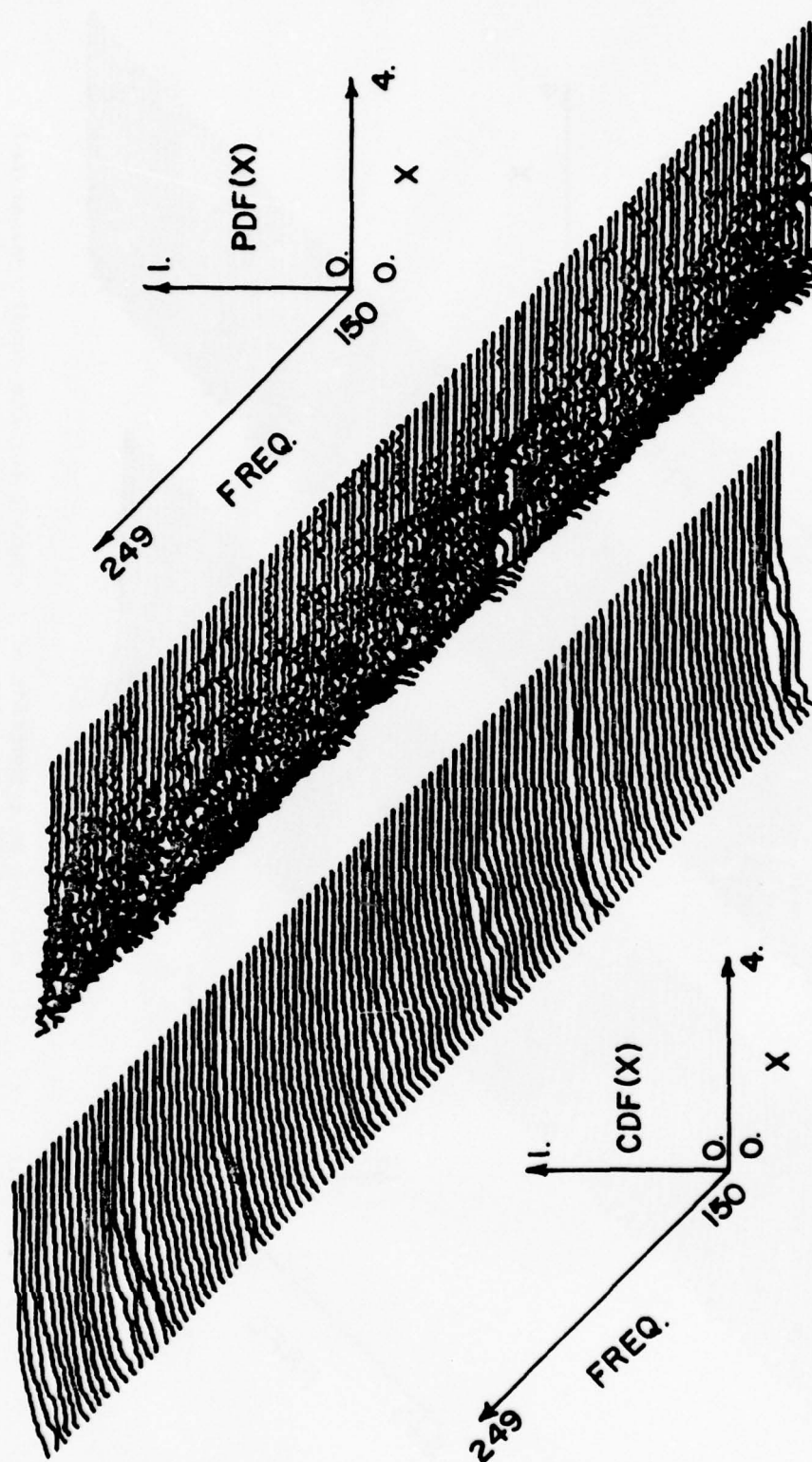
Figure 3.12. CDF and PDF as a function of frequency for the conditions stated in Figure 3.11, 150 - 249 Hz.
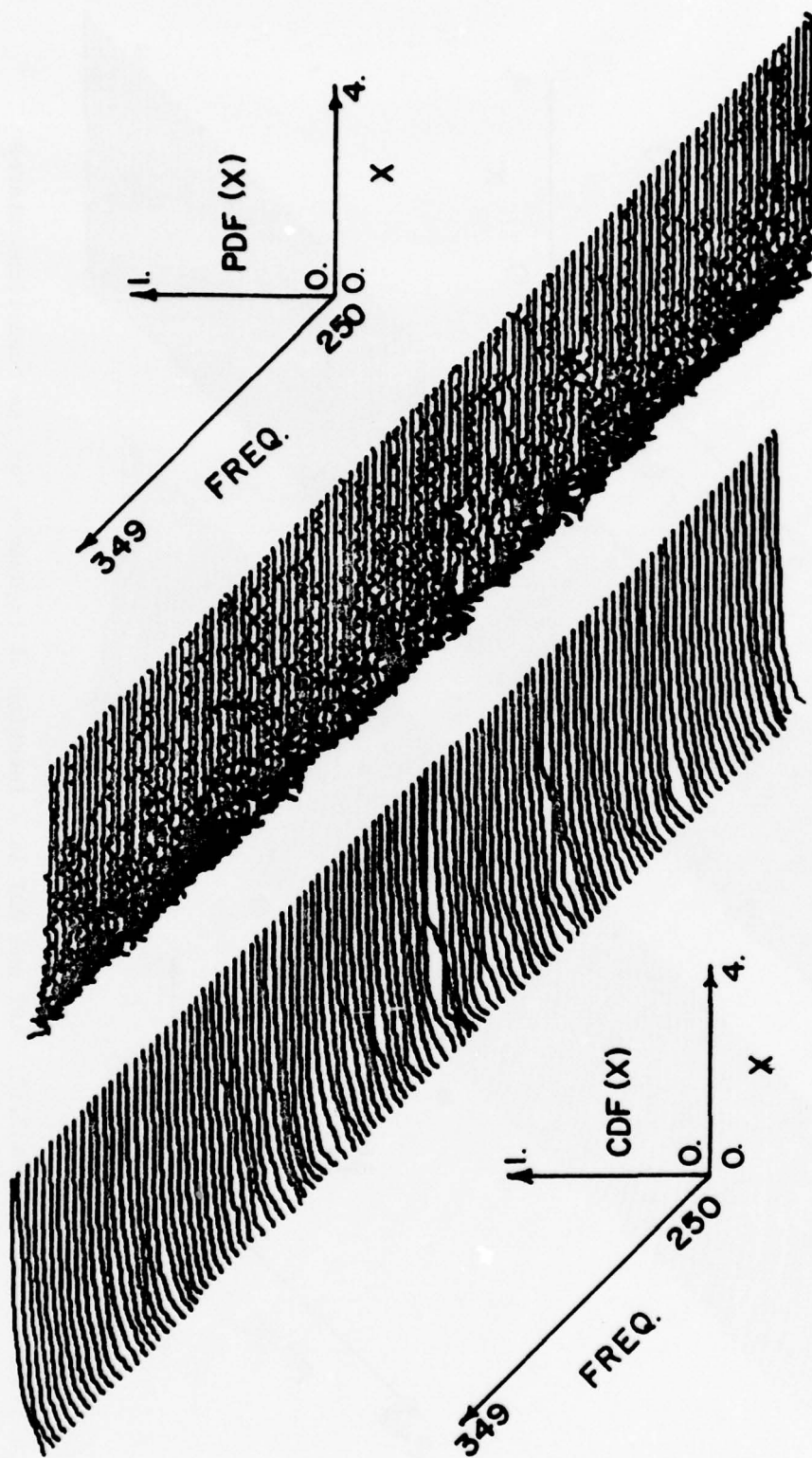
Figure 3.13. CDF and PDF as a function of frequency for the conditions stated in Figure 3.11, 250 - 349 Hz.
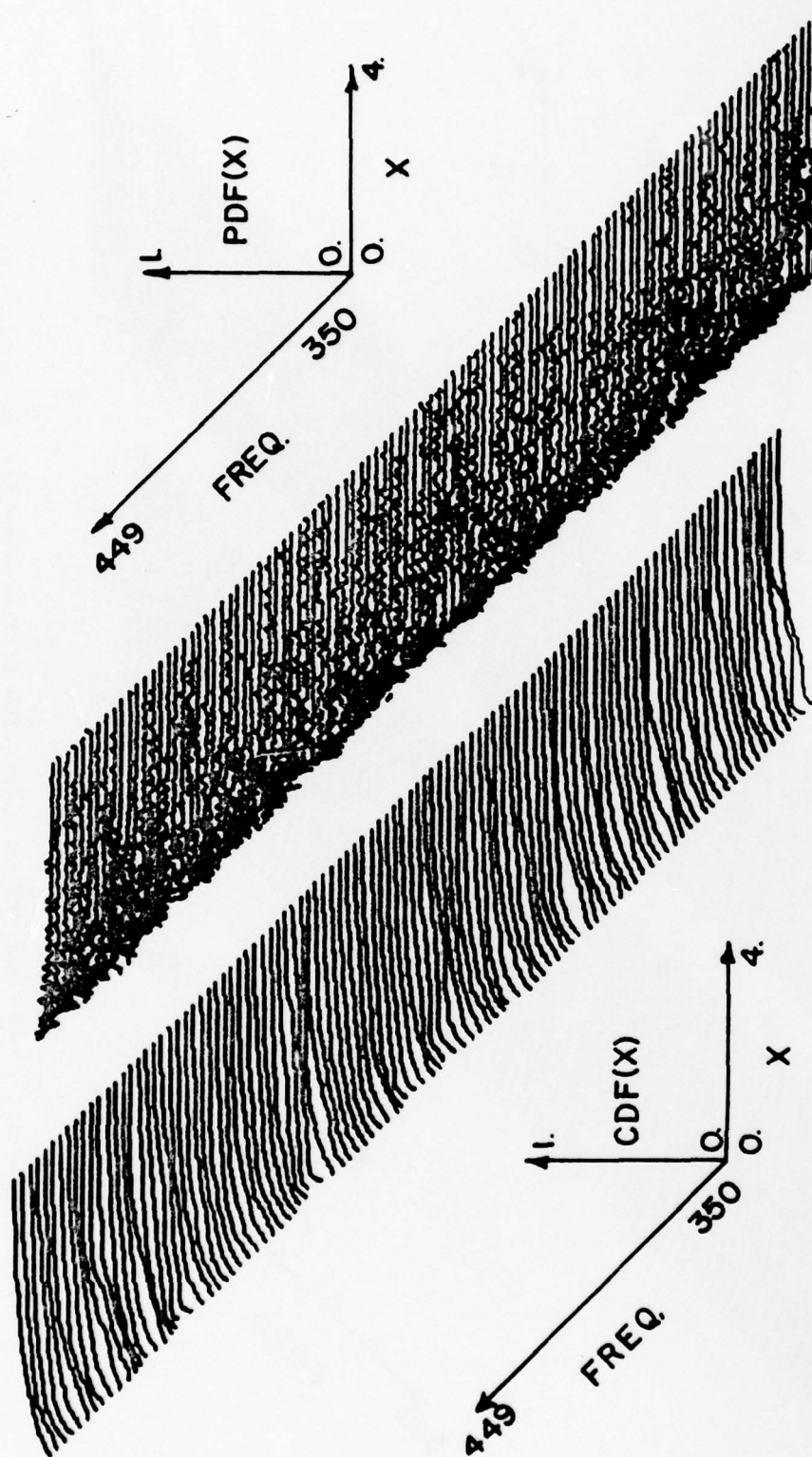
Figure 3.14. CDF and PDF as a function of frequency for the conditions stated in Figure 3.11, 350 - 449 Hz.
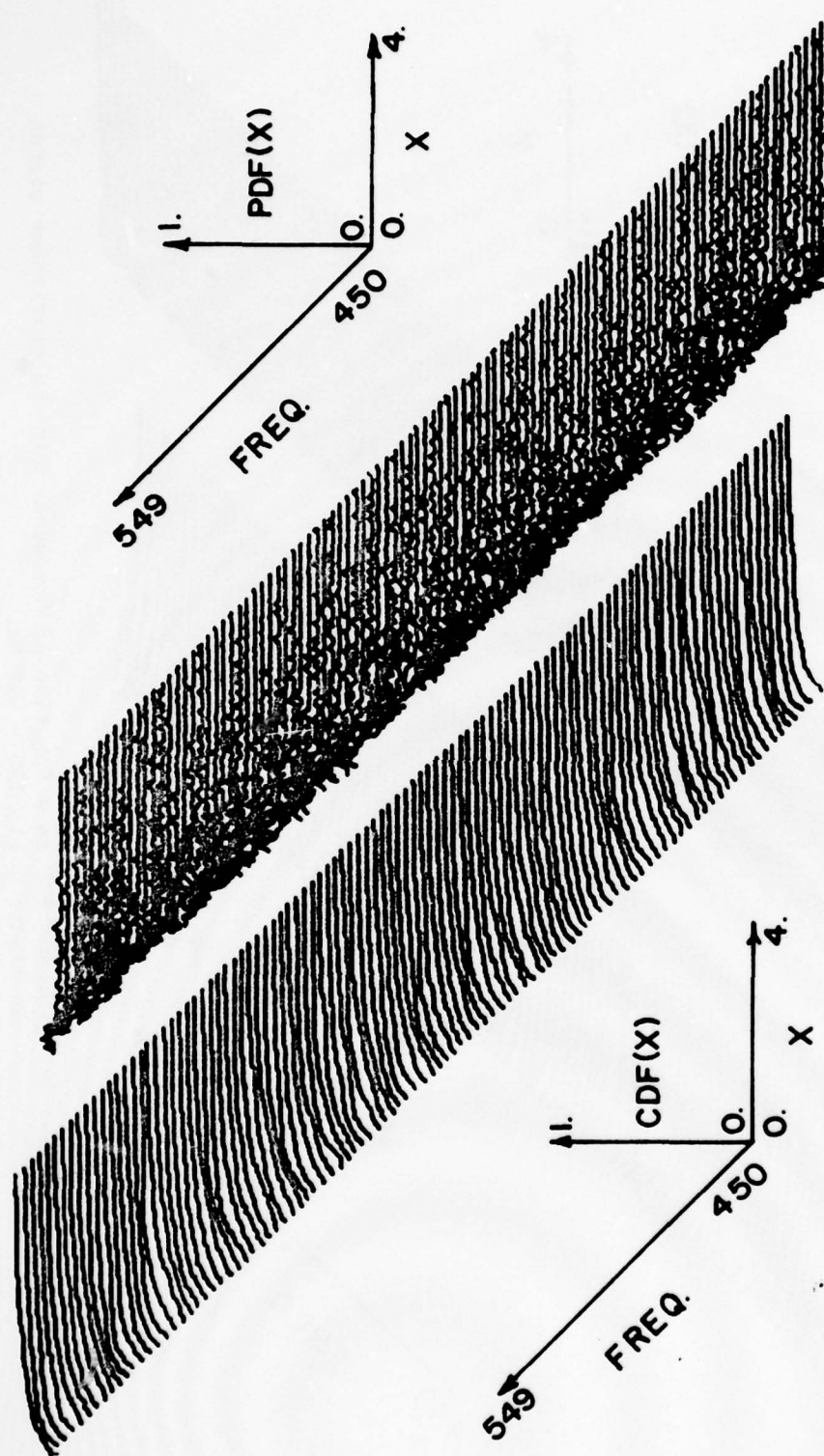
Figure 3.15. CDF and PDF as a function of frequency for the conditions stated in Figure 3.11, 450 – 549 Hz.
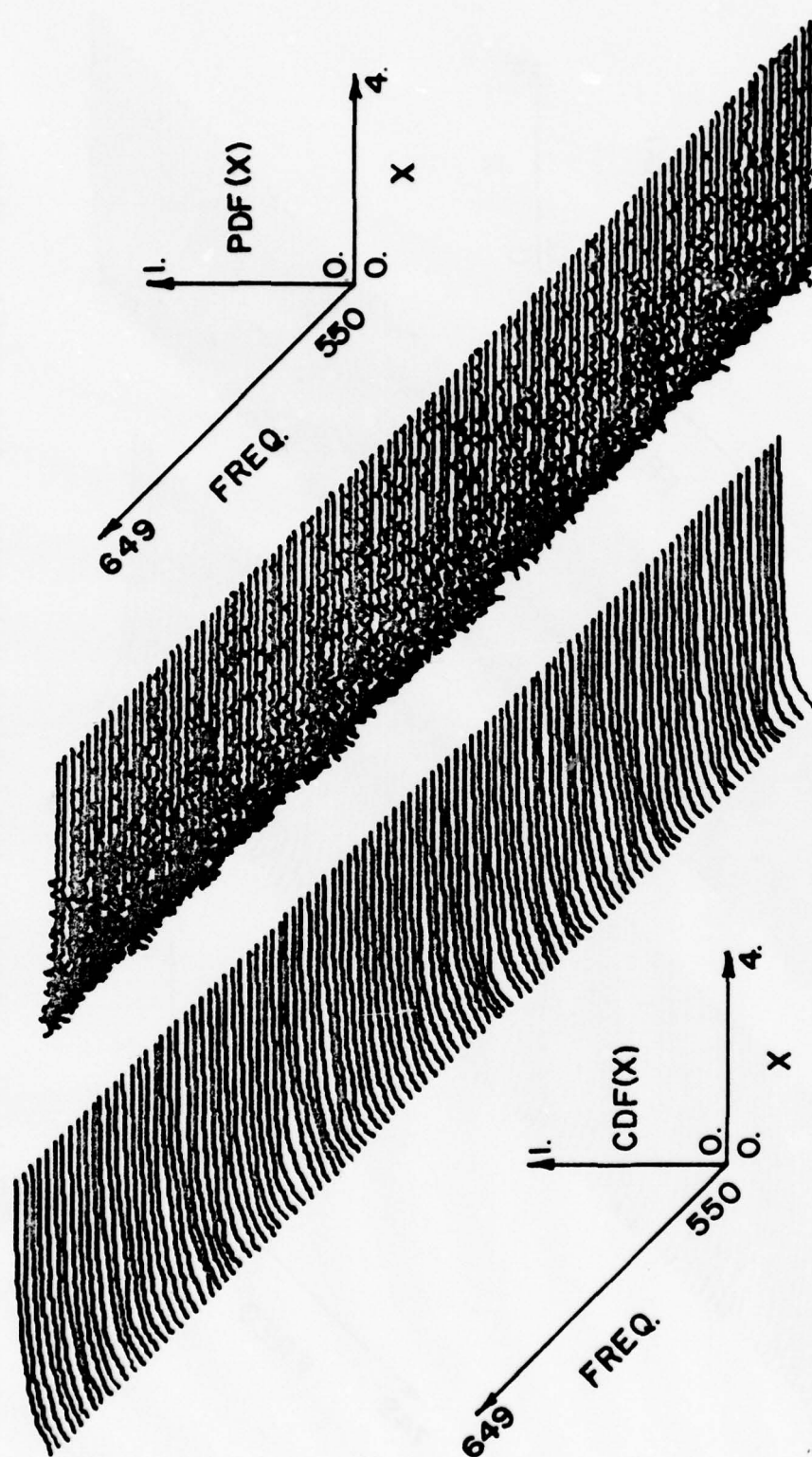
Figure 3.16. CDF and PDF as a function of frequency for the conditions stated in Figure 3.11, 550 – 649 Hz.
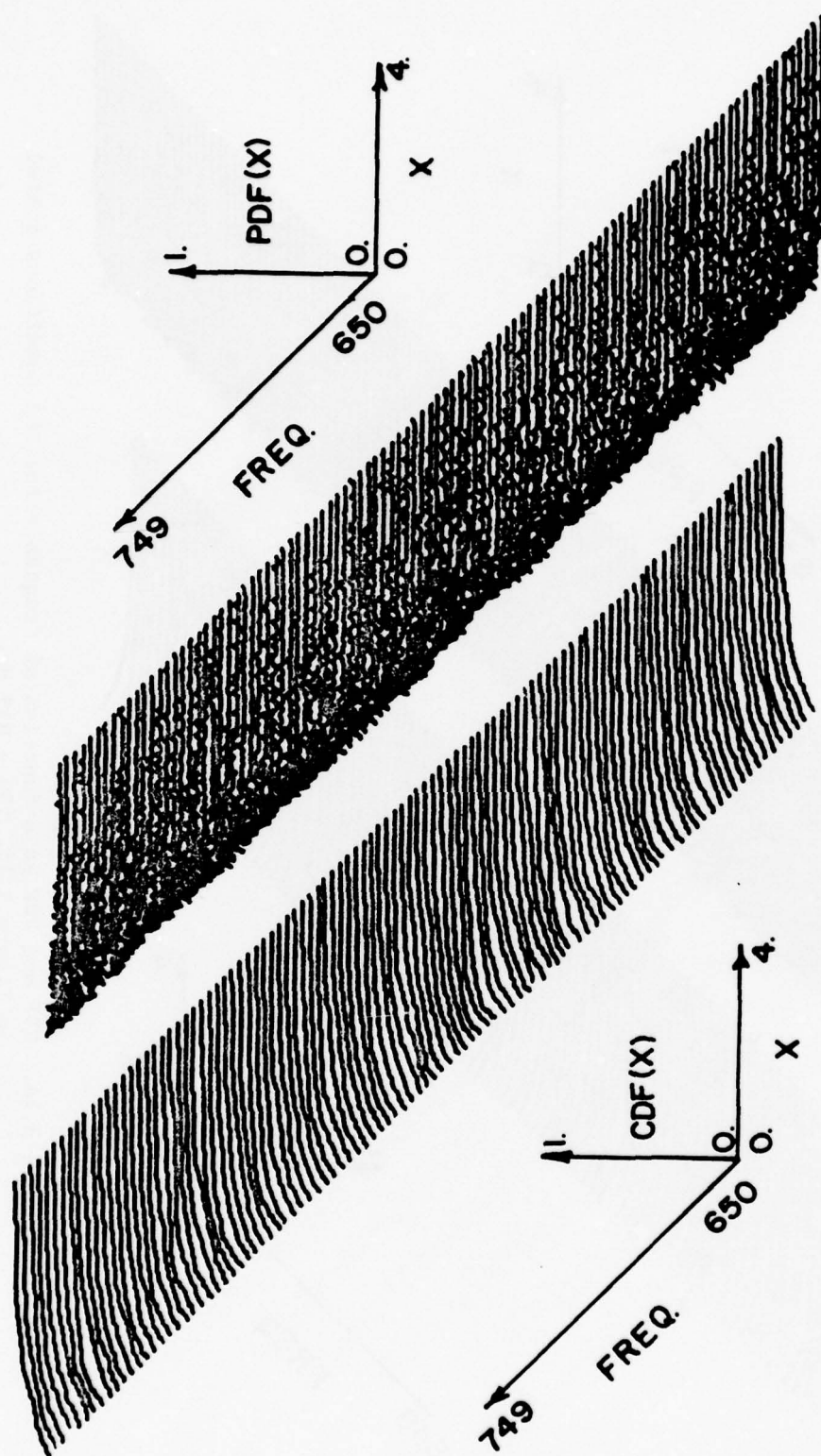
Figure 3.17. CDF and PDF as a function of frequency for the conditions stated in Figure 3.11, 650 – 749 Hz.
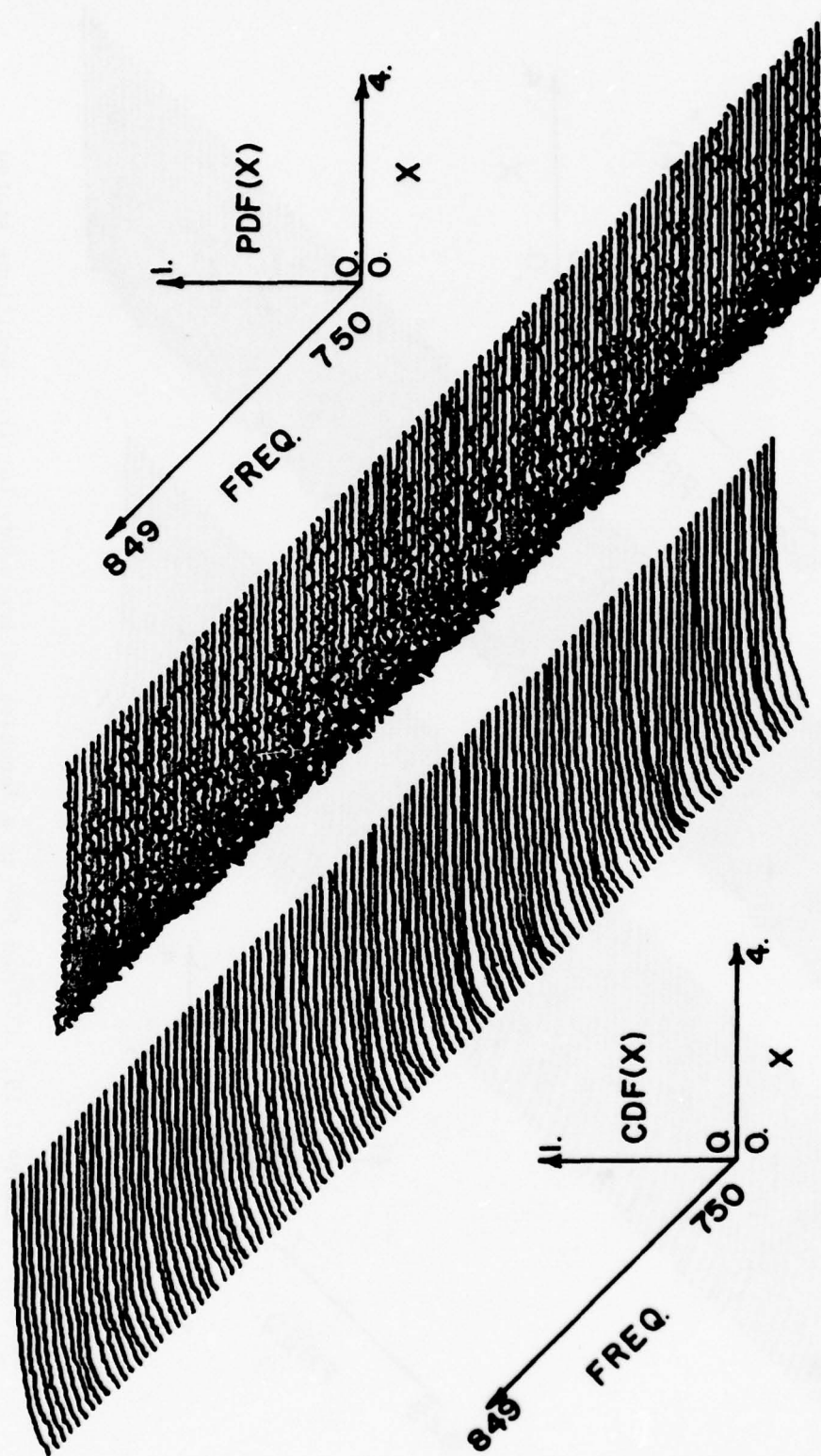
Figure 3.18. CDF and PDF as a function of frequency for the conditions stated in Figure 3.11, 750 – 849 Hz.
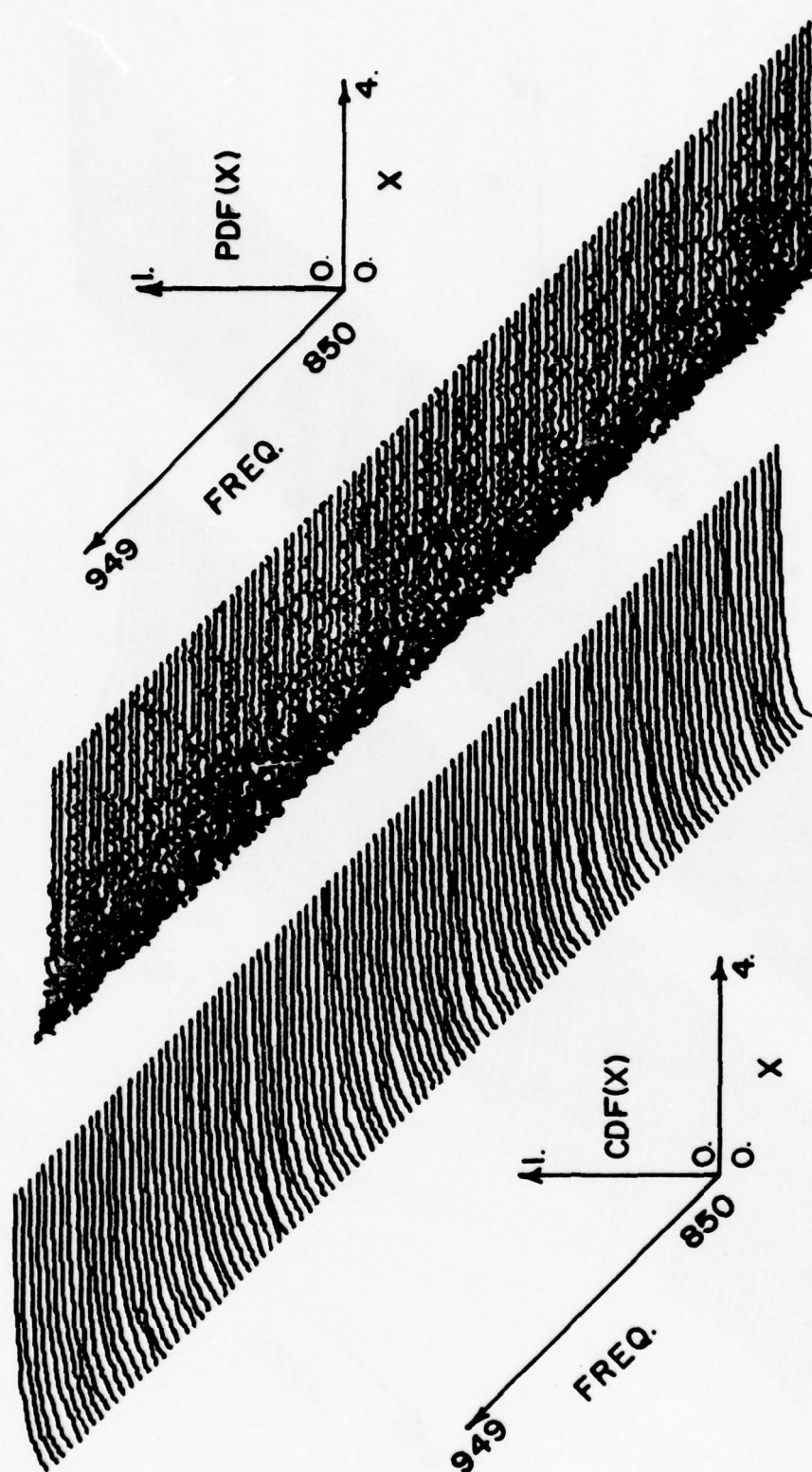
Figure 3.19. CDF and PDF as a function of frequency for the conditions stated
in Figure 3.11, 850 – 949 Hz.
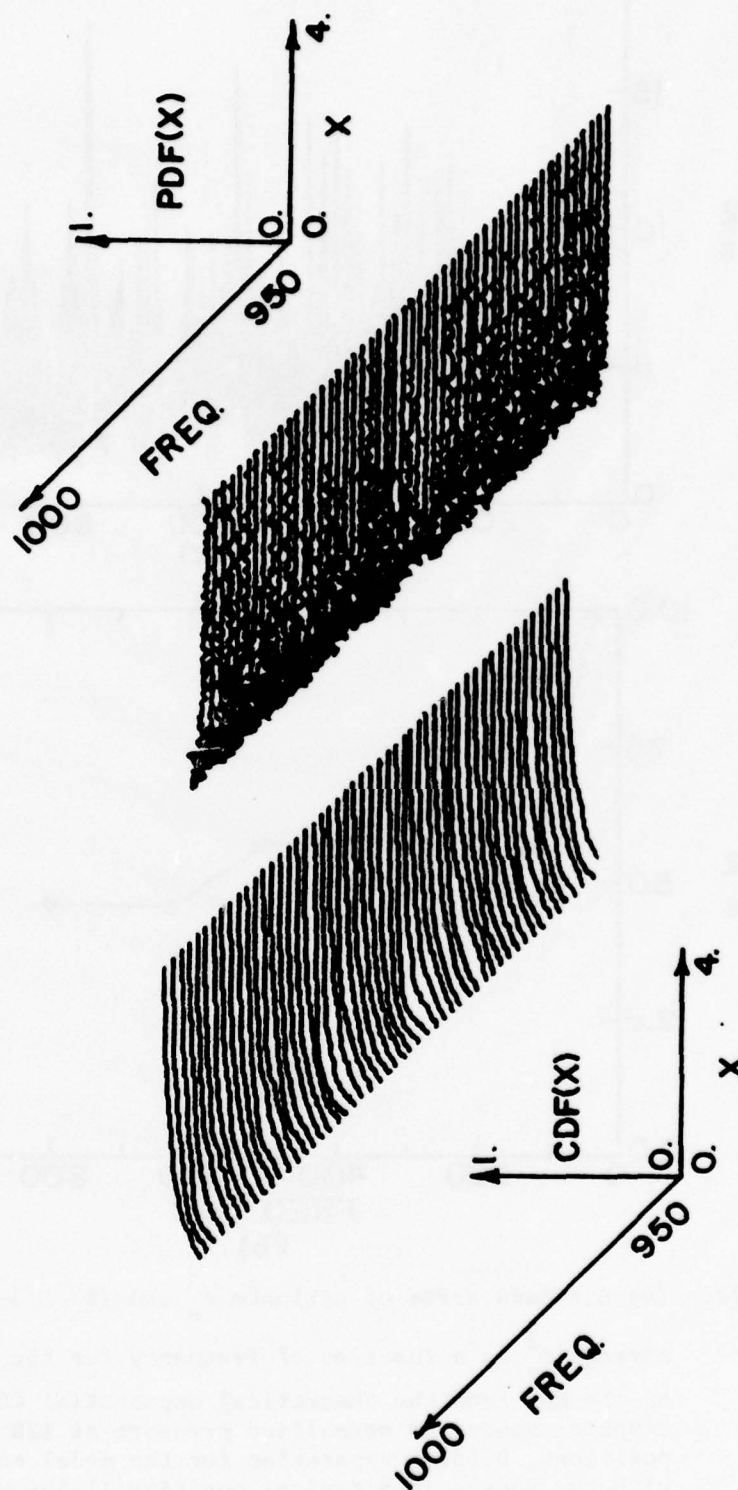
Figure 3.20. CDF and PDF as a function of frequency for the conditions stated in Figure 3.11, 950 - 1000 Hz.
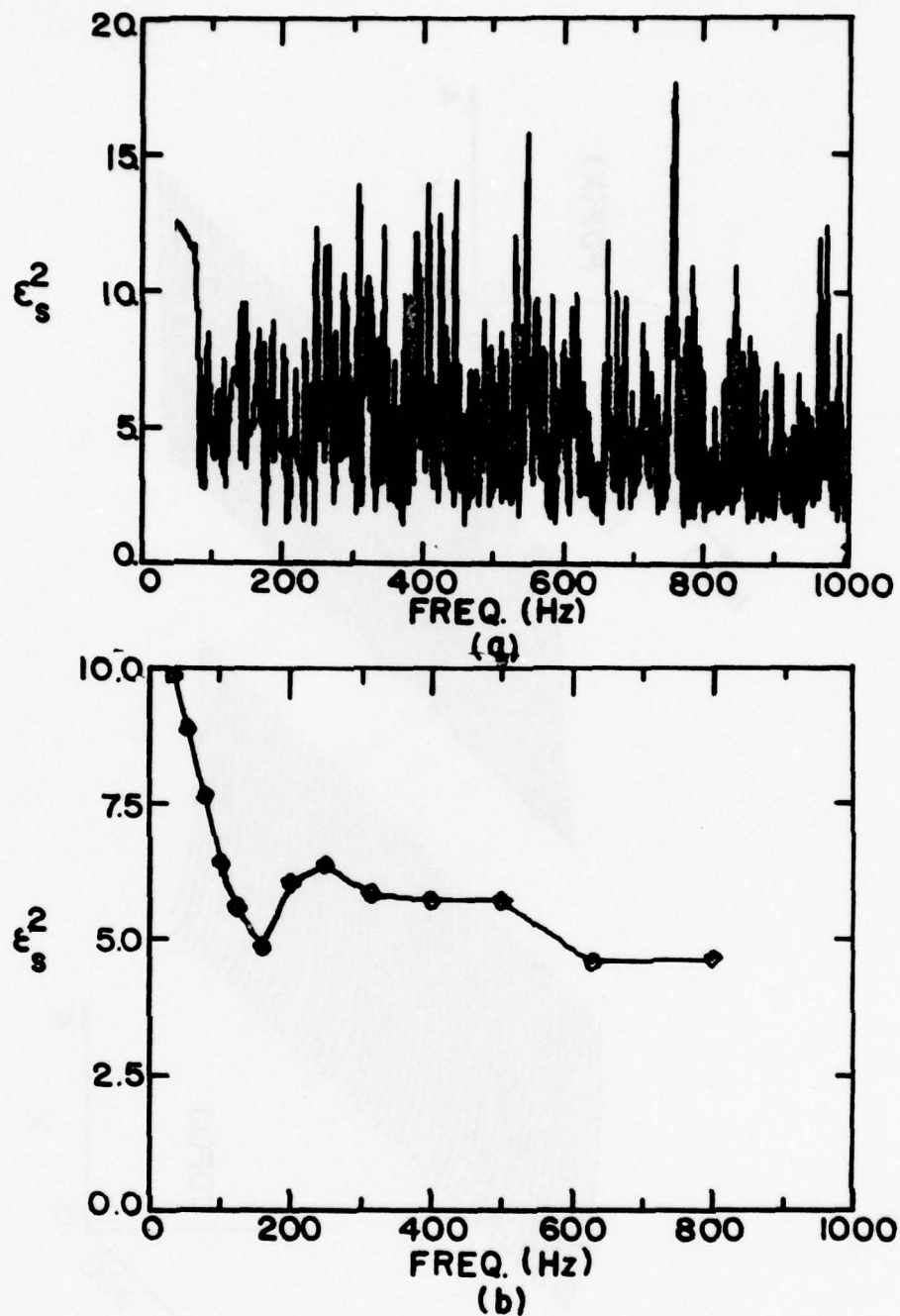
Figure 3.21. (a) Standard error of estimate ε_s^2 and (b) 1/3-octave

average ε_s^2 as a function of frequency for the variation
of the CDF from the theoretical exponential CDF for the
computer generated normalized pressure at 120 spatial
positions, 0.152 m separation for the model enclosure
with the source in a typical position (1.596 m. 1.005 m,
0.785 m) and β = 0.005.

In order to determine the accuracy of using 120 positions for sampling the sound field of unknown and changing statistical characteristics, the computer implementation of the normal mode model based on Equation (3.1) has been used to generate 200 sets each of data sampled at 10, 25, 50, 100, 120, 150, and 200 points randomly positioned 0.152 m apart in the interior space of the enclosure, 0.152 m from any wall at 200, 500, and 800 Hz. The 95% confidence limits for calculated value ϵ_s^2 for the 200 sets of these numbers of spatial positions have been calculated and are plotted in Figure 3.22. Thus, for 120 points, the 95% confidence limits of the measured ϵ_s^2 are +1.25 and −0.8.

For completeness, the computer model has been used to generate data sets similar to those presented in Figures 3.11 through 3.22. Figure 3.23 shows the values of ϵ_s^2 for the source in a typical spatial position and $\beta = 0.01$. Figure 3.24 shows the 1/3-octave average of ϵ_s^2 for the source near a corner with $\beta = 0.005$ and 0.01. All of these plots of ϵ_s^2 (Figures 3.21, 3.23, and 3.24) exhibit similar reduction in ϵ_s^2 as frequency increases. For the source located at the typical spatial position, ϵ_s^2 drops below 5 above 400 Hz.

3.4 Estimate of Spatial Mean of Squared Pressure in a Non-Diffuse Field

In order to investigate the fluctuation of $\overline{<p^2>}$ as frequency increases from low modal overlap to high modal overlap regions, $\overline{p^2}$, as given in Equation (3.8), can be evaluated over a volume integral. The spatial mean of the squared pressure can be expressed as

$$\overline{<p^2>}_V = \frac{\omega^2 Q_o^2}{2v^2} \sum_N \frac{E_N \psi_N^2(r_0)}{(k^2 - k_N^2)^2 + (2k\delta_N)^2} \quad . \tag{3.14}$$
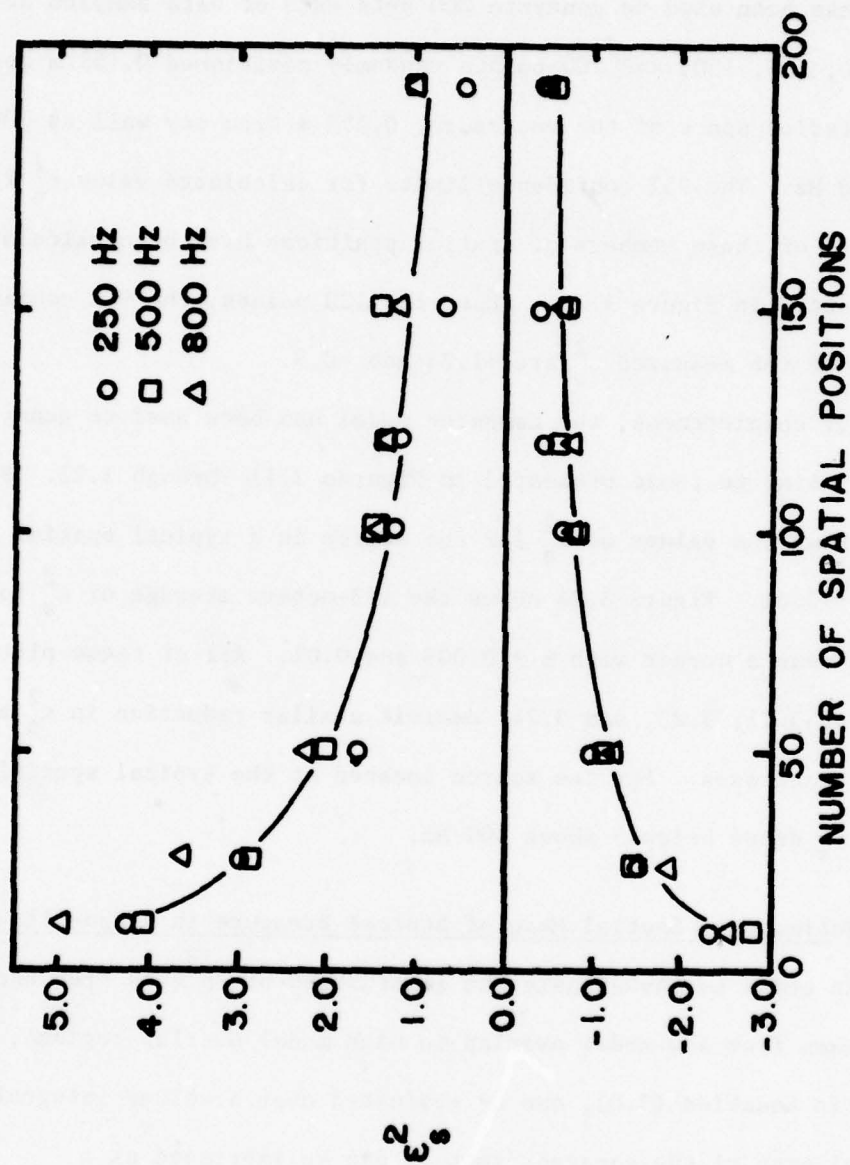
Figure 3.22. Confidence limits of 95% for ϵ_s^2 at 250, 500, and 800 Hz as a function of the number of randomly located spatial points with 0.152 m minimum separation for the model enclosure with $\beta = 0.005$ and the source in a typical spatial position (1.596 m, 1.005 m, 0.785 m).
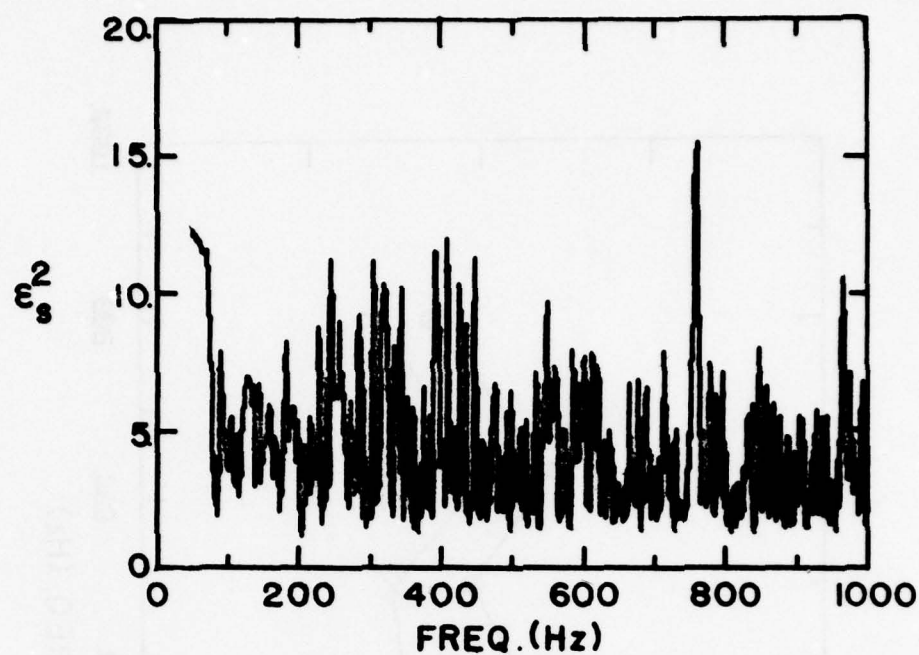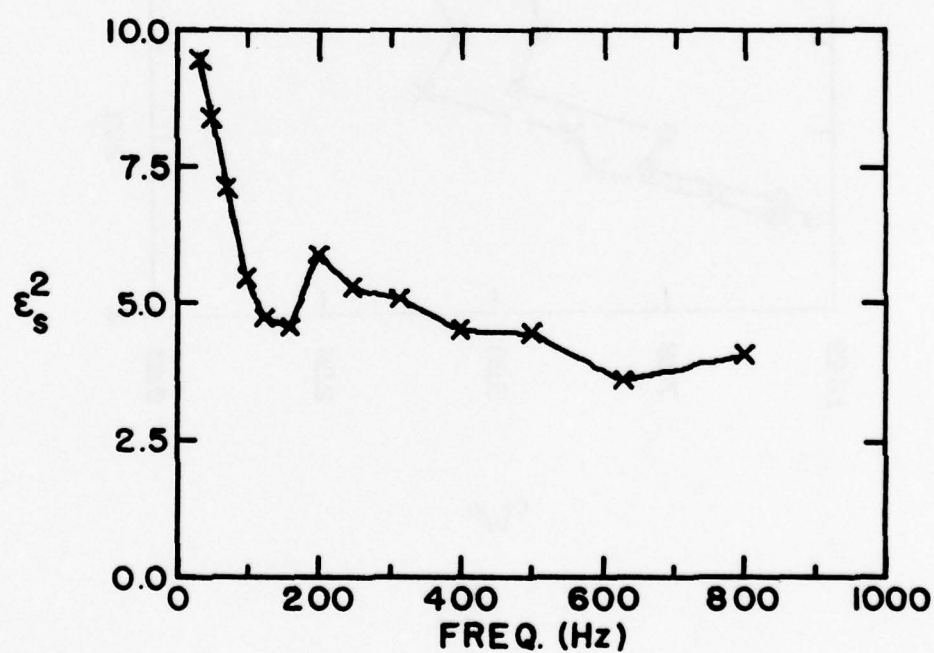
Figure 3.23. (a) Standard error of estimate ϵ_s^2 and (b) 1/3-octave average of ϵ_s^2 as a function of frequency for the same conditions as in Figure 3.21 but with $\beta = 0.01$.
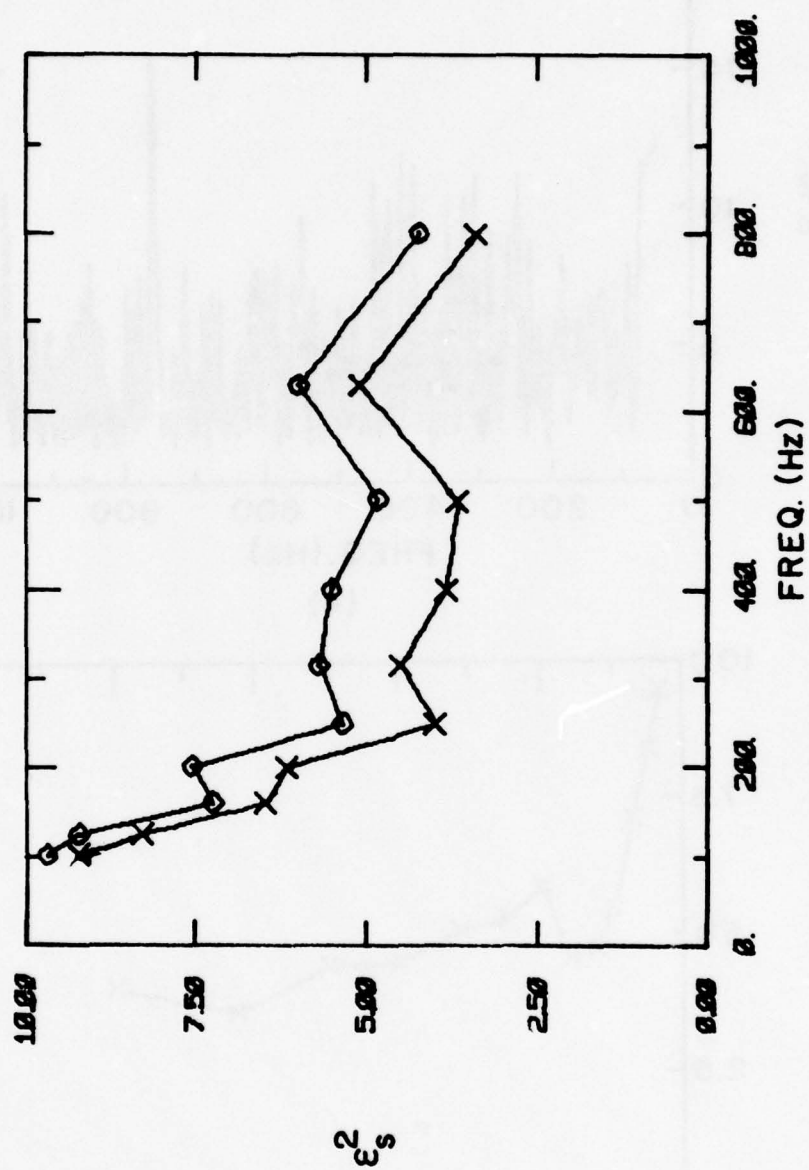
Figure 3.24. One-third-octave average of the standard error of estimate ε_s^2 for the same conditions as in Figure 3.22 but with the source near a corner (0.18 m, 0.18 m, 0.18 m) and β = 0.01, (x) and β = 0.005 ($\diamondsuit$).

Note that the term inside the summation in Equation (3.14) differs from that in Equation (3.9) by the factor δ_N. In the high frequency region where oblique modes dominate, the sound power as expressed by the surface integral of Equation (3.9) and the volume integral of Equation (3.14) are equal, and

$$W_V = \frac{2\beta S}{\rho c} \overline{<p^2>}_V \quad . \tag{3.15}$$

As with the surface integral representation of sound power, which is true for all frequencies, if Equation (3.15), which is true only at high frequency, is compared to the free-field sound power W_0, then

$$\frac{W_V}{W_0} = \frac{8\pi\beta S}{V^2} \sum \frac{E_N \psi_N^2(r_0)}{(k^2 - k_N^2)^2 + (2k\delta_N)^2} \quad . \tag{3.16}$$

Finally, if the volume integral determination of the mean is replaced by the mean sampled at N positions $\overline{<p^2>}_N$, the sound power is given by

$$W_N = \frac{2\beta S}{\rho c} \overline{<p^2>}_N \quad , \tag{3.17}$$

and W_N/W_0 is given by

$$\frac{W_N}{W_0} = \frac{16\pi\beta S}{\omega^2 Q_0^2} \overline{<p^2>}_N \quad . \tag{3.18}$$

Comparisons between W_S/W_0 (Equation (3.12)), W_V/W_0 (Equation (3.16)), and W_N/W_0 (Equation (3.18)) can be seen in Figure 3.25, where the source is located at a typical position within the enclosure,
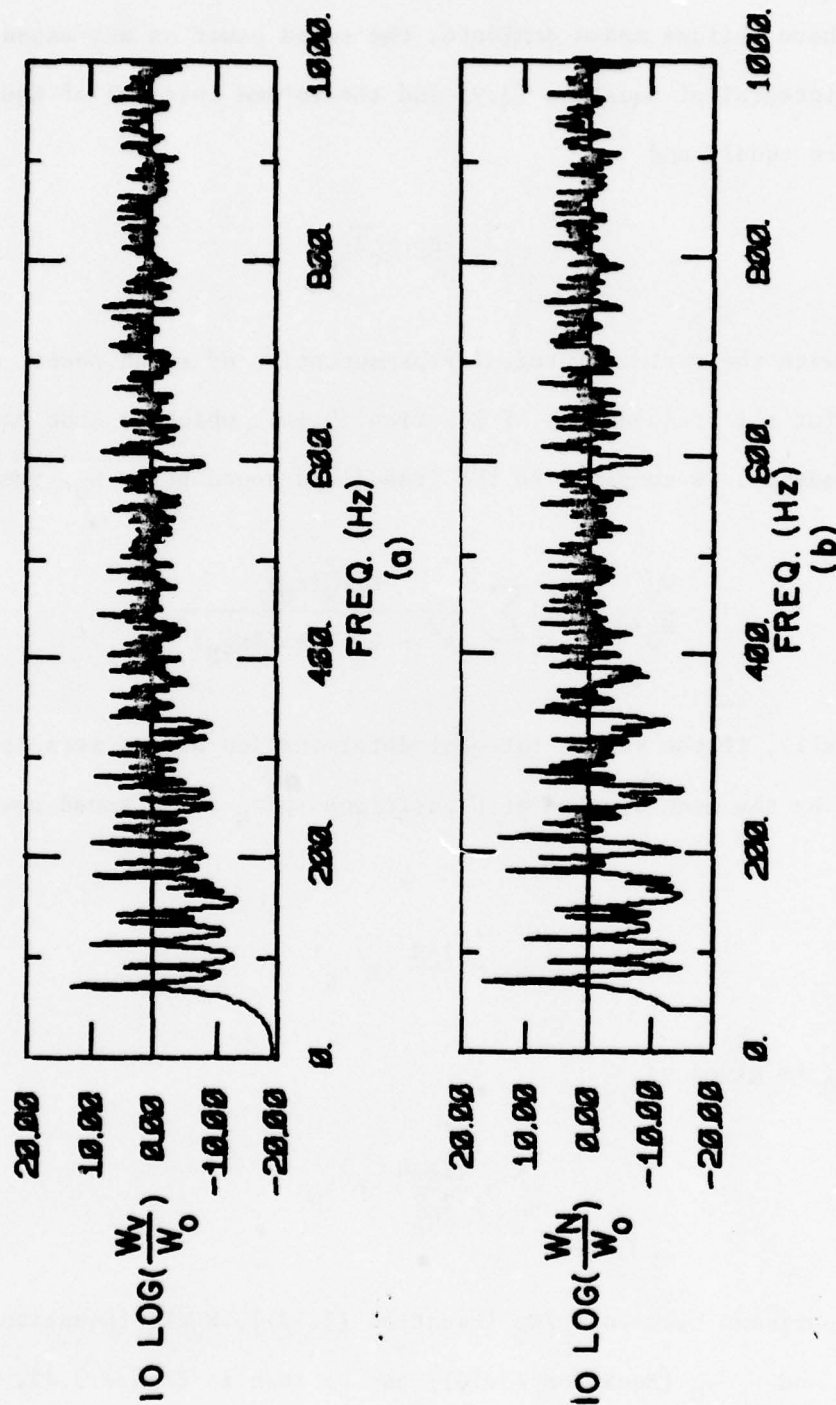
Figure 3.25. Ratio of the estimate for the sound power radiated in a reverberant enclosure to the free-field sound power W_0 as a function of frequency for the reverberant sound power proportional to the spatial mean of squared pressure given by (a) the volume integral mean W_V and (b) the spatial sampled mean W_N with source in typical spatial position (1.596 m, 1.005 m, 0.785 m) and $\beta = 0.005$.
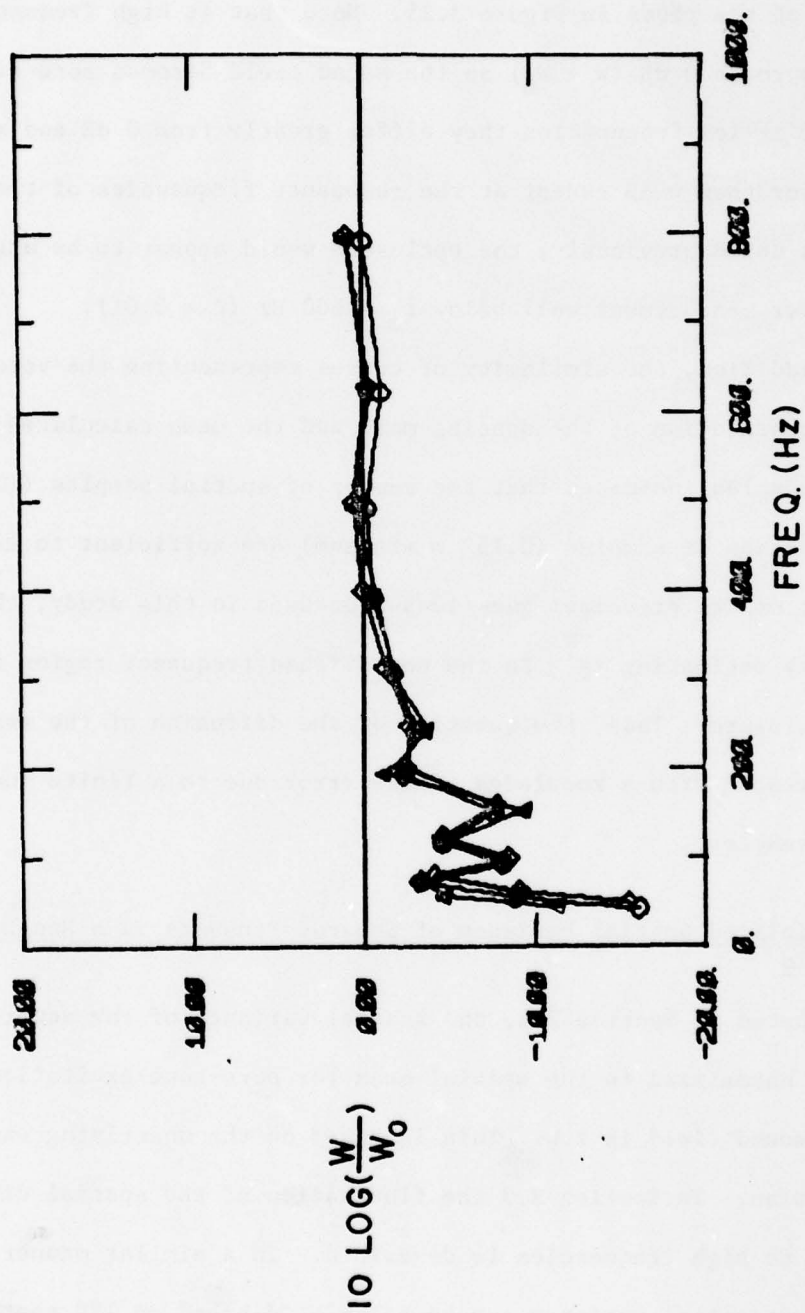
Figure 3.26. One-third-octave average of the curves of Figure 3.25, W_V/W_0 ($\diamond$), W_N/W_0 ($\triangle$), and, for comparison, W_S/W_0 (o) from Figure 3.7.

$\beta = 0.01$, and, for W_N/W_0, the sound field is sampled at 120 positions in a rectangular grid with 0.152 m separation. Figure 3.26 gives 1/3-octave averages of the plots in Figure 3.25. Note that at high frequencies all curves approach 0 dB ($W \to W_0$) as the sound field becomes more diffuse. Note that at low frequencies they differ greatly from 0 dB and are typically lower than 0 dB except at the resonance frequencies of the enclosure. As noted previously, the enclosure would appear to be useful for sound power measurement well below $f_c \simeq 600$ Hz ($\beta = 0.01$).

In addition, the similarity of curves representing the volume integral representation of the spatial mean and the mean calculated from 120 spatial samples indicates that the number of spatial samples (120) and the separation of samples (0.152 m minimum) are sufficient to eliminate the first of the principal questions addressed in this study, that of adequately estimating $\overline{\langle p^2 \rangle}$ in the non-diffuse frequency region for a given enclosure. Thus, the question of the diffusion of the sound field can be treated with a knowledge of the error due to a finite number of spatial samples.

3.5 Normalized Spatial Variance of Squared Pressure in a Non-Diffuse Field

As noted in Section 2.4, the spatial variance of the squared pressure normalized to the spatial mean for pure-tone excitation in a diffuse sound field is 1.0. This is based on the underlying exponential distribution. In Section 3.3 the fluctuation of the spatial distribution from low to high frequencies is described. In a similar manner the normalized spatial variance can be calculated based on 120 spatial positions with 0.152 m separation from 50 to 1000 Hz for various damping factors and source positions.

Figures 3.27 and 3.28 plot the normalized spatial variance and the 1/3-octave average for the source in the corner with $\beta = 0.005$ (Figure 3.27) and for the source in the typical spatial position with $\beta = 0.005$ (Figure 3.28). Note that the fluctuations of the spatial variance follow the same trends for the corresponding source position and β as ϵ_s^2 (compare Figures 3.27 to 3.24 and 3.28 to 3.21). This similarity is expected due to the relationship between the variance and CDF. For the source in a typical spatial position, Figure 3.29 shows that the 1/3-octave average of $\sigma^2/\overline{\langle p^2 \rangle}$ is very close to unity over the entire frequency range for $\beta = 0.01$. This study leads to the conclusion that the optimum choice of the source position is away from the enclosure boundaries and that known beneficial effects of adding a small amount of absorption are reflected in both indicators of diffusion.

As with the case for ϵ_s^2, the 90% and 95% confidence limits for $\sigma^2/\overline{\langle p^2 \rangle}$ for discrete frequencies have been calculated as a function of the number of spatial samples of the non-diffuse field. These results showed a trend similar to that seen in Figure 2.3 for the diffuse field and in Figure 3.22. The 95% confidence limits for the estimate of the normalized variance (assumed to be that calculated for 200 spatial samples) by the value of the normalized variance calculated at 120 spatial samples is +1.42 and -0.87.

3.6 Cross Correlation Coefficient in a Non-Diffuse Field

Several researchers have recently noted that the cross correlation coefficient measured for pure-tone excitation in a reverberant enclosure at high frequency varies widely from the sin(kr)/kr behavior predicted by Cook et al. (20), but yet satisfactory agreement is realized when
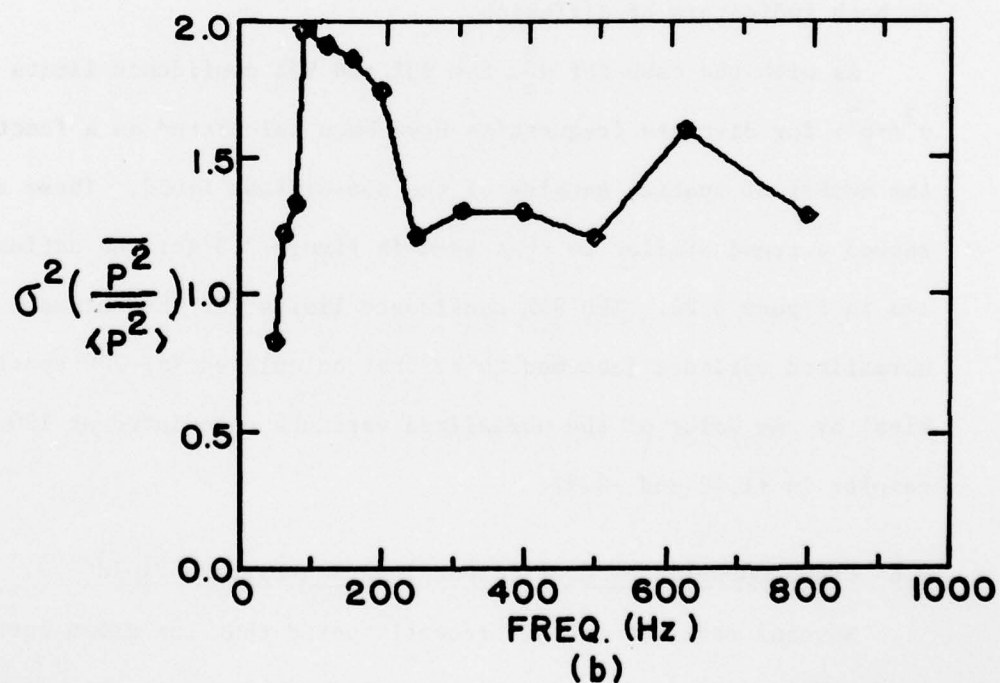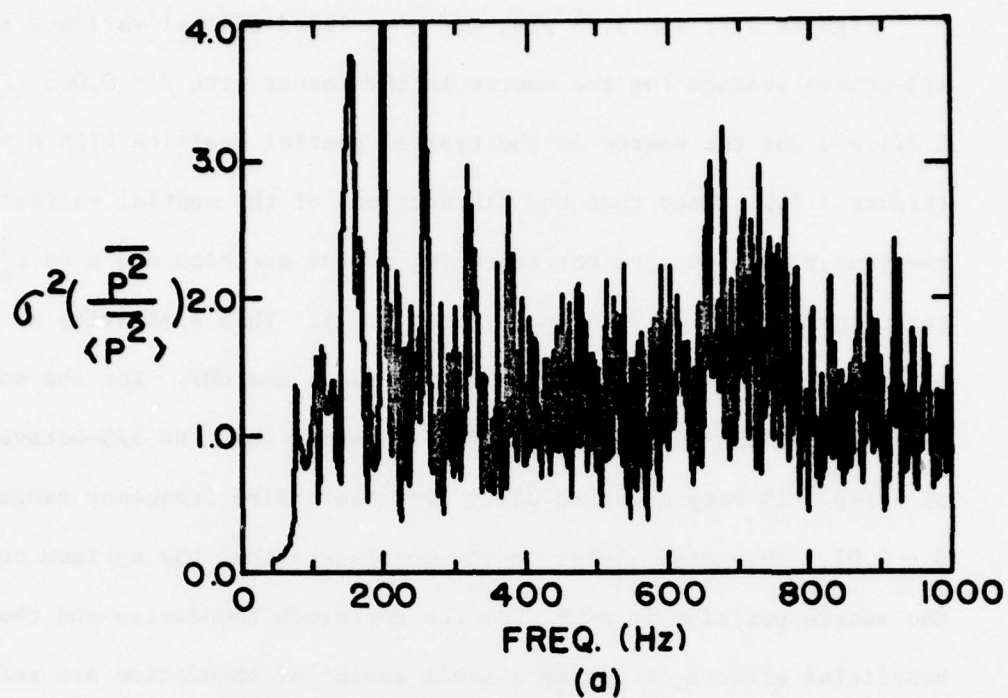
Figure 3.27. (a) Normalized spatial variance of squared pressure and
(b) 1/3-octave average for 120 positions, 0.152 m
separations as a function of frequency for the model
enclosure with β = 0.005 and source near corner (0.18 m,
0.18 m, 0.18 m).
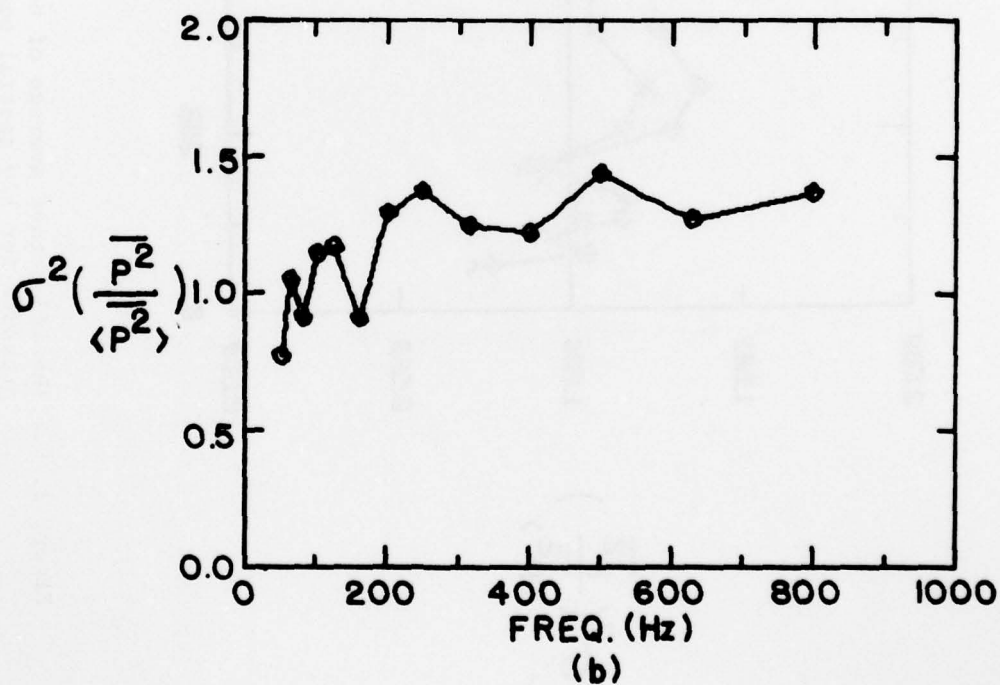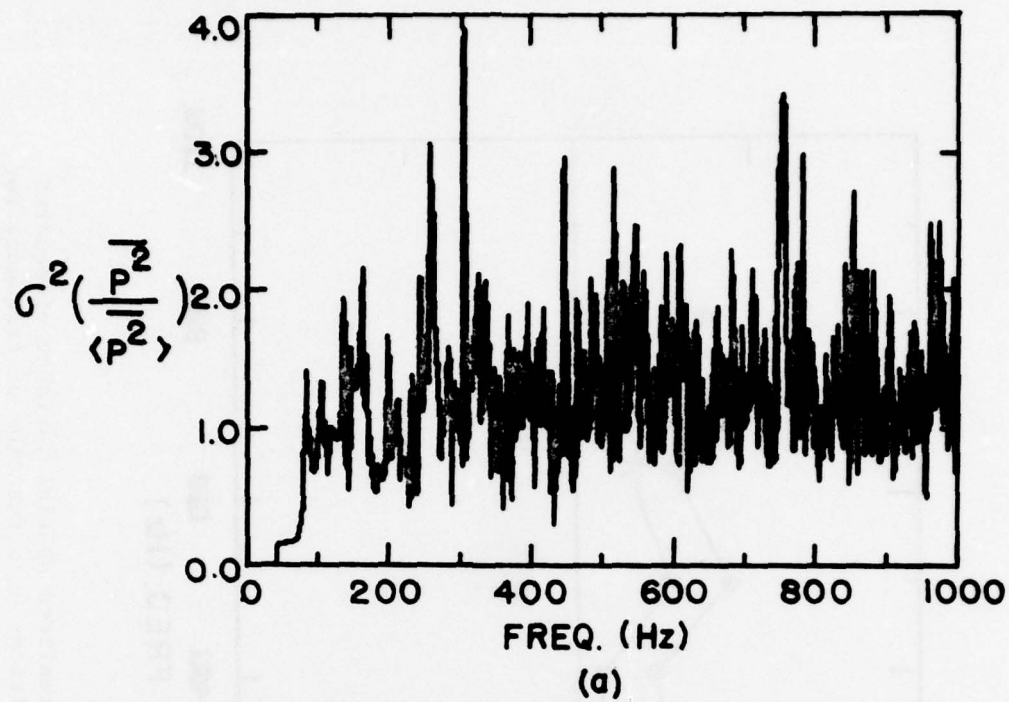
Figure 3.28.   (a) Normalized spatial variance and (b) 1/3-octave average
of squared pressure for 120 positions, 0.152 m separations
as a function of frequency for the model enclosure with
$\beta = 0.005$ and the source in a typical spatial position
(1.596 m, 1.005 m, 0.785 m).
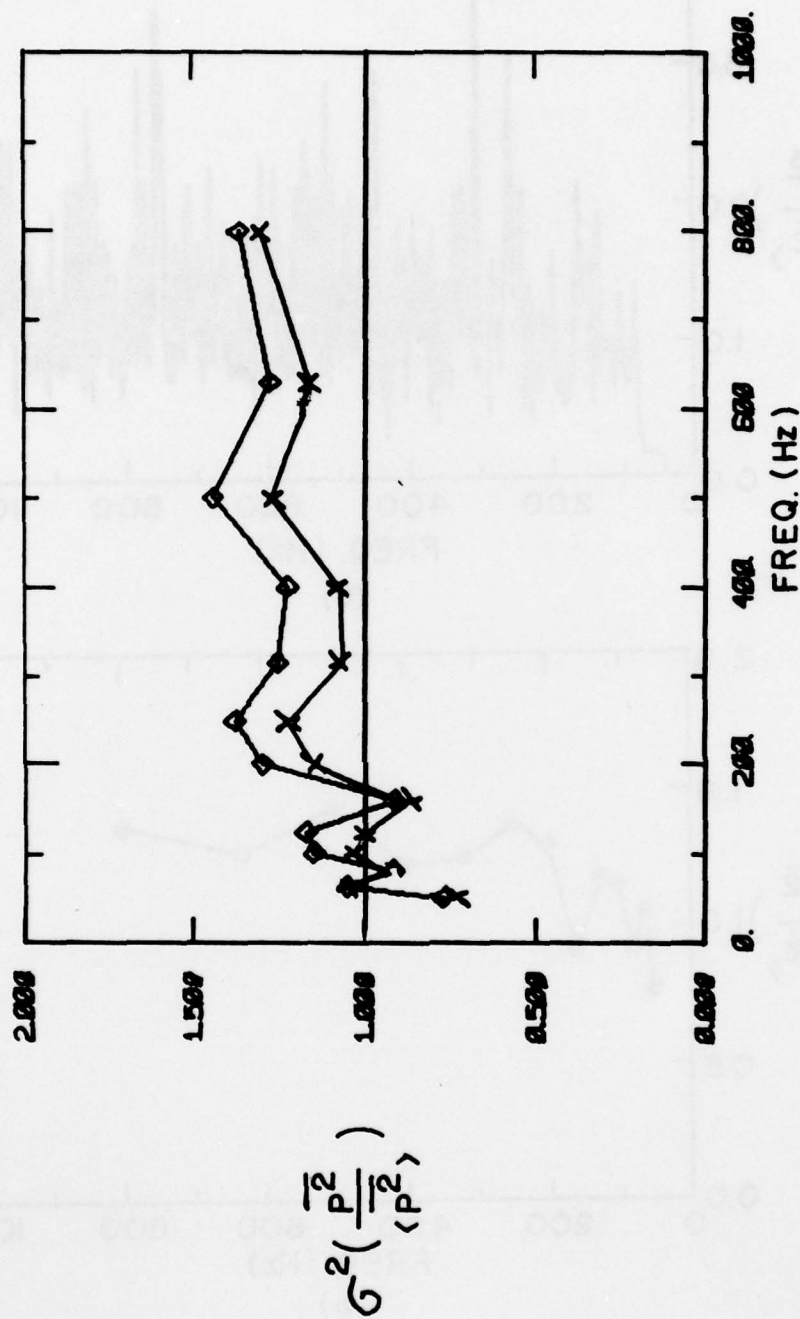
Figure 3.29. The 1/3-octave average of normalized spatial variance of squared pressure for 120 spatial positions as a function of frequency for the source in a typical spatial position (1.596 m, 1.005 m, 0.785 m) for $\beta = 0.01$ (X) and 0.005 ($\diamondsuit$).

narrowband noise excitation is used (17). Similar results for pure tones are predicted and measured in this study as shown in Figure 2.5.

In order to investigate the spatial variations of R(kr) with frequency, the computer model based on Equation (3.1) is programmed to calculate the magnitude and phase of the pressure for 120 randomly spaced lines at increments of $kr = \pi/5$. Each of these 120 lines emanates from a randomly chosen reference point located in the reverberant field. Due to the large number of spatial points at which the pressure is to be calculated, the frequency increment is chosen to be 5 Hz rather than 1 Hz to keep the computer time within reasonable limits. Due to the size of the enclosure, the maximum value of $kr = \pi$ is used from 250 Hz to 500 Hz and increased to 2π from 500 Hz to 1000 Hz.

For a given direction, large differences are observed between R(kr) and sin(kr)/kr, but, if the 120 values for R(kr) for each kr are averaged, the resultant $R(kr)_{avg}$ differs little from sin(kr)/kr. As an example, Figure 3.30 shows the average cross correlation coefficient at 1000 Hz along with the theoretical sin(kr)/kr for a diffuse field.

The frequency-by-frequency transition of $R(kr)_{avg}$ from non-diffuse to diffuse behavior can be seen in Figures 3.31 to 3.33, where $R(kr)_{avg}$ is plotted as a function of frequency from front to back in 5 Hz steps with 250 Hz per plot. Based on a visual interpretation of these plots, there is no clear improvement with increasing frequency.

The standard error of estimate ϵ_r^2 for the variation of the calculated (or measured) $R(kr)_{avg}$ about the theoretical $R(kr)_T$ (sin(kr)/kr) is given by

$$\epsilon_r^2 = \frac{1}{n} \sum \left(R(kr)_T - R(kr)_{avg} \right)^2 \quad . \tag{3.19}$$
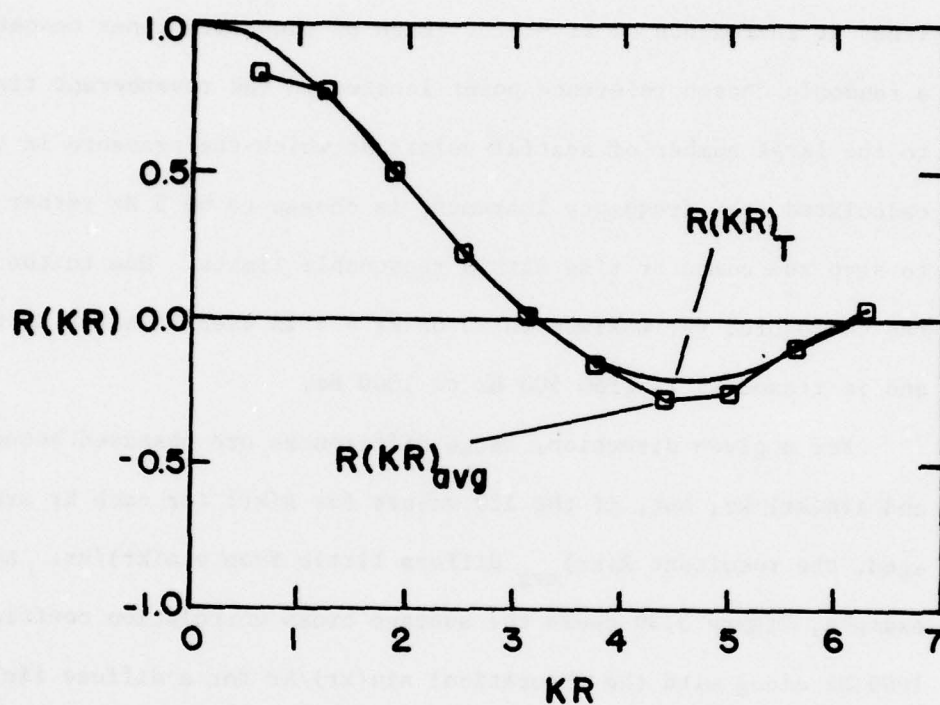
Figure 3.30. Average cross correlation coefficient R(kr)$_{avg}$ as a function of microphone separation r at 1000 Hz with the source in a typical position for the model enclosure with β = 0.01, the reference position at (0.841 m, 0.841 m, 0.841 m) and 120 averages for each of 10 r, and R(kr)$_T$ = sin(kr)/kr for a diffuse field.
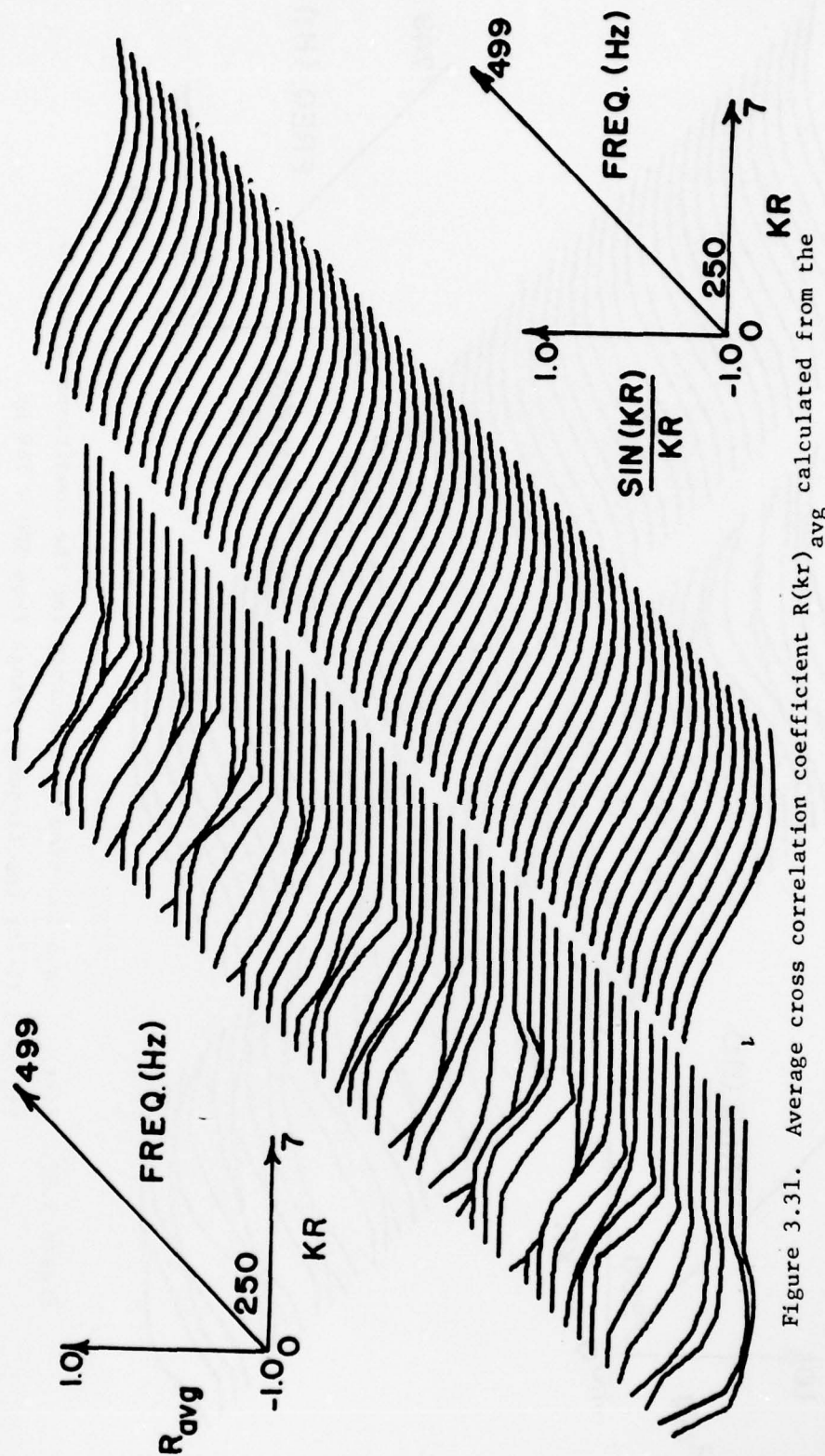
Figure 3.31. Average cross correlation coefficient $R(kr)_{avg}$ calculated from the computer generated pressure at 120 positions, r meters from the reference position as a function of frequency with $\Delta f = 5$ Hz, for the model enclosure with $\beta = 0.005$ and the source in a typical spatial position (1.596 m, 1.005 m, 0.785 m) for the frequency range from 250 – 499 Hz.
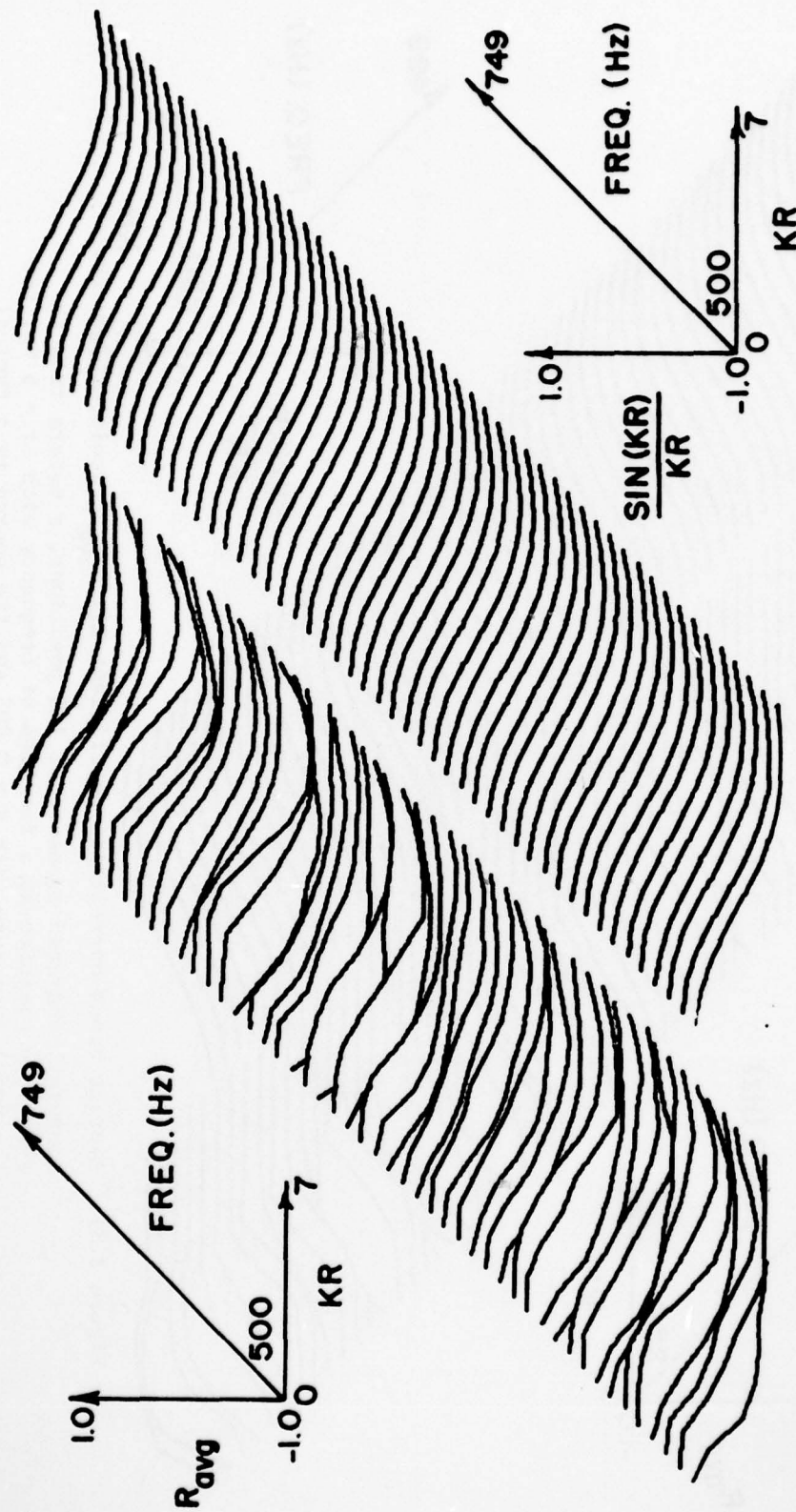
Figure 3.32. R(kr)$_{avg}$ as a function of frequency for the conditions stated in Figure 3.31 for the frequency range from 500 – 749 Hz.
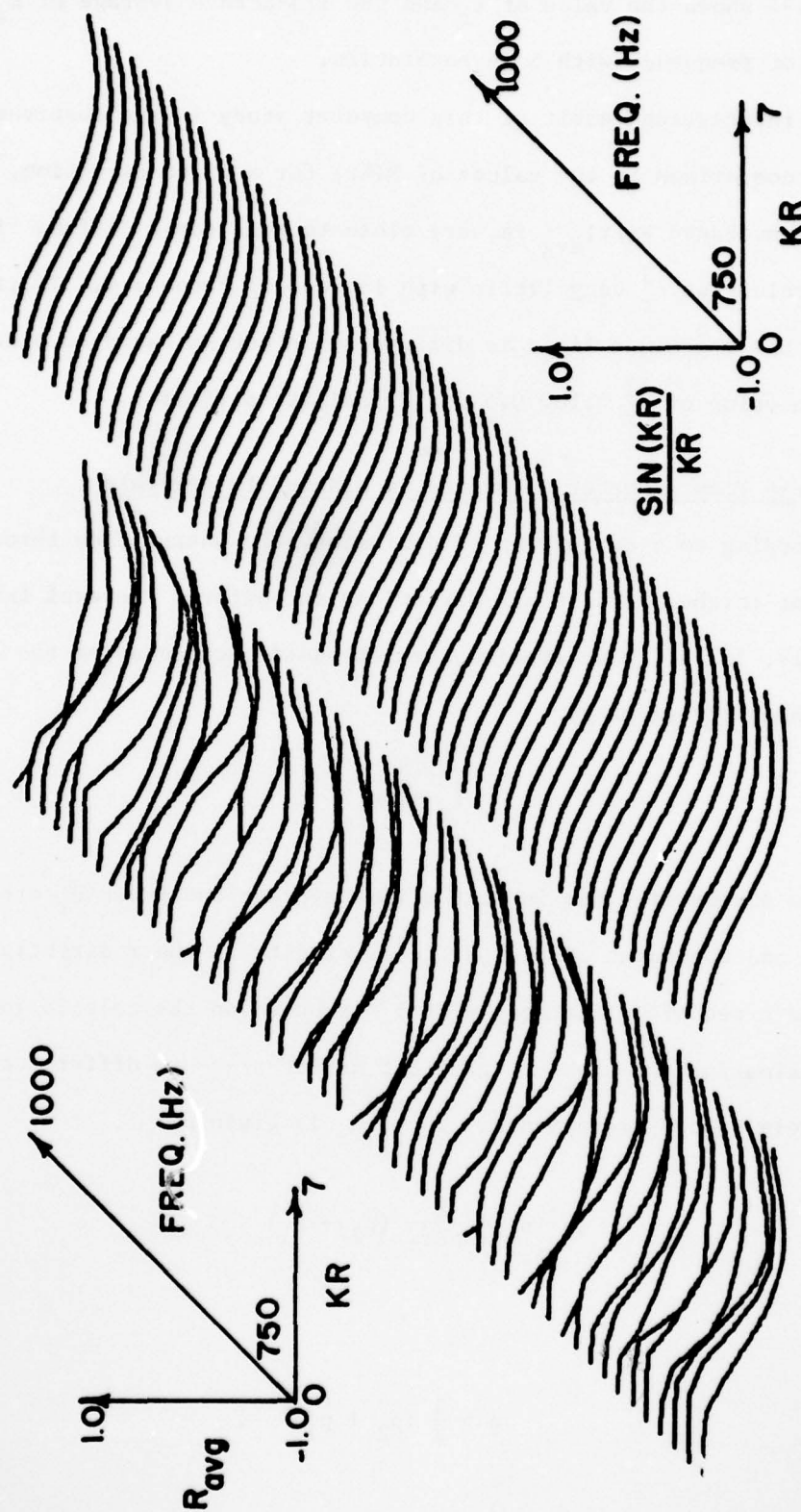
Figure 3.33. $R(kr)_{avg}$ as a function of frequency for the conditions stated in Figure 3.31 for the frequency range from 750 – 1000 Hz.

Figure 3.34 shows the value of ε_r^2 and the 1/3-octave average of ε_r^2 as a function of frequency with 5 Hz resolution.

One interesting result of this computer study is the observation that, in comparison to the values of R(kr) for a given direction, the spatially averaged $R(kr)_{avg}$ is very close to that for a diffuse field, and the values of ε_r^2 vary little with increasing frequency. If it is assumed that the sound field is diffuse above 400 Hz based on other indicators, a value of ε_r^2 below 0.5 would indicate diffusion.

3.7 Energy Flow - Vector Intensity in a Non-Diffuse Field

According to a definition of diffusion, the energy flow through each point in the field in all directions is uniform. Several investigators (19, 31, 42) have studied the methods for calculating the acoustic vector intensity given by

$$\vec{I}_r = \overline{pu_r} \quad , \tag{3.20}$$

where the superscript bar indicates time average and p and u_r are the pressure and component of the particle velocity in the r direction. An approximate technique for measuring $\vec{I}_r$ is based on the calculation of u_r by approximating the pressure gradient as the pressure difference between two closely spaced microphones. Thus, u_r is given by

$$u_r \simeq \frac{i}{\rho \Delta r \omega} (p_2 - p_1) \tag{3.21}$$

and

$$p \simeq \frac{1}{2} (p_2 + p_1) \quad . \tag{3.22}$$
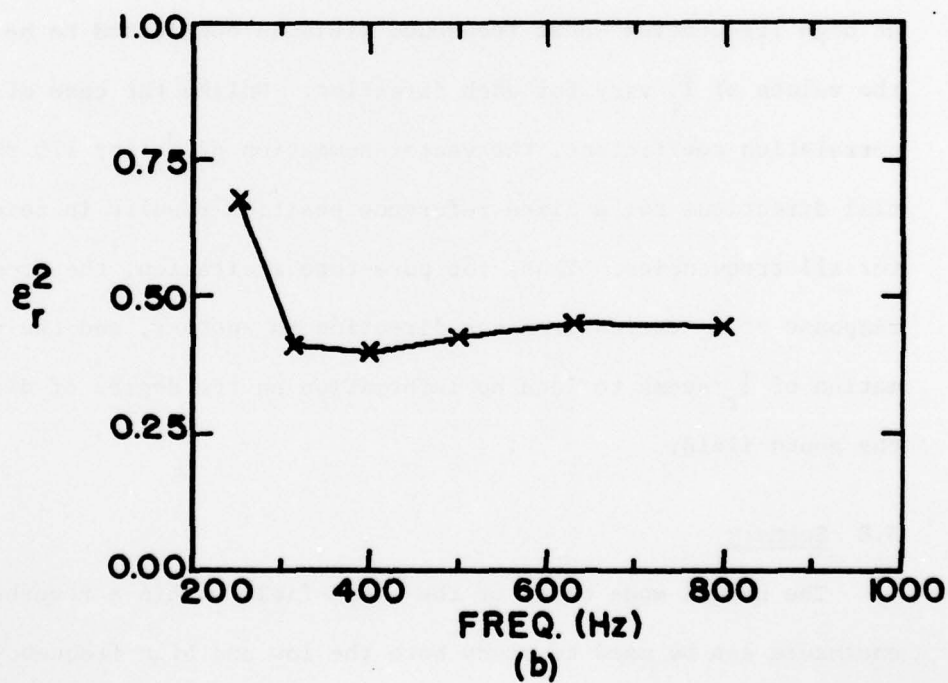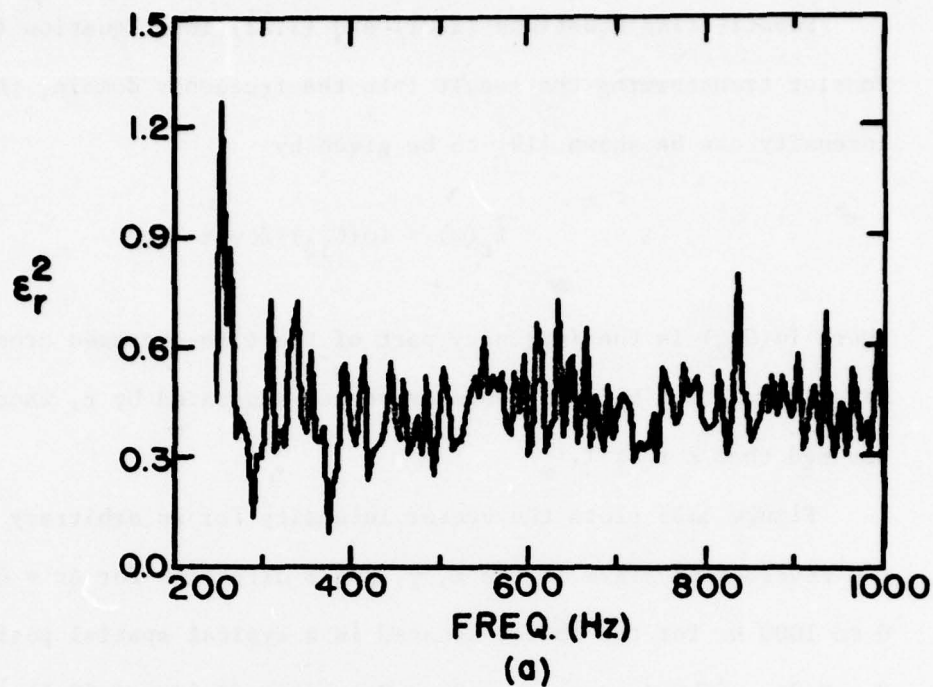
Figure 3.34. (a) Standard error of estimate ε_r^2 and (b) 1/3-octave average of ε_r^2 as a function of frequency for the variation of $R(kr)_{avg}$ (see Figures 3.31 through 3.33) from $R(kr)_T = \sin(kr)/kr$.

Substituting Equations (3.21) and (3.22) into Equation (3.20) and Fourier transforming the result into the frequency domain, the vector intensity can be shown (19) to be given by

$$\vec{I}_r(\omega) \simeq Im(G_{12})/2\rho\omega\ r \quad , \tag{3.23}$$

where $Im(G_{12})$ is the imaginary part of the time-averaged cross spectral density function between two microphones separated by r, where it is assumed that k r << 1.

Figure 3.35 plots the vector intensity for an arbitrary point in the reverberant field in the x, y, and z direction for $\Delta r = 0.04$ m from 0 to 1000 Hz for the source located in a typical spatial position and $\beta = 0.01$. (The data are based on Equations (3.23 and (3.1).) Note that, at high frequencies where the sound field is considered to be diffuse, the values of $\vec{I}_r$ vary for each direction. Unlike the case of the cross correlation coefficient, the vector summation of $\vec{I}_r$ for 120 random spatial directions for a fixed reference position results in zero intensity for all frequencies. Thus, for pure-tone excitation, the frequency response of $\vec{I}_r$ varies from one direction to another, and the vector summation of $\vec{I}_r$ seems to lend no information on the degree of diffusion of the sound field.

3.8 Summary

The normal mode model of the sound field within a reverberant enclosure can be used to study both the low and high frequency characteristics of the field. The model is particularly suited for pure-tone excitation of the field, and 1/3-octave analysis can be predicted by averaging over the suitable bandwidths. The investigation of the
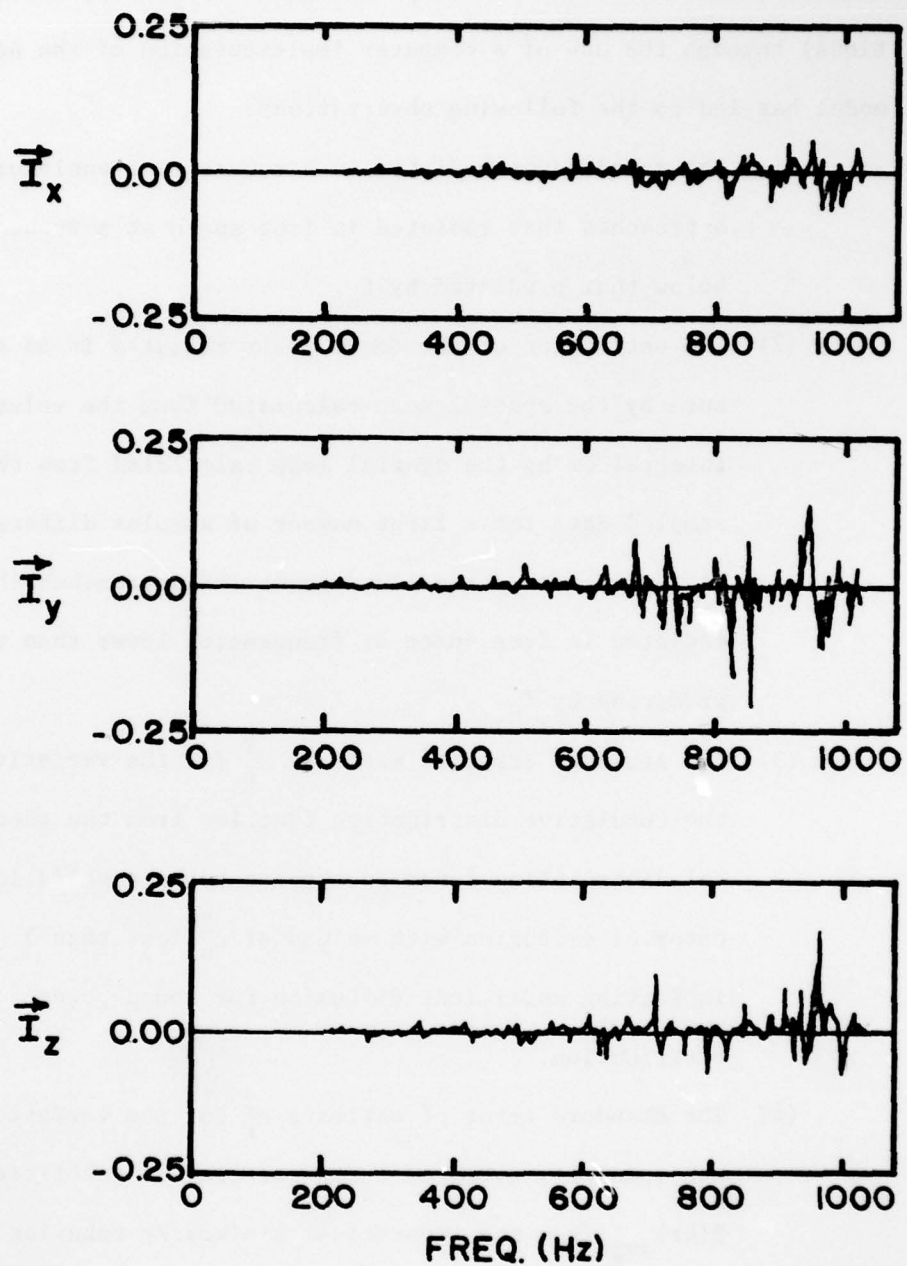
Figure 3.35. Computer generated vector intensity $\vec{I}$ in the x, y, and z
directions for a random point (0.841 m, 0.841 m, 0.841 m)
in the model enclosure with the source near a corner
(0.18 m, 0.18 m, 0.18 m), β = 0.005 and Δr = 0.04 m.

1.0

4.5
5.0
5.6

2.8

2.5

3.2

2.2

3.6

1.1

4.0

2.0

1.8

1.25 1.4 1.6

MICROCOPY RESOLUTION TEST CHART
NATIONAL BUREAU OF STANDARDS-1963-A
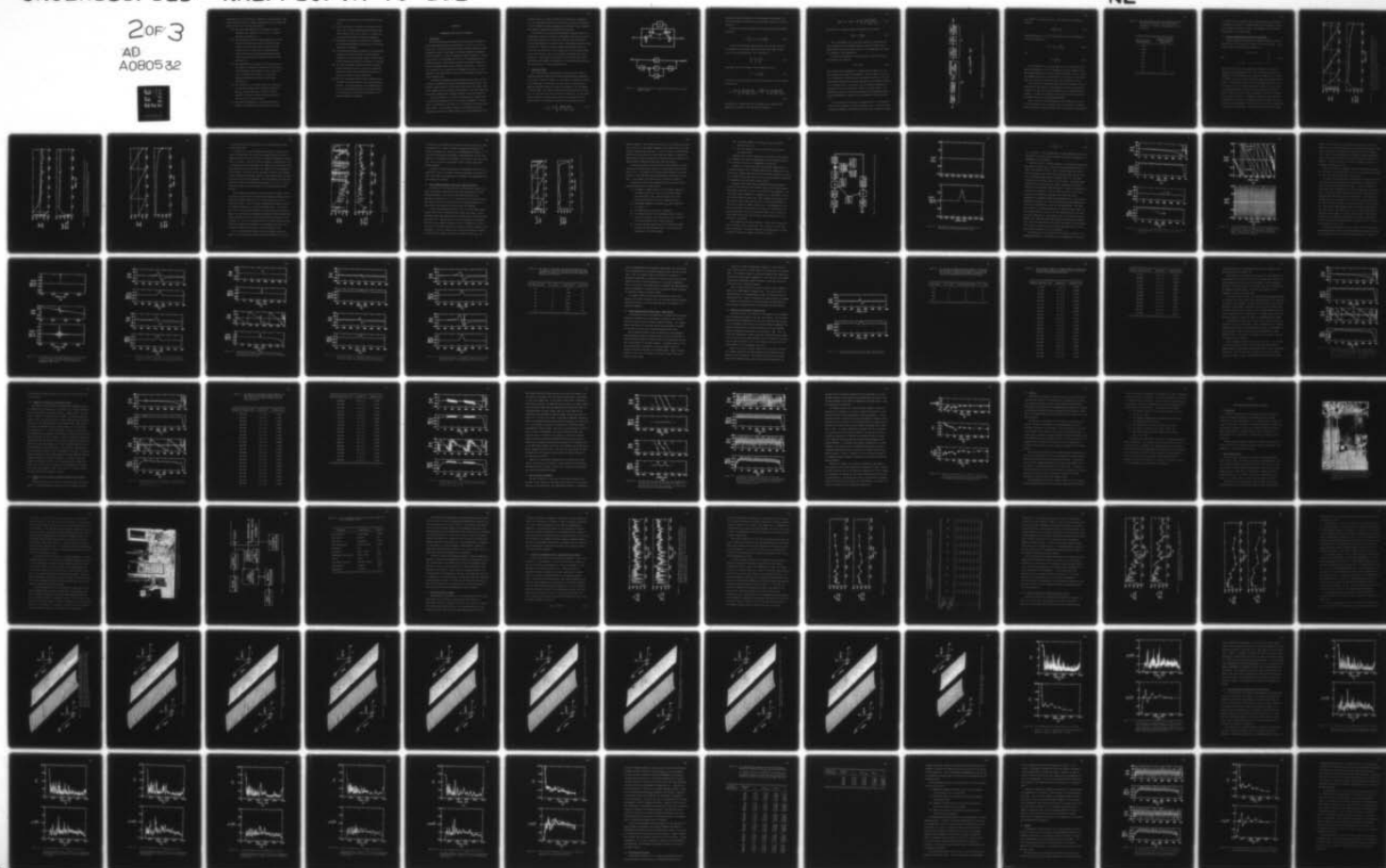
transition from low modal overlap to high modal overlap (diffuse conditions) through the use of a computer implementation of the normal mode model has led to the following observations:

(1) The sound power radiated in a reverberant enclosure approaches that radiated in free space at a frequency below that predicted by f_c.

(2) The estimation of the sound power radiated in an enclosure by the spatial mean calculated from the volume integral or by the spatial mean calculated from the sampled data for a large number of samples differs little from the true sound power and approaches that radiated in free space at frequencies lower than that predicted by f_c.

(3) The standard error of estimate ε_s^2 for the variation of the cumulative distribution function from the theoretical distribution function appears to be a valid indicator of diffusion with values of ε_s^2 less than 5 indicating sufficient diffusion for sound power distribution.

(4) The standard error of estimate ε_r^2 for the variation of the spatially averaged cross correlation coefficient $R(kr)_{avg}$ from the theoretical $\sin(kr)/kr$ behavior appears to be another indicator of diffusion with ε_r^2 less than 0.5 as a relative cutoff.

(5) The frequency dependance of the normalized spatial variance of squared pressure follows the same trends

for various source positions and the damping as noted for ε_s^2.

(6) For all indicators of diffusion, the location of the source near a corner produced larger fluctuation from ideal diffusion than for the source in a typical spatial position away from the enclosure boundaries.

(7) The addition of absorption (increases in β) produced less frequency-by-frequency fluctuation of the various indicators of diffusion.

(8) The frequency-by-frequency variation of the statistical characteristics shows the effect of well-separated resonances in the low frequency region, and these variations become less pronounced as frequency is increased.

(9) The normal mode model accurately predicts the experimentally measured deviation of the cross correlation coefficient from sin(kr)/kr behavior encountered for pure-tone excitation at high frequencies.

(10) The cross correlation and the vector intensity can be calculated or measured from the cross spectral density function. The vector summation of the imaginary part of the cross spectrum will yield zero vector intensity at all frequencies, and this does not appear to be a suitable indicator of diffusion.

CHAPTER IV

REVERBERANT SOUND FIELD WITH FEEDBACK

4.1 Introduction

The uses and problems associated with electroacoustic feedback in
sound reinforcement systems are well known (4, 14, 22, 23, 32, 37, 57,
69, 83, 89). In recent studies (27) multiple channel feedback has been
implemented through a large number of spatially separated narrowband
filters and delays to increase reverberation time in auditoria. The aim
of this study is to investigate the effect of the implementation of a
feedback system at a single spatial position for multiple frequencies
using a programmable Finite Impulse Response (FIR) filter. In particu-
lar, the merits of the feedback will be judged by the effects on the
diffusion of the sound field as related to the measurable parameter dis-
cussed in Chapter III.

A particular configuration studied analytically by Lilly (43) was
selected for implementation using an experimental model enclosure. The
defining characteristics of the enclosure and those of the digital FIR
filter together with the analytical expressions for the sound field with
and without feedback make a computer analysis of the system possible.

As seen in Chapter II, the lack of diffusion in an enclosure used
for sound power measurements is a low frequency phenomenon. The FIR
filter is implemented in real time for a low frequency or base band fre-
quency range. In reverberant enclosures, the amplitude and phase
responses of pressure are rather irregular and change substantially for

different source or receiver positions, wall absorption, temperature, etc. The programmable feature of the FIR filter allows for flexibility in filter design and allows programming of complicated filter responses which would be tedious using ordinary analog circuits.

The addition of a non-inline electroacoustic feedback system to a reverberant enclosure is intended to add energy to the field at frequencies between the resonance frequencies of the enclosure and thereby increase the diffusion of the sound field. The resultant sound field can be modeled as a system of coupled resonators which exhibit characteristics that are governed by (1) the sound field, (2) the design parameters of the FIR filter, and (3) the stability requirements for their interaction. This chapter will consider the theoretical model of the sound field with feedback and concentrate on the stability condition and the characteristics of the FIR digital filter.

4.2 Theoretical Model

The illustration and block diagram of the acoustically coupled feedback system described by Lilly (43) and experimentally implemented in the study are shown in Figure 4.1. The system is excited by a source with strength Q_0 at position ①, and the output is measured as the magnitude and phase (relative to Q_0) of the pressure at the microphone in position ④. The enclosure transfer functions are given by capital G_i i = 1,2,3,4, while the filter function is given by H. For the system without feedback, the input-output relation is determined by the G_1 function which can be expressed analytically from Equation (3.1) as

$$G_1 = \frac{p}{Q_0} = \frac{i\omega\rho}{V} \sum_N \frac{E_N \psi_N(r_1) \psi_N(r_4)}{(k^2 - k_N^2) + 2ik\delta_N} \quad . \qquad (4.1)$$
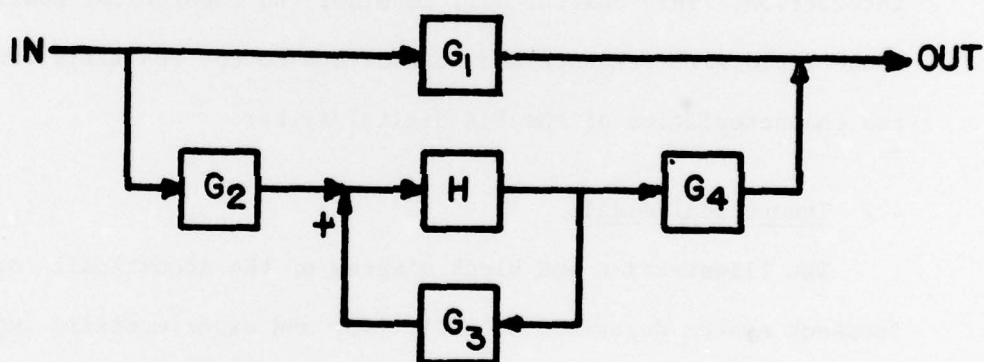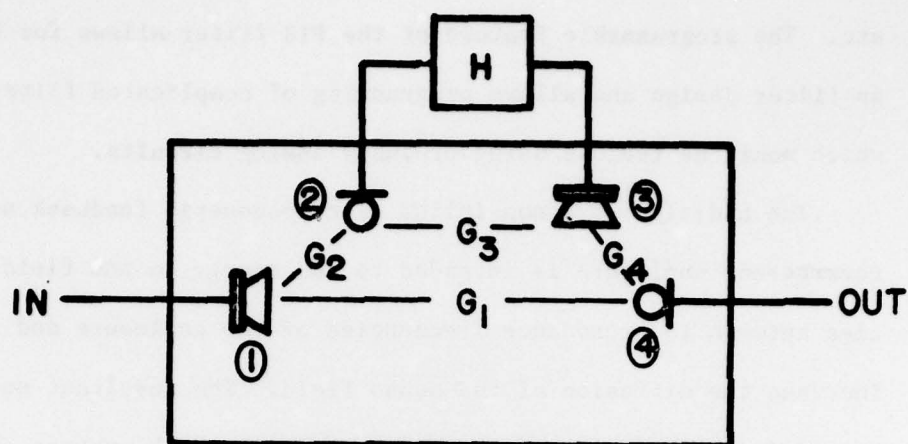
Figure 4.1. Illustration and block diagram of the acoustically coupled feedback system.

Likewise, the other G_i functions can be described as in Equation (4.1) with the appropriate values of the source strength, source, and receiver positions.

The total input-output expression for the sound field with feedback is given by

$$T = \frac{P_T}{Q_0} = G_1 + G_4 G_2 \frac{H}{1 + G_3 H} \quad . \tag{4.2}$$

In terms of the transfer functions that vary with the position of the microphone that spatially samples the sound field (④ in Figure 4.1), the total system function can be rewritten as

$$\frac{P_T}{Q_0} = \frac{P_1}{Q_0} + \frac{P_4}{Q_0^f} K^* \quad , \tag{4.3}$$

where Q_0^f is the source strength of the feedback source and

$$K^* = G_2 \frac{H}{1 - G_3 H} \quad . \tag{4.4}$$

In terms of the normal mode model for the sound field, the total pressure P_T is given by

$$P_T = \frac{i\omega\rho Q_0}{V} \sum_N \frac{\psi_N(r_4)\psi_N(r_1)E_N}{(k^2 - k_N^2) + 2ik\delta_N} + \frac{i\omega\rho Q_0^f(\omega)}{V} \sum_N \frac{\psi_N(r_3)\psi_N(r_4)E_N}{(k^2 - k_N^2) + 2ik\delta_N} \quad , \tag{4.5}$$

where $Q_0^f(\omega)$ is a complex function of frequency (i.e., magnitude and phase) and is related to the input source strength as

$$Q_0^f(\omega) = Q_0 \cdot CLR(\omega) \cdot \frac{i\omega\rho}{V} \sum \frac{E_N \psi_N(r_1) \psi_N(r_2)}{(k^2 - k_N^2) + 2ik\delta_N} \quad , \quad (4.6)$$

where $CLR(\omega)$ is a complex closed loop response and is given by

$$CLR(\omega) = \frac{H}{1 + G_3 H} \quad . \quad\quad (4.7)$$

Thus, from Equation (4.5), the total pressure can be seen as the sum of pressures of two resonant systems, the second of which, for a given feedback source and receiver position, is determined by the closed loop response of the feedback loop.

The closed loop response is often expressed in terms of the open loop response $L(\omega)$ given by

$$L(\omega) = G_3 H \quad . \quad\quad (4.8)$$

For the particular configuration of feedback shown in Figure 4.1, the block diagram for the open loop response is shown in Figure 4.2 as it is to be implemented in this study using the digital FIR filter. The open loop transfer function is the series combination of the transfer function of the feedback source, the enclosure G_3, the feedback microphone and preamplifier, the two antialiasing filters, and the FIR filter. The magnitude and phase of the open loop response are the measurable quantities that determine the stability of the feedback system (see Section 4.3).

In his analytical study Lilly has suggested that, in a statistical sense, the total pressure, as given by Equation (4.5), is the sum of two uncorrelated pressures, and beneficial results can be achieved by setting

$$L(w) = |L(w)| e^{i\theta_L} = G_3 H$$
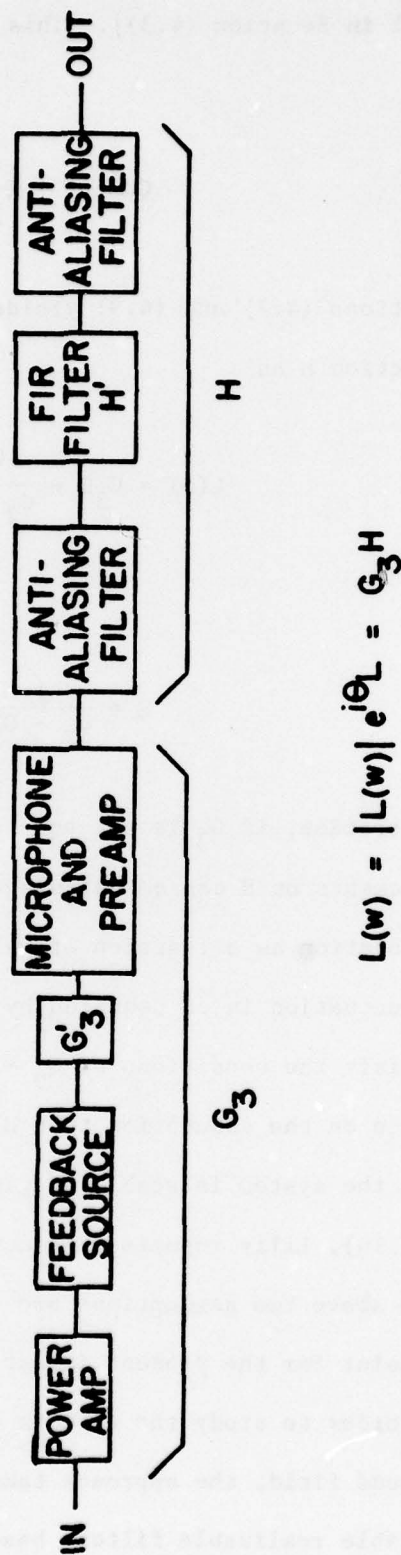
Figure 4.2. Block diagram of the open loop response as implemented with the Finite Impulse Response (FIR) filter.

$Q_0 = Q_0^f$ $\left(K^* = 1 \text{ in Equation } (4.3)\right)$. This condition is equivalent to setting

$$CLR(\omega) = \frac{1}{G_2} \quad . \tag{4.9}$$

Combining Equations (4.7) and (4.9) yields the open loop response and the filter function H as

$$L(\omega) = G_3 H = \frac{G_3}{G_2 - G_3} \tag{4.10}$$

and

$$H = \frac{1}{G_2 - G_3} \quad . \tag{4.11}$$

For illustration, if G_3 is set equal to 1.0, an indication of the general requirements on H can be calculated for a given primary source and feedback location as a function of wall absorption. Table 4.1 shows the maximum fluctuation in dB required by H as a function of wall admittance β to satisfy the conditions of $Q_0 = Q_0^f$ as described by Lilly.

Thus, based on the assumption that H as given by Equation (4.11) is realizable and the system is stable as given by the open loop response in Equation (4.10), Lilly reports a reduction in the normalized spatial variance. The above two assumptions are critical, however, and will be the starting point for the present investigation.

Thus, in order to study the effects of the feedback on the statistics of the sound field, the approach taken in this study is to experiment with possible realizable filters based on the design characteristics

Table 4.1. Required dynamic range of the feedback function H
for various values of the wall admittance β,
assuming $G_3 = 1.0$ and $Q_0 = Q_0^f$ in Equations (4.4)
and (4.5).

Real Part of the Wall Admittance β	Maximum dB Change in Pressure Amplitude Above 70 Hz
0.005	38
0.0075	37
0.010	35
0.02	30
0.04	27
0.06	25
0.08	24
0.1	20

of the FIR filter in conjunction with classical stability requirements,
to implement the filters in a computer model and in the model enclosure,
and to measure the effects, if any, of the feedback on the statistical
characteristics of the sound field.

4.3 Stability Requirements and the Open Loop Response

Classical stability requirements for feedback systems are found in
several texts (25, 41) and are all based on the work by Nyquist. In its
simplest form a system will become unstable if

$$|L(\omega)| \geq 1.0$$

and

$$\theta_2 = 2n\pi \quad , \quad n = 0, \pm1, \pm2 \ldots$$

$$(4.12)$$

where $|L(\omega)|$ and $\theta_2(\omega)$ are the magnitude and phase of the open loop
response as given in Equation (4.8). For illustration, the open loop
response for the FIR filter in the so-called all pass mode (i.e., $H(\omega) =$
$1.0 \ e^{i\theta_{Ap}}$, where θ_{Ap} is the all pass linear phase lag) as implemented in
Figure 4.2 is plotted in Figure 4.3 for the feedback source in a corner
of the enclosure, and, in order to minimize the effect of G_3 function,
the feedback microphone is placed in the near field of the feedback
source. Figures 4.4 and 4.5 show the magnitude and phase for the modi-
fied G_3 function and for H. In Figure 4.4 note that, even though the
microphone is very close to the feedback source, the ripples are due to
various enclosure resonances. The roll off of G_3 at very low frequencies
is due to the feedback source. Also note that the phase lag in Figure
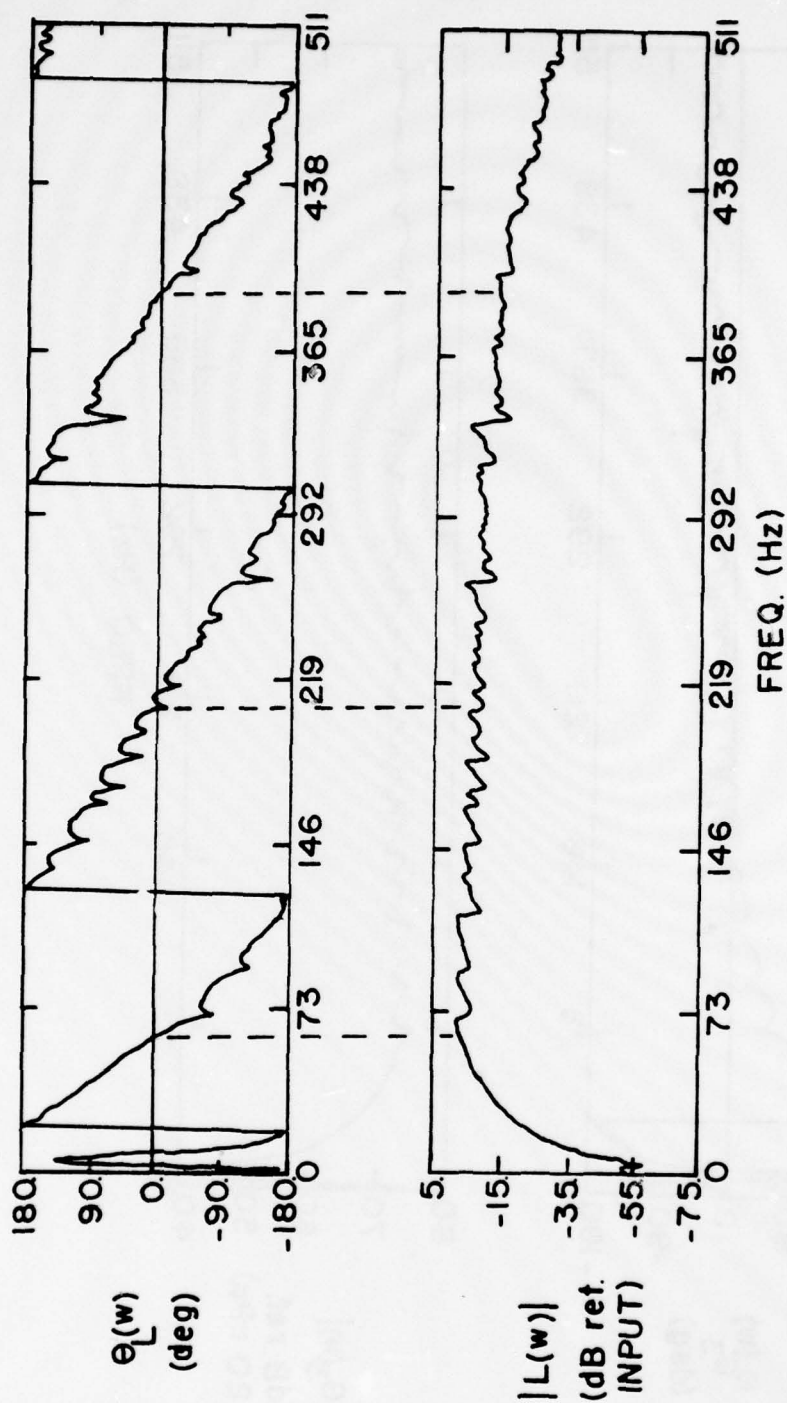
Figure 4.3. An example of the experimentally measured magnitude and phase of the open loop response for the feedback microphone in the near field of the feedback source and the FIR filter specified as all pass where the vertical dashed lines indicate the critical frequencies, where $\theta_L(\omega) = 0.0^\circ$.
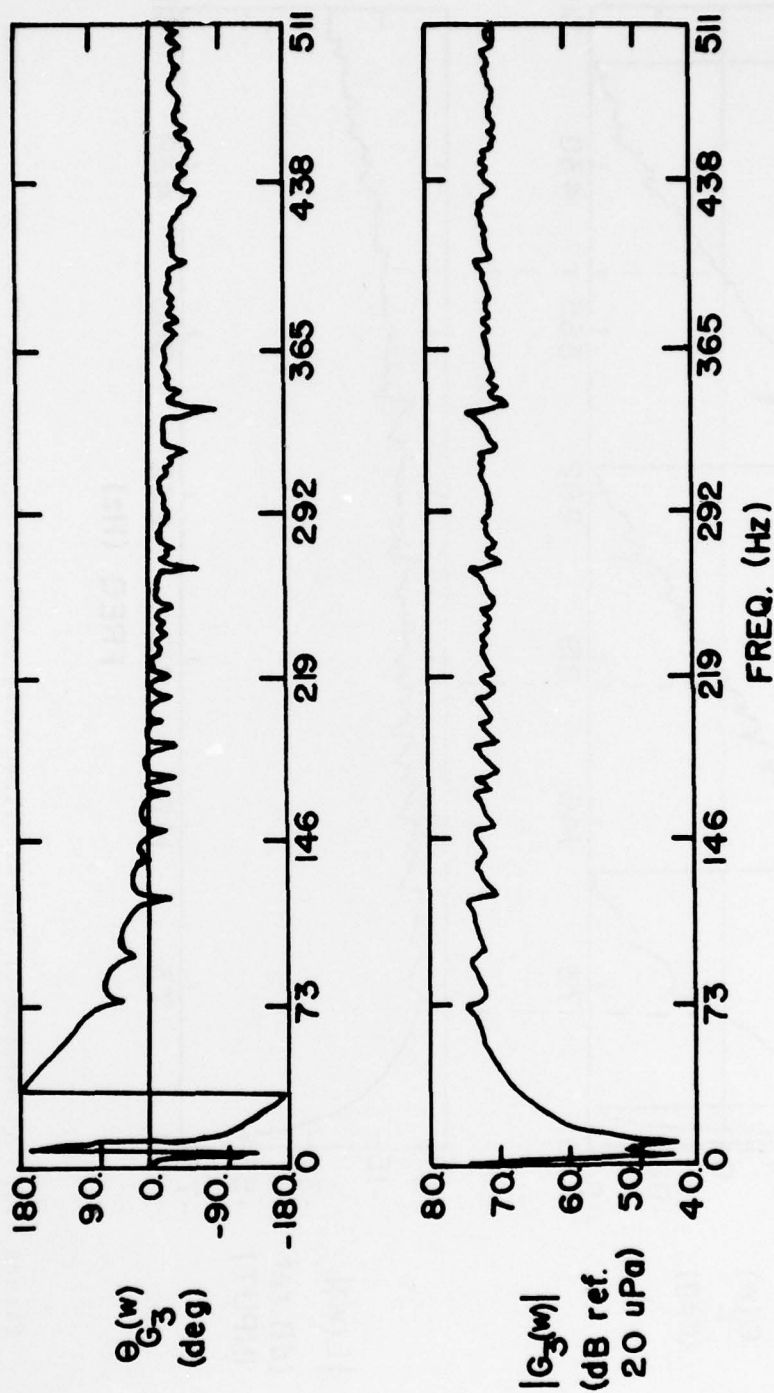
Figure 4.4. The experimentally measured magnitude and phase of the G_3 function for the feedback source in an enclosure corner and the feedback microphone in the near field of the feedback source.
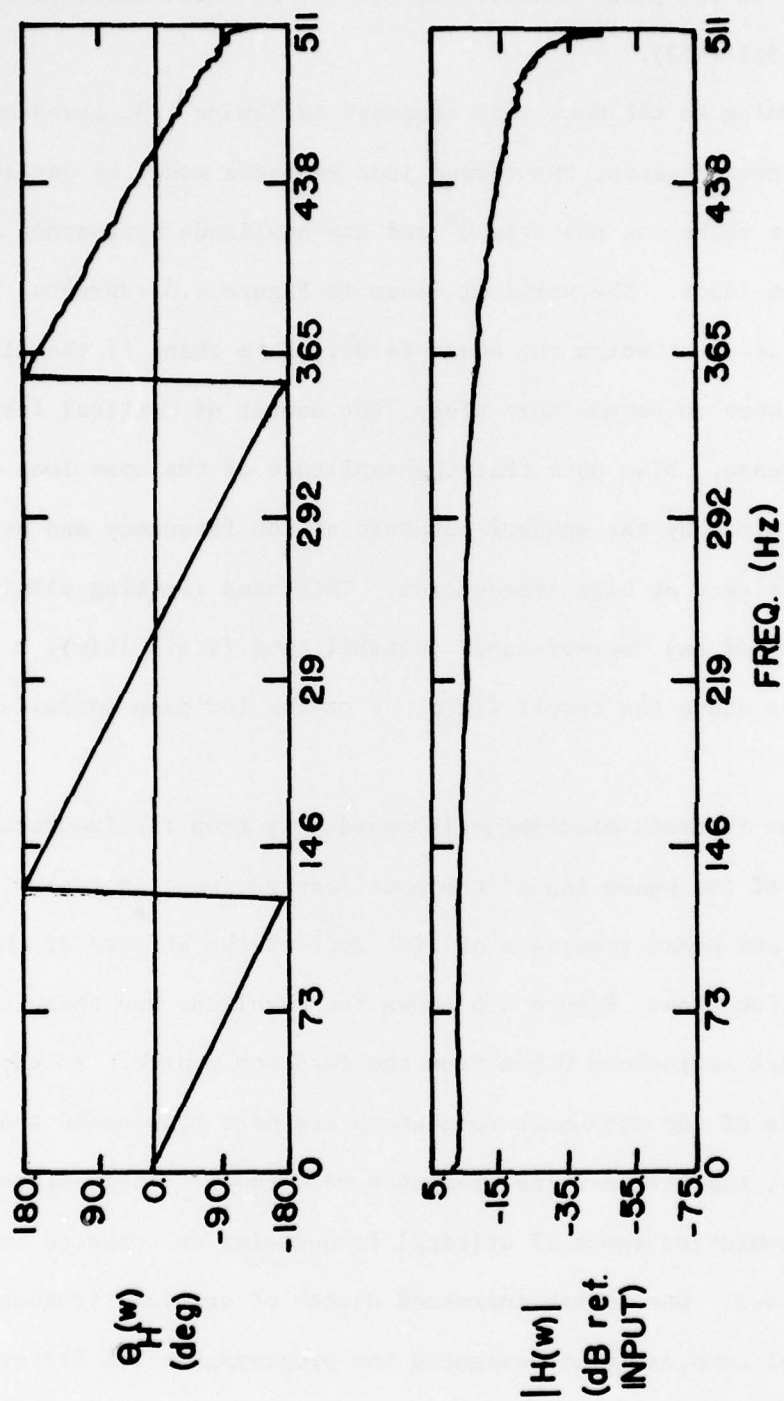
Figure 4.5. The experimentally measured magnitude and phase of the FIR filter for the all pass design where the linear phase lag is due to the antialiasing filters.

4.5 is due to the phase characteristics of the antialiasing filters (Ithaco Model #453).

Returning to the open loop response in Figure 4.3, based on the stability requirements, the closed loop response would be unstable at frequencies where the phase is 0° and the amplitude approaches 0 dB relative to the input. The vertical lines in Figure 4.3 represent the critical frequencies at which the phase is 0°. Note that, if the slope of the phase lag were to become more steep, the number of critical frequencies would increase. Also note that the amplitude of the open loop response is band limited by the speaker response at low frequency and by the antialiasing filters at high frequencies. This band limiting eliminates the possibility of any "out-of-band" instabilities (i.e., $|L(\omega)| < 1.0$ for frequencies above the cutoff frequency of the low pass antialiasing filters).

As the feedback microphone is moved away from the feedback source, the slope of the phase lag of the open loop response increases, and the amplitude and phase responses of $L(\omega)$ reflect the effects of the G_3 enclosure function. Figure 4.6 shows the magnitude and phase of G_3 for the feedback microphone 0.5 m from the feedback source. As expected, the effects of the enclosure resonances are more pronounced than seen in Figure 4.4, and the open loop response measured with this microphone and speaker separation shows 27 critical frequencies as compared to 3 seen in Figure 4.3. Due to the increased number of critical frequencies and the general complexity of designing the programmable FIR filter, the feedback microphone is placed 0.01 m from the feedback source.

For the experimentally measured open loop response as given in Figure 4.3, the closed loop response as given by Equation (4.7) can be
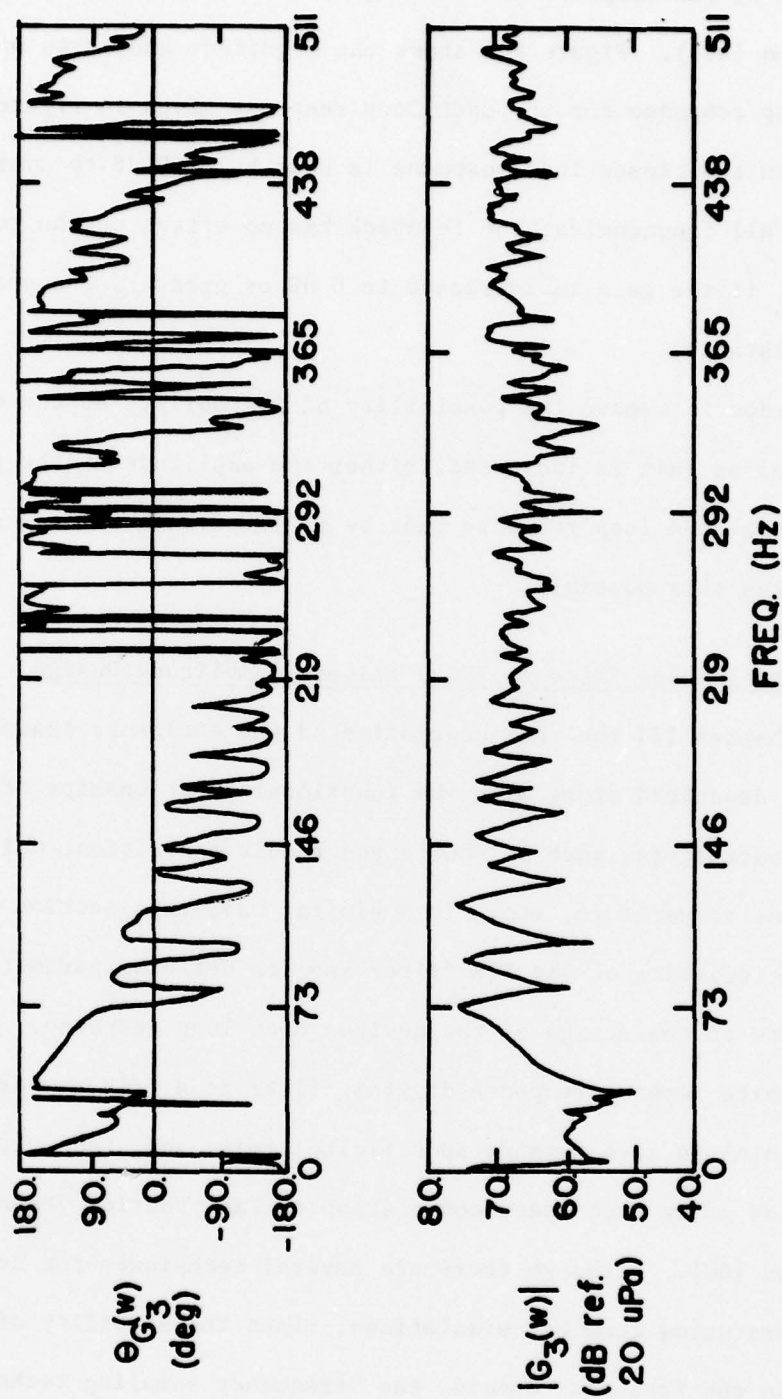
Figure 4.6. An example of the experimentally measured magnitude and phase of the G_3 function for the feedback microphone 0.5 m from the feedback source.

calculated by the computer model along with the total pressure P_T given by Equation (4.5). Figure 4.7 shows the magnitude and phase of the closed loop response for the open loop response given in Figure 4.3. If the gain in the closed loop response is kept below 0 dB to avoid instability at all frequencies, the feedback has no effect on the total pressure, and, if the gain is increased to 0 dB or greater, the system becomes unstable.

In order to remove the possibility of instability at the critical frequencies as gain is increased, either the amplitude or the phase (or both) of the open loop response must be modified. The programmable FIR filter makes this possible.

4.4 Finite Impulse Response (FIR) Filter – Amplitude Design

In Chapter III the characteristics of the enclosure transfer functions are described along with the functional relationships of their defining parameters, such as source and receiver position, wall absorption, temperature, etc. In a similar way, this section describes the characteristics of the FIR filter and its defining parameters as they relate to the design of the desired open loop response.

A finite impulse response digital filter is a filter whose impulse response h(n) is zero outside some finite limit, and, thus, it can be implemented using high speed convolution or Fast Fourier Transform (FFT) techniques (60). Although there are several techniques for designing FIR filters using computer simulations, since the stability criteria is defined in the frequency domain, the "frequency sampling technique" seems appropriate. For this design procedure the desired frequency response is specified at N_t equally spaced points between 0 Hz and f_{max}, the
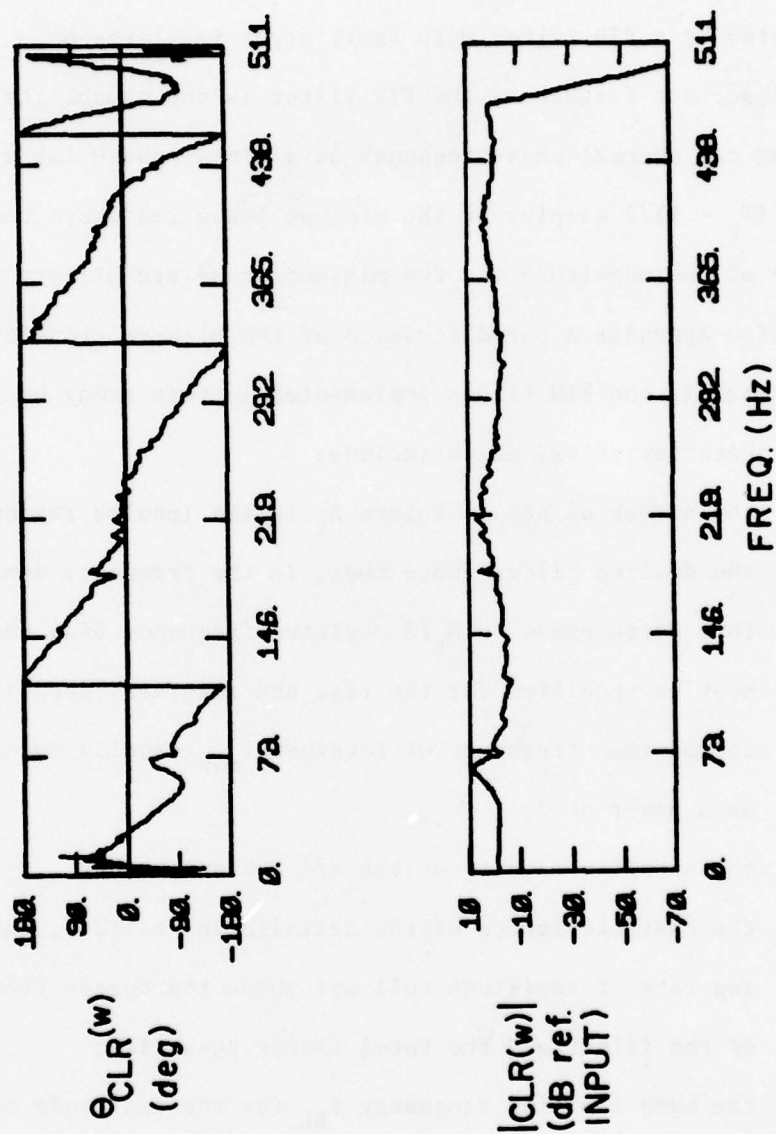
Figure 4.7. The computer generated magnitude of the closed loop response given in Figure 4.6 with a gain of -0.5 dB (ref input).

highest frequency. The frequency resolution Δf is determined by the number of points N_t in the impulse response and the sampling rate f_S of the analog to digital (a/d) converters. If care is taken to avoid the Gibbs phenomenon (33, 60, 63) due to specifying large changes in amplitude or phase between consecutive samples, the desired frequency response can be approximated by a FIR filter with small error for large N_t.

An important feature of the FIR filter is the capability of easily specifying the overall phase response as a linear phase lag with delay equal to $(N_t - 1)/2$ samples or the minimum phase lag where the natural logarithm of the magnitude and the minimum phase are Hilbert transform pairs. (See Appendix A for discussion of the Hilbert transform.)

In general, the FIR filter implemented in this study has several defining characteristics, which include:

(1) the number of sample points N_t in the impulse response of the desired filter (note that, in the frequency domain, this corresponds to $N_t/2$ positive frequency bins that must be specified for the real and imaginary parts);

(2) the maximum frequency of interest f_{max} usually specified as a power of 2;

(3) the sampling rate f_S of the a/d converters;

(4) the characteristics of the antialiasing filters, including rate of amplitude roll off above the corner frequency of the filter and the total linear phase lag;

(5) the band limiting frequency f_{BL} for the amplitude design to avoid the Gibbs phenomenon due to the band limiting assumptions of the FFT algorithm;

(6)   the maximum change in dB, ΔdB_{max}, between consecutive

frequency bins; and

(7)   the total number of bins that the FIR filter quantizes

the sampled data.

Through the use of FFT techniques various filters can be designed
on a computer, and, using the programmable FIR filter shown in Figure
4.8, the desired filter can be implemented in real time.

In order to illustrate the above list of filter characteristics,
the design procedure for an arbitrary desired filter shape will be con-
sidered, the computer model will be used to generate the impulse response
of the example filter, and this filter will be experimentally implemented
for comparison with the original desired filter.

The Spectra Data Model 618 programmable FIR filter implements a
filter by convolving its stored impulse response with the time sampled
input signal digitized to 12 bits. The FIR filter will implement a fil-
ter with an impulse response for a maximum of N_t = 1024 points fed into
the filter's memory via paper tape. For a maximum of 1024 points, the
a/d converters have a real time rate up to 10 kHz with a maximum real
time rate of 40 kHz for smaller values of N_t. The sampling rate f_S of
the a/d converters is controlled by an external (to the FIR unit) fre-
quency synthesizer, and the low pass antialiasing filters, which are
Ithaco Model #453 filters with selectable cutoff frequency, are also
external to the FIR unit.

As an example of the design procedure, a filter with a narrowband
peak of +30 dB at 250 Hz and otherwise flat (0 dB) up to 475 Hz (f_{BL})
will be considered. The desired amplitude and minimum phase are shown
in Figure 4.9 where the frequency resolution is given by
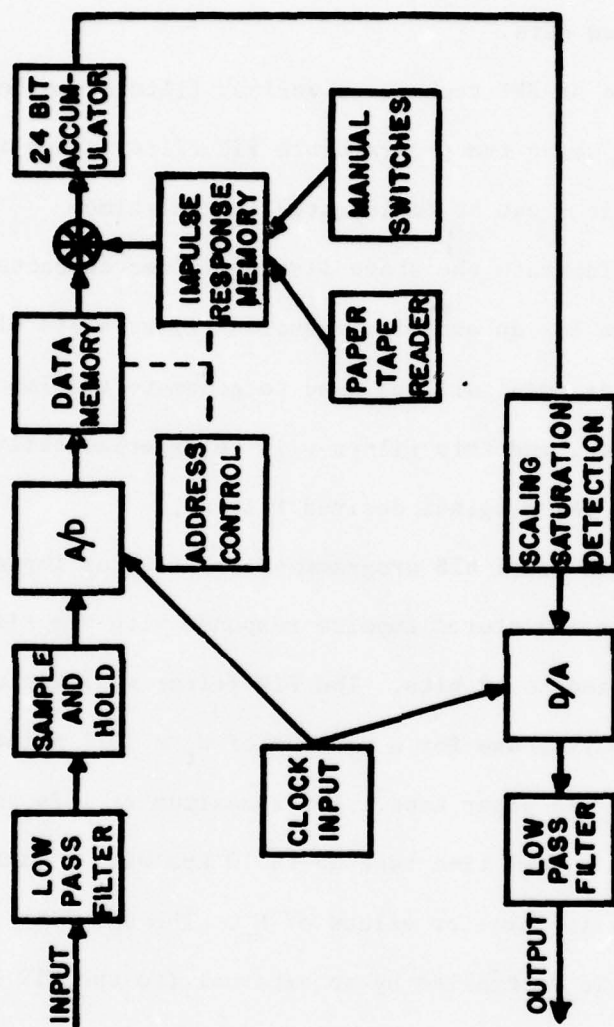
Figure 4.8. The programmable FIR filter manufactured by Spectra Data.
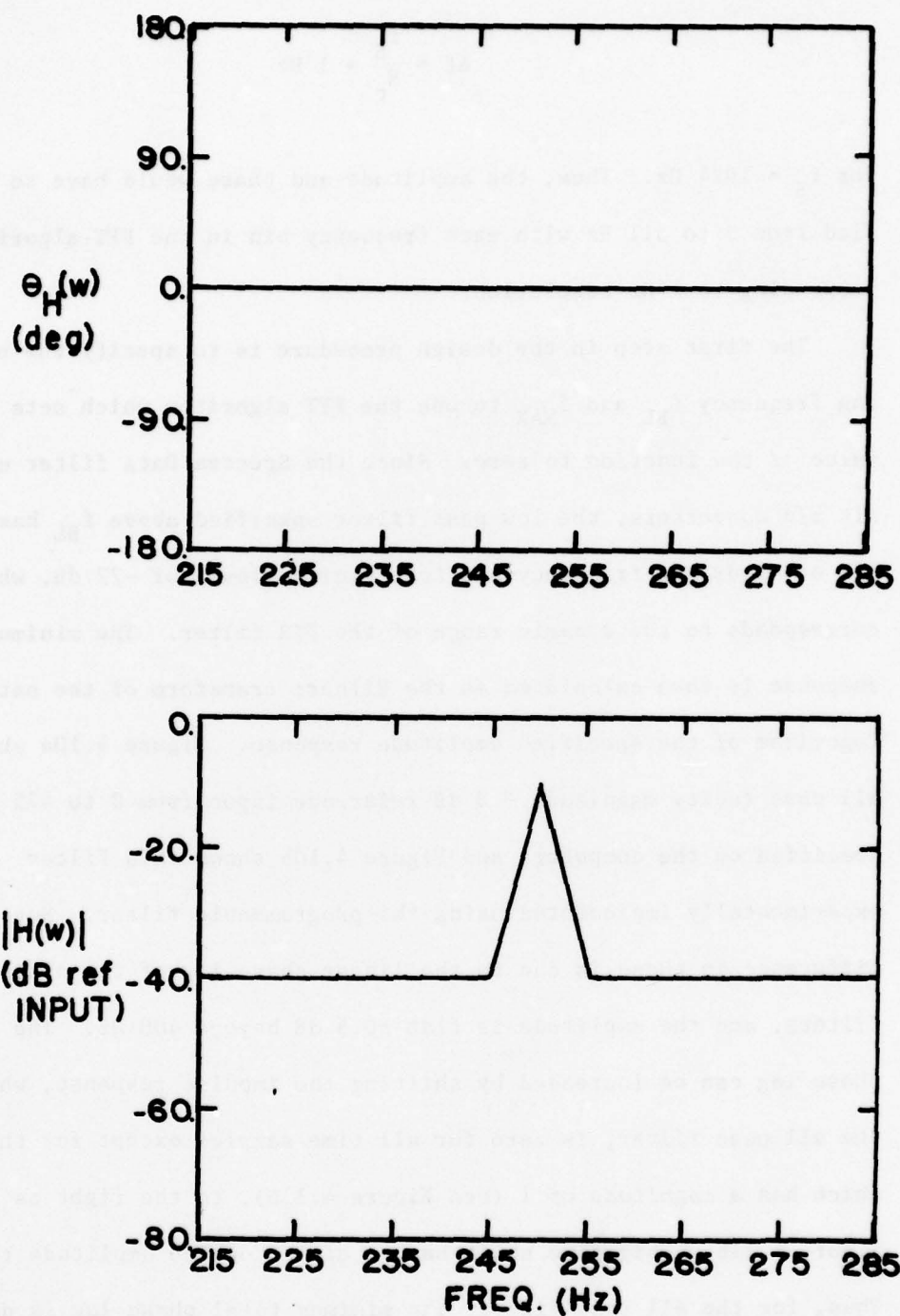
Figure 4.9.   The magnitude and phase of a desired filter to be
implemented by the programmable FIR filter.

$$\Delta f = \frac{f_S}{N_t} = 1 \text{ Hz} \qquad (4.13)$$

for f_S = 1024 Hz. Thus, the amplitude and phase would have to be speci-
fied from 0 to 511 Hz with each frequency bin in the FFT algorithm cor-
responding to 1 Hz resolution.

The first step in the design procedure is to specify the band limit-
ing frequency f_{BL} and f_{MAX} to use the FFT algorithm which sets the N - 1
value of the function to zero. Since the Spectra Data filter uses 12
bit a/d converters, the low pass filter specified above f_{BL} has a roll
off of -3 dB per frequency bin to a minimum level of -72 dB, which
corresponds to the dynamic range of the FIR filter. The minimum phase
response is then calculated as the Hilbert transform of the natural
logorithm of the specified amplitude response. Figure 4.10a shows this
all pass (unity magnitude - 0 dB reference input from 0 to 475 Hz) as
specified on the computer, and Figure 4.10b shows this filter
experimentally implemented using the programmable filter. Note that the
difference in phase is due to the linear phase lag of the antialiasing
filters, and the amplitude is flat ±0.5 dB beyond 400 Hz. The linear
phase lag can be increased by shifting the impulse response, which, for
the all pass filter, is zero for all time samples except for the first
which has a magnitude of 1 (see Figure 4.11a), to the right as shown in
Figure 4.11b. This time shift has no effect on the amplitude response.
Thus, for the all pass filter, the minimum total phase lag is determined
by the slope of the phase lag of the two antialiasing filters, and the
desired phase in Figure 4.9 is not realizable.

The second step is the design of the +30 dB peak at 250 Hz. In a
simpleminded fashion, if the frequency bin corresponding to 250 Hz were
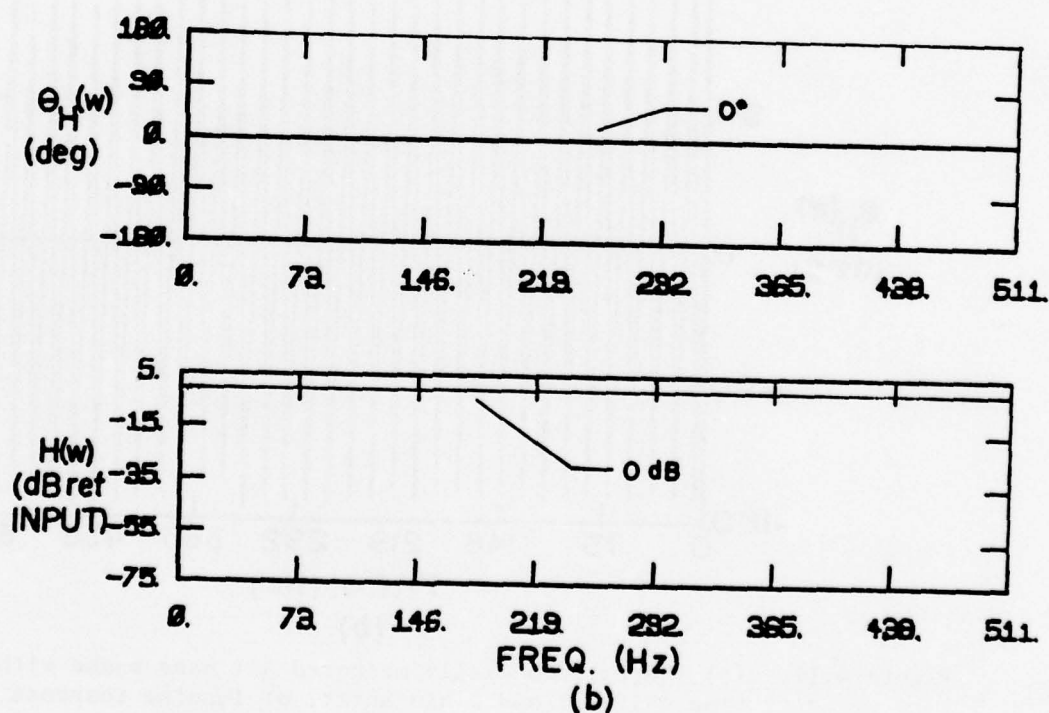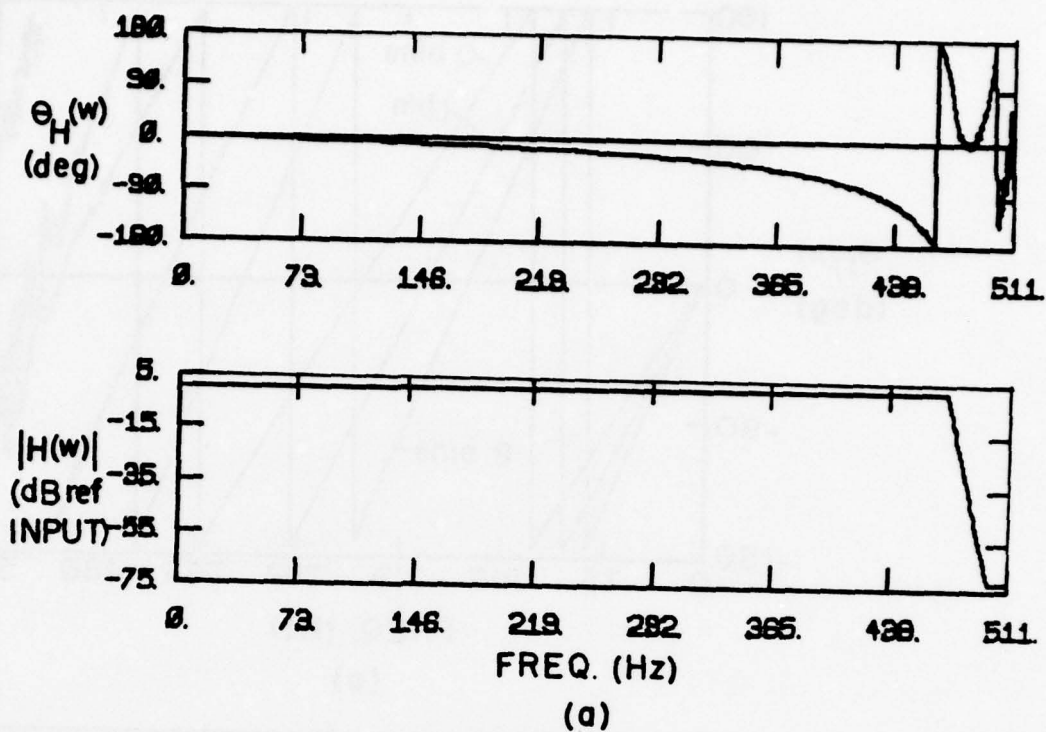
Figure 4.10. The magnitude and phase of an ideal (a) all pass filter and (b) band limited FIR filter with constant linear phase lag.
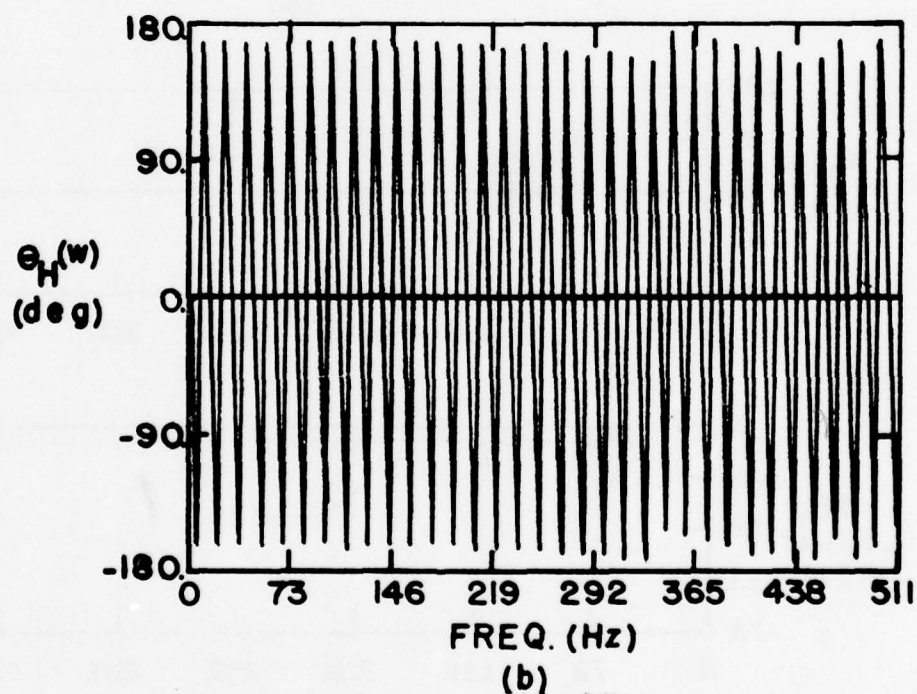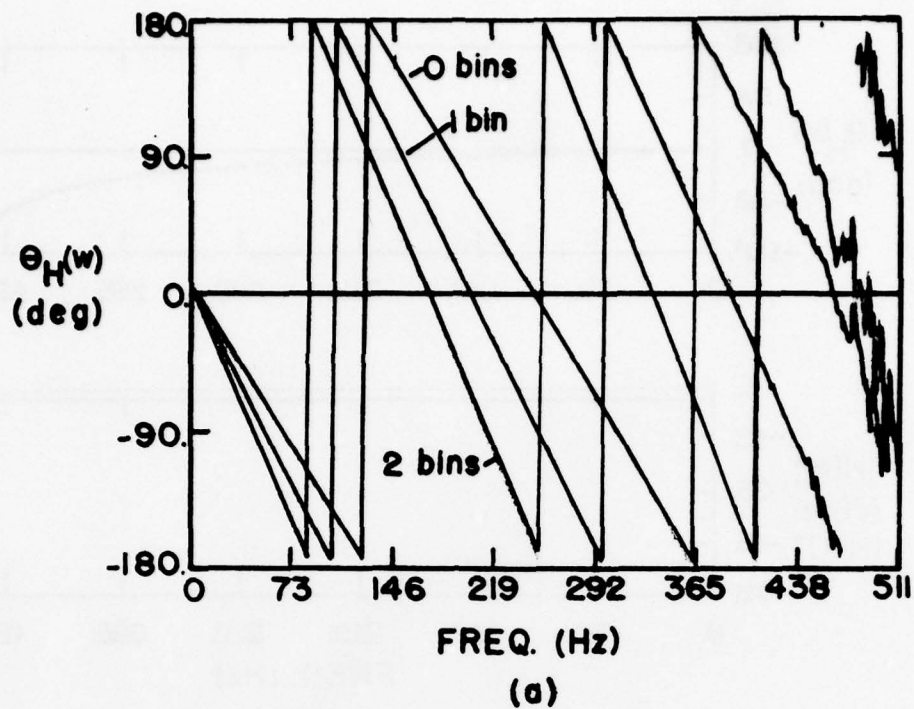
Figure 4.11. (a) The experimentally measured all pass phase with no time shift, 1 and 2 bin shift, of impulse response of the FIR filter; (b) The all pass phase for a 64 bin time delay. (Note that all cases have the same amplitude response, which is not shown.)

simply set to +30 dB, while the remaining bins were set to 0 dB as in Figure 4.12a, the large discontinuity in levels between consecutive bins results in the Gibb's phenomenon when implemented as shown in Figure 4.12b. Based on the experimenting with different filters, the maximum change in dB between consecutive bins has been found to be ±10 dB. In addition, in order to achieve the desired peak height, a minimum of two bins must be specified at 30 dB.

Figure 4.13a shows the expanded frequency domain amplitude response for the desired filter as specified based on the considerations mentioned above and its measured realization in Figure 4.13b.

As a result of the FFT process, the amplitude and phase design needs to be specified before generating the time domain that represents the filter with the desired amplitude and phase. In order to obtain the minimum phase lag corresponding to the specified amplitude fluctuation in Step 1, the Discrete Hilbert Transform of the natural logarithm of the amplitude $(DHT(\ln|H|))$ will yield the minimum phase. The amplitude and minimum phase of the realizable filter are shown in Figure 4.14a, with the filter specified in Figure 4.9 repeated in Figure 4.14b for comparison. Note that the main difference between the desired filter and the realizable filter is the linear phase lag of the antialiasing filters. Also note that the number of bins that specify a peak in the amplitude response (6), the number of affected bins in the phase response (23), and the total positive and negative change in phase ($\pm 34^{\circ}$) is related to the peak amplitude value in dB.

In order to quantify this relation, Figures 4.15 and 4.16 show the magnitude and phase for four filters designed with progressively increasing peak heights with +10 dB change between adjacent bins. Table 4.2
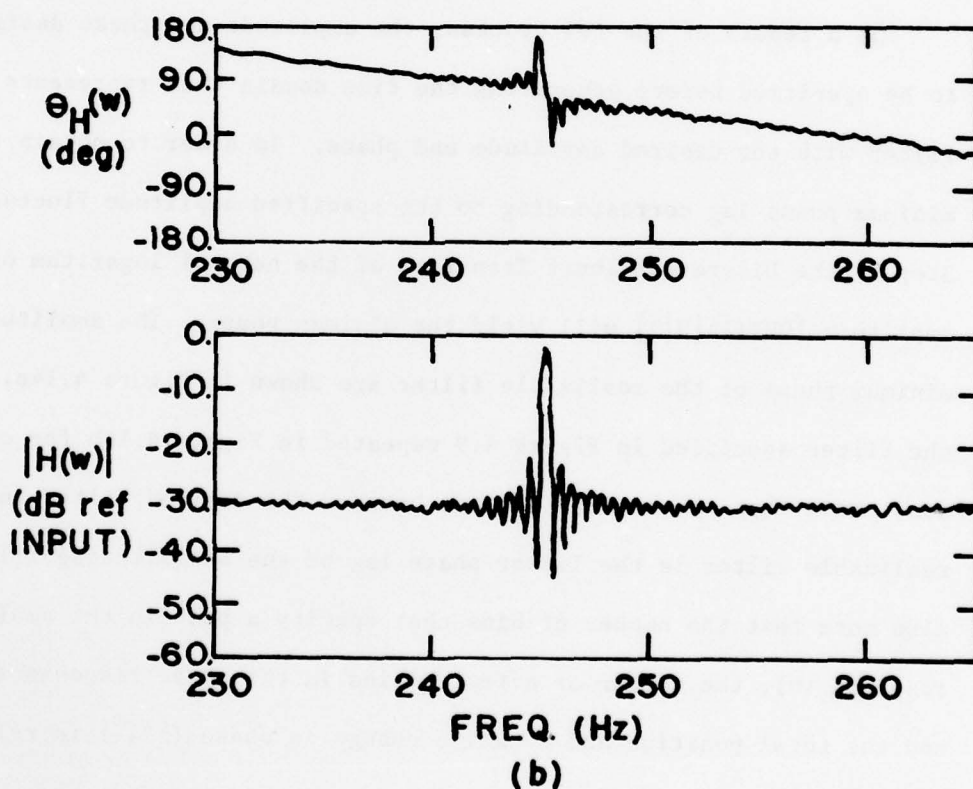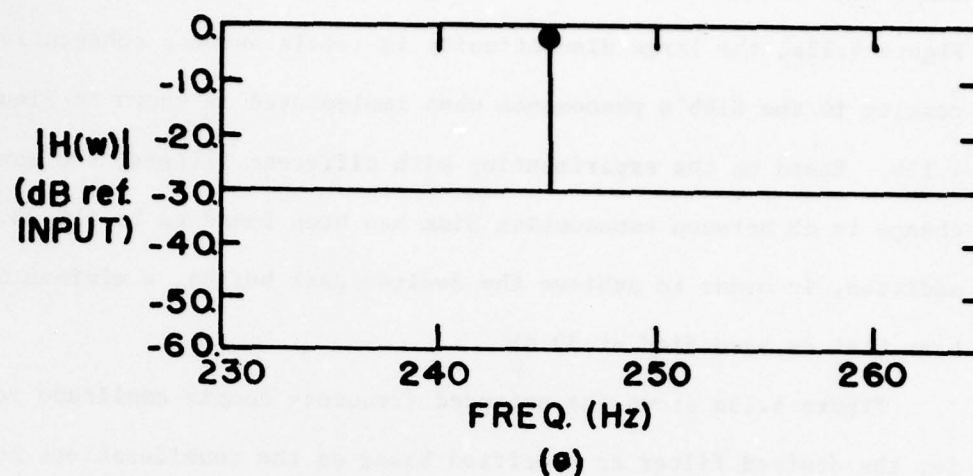
Figure 4.12. An example of the Gibbs Phenomenon caused a large change
in levels between consecutive frequency bins: (a)
specified design, (b) actual filter implemented on
programmable FIR filter.
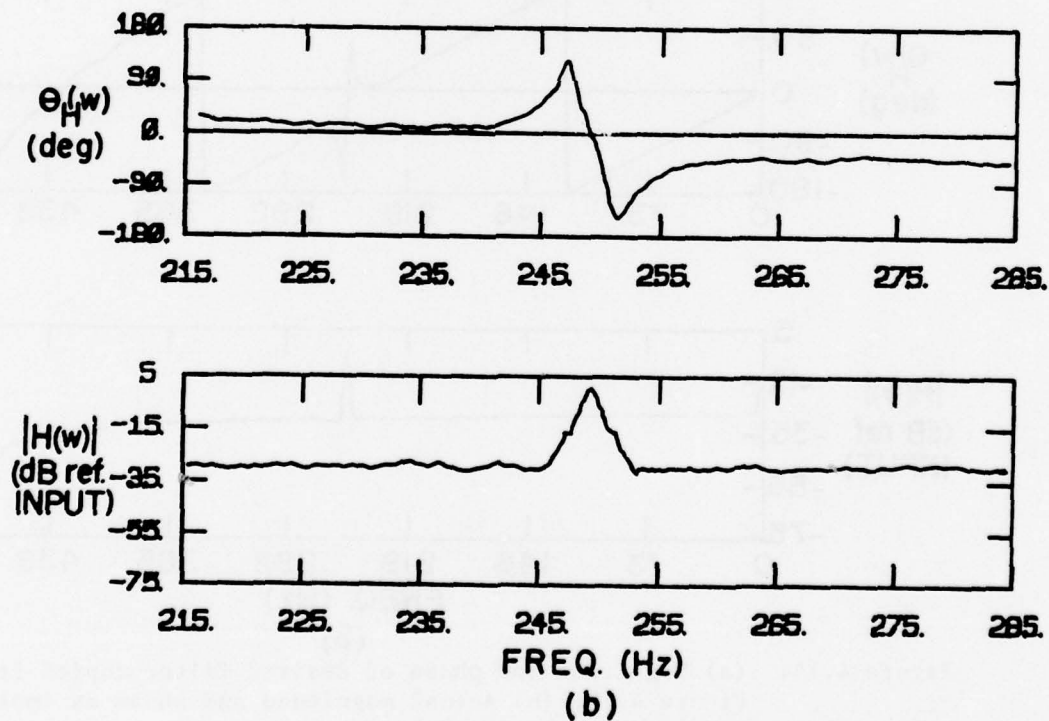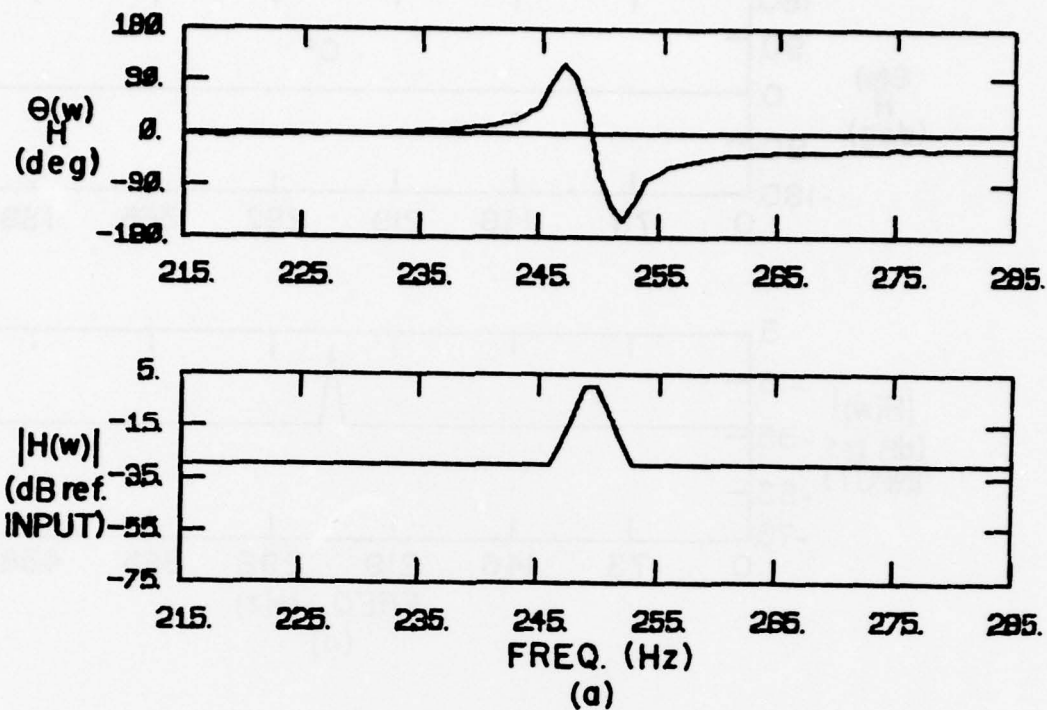
Figure 4.13. (a) Specified amplitude response of a filter with 40 dB peak with ±10 dB per frequency bin; (b) Actual amplitude response of filter implemented on programmable FIR filter.
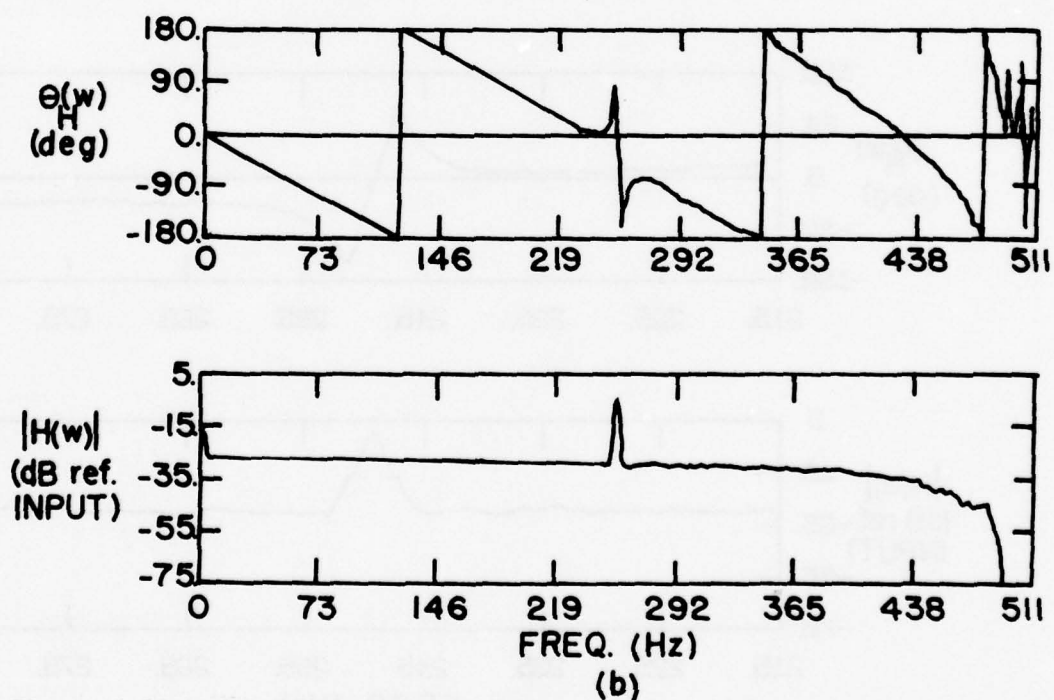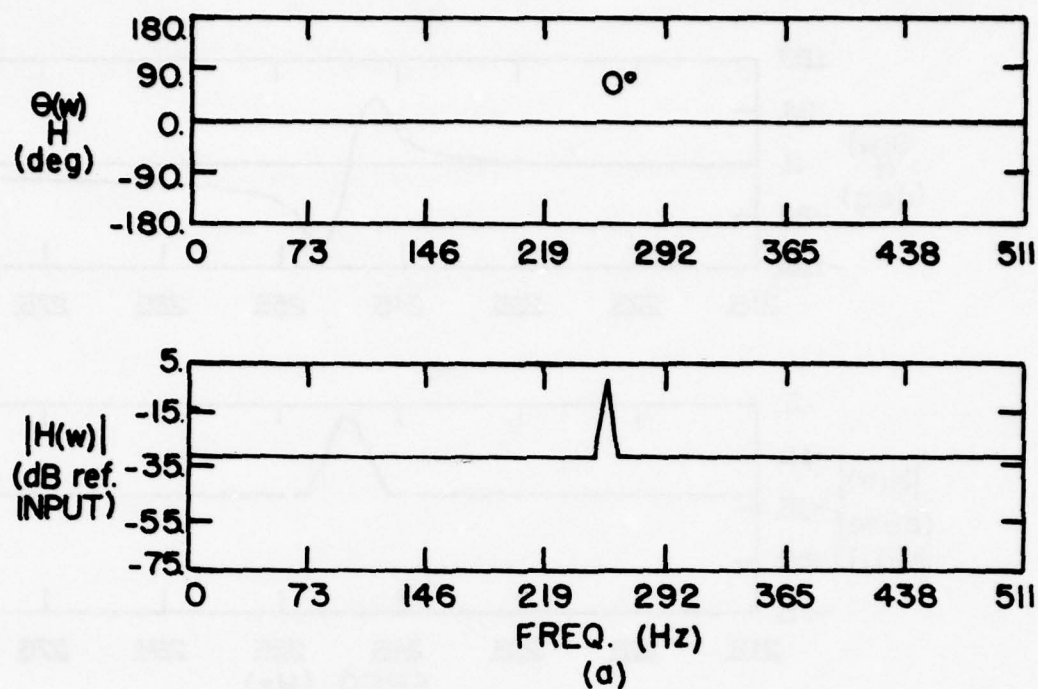
Figure 4.14. (a) Magnitude and phase of desired filter copied from Figure 4.10; (b) Actual magnitude and phase as implemented on programmable FIR filter.
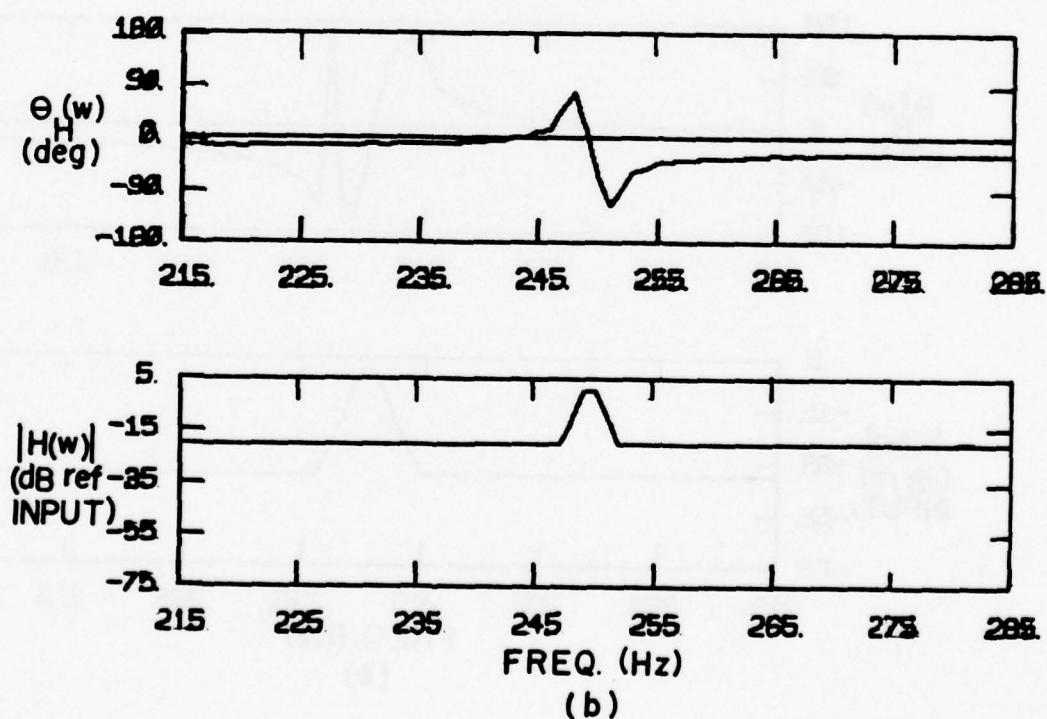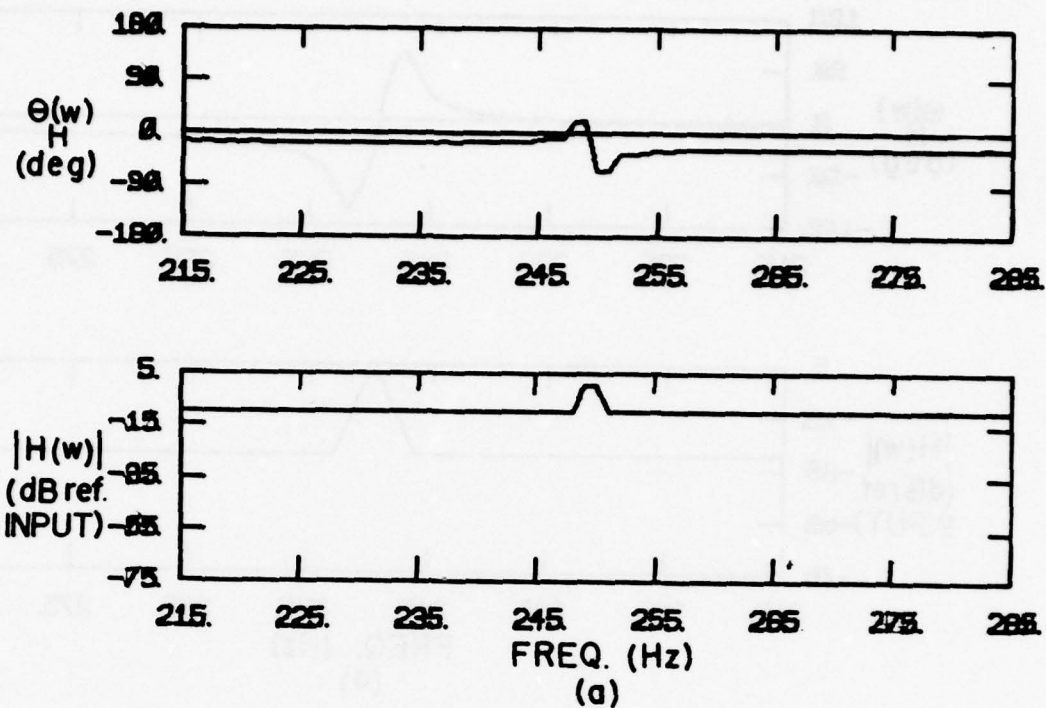
Figure 4.15. Magnitude and phase of two minimum phase FIR filters with increasing peaks with a maximum ±10 dB change between consecutive bins: (a) +10 dB peak and (b) +20 dB peak.
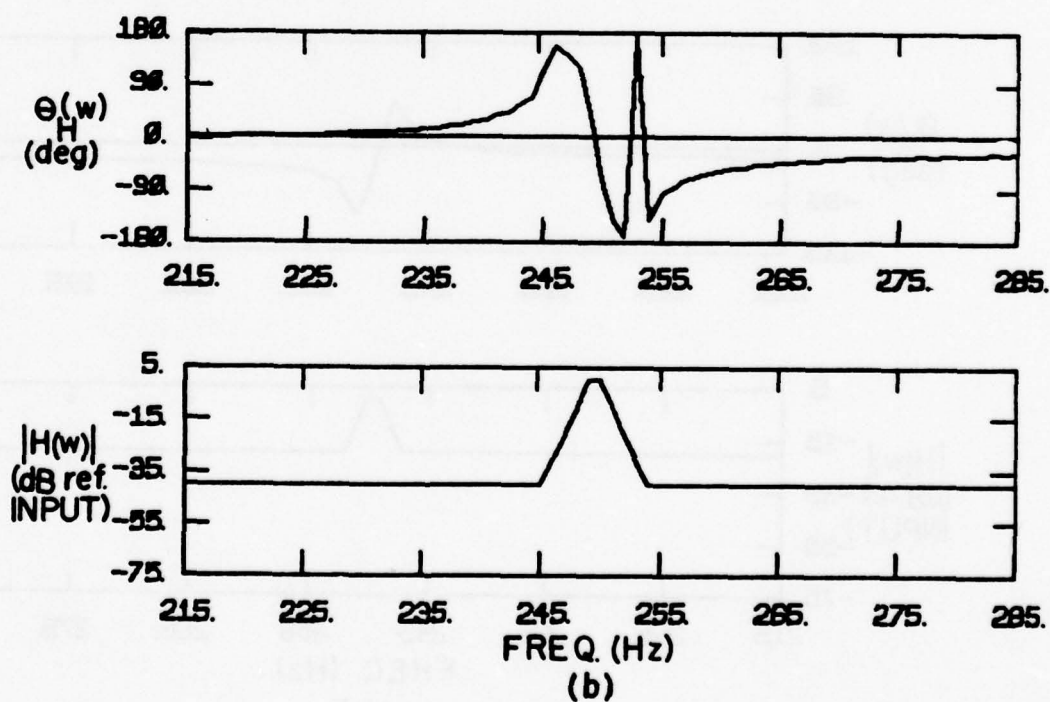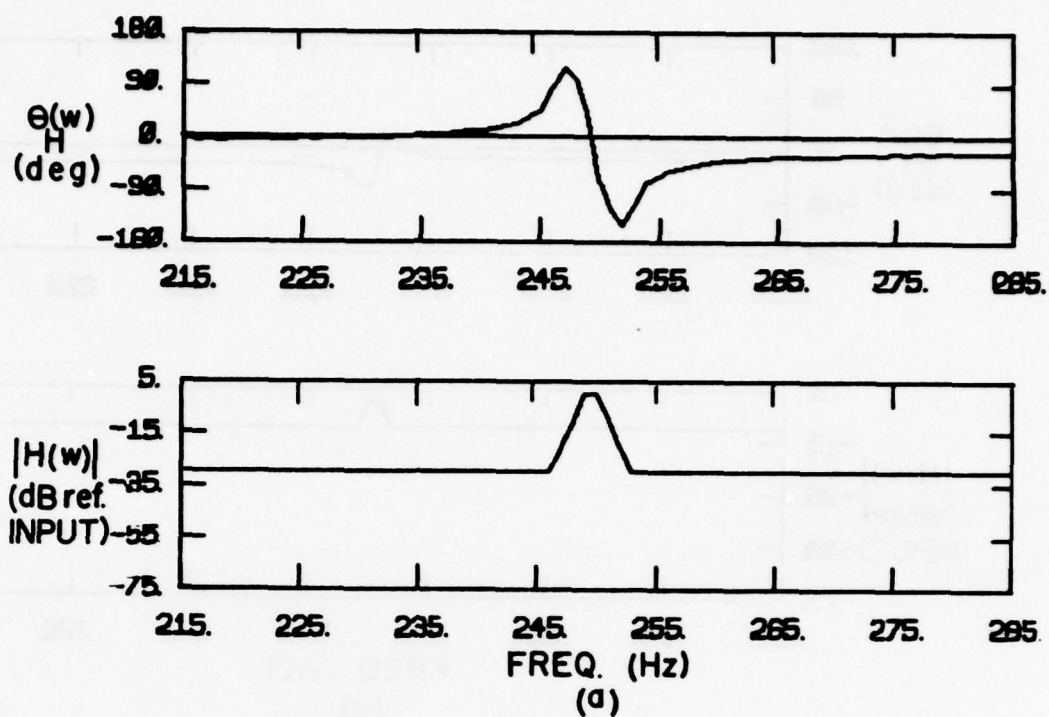
Figure 4.16. Magnitude and phase of two minimum phase FIR filters with increasing peaks with a maximum of +30 dB change between consecutive bins: (a) +30 dB peak and (b) +40 dB peak.

Table 4.2. The positive and negative maximum phase fluctuation and the number of phase bins affected by specifying the peak amplitude and number of amplitude bins in the "amplitude" design of the FIR filter.

Peak Amplitude (dB)	No. of Bins	± Phase (Deg.)	No. of Bins
10	2	$\pm 42^\circ$	5
20	4	$\pm 98^\circ$	11
30	6	$\pm 134^\circ$	23
40	8	$\pm 171^\circ$	35
50	10	$\pm 205^\circ$	45
60	12	$\pm 238^\circ$	57
70	14	$\pm 275^\circ$	80

lists the maximum positive and negative phase change, the affected num-
ber of frequency bins in amplitude and phase for the increase in 10 dB
steps. Note, for example, Figure 4.16b and line 4 in Table 4.2.
Although the amplitude is specified for 8 bins for +40 dB, the affected
number of bins in the phase response is 35. As noted in Appendix A,
this is the result of the minimum phase relationship that maps maxima and
minima in amplitude to inflection points in phase and inflection points
in amplitude to maxima and minima in phase.

In a manner similar to the steps outlined above, other filter
shapes, such as notch, bandpass, etc., can be studied with the amplitude
and phase limited by the factors discussed above (see Appendix A for
additional examples).

4.5 Finite Impulse Response (FIR) Filter - Phase Design

In the previous section the amplitude of a desired FIR filter imple-
mentation is specified for a given number of frequency bins, and the
phase is calculated using the discrete Hilbert transform. In a similar
manner, the phase can be specified and the discrete Hilbert transform
can be used to calculate the corresponding amplitude function.

For the amplitude design, Table 4.2 shows that a given amplitude
peak determines the number of amplitude bins that must be specified to
obtain the desired amplitude response, which in turn determines the num-
ber of bins affected in the phase response. A desirable feature of the
filter design would be the ability to specify amplitude peaks at
frequency locations independent of surrounding peaks. Again, as noted
in Table 4.2 for, say, a 30 dB peak, the number of phase bins that is
affected is quite large.

Figure 4.17 shows the magnitude and phase of a filter where the phase is specified over a finite number of frequency bins in a sawtooth shape. The amplitude response is calculated using the DHT technique as described for phase design in Appendix A. As is the case for the amplitude design, the DHT maps maxima and minima to inflection points and inflection points to maxima and minima.

Thus, the phase design can be used to specify a finite change in phase over a given number of frequency bins. (In order to avoid the Gibbs phenomenon, the maximum change in phase for consecutive bins is approximately 45°.) Table 4.3 specifies the change in phase, the number of frequency bins specified for the phase design, the peak amplitude, and the number of frequency bins in the amplitude that are affected.

4.6 Design of the FIR Filter - Multiple Peak

As noted in Section 4.4, stability of the system can be determined from the magnitude and phase of the open loop response. For the stable system described by Equations (4.5) and (4.6), the closed loop response is to be designed to add energy at the desired feedback "resonance" frequencies located between the resonance frequencies of the enclosure $\left(\text{this is approximately equivalent to setting } CLR(\omega) = \frac{1}{G^2}\right)$. Thus, the closed loop response for a stable system will exhibit a series of peaks with the location of the peaks determined by the resonances of the enclosure as given by Equation (3.1), by the stability criteria, and by the design features of the programmable FIR filter.

Table 4.4 lists the resonance frequencies for the model enclosure up to 400 Hz along with the quantum numbers and the separation in Hz between adjacent resonances. Four hundred Hz is chosen as the upper limit for the frequency range, since the sound power radiated in the
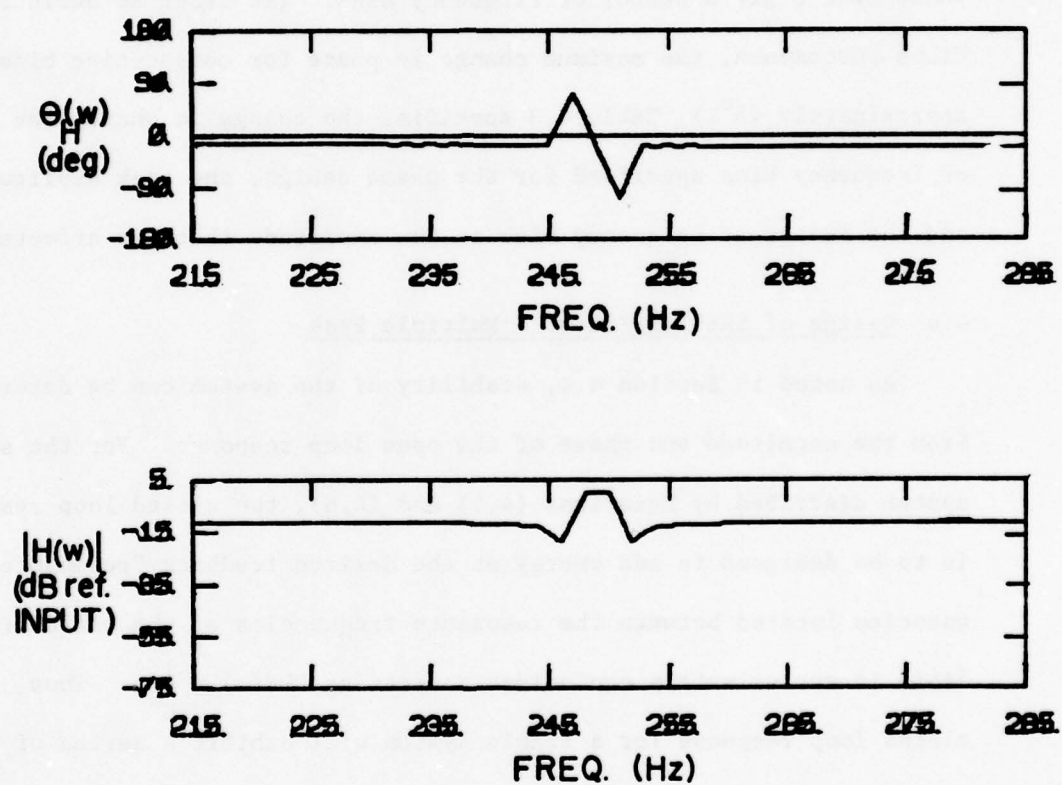
Figure 4.17.   The magnitude and phase of a minimum phase FIR filter based on specifying the desired phase (phase design).

Table 4.3. The positive and negative maximum amplitude fluctuations and the number of amplitude bins affected by specifying the peak phase fluctuations and number of phase bins in the sawtooth shaped phase design of the FIR filter.

± Phase (Deg.)	No. of Bins	Peak Amplitude (dB)	No. of Bins
45°	3	7	10
90°	7	12	16
135°	11	23	23
180°	15	30	30

Table 4.4. The resonance frequencies, quantum numbers, and separation between adjacent modes in Hz from 0 - 300 Hz in the model enclosure using the normal mode model.

Resonance Frequencies (Hz)	Quantum No.	Separation (Hz)
72.2369	(1, 0, 0)	0.0000
91.3349	(0, 0, 1)	19.0980
115.0032	(0, 1, 0)	23.6682
116.4485	(1, 0, 1)	1.4453
135.8084	(1, 1, 0)	19.3599
144.4739	(2, 0, 0)	8.6655
146.8598	(0, 1, 1)	2.3859
163.6642	(1, 1, 1)	16.8044
170.9233	(2, 0, 1)	7.2591
182.6698	(0, 0, 2)	11.7465
184.6575	(2, 1, 0)	1.9877
196.4343	(1, 0, 2)	11.7768
206.0108	(2, 1, 1)	9.5768
215.8564	(0, 1, 2)	9.8456
216.7106	(3, 0, 0)	0.8542
227.6228	(1, 1, 2)	10.9122
230.0062	(0, 2, 0)	2.3833
232.8969	(2, 0, 2)	2.8907
235.1714	(3, 0, 1)	2.2746
241.0831	(1, 2, 0)	5.9117
245.3350	(3, 1, 0)	4.2518

Resonance Frequencies (Hz)	Quantum No.	Separation (Hz)
247.4771	(0, 2, 1)	2.1422
257.8044	(1, 2, 1)	10.3273
259.7434	(2, 1, 2)	1.9390
261.7849	(3, 1, 1)	2.0415
271.6167	(2, 2, 0)	9.8318
274.0046	(0, 0, 3)	2.3879
283.3669	(1, 0, 3)	9.3623
283.4287	(3, 0, 2)	0.0618
286.5618	(2, 2, 1)	3.1331
288.9475	(4, 0, 0)	2.3857
293.7195	(0, 2, 2)	4.7720
297.1606	(0, 1, 3)	3.4412

enclosure above 400 Hz is approximately equal to that radiated in the free field as shown in Figure 3.26.

As described in the previous two sections, for a given amplitude or phase design of the FIR filter, the open loop response for a given feedback microphone and source position is specified. With the stability criterion, the design characters of the FIR filter, and the desired overall pressure as specifications, the closed loop response is to be designed as a series of multiple peaks.

The starting point in either the amplitude or phase design procedure is to specify the desired phase or gain stability margin of the resulting or final open loop response. The gain margin is defined as the minimum difference in dB between the amplitude of the open loop response at the 0° phase crossing (critical frequency) and the maximum amplitude of the filter (always 0 dB due to normalization). The phase margin is the minimum phase difference between the phase at 0 dB amplitude and 0° phase.

As implemented in this study, the gain in the feedback loop can be adjusted for a given filter design. Since the amplitude of the computer designed filter $|H|$ will also be normalized to 0 dB, the phase margin is to be specified. Based on trial and error experimentation, a phase margin of $\pm 20^o$, as illustrated by the dashed lines in Figure 4.18a, has been specified of all designs.

Thus, the design criterion can be stated as follows: for a stable system with 20° phase margin, the FIR filter should consist of the maximum number of independently located peaks with as large a peak height as possible. From the work thus far presented, there is a tradeoff between the number of peaks and the maximum peak height and the number
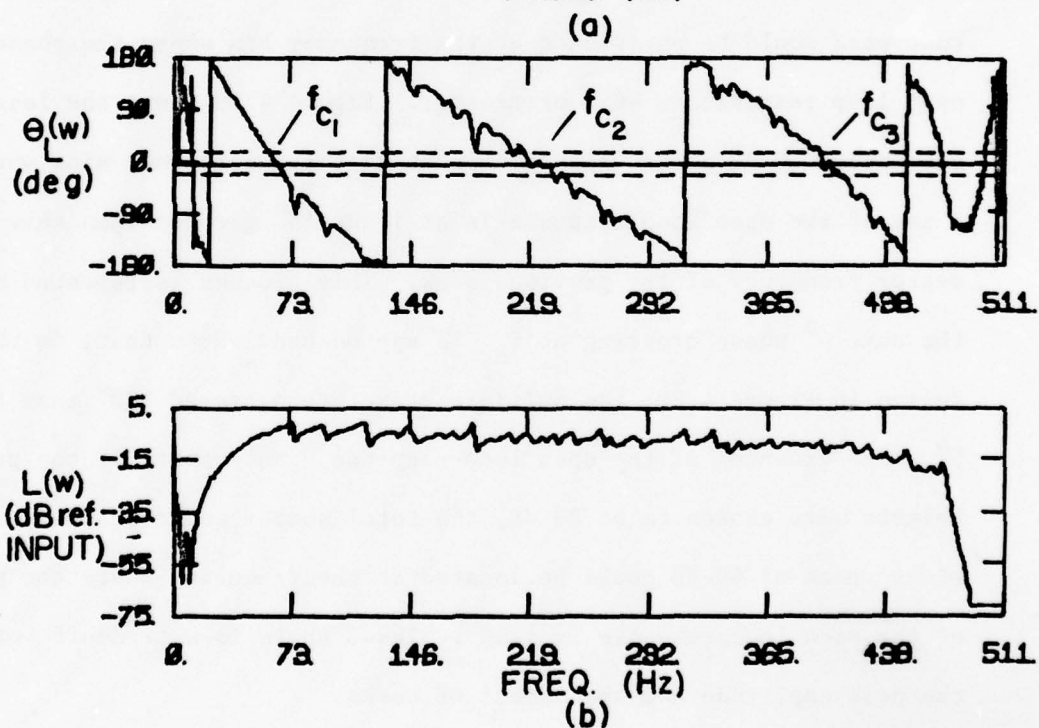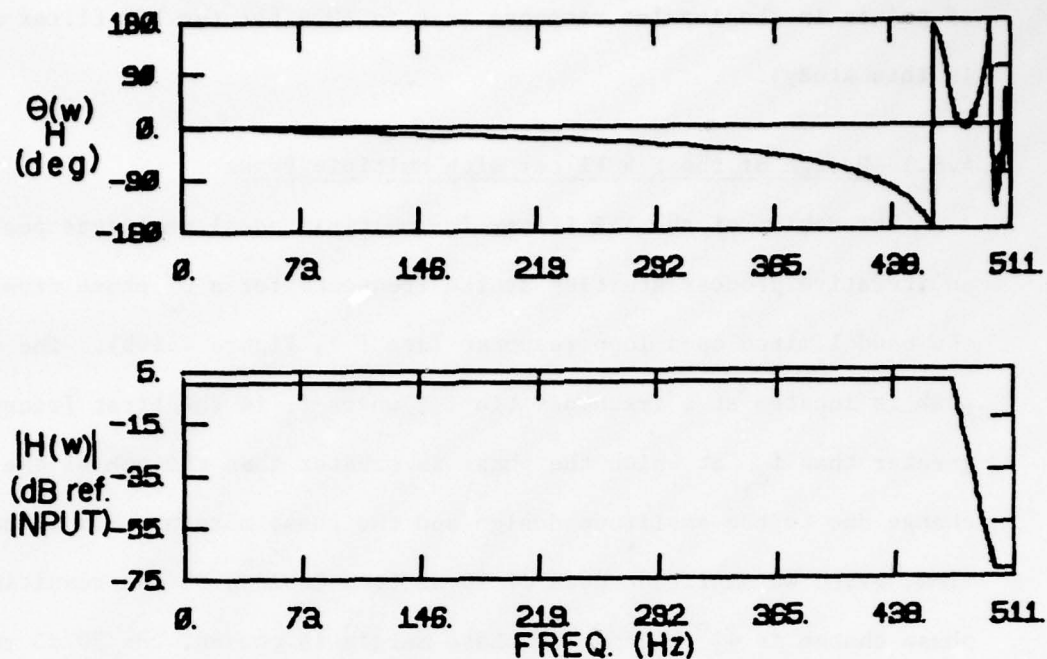
Figure 4.18. Progression of steps for the design of equal amplitude multiple peaks, Step 1 – band limiting and designation of frequency range as determined by the critical frequencies f_{c_1}, f_{c_2}, f_{c_3} and phase margin: (a) computer designed FIR filter $|H|e^{i\theta_H}$ and (b) open loop response $|L|e^{i\theta_L}$.

of points in the impulse response (set to 1024 for the FIR filter used in this study).

4.6.1 Design of the FIR Filter with Multiple Peaks

The design of the FIR filter for multiple equal amplitude peaks is an iterative process starting at the frequency for a 0° phase crossing of the band limited open loop response (see f_{c_1}, Figure 4.19b). The first peak is located at a frequency bin f_1, where f_1 is the first frequency greater than f_{c_1} at which the phase is greater than the sum of the phase change due to the amplitude design and the phase margin. For illustration, given an amplitude peak of 10 dB from Table 4.5, the resulting phase change is 42°. If a 20° phase margin is chosen, the 20 dB amplitude peak would be positioned at the frequency bin where the phase of the open loop response is -65° or greater. Figure 4.19 shows the location of successive 20 dB peaks which are located at the frequency bins where the phase of the open loop response is at least 45° greater than that at the center frequency of the previous peak. This process is repeated until the next 0° phase crossing at f_{c_2} is approached. Note that, in the final design in Figure 4.20, the multiple peaks are centered 180° away from the 0° phase crossing of the open loop response. Note that, if the peak heights were chosen to be 20 dB, the total number would be fewer and a single peak of 40 dB could be located at the frequency where the phase of the open loop response is $\pm 180^o$. Thus, there is a tradeoff between the peak amplitude and the number of peaks.

4.6.2 Design of the FIR Filter with Multiple Peaks and Linear Phase Delay

A general observation can be made for either the amplitude or phase design. If the peak amplitude is placed at the next highest frequency
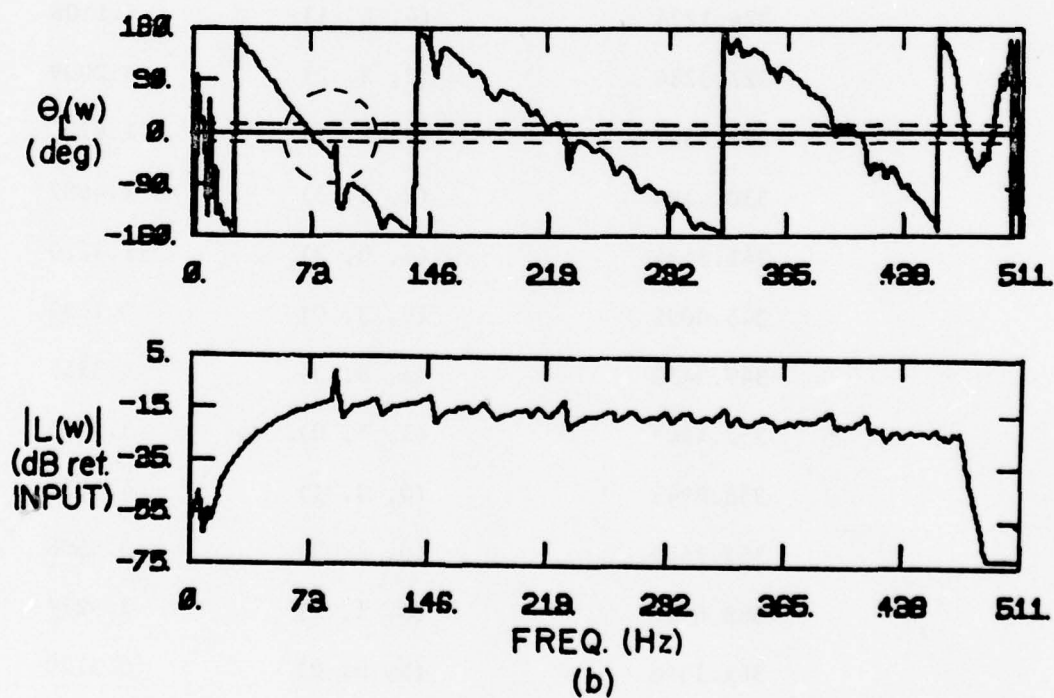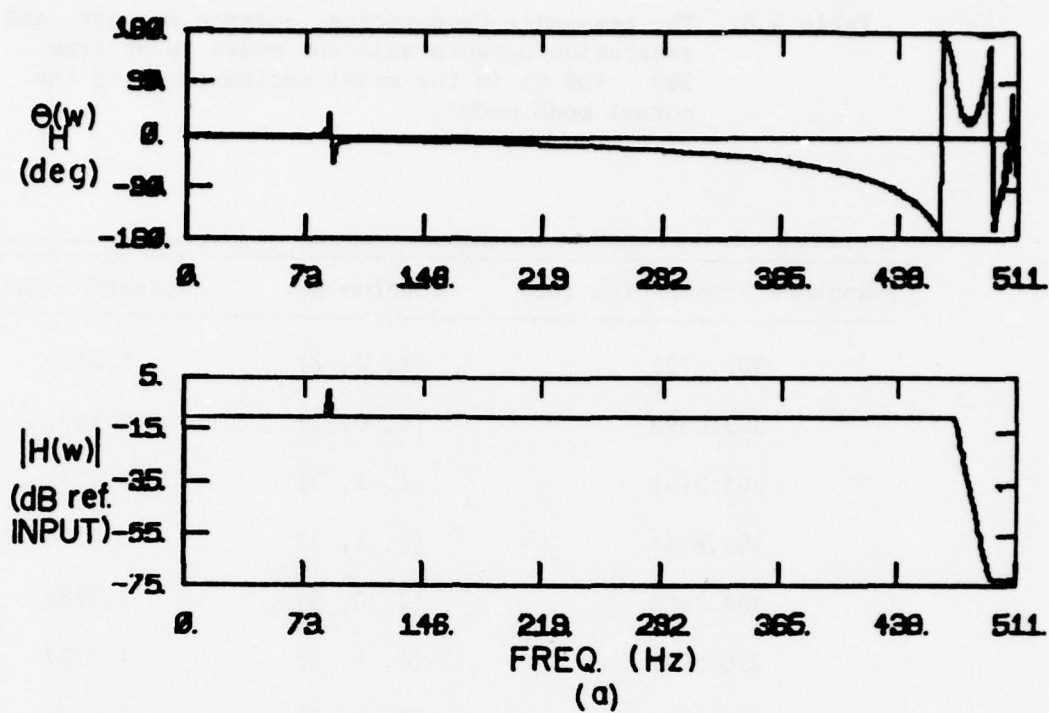
Figure 4.19. Progression of steps for the design of equal amplitude multiple peaks, Step 2 - location of first peak: (a) $|H| \ell^{j\theta_H}$ and (b) $|L| \ell^{i\theta_L}$.

114

Table 4.5. The resonance frequencies, quantum numbers, and separation between adjacent modes in Hz from 300 - 400 Hz in the model enclosure using the normal mode model.

Resonance Frequencies (Hz)	Quantum No.	Separation (Hz)
302.4722	(1, 2, 2)	5.3115
303.0393	(4, 0, 1)	0.5671
305.8145	(1, 1, 3)	2.7751
305.8718	(3, 1, 2)	0.0574
309.7600	(2, 0, 3)	3.8882
310.9927	(4, 1, 0)	1.2327
316.0166	(3, 2, 0)	5.0239
324.1274	(4, 1, 1)	8.1108
327.3284	(2, 2, 2)	3.2009
328.9507	(3, 2, 1)	1.6223
330.4194	(2, 1, 3)	1.4687
341.8464	(4, 0, 2)	11.4270
345.0095	(0, 3, 0)	3.1631
349.3452	(3, 0, 3)	4.3357
352.4907	(1, 3, 0)	3.1455
356.8943	(0, 3, 1)	4.4036
357.7449	(0, 2, 3)	0.8506
368.6726	(4, 1, 2)	2.9277
361.1846	(5, 0, 0)	0.5120
364.1316	(1, 3, 1)	2.9470
364.9653	(1, 2, 3)	8.8337

Resonance Frequencies (Hz)	Quantum No.	Separation (Hz)
365.0132	(3, 2, 2)	0.0479
365.3398	(0, 0, 4)	0.3267
367.7878	(3, 1, 3)	2.4480
369.3152	(4, 2, 0)	1.5273
372.4128	(1, 0, 4)	3.0977
372.5537	(5, 0, 1)	0.1409
374.0378	(2, 3, 0)	1.4841
379.0515	(5, 1, 0)	5.0137
380.4414	(4, 2, 1)	1.3893
383.0129	(0, 1, 4)	2.5715
385.0276	(2, 3, 1)	2.0146
385.8164	(2, 2, 3)	0.7888
389.7654	(1, 1, 4)	3.9490
389.9001	(5, 1, 1)	0.1348
390.3843	(0, 3, 2)	0.4841
392.8687	(2, 0, 4)	2.4844
397.0115	(1, 3, 2)	4.1428
398.2078	(4, 0, 3)	1.1963
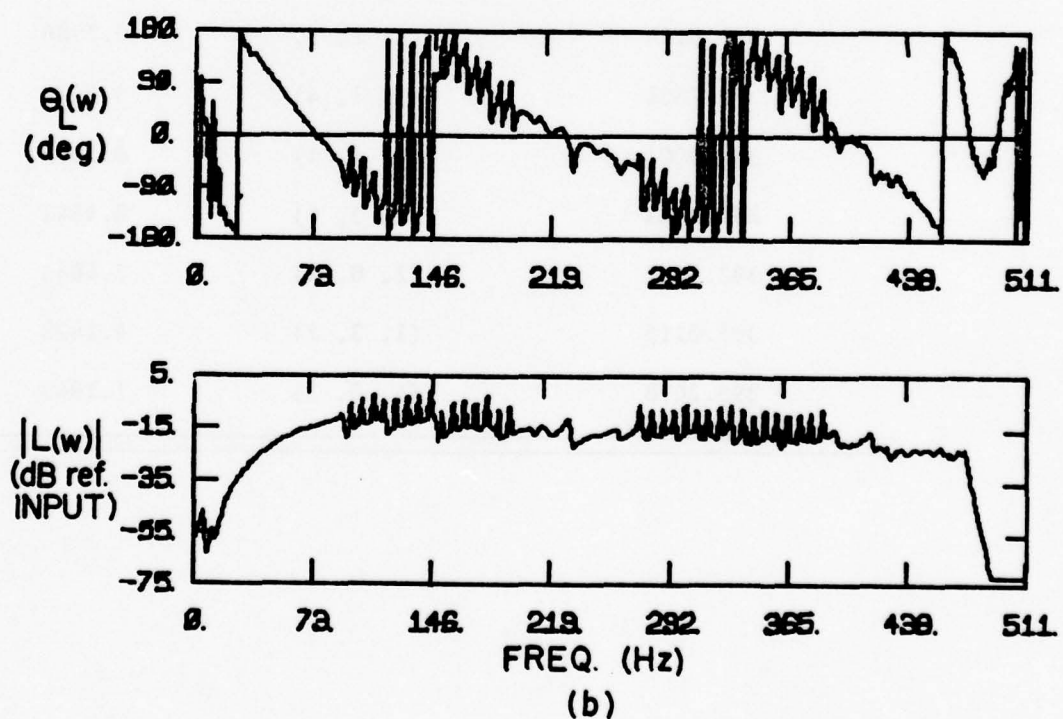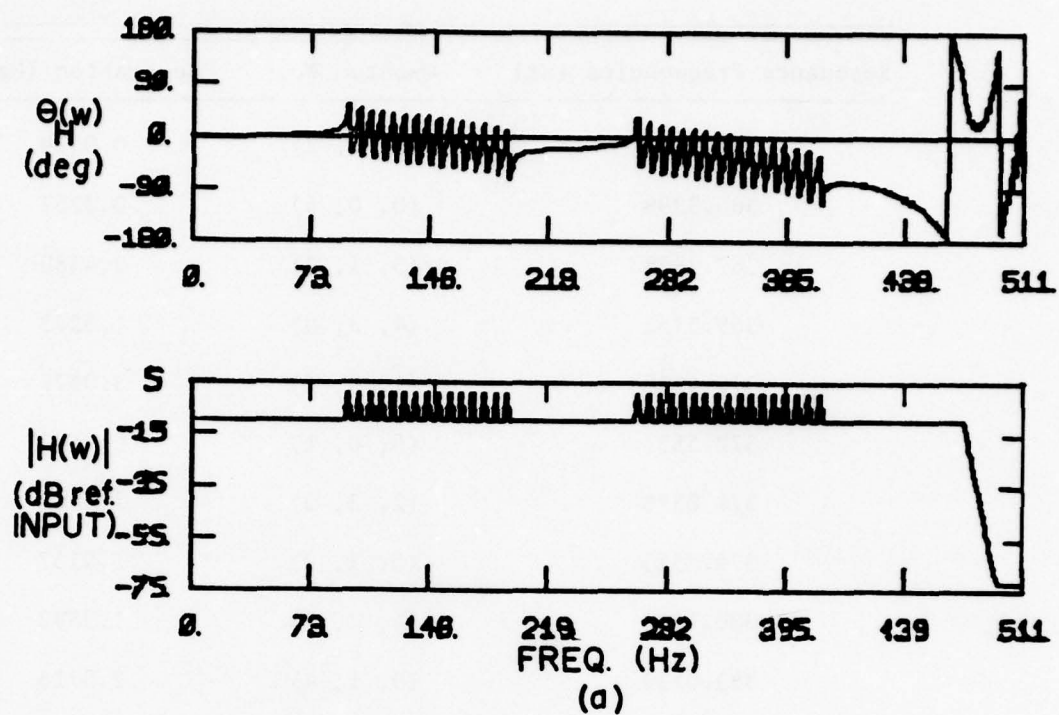
Figure 4.20. Progression of steps for the design of equal amplitude multiple peaks, Step 3 – location of successive peaks: (a) $|H| e^{i\theta_H}$ and (b) $|L| e^{i\theta_L}$.

180° removed from the 0° phase crossing in the open loop response, the fluctuation of the phase due to the change in amplitude is least likely to cross the 0° phase line. As the peak is moved closer in frequency to the 0° phase frequency, the amplitude must be reduced. In order to separate the multiple peaks from one another and to increase the number of frequencies where the phase crosses $\pm 180^\circ$, the linear phase lag is increased by time shifting the impulse response as shown previously in Figure 4.12. The idea is to place a 20 dB peak at each 180° crossing as shown in the expanded frequency range plotted in Figure 4.21. From Table 4.2, the 20 dB peak corresponds to a phase shift of $\pm 97^\circ$ and requires approximately 10 bins per peak. Note that, at the frequencies of the 0° phase crossing, the amplitude is 20 dB down from that at 180°, thus allowing a gain of 20 dB before the stability criteria are violated. Figure 4.22 shows the computer designed FIR filter and the open loop response for the design of multiple peaks centered at the frequency bins of the 180° phase crossings of the open loop response with the FIR filter impulse response delayed 64 bins. Note that, for this design, the peaks are spaced over the frequency range from below the first resonance in the enclosure up to 400 Hz.

Based on the experimental implementation of several dozen filter designs, the filter given in Figure 4.22a has proven to be the optimum compromise between the number of peaks, their location on the frequency axis, and the peak amplitude height.

4.7 Spatial Effect of Feedback

As seen in Section 3.2, the ratio of sound power radiated in the enclosure to that radiated in free space is an indication of the spatial diffusion of the sound field. The sound power radiated in a reverberant
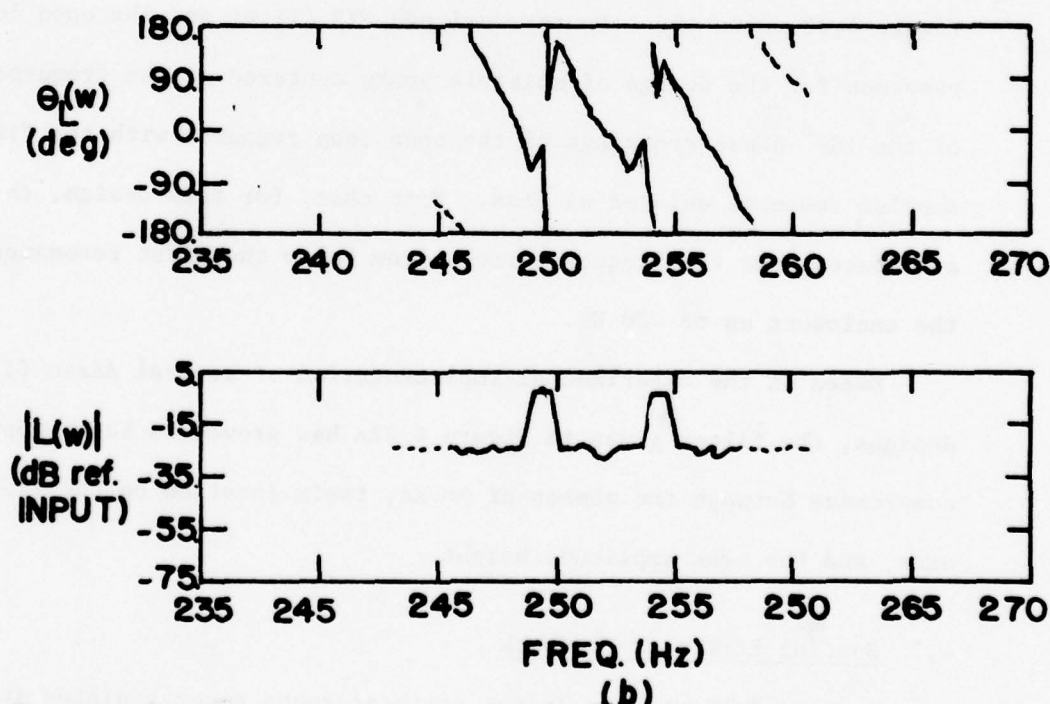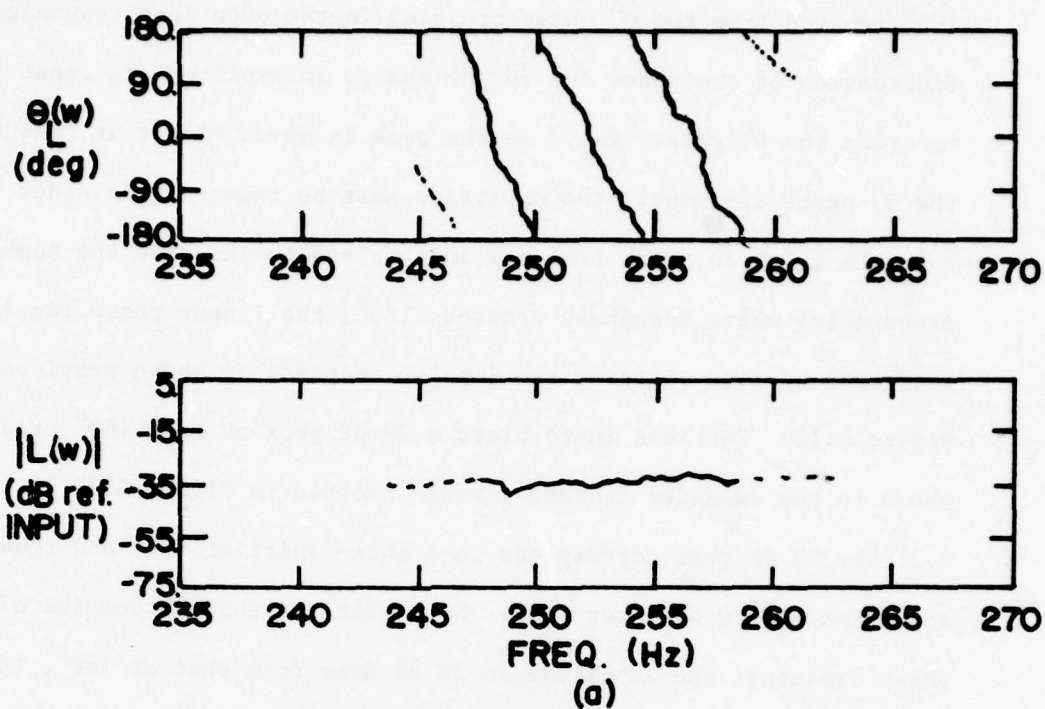
Figure 4.21. The magnitude and phase of the open loop response for an expanded frequency axis to illustrate the location of multiple peaks at 180° phase crossing: (a) for 64 bins delay and (b) for the location of peaks.
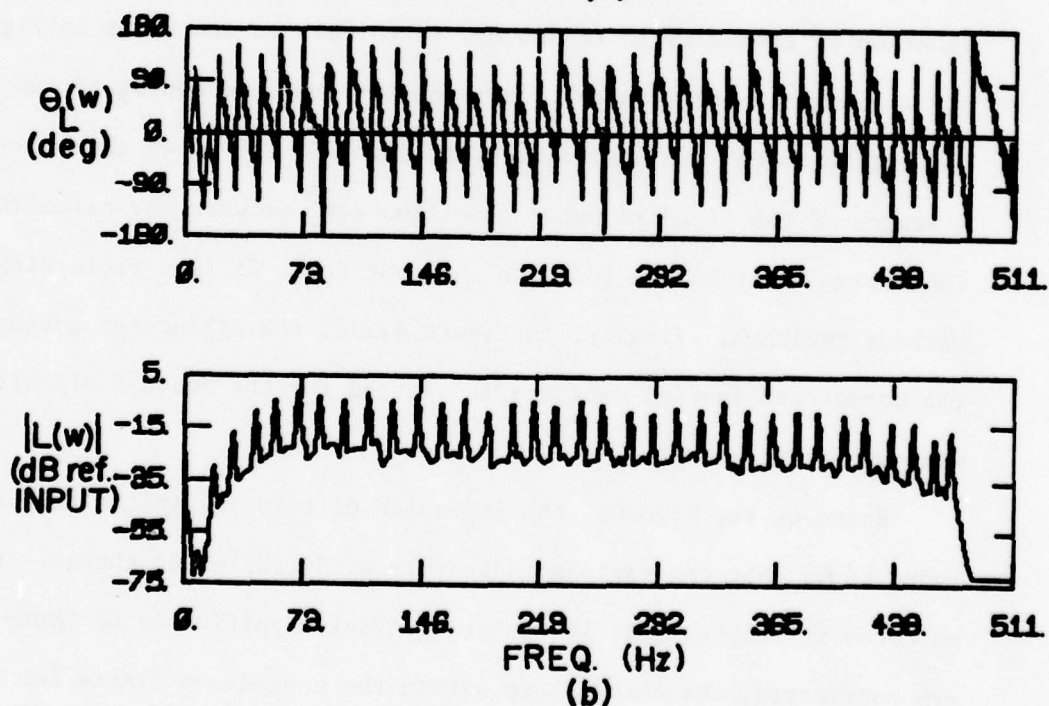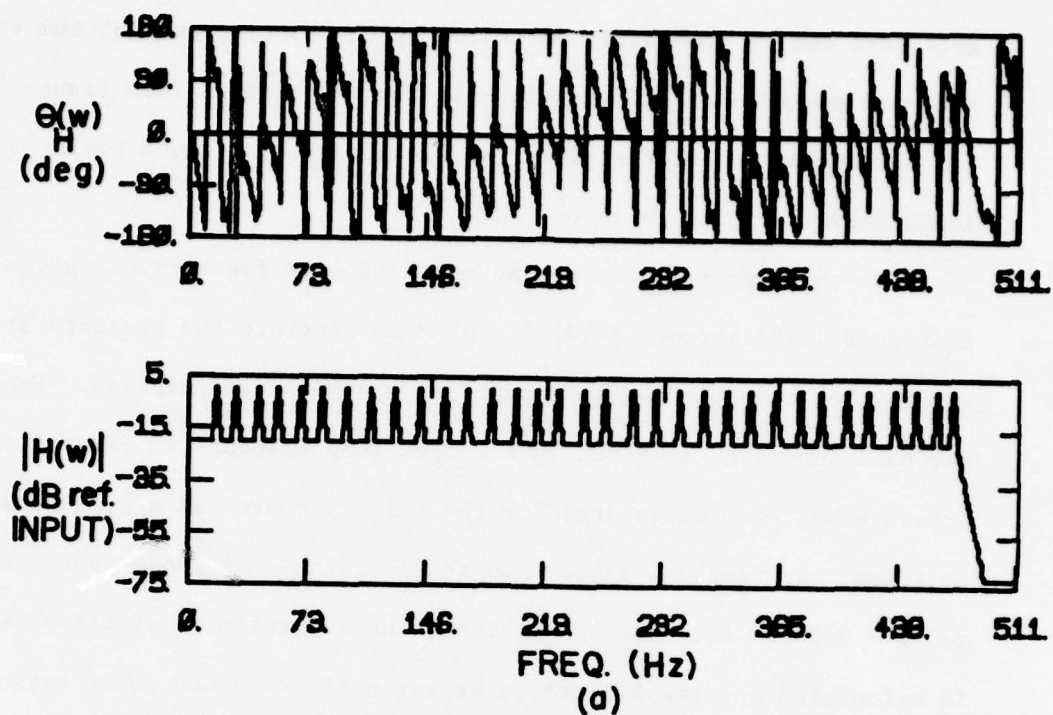
Figure 4.22. (a) Computer designed FIR filter and (b) open loop response for multiple peaks centered at the frequencies of 180° phase crossing of the open loop response with the FIR filter in the all pass mode but for the impulse response delayed 64 bins.

enclosure can be accurately estimated by the spatial mean of the time-averaged pressure at 120 positions in the sound field (see Figure 3.15). For the evaluation of the effect of feedback on the sound field, a similar procedure can be followed.

The computer model of the sound field with feedback, as given in Equations (4.5) through (4.7), is used to generate the pressure at 120 spatial locations in the enclosure for a given configuration. For the feedback function, as given by the open loop response in Figure 4.23, the pressure has been calculated for the primary source in a typical spatial position, the feedback source and the feedback microphone near a corner, and $\beta = 0.005$. For these conditions, the spatial mean of the pressure is calculated and the 1/3-octave averages of the sound power ratio as a function of frequency (0 to 400 Hz) is calculated and shown in Figure 4.23a along with the sound power ratio for the same configuration but without feedback. In a similar vein, Figure 4.23b shows the 1/3-octave averages of the standard error of estimate ε_s^2 between the calculated cumulative distribution function and that for a diffuse field with and without feedback. Finally, in Figure 4.23c, the 1/3-octave average of the normalized spatial variance is plotted for the sound field with and without feedback.

Based on the figures, the inclusion of feedback in the computer model shows that the various indicators of diffusion do change. However, as noted in Chapter III, if the statistical significance of these changes are considered, the changes are within the confidence limits for the calculated quantities. For example, the value of ε_s^2 has the 95% confidence limits for 120 points of +1.25 and -0.8. When viewed in this light, the effects of feedback are not statistically significant.
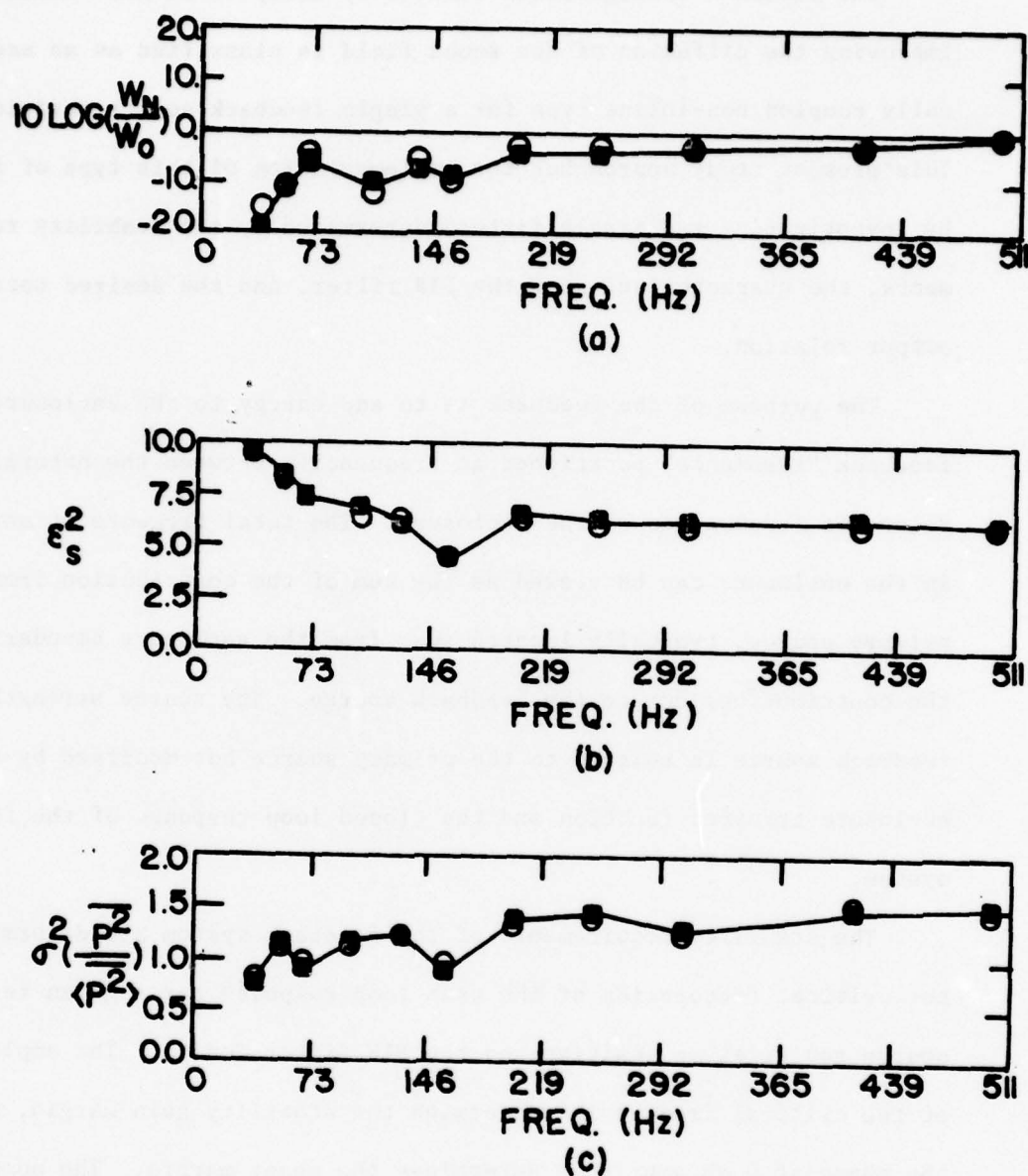
Figure 4.23.   The 1/3-octave average of (a) W/W_0, (b) ε_s^2, and (c) $\sigma^2/\langle p^2 \rangle$ for the sound field with (O) and without (■) the feedback function shown in Figure 4.22a.

4.8 Summary

The feedback configuration derived by Lilly to be most suitable for improving the diffusion of the sound field is classified as an acoustically coupled non-inline type for a single feedback source position. This present study approaches the implementation of this type of feedback by investigating realizable filters determined by the stability requirements, the characteristics of the FIR filter, and the desired total input-output relation.

The purpose of the feedback is to add energy to the enclosure at feedback "resonance" positioned at frequencies between the natural resonance frequencies of the enclosure. The total pressure at any point in the enclosure can be viewed as the sum of the contribution from the primary source, typically located away from the enclosure boundaries, and the contributions due to the feedback source. The source strength of the feedback source is related to the primary source but modified by an enclosure transfer function and the closed loop response of the feedback system.

The stability requirements of the feedback system are determined by the critical frequencies of the open loop response for a given feedback source and receiver position and the FIR filter design. The amplitude at the critical frequencies determine the stability gain margin, while the phase at 0 dB amplitude determines the phase margin. The number of critical frequencies is related to the slope of the phase lag of the open loop response, and the slope is minimized by keeping the feedback microphone in the near field of the feedback source.

The programmable Finite Impulse Response (FIR) filter, the Discrete Hilbert Transform (DHT), and the Fast Fourier Transform (FFT) techniques

allow a great deal of flexibility in the design of the filter implemented as part of the open loop response. The filters considered in this study are minimum phase and consist of a series of multiple peaks whose level and frequency position are determined by the open loop response and the characteristics of the FIR filter. The characteristics include:

(1) the number of points N in the impulse response of the FIR filter (N_t = 1024),

(2) the maximum allowable change in amplitude between consecutive frequency bins (ΔdB = 10),

(3) the sampling rate of the a/d converter (f_S = 1024),

(4) the frequency resolution ($\Delta f = f_S/N_t$ = 1 Hz), and

(5) the dynamic range of the filter given by the number of bits (12 → 72 dB).

The amplitude and phase design procedures for implementing multiple peaks is nontrivial. The stability criteria restrict the band width and the effectiveness of feedback. The computer model of the sound field with feedback based on an experimentally optimized FIR filter design predicts a reduction for certain frequency ranges in the indicators of diffusion for the FIR filters consisting of multiple peaks over the frequency range from 0 to 400 Hz, but, based on the analysis of Chapter III, these changes are not statistically significant.

CHAPTER V

EXPERIMENTAL MODEL REVERBERANT ENCLOSURE

5.1 Introduction

In order to investigate the characteristics of the low frequency
region of reverberant enclosures, an experimental model enclosure
together with a three-dimensional (x, y, z) scanning system to sample the
sound field have been constructed. The amplitude spectrum of pressure or
the magnitude and phase of the various transfer functions are measured
using a dual channel FFT analyzer which, in turn, is interfaced to a
minicomputer via a microprocessor for mass storage of the data on mag-
netic tape.

The time-averaged pressure is measured at various locations in the
sound field for various source and receiver positions, temperature, wall
absorption, or various FIR filter designs.

5.2 Model Chamber Design

Figure 5.1 shows a photograph of the model chamber designed and
built for this study. Due to the constraints on the maximum size of the
chamber based on available space and due to the choice of low cost par-
ticle board as a highly damped building material, the floor-to-ceiling
height was set at 1.895 meters. Following the recommended length-to-
width-to-height ratio of $1:\sqrt{2}:\sqrt[3]{2}$, the enclosure dimensions are L_x =
2.396 m, L_y = 1.505 m, and L_z = 1.895 m with the volume of 6.82 m^3.

The enclosure is set on vibration isolation mounts, and the door
consists of the entire front wall which moves on heavy duty wheels set
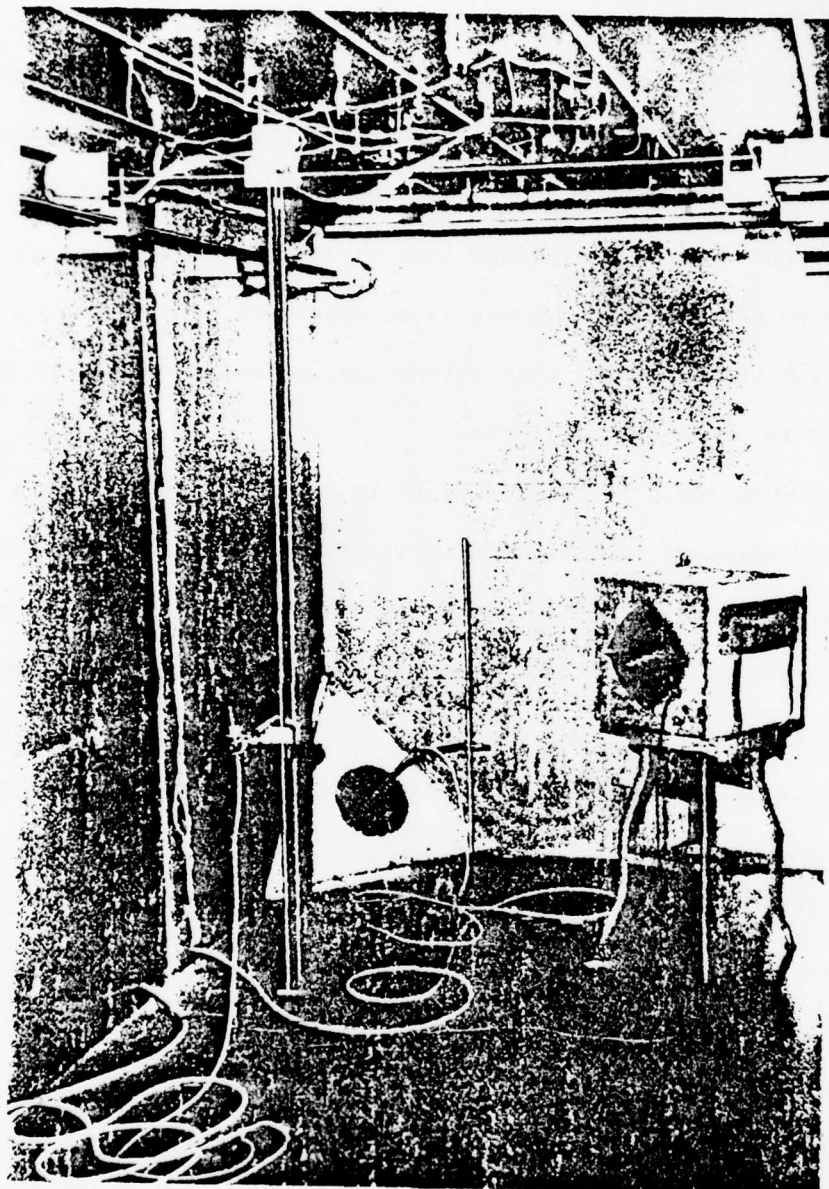
Figure 5.1 The experimental model enclosure (6.82m^3) with feedback source and receiver near a corner, the microphone attached to a three-dimensional scanning system, and the source in the reverberant field.

in a track. The front door is secured by means of 12 throw bolts to ensure a tight fit. Each wall consists of two layers of 1-inch particle board screwed together at several dozen places and reinforced with 2" x 4" wood braces. A 1/4-inch thick piece of particle board forms an outer skin for each wall. In order to increase the mass effect of the wall to decrease sound transmission and to increase the damping of plate-like vibrations, sand has been poured between the outer layer of 1/4-inch board and the 2-inch thick inner layer. The interior of the enclosure has been painted with four coats of polyurethane, and all seams have been sealed with wood cement. With rubber gaskets around the front door, the enclosure is virtually air tight.

The sound field in the enclosure is spatially sampled by a 1/2-inch microphone attached to a three-dimensional scanning system which consists of three individually controlled stepping motors with 0.025 mm accuracy in the length, width, or height directions. The scanning system was built by Paul Kitek as part of his thesis work, and a detailed description of the scanning system will be included in his thesis. Figure 5.2 shows a photograph of the on-site equipment; Figure 5.3 is the block diagram of the instrumentation used in this study; and Table 5.1 lists the equipment, manufacturer, and model number.

An 8-inch loudspeaker in a 1-cubic-foot box is driven by 2.0 volts (rms) broadband noise to excite the sound field. The amplified output of the 1/2-inch microphone is fed into the dual channel FFT analyzer, and the random time signal is averaged 256 times. With the dual channel analyzer, a 1024 point amplitude spectrum of pressure at any point in the enclosure can be measured. In addition, the cross spectrum or transfer function between the output of two microphones can be measured.
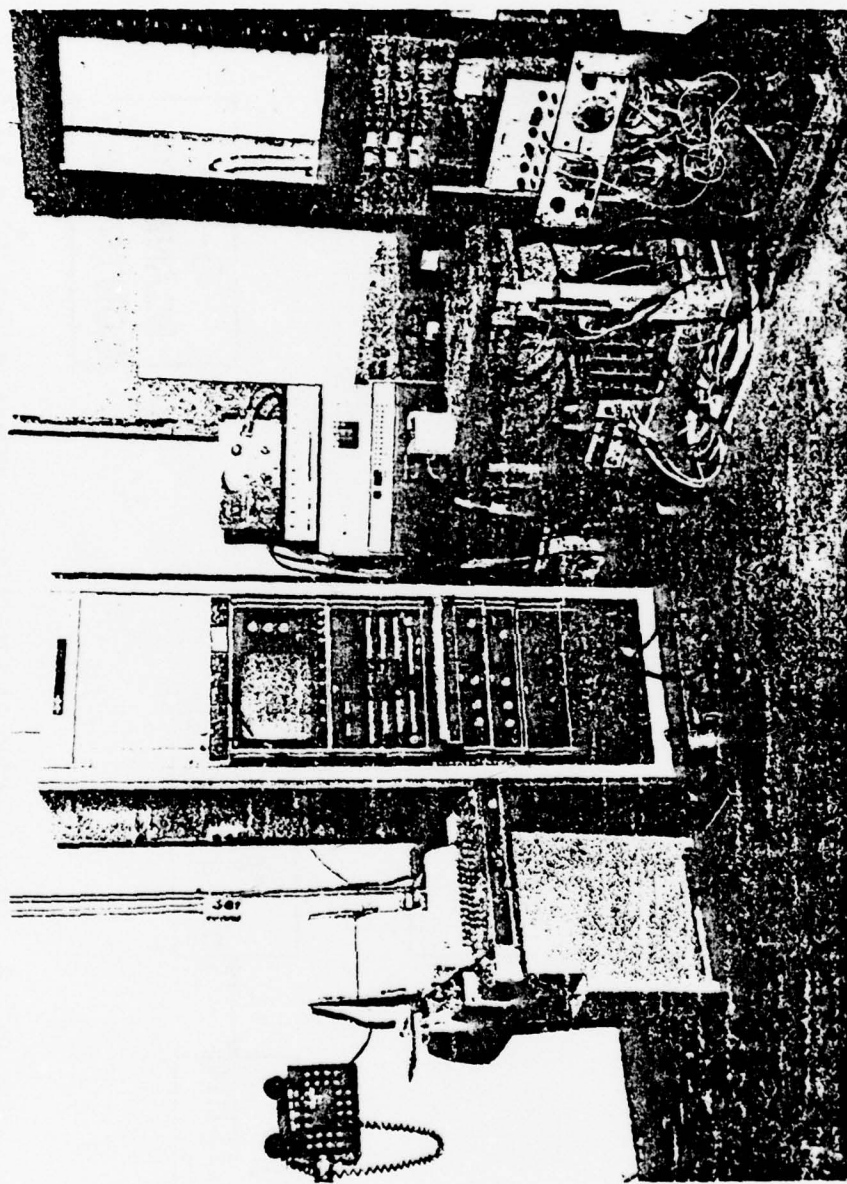
Figure 5.2 On-site instrumentation used to study the characteristics of the sound field and the effects of feedback.
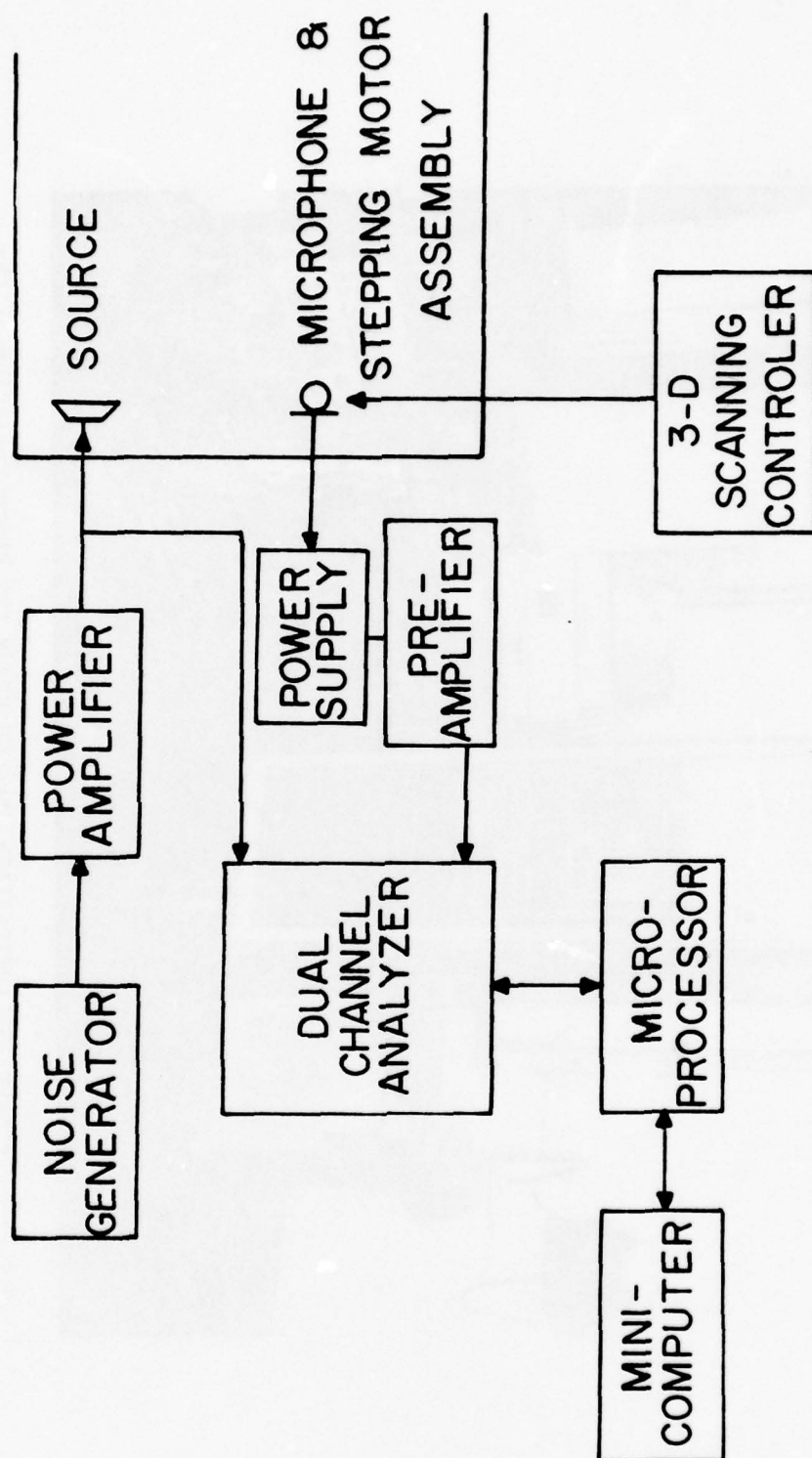
Figure 5.3. Block diagram of experimental apparatus (see Table 5.1 for manufacturer and model numbers).

Table 5.1. List of equipment, manufacturer, and model number used
in the experimental study.

Equipment	Manufacturer	Model #
Noise Generator	General Radio	1390-B
Power Amp #1	McIntosh	250
Power Amp #2	Tigersaurus	210/A
True RMS Voltmeter	Hewlett Packard	3403C
8" Speaker	CTS	8"
Microphone	Bruel & Kjaer	2619
Two-Channel Power Supply	Bruel & Kjaer	2807
Pre Amp	Ithaco	453
Dual Channel Analyzer	Spectral Dynamics	SD360
Microprocessor	Motorola	6800
Minicomputer	Interdata	716

Since the spatial fluctuations of various quantities are of concern, there is a need to store each amplitude and phase versus frequency function associated with each spatial position. The amplitude spectrum for each of the 1024 frequency samples (or the amplitude and phase at 512 frequency samples each) is represented in the internal logic of the SD360 dual channel analyzer by a 16 bit word. Thus, for each of 120 spatial samples, over 1600 bits of information must be stored for frequency-by-frequency analysis of the spatial data. The SD360 analyzer is designed for interfacing to a Digital Equipment Company PDP11-34 computer for front panel settings and data transfer. At the time of this study, the funding for this on-site computer was not available.

In order to store the 120 amplitude spectra, a Motorola 6800 microprocessor is used to set the appropriate protocol to transfer the 16 bit data representation in the SD360 analyzer into four hexidecimal digits and then to transfer these four digits to a remote minicomputer using IEEE RS232 serial format. Using a Fortran IV program running on the Interdata Model 716 minicomputer to read the four hexidecimal digits and to translate to the calibrated data, the 1024 data points are transferred in approximately 2 minutes. At this rate, with the additional time to position the microphone in a desired location, 120 spatial samples of 1024 data points each takes approximately 4 hours to measure.

5.3 Sound Field Without Feedback

The experimental investigation of the characteristics of the sound field within the reverberant enclosure follows the theoretical development presented in Chapters III and IV. This section of Chapter V will deal with the characteristics of the experimental sources; the differences between theoretical and experimental enclosure transfer

functions; the effects of changes in temperature on these transfer functions; and, in particular, the manner in which the spatial characteristics of the sound field vary with source position and additional absorption. As described in Chapter III, the quantities of interest will be the frequency fluctuation of the standard error of estimate of the variation of the measured CDF from the exponential CDF; the variation with frequency of the normalized spatial variance of pressure squared; and, for a limited number of frequencies, standard error of estimate for the difference between the measured averaged cross correlation coefficient and sin(kr)/kr behavior.

5.3.1 Enclosure Transfer Functions: Experimental Versus Theory

As seen in Section 3.1, the theoretical pressure at a point in the enclosure for a point source is a function of the source strength Q_o, the real part of the wall admittance β, the size and geometry of the enclosure, and the speed of sound in air. Figure 5.4 shows the experimental pressure response in the model enclosure for an 8-inch source in one corner and the microphone in the diagonally opposite corner. Also plotted is the theoretical curve based on Equation (3.1) where the eigen frequencies are calculated for a perfectly rectangular enclosure with the speed of sound determined for $T = 24.5^{\circ}C$, with the dimensions specified as those of the experimental enclosure, with the point source located at the center of the experimental speaker cone (0.18 m, 0.18 m, 0.18 m), and with the receiver located at (L_x, L_y, L_z). The source strength Q_o is given by

$$Q_o(\omega) = \pi a^2 v(\omega)\rho \quad , \qquad\qquad (5.1)$$
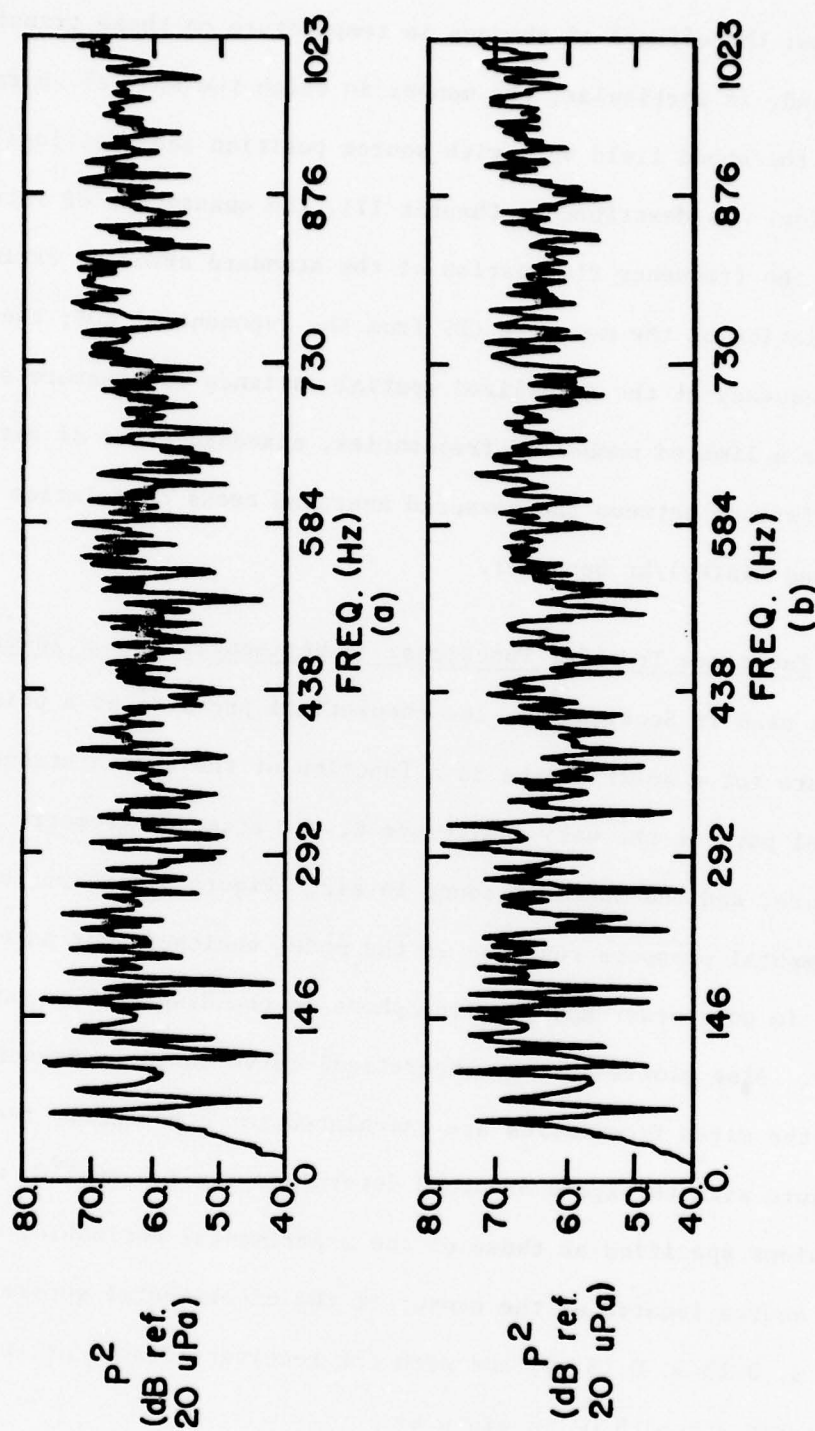
Figure 5.4. (a) Experimental and (b) theoretical amplitude versus frequency response for the source near a corner (0.18 m, 0.18 m, 0.18 m) and the receiver in another corner (2.396 m, 1.505 m, 1.895 m) of the experimental enclosure (6.82 m^3) with theoretical pressure based on Equation (3.1) with β = 0.005.

where a is the radius of the speaker, ρ is the density of air, and $v(\omega)$ is the velocity response of the speaker measured by attaching an Endevco Picomin accelerator to the center of the speaker cone. By measuring the 3 dB down points on several well separated modes, the value of β is calculated to be approximately 0.005 and is assumed to be constant over the frequency range chosen.

Note that in Figure 5.4 the two curves only agree for the first few modes. Despite the differences, the statistical behavior of the experimental data averaged over 1/3-octave bands follows the theoretical data as seen in Figure 5.5. As seen in the next section, the statistical behavior of the experimental data follows the theoretical data for spatially averaged data as well.

In order to measure the effects of absorption on the spatial and frequency fluctuations of pressure, sheets of open cell foam were attached via Velcroe to each of the chamber walls, floor, and ceiling. Details on the characteristics of the open cell foam and other absorption material will be found in Mr. Kitek's yet-to-be-published thesis. The average reverberation times T_{60} for the enclosure with absorption on no walls to six walls have been measured in 1/3-octave bands using standard techniques, and the results are listed in Table 5.2. Note that the addition of absorption on more than three walls, one in each of the length, width, and height directions, has little effect on the reverberation time. The theoretical and experimental pressure responses for the addition of absorption on successive walls follow the same trend as noted for Figures 5.4 and 5.5; that is, for the proper values of β, the frequency response agrees in general shape only at very low

Figure 5.5. The 1/3-octave average of the experimental (O) and theoretical (X) pressure amplitude as plotted in Figure 5.4.

Table 5.2. The reverberation times T_{60} measured in 1/3 octaves from 100 - 1000 Hz for the experimental enclosure with additional absorption on no walls to six walls.

Number of Walls Covered \ Center Frequency (Hz)	100	125	150	200	315	400	500	630	800	1000
0	2.37	2.59	1.76	1.55	0.84	0.92	0.72	0.85	0.80	0.81
1	1.34	1.43	0.63	0.56	0.44	0.49	0.43	0.39	0.42	0.47
2	1.01	0.96	0.43	0.31	0.30	0.30	0.33	0.31	0.38	0.30
3	0.78	0.63	0.38	0.27	0.30	0.28	0.27	0.27	0.27	0.27
4	0.62	0.45	0.33	0.24	0.28	0.25	0.26	0.24	0.22	0.24
5	0.62	0.35	0.32	0.20	0.26	0.20	0.21	0.19	0.17	0.20
6	0.62	0.34	0.30	0.19	0.20	0.17	0.17	0.16	0.14	0.15

frequency, but, for 1/3-octave averages, the theory and experimental results are in good agreement. Figures 5.6 and 5.7 illustrate this point. For these plots the experimental enclosure has absorption on three non-parallel walls and no additional absorption on the remaining three. The pressure amplitude versus frequency response for the measured data is not in good agreement with the theoretically predicted response for the appropriate choice of source and receive positions, β and room geometry. However, as noted in Figure 5.7, the 1/3-octave-band averages do agree fairly well, even for large values of β. As more absorption is added, it has been observed that the experimentally measured resonances shift as the boundary conditions become more reactive.

Thus, although the theoretical development for the normal mode model assumes that the admittance at the wall is small, real, and uniformly distributed over the surface of the enclosure, with the proper choice of β the 1/3-octave-band averages of the theoretical and experimental frequency response are in good agreement. It is believed that, with additional study, the average frequency fluctuation of β for a given material can be determined in situ by an iterative comparison of 1/3-octave average of experimentally measured amplitude responses in this enclosure with the 1/3-octave average of theoretical amplitude response for various values of β.

5.3.2 Pressure Distribution, Normalized Variance, and ε_s^2

Based on the results of the theoretical development as presented in Chapter III, the pressure amplitude spectra at each of 120 spatial positions in a rectangular grid of points with 0.152 m separation have
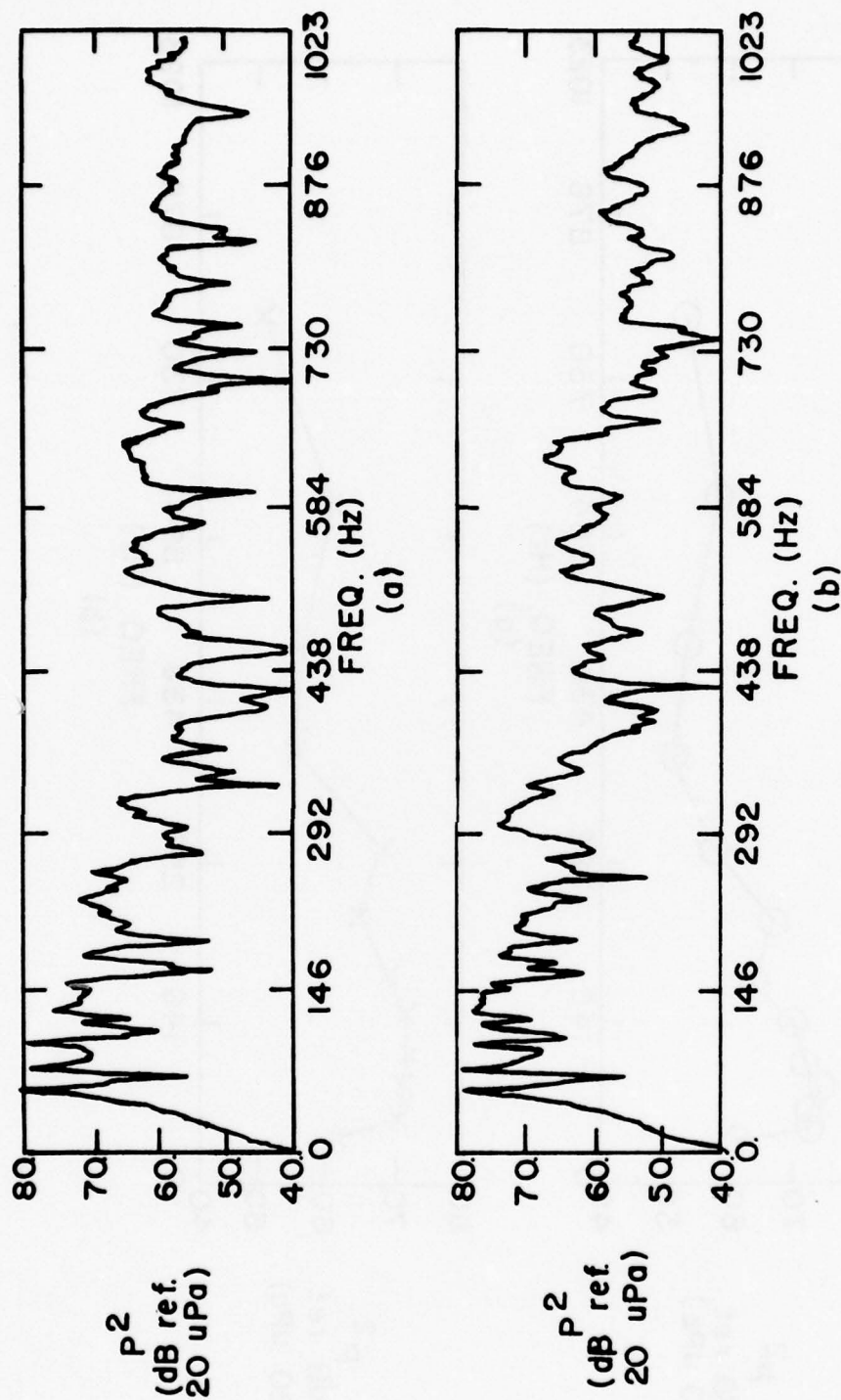
Figure 5.6. (a) The experimental and (b) theoretical pressure amplitude for the same condition as in Figure 5.4 but with absorption on the nonparallel walls and $\beta = 0.059$.

138
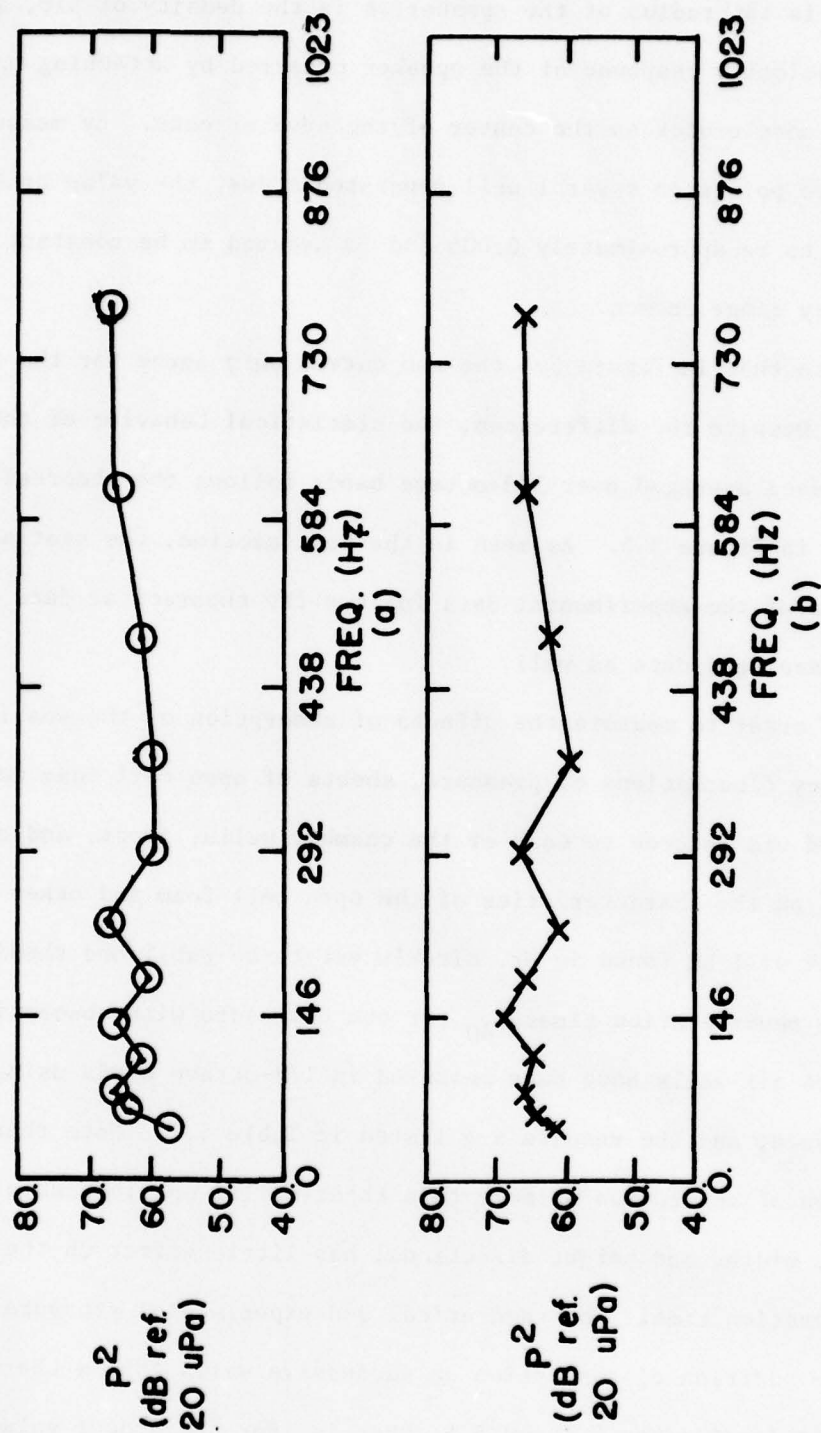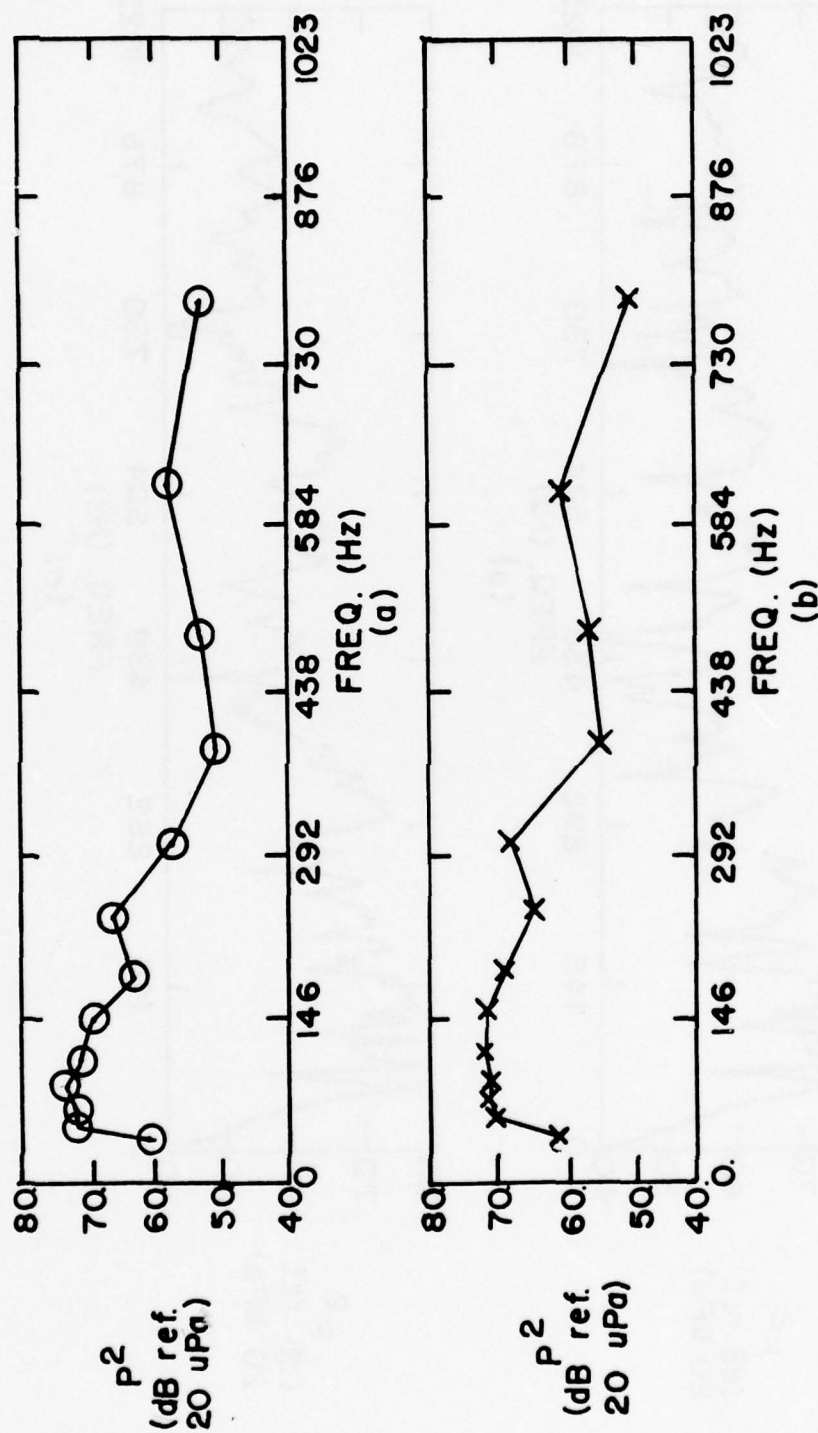

Figure 5.7. The 1/3-octave average of the experimental (O) and theoretical (X) pressure amplitude as plotted in Figure 5.6.

been measured for various source positions and wall absorptions in the experimental enclosure.

Nine experimental configurations have been considered and include the source in a corner of the enclosure with no additional absorption on the walls and with additional absorption on six walls and the source in a typical spatial position with no additional absorption and with additional absorption on one through six walls. For each configuration, the cumulative distribution functions, the normalized spatial variance, and the standard error of estimate for the variation of the CDF from the exponential CDF have been calculated from the experimental data on a frequency-by-frequency basis from 0 to 1000 Hz with 1 Hz resolution.

As an example, Figures 5.8 to 5.17 show the frequency-by-frequency variation in the CDF and PDF calculated from experimental data at 120 spatial positions for the source in a typical spatial position and no additional absorption on the enclosure walls. In comparison with Figures 3.11 to 3.20, the experimental CDF follow the trend predicted by the normal mode model. At low frequencies the CDF's exhibit variations from experimental CDF, and, as frequency is increased, fewer variations from the experimental CDF are noticed. As described in Section 3.4, the fluctuation of the experimental CDF about the exponential CDF can be quantified by ϵ_s^2 $\left(\text{Equation (3.13)}\right)$. Figure 5.18 shows the value of ϵ_s^2 and the 1/3-octave average for this experimental configuration.

The experimentally measured normalized spatial variance and 1/3-octave average of the normalized spatial variance are also shown in Figure 5.19.

In order to investigate the effects of absorption on the fluctuation of ϵ_s^2 and $\sigma^2/\overline{\langle p^2 \rangle}$, these quantities have been calculated for six
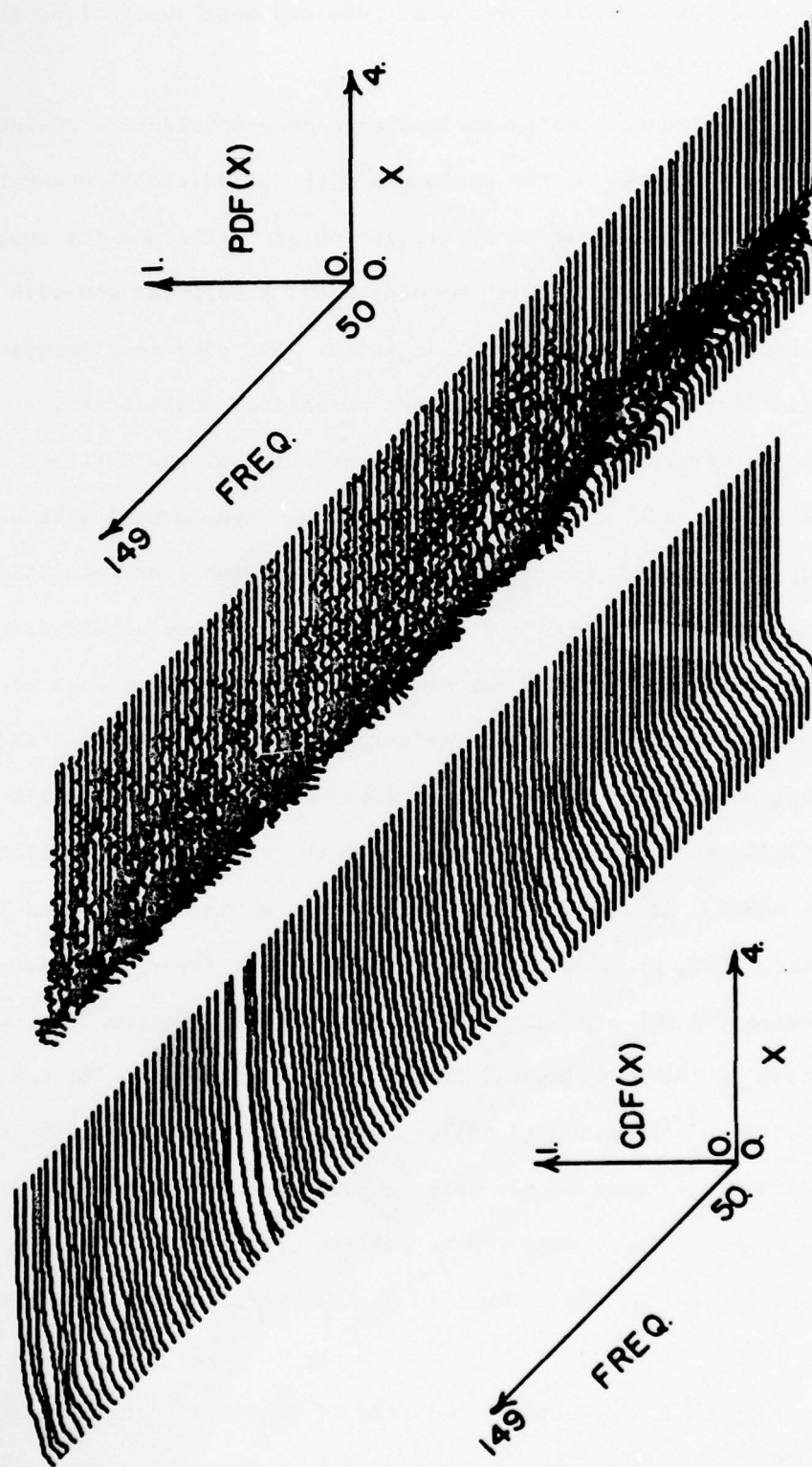
Figure 5.8. Cumulative Distribution Function (CDF) and Probability Density Function (PDF) calculated from experimentally measured squared pressure at 120 spatial positions in the model enclosure (6.82 m³) with the source centered in a typical spatial position (1.596 m, 1.005 m, 0.785 m) and no absorption on the walls for the frequency range from 50 – 149 Hz.
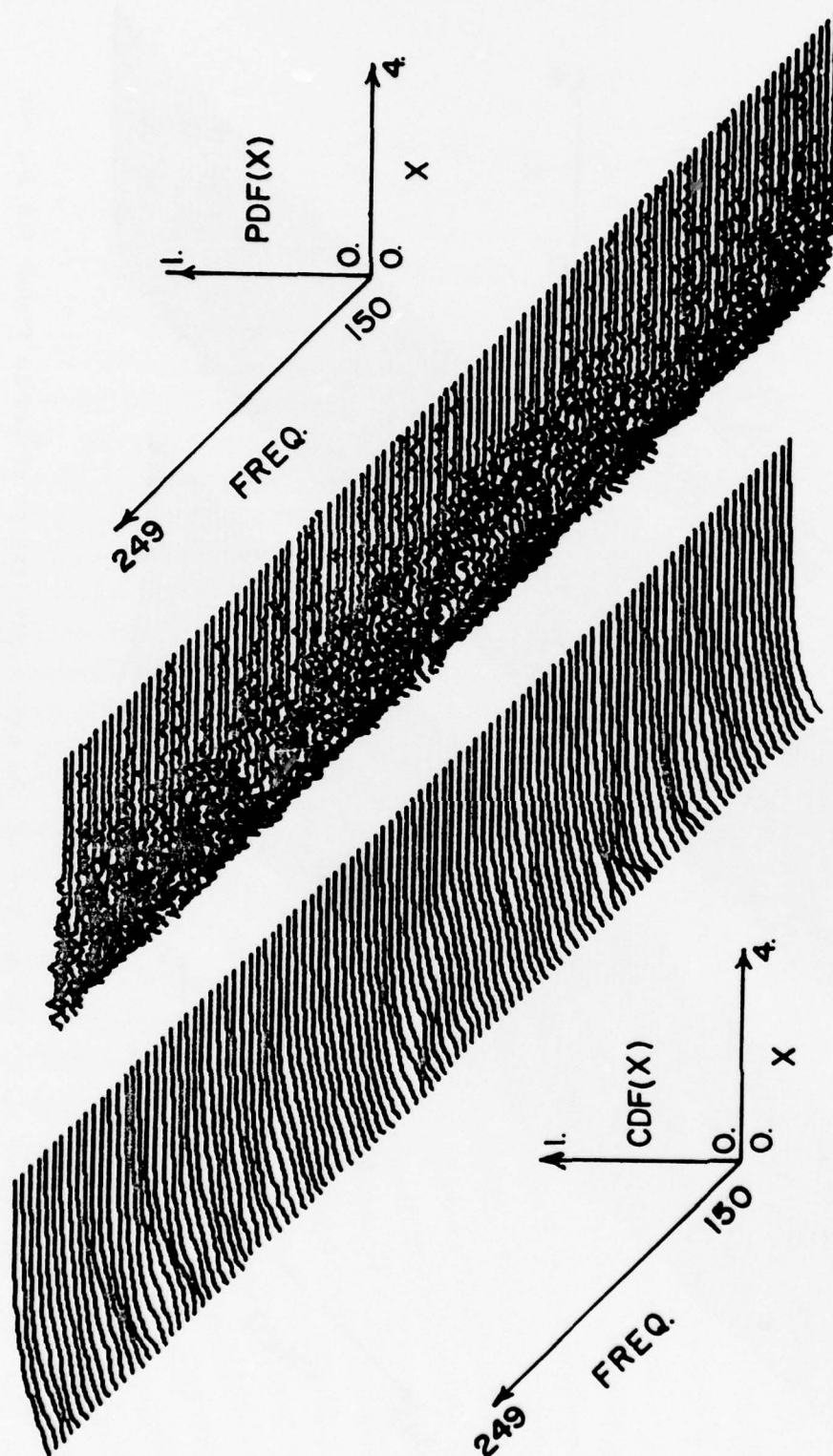
Figure 5.9. CDF and PDF for the same conditions as stated in Figure 5.8 for the frequency range from 150 - 249 Hz.
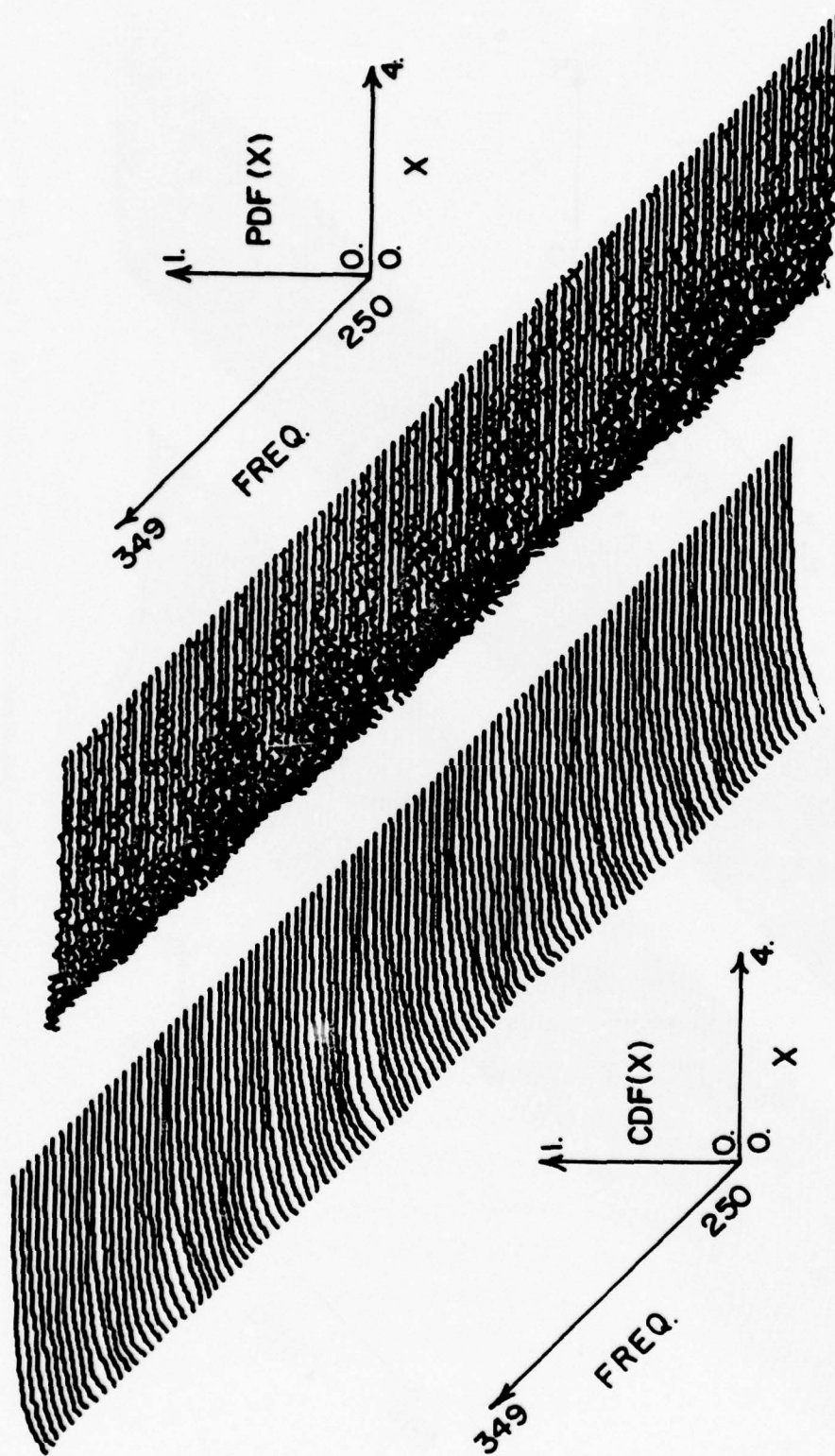
Figure 5.10. CDF and PDF for the same conditions as stated in Figure 5.8 for the frequency range from 250 – 349 Hz.
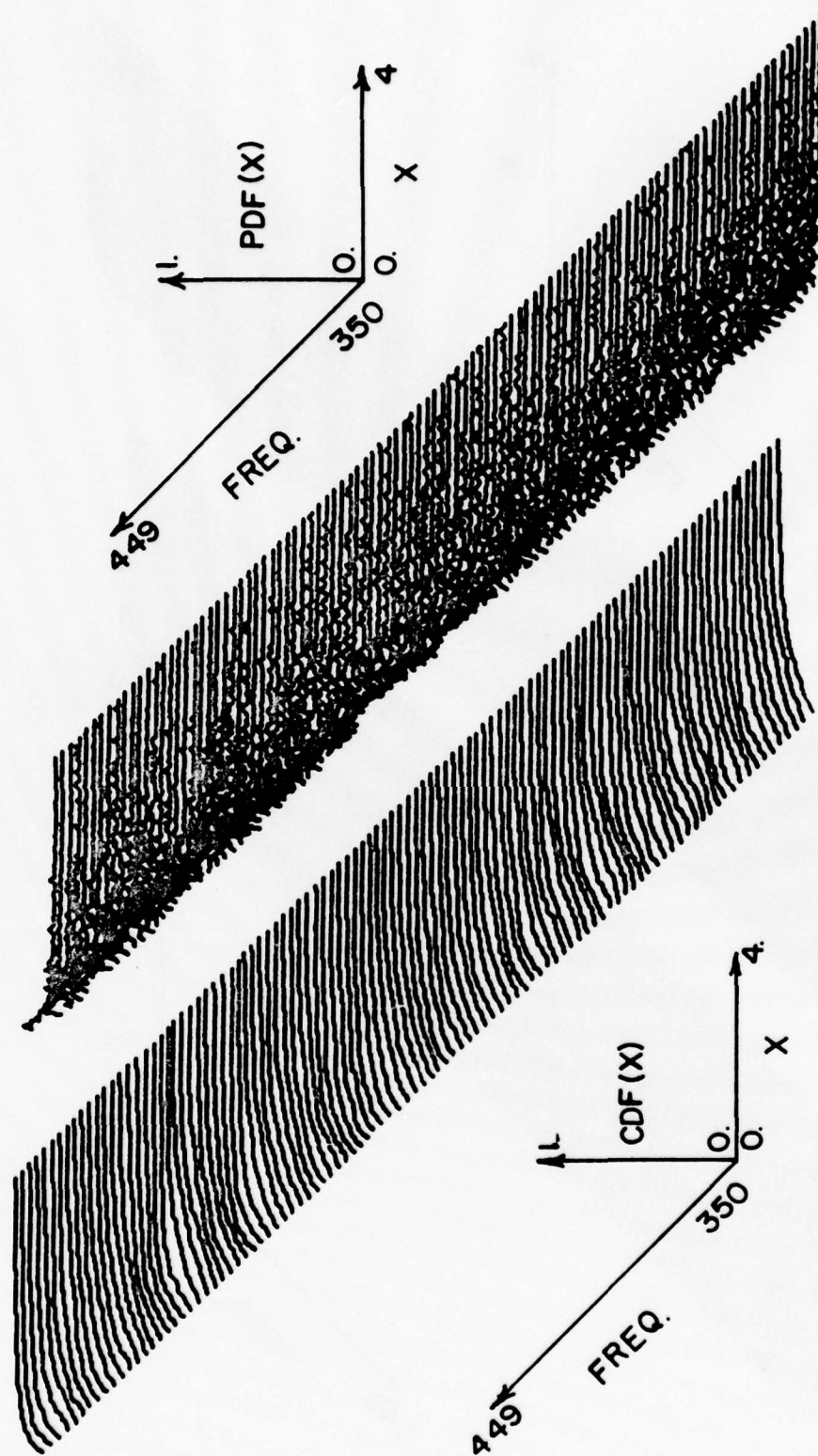
Figure 5.11. CDF and PDF for the same conditions as stated in Figure 5.8 for the frequency range from 350 – 449 Hz.
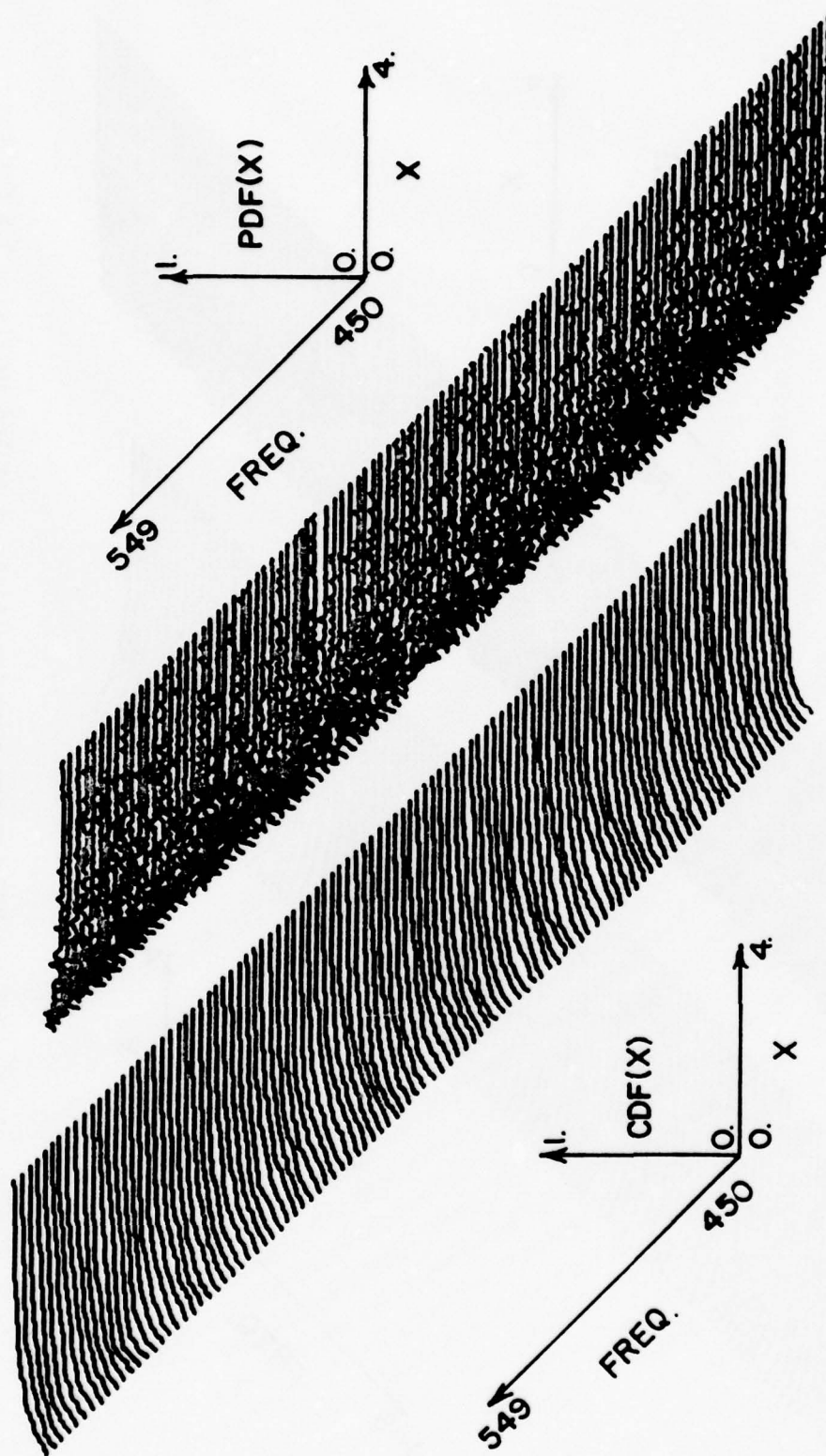
Figure 5.12. CDF and PDF for the same conditions as stated in Figure 5.8 for the frequency range from 450 – 549 Hz.
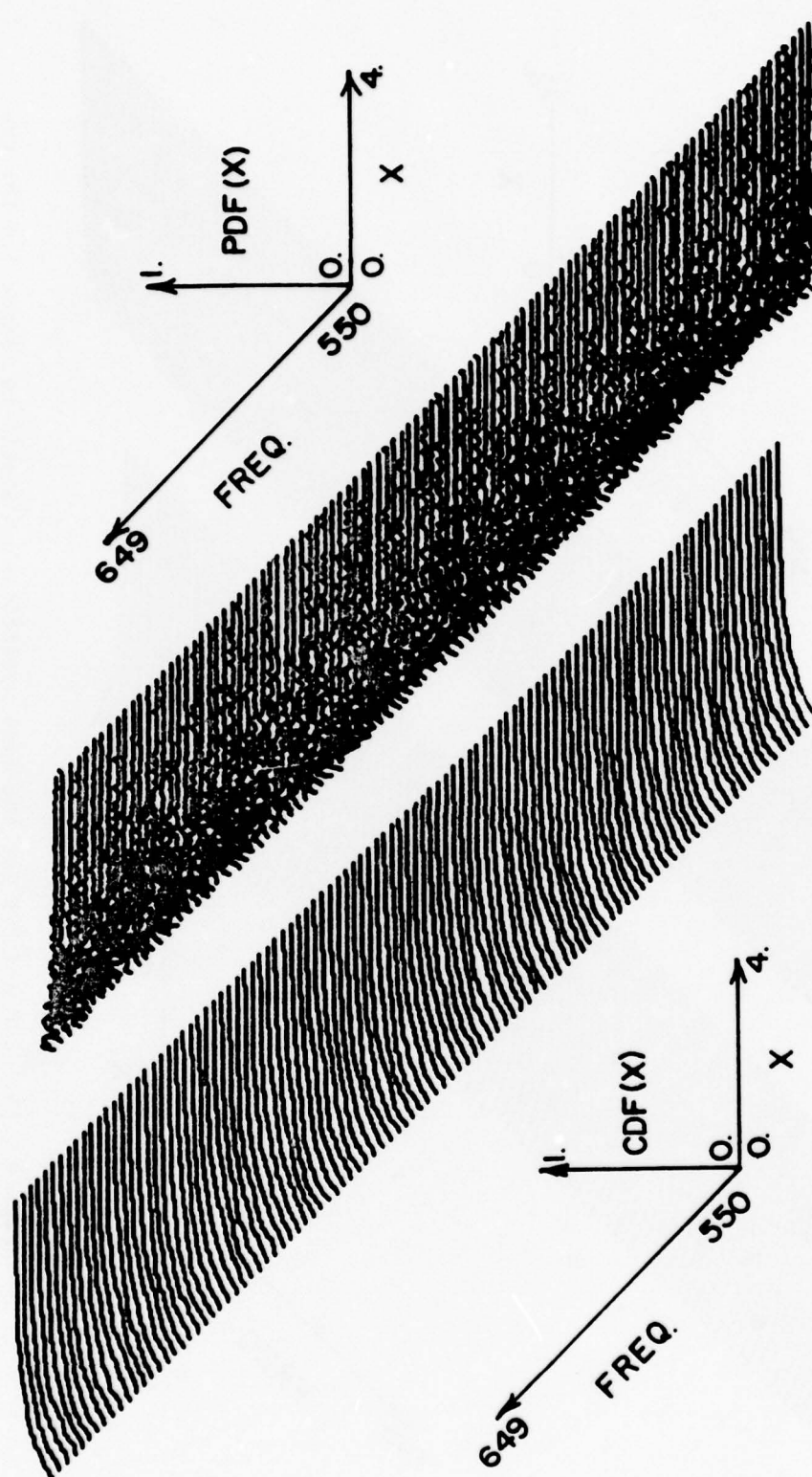
Figure 5.13. CDF and PDF for the same conditions as stated in Figure 5.8 for the frequency range from 550 – 649 Hz.
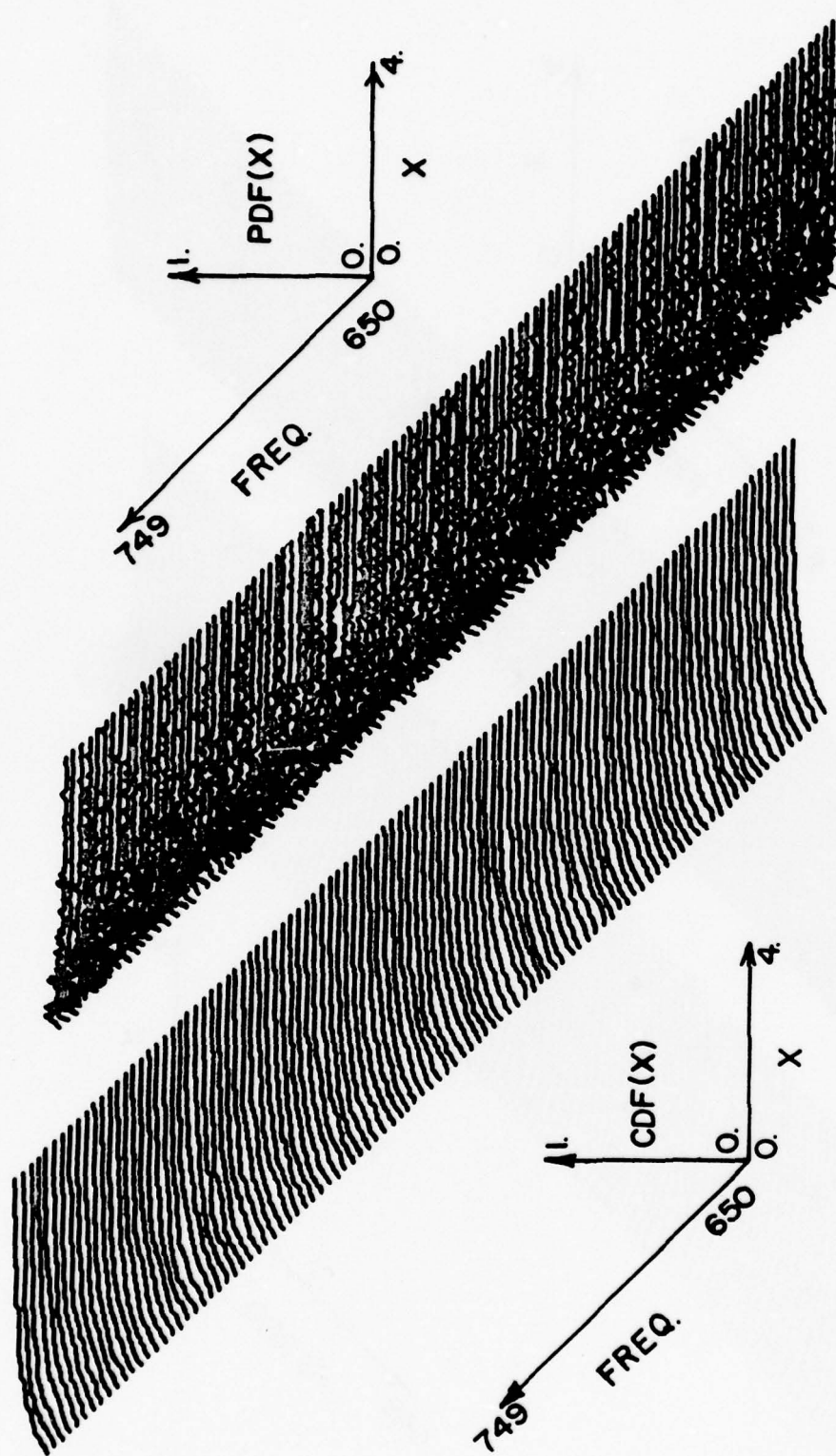
Figure 5.14. CDF and PDF for the same conditions as stated in Figure 5.8 for the frequency range from 650 - 749 Hz.
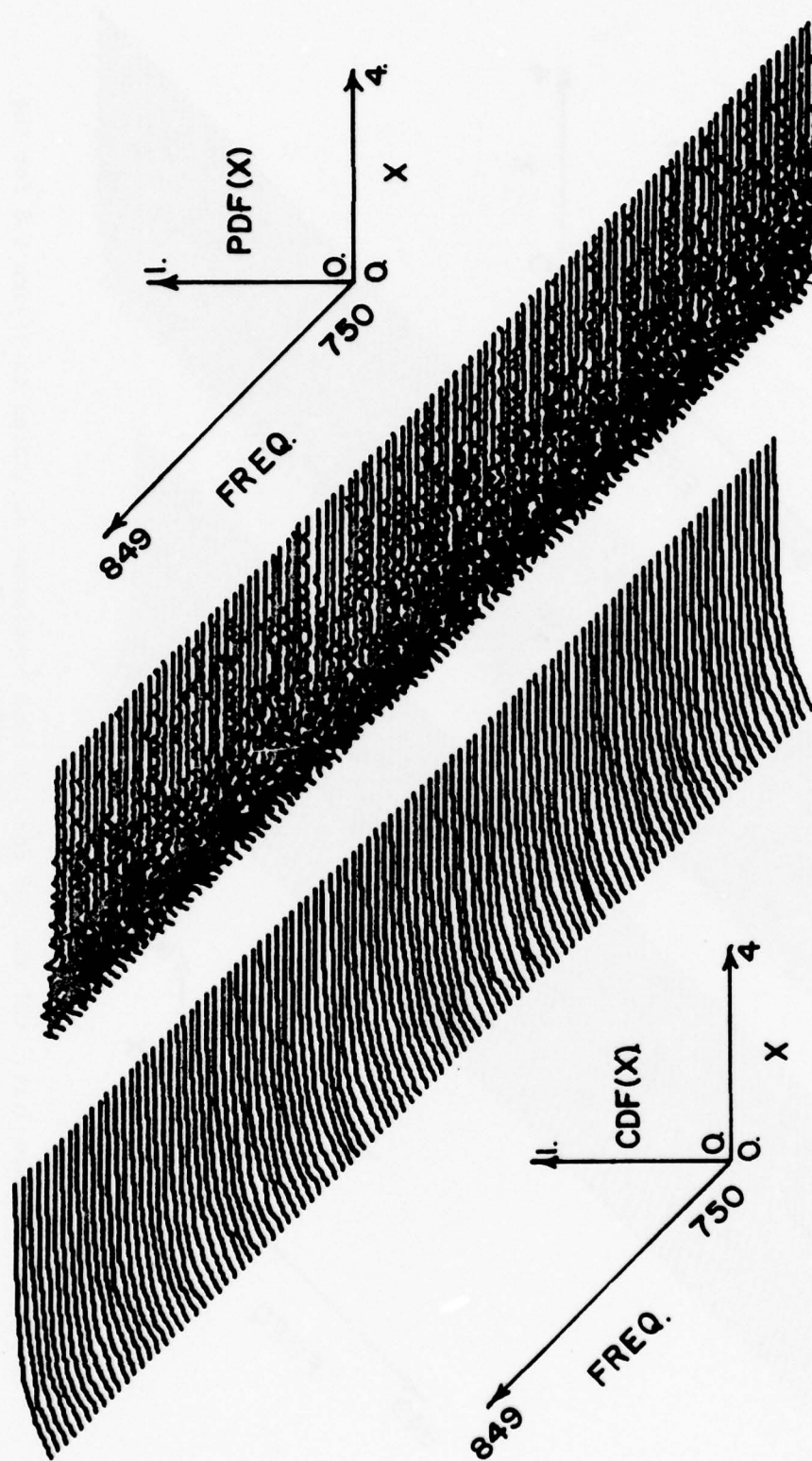
Figure 5.15. CDF and PDF for the same conditions as stated in Figure 5.8 for the frequency range from 750 – 849 Hz.
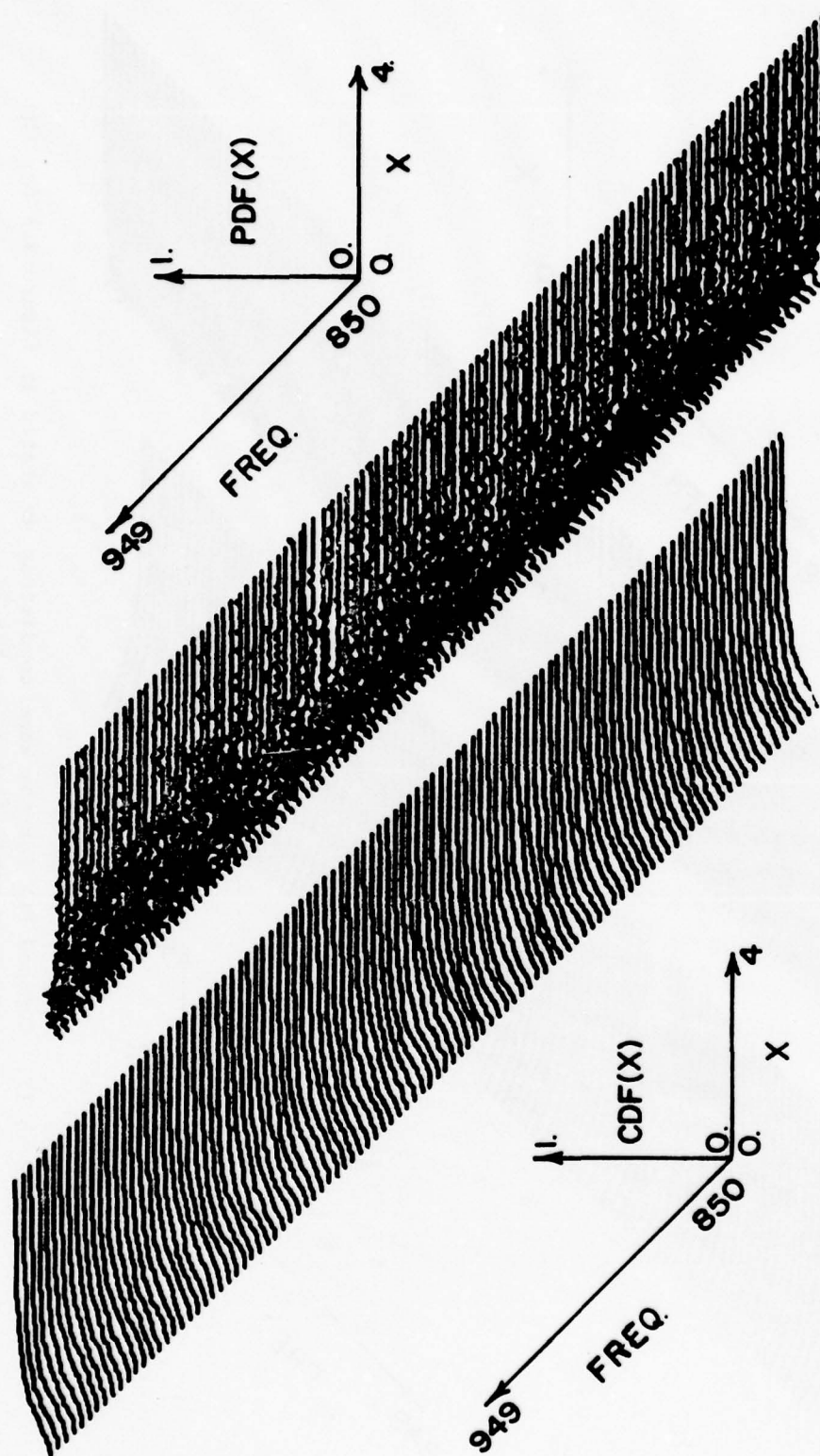
Figure 5.16. CDF and PDF for the same conditions as stated in Figure 5.8 for the frequency range from 850 – 949 Hz.
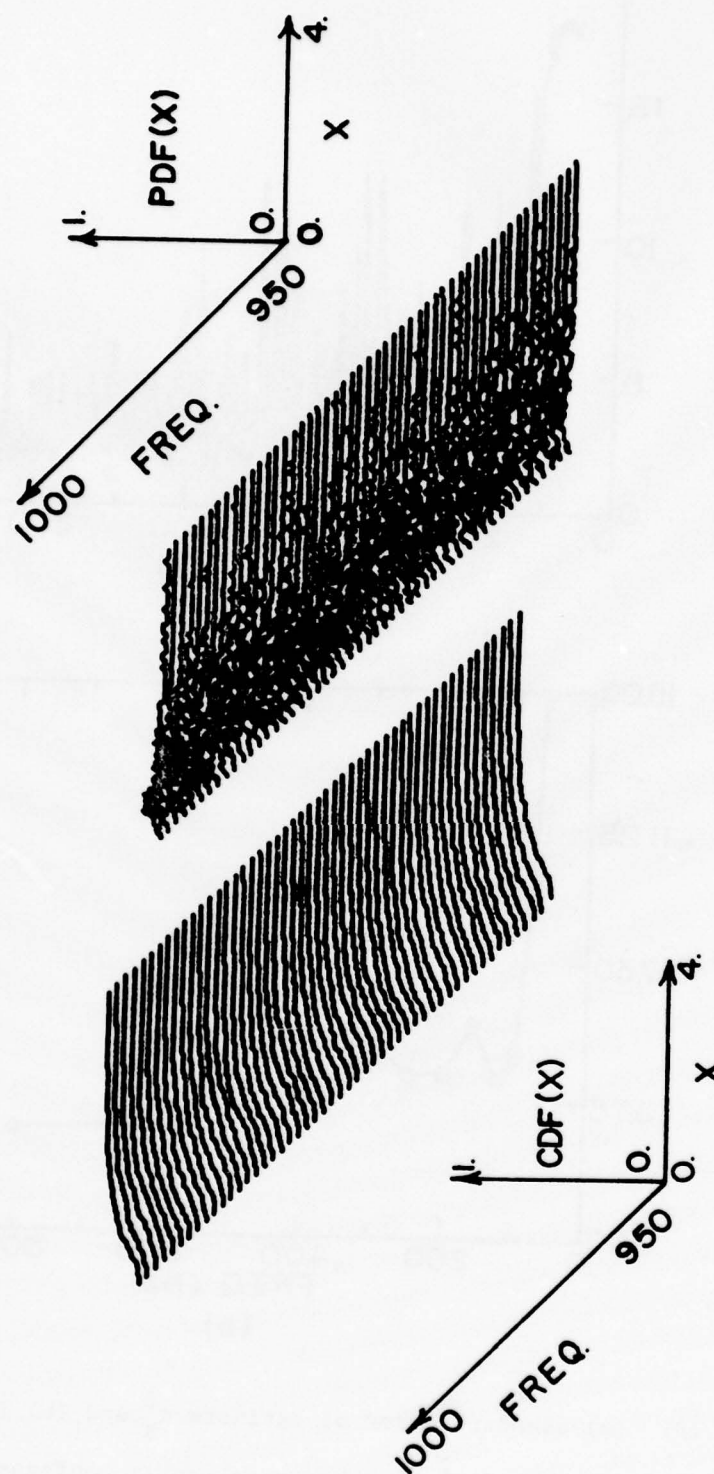
Figure 5.17. CDF and PDF for the same conditions as stated in Figure 5.8 for the frequency range from 950 - 1000 Hz.
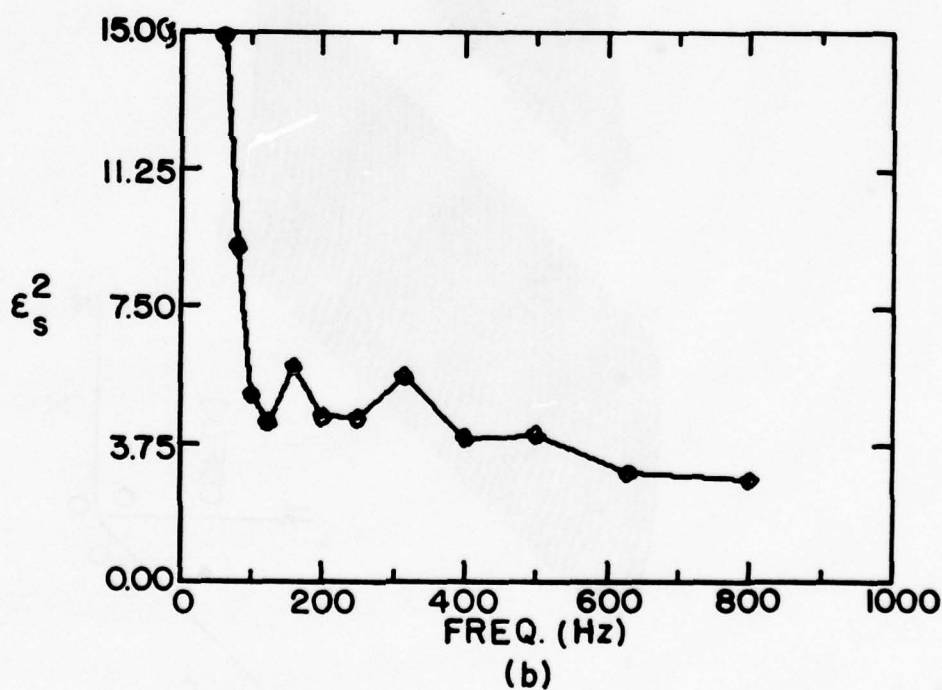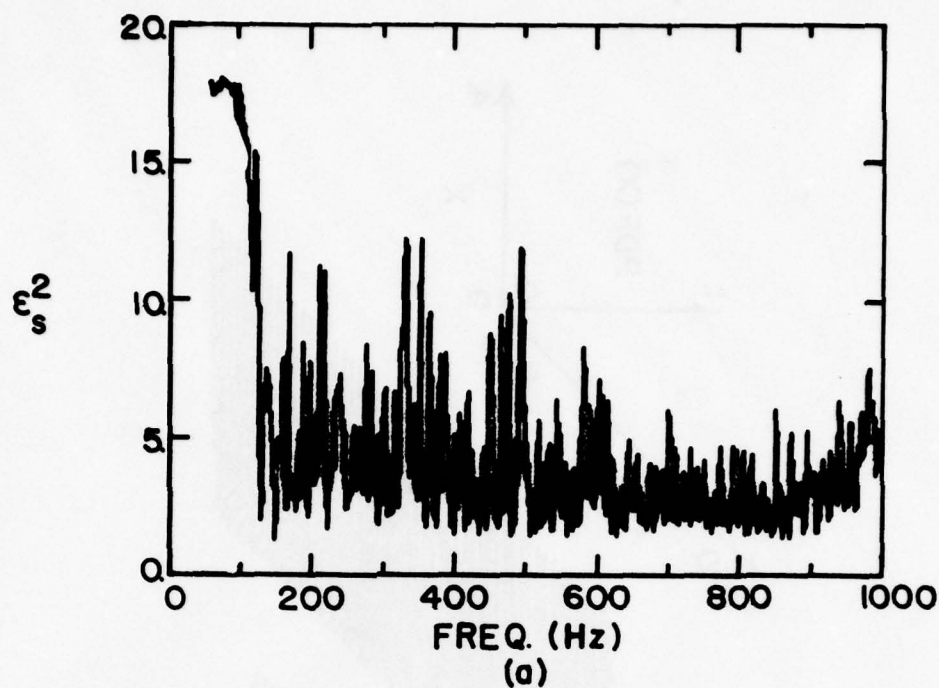
Figure 5.18. (a) Standard error of estimate ε_s^2 and (b) 1/3-octave

average of ε_s^2 for the experimental configuration given in

Figure 5.8 from 50 – 1000 Hz ($\Delta f = 1.0$ Hz).
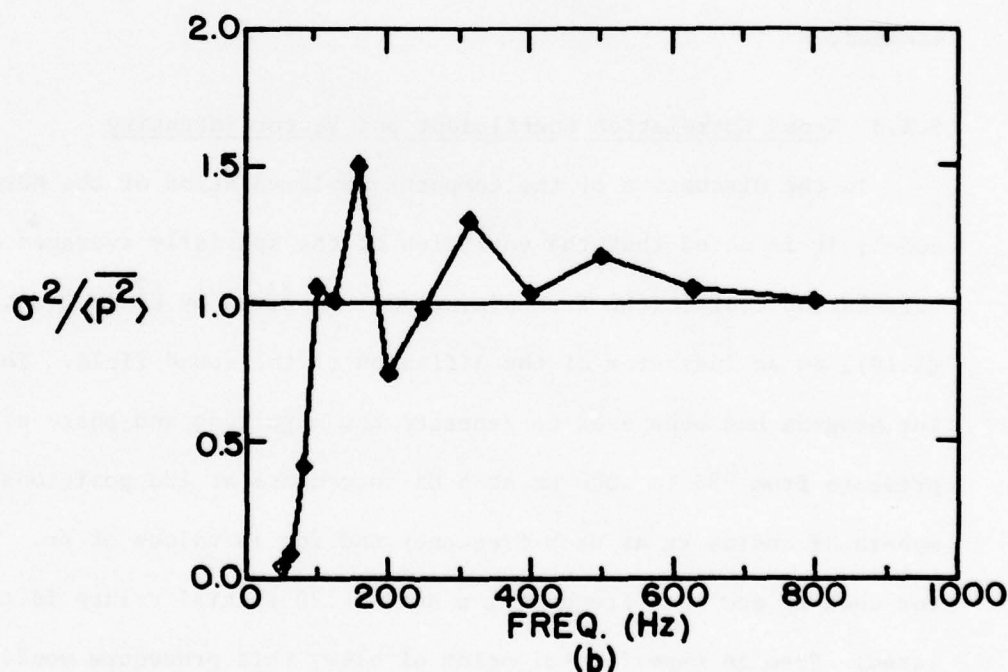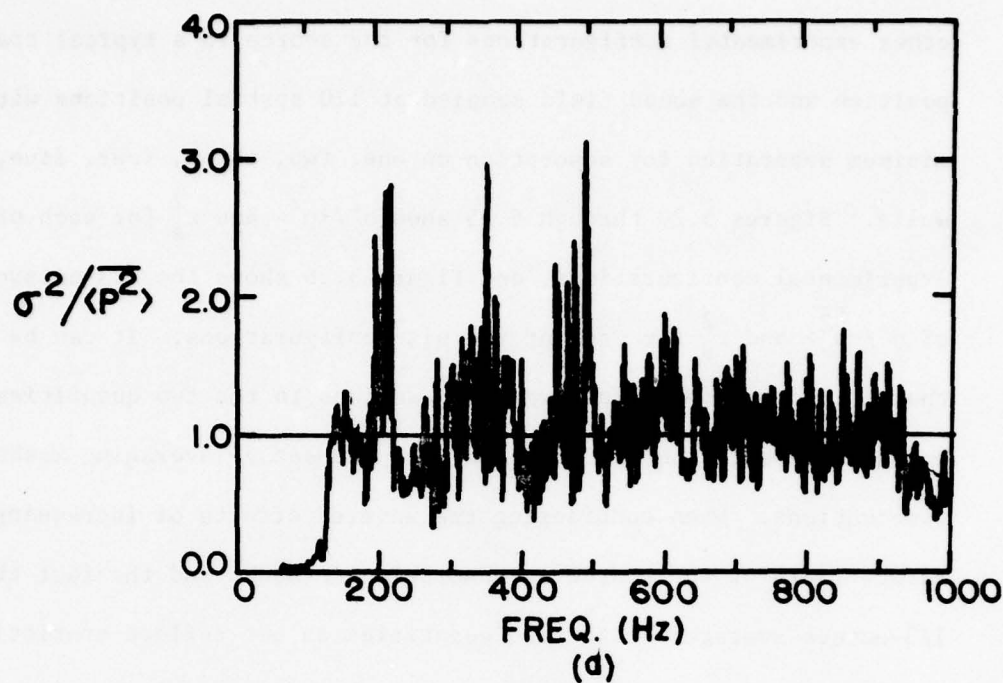
Figure 5.19. (a) Experimentally measured normalized spatial variance $\sigma^2/<p^2>$ and (b) 1/3-octave average of $\sigma^2/<p^2>$ calculated from experimentally measured squared pressure at 120 spatial positions in the model chamber (6.83 m^3) with the source centered in a typical position (1.596 m, 1.005 m, 0.785 m) and no absorption on the walls.

other experimental configurations for the source in a typical spatial position and the sound field sampled at 120 spatial positions with .015 m minimum separation for absorption on one, two, three, four, five, and six walls. Figures 5.20 through 5.25 show $\sigma^2/<\overline{p^2}>$ and ε_s^2 for each of these experimental configurations, and Figure 5.26 shows the 1/3-octave average of $\sigma^2/<\overline{p^2}>$ and ε_s^2 for each of the six configurations. It can be observed that, although there are fewer fluctuations in the two quantities as the amount of absorption is increased, the 1/3-octave averaging masks these fluctuations. When considering the adverse effects of increasing the direct field of the source as absorption is added and the fact that the 1/3-octave averages of the two quantities do not reflect statistically significant changes, the advantages of the addition of absorption are minimal.

5.3.3 Cross Correlation Coefficient and Vector Intensity

In the discussion of the computer implementation of the normal mode model, it is noted that the variation of the spatially averaged cross correlation coefficient from sin(kr)/kr, as given by ε_r^2 in Equation (3.19), is an indicator of the diffusion of the sound field. The computer program has been used to generate the magnitude and phase of the pressure from 250 to 1000 Hz at 5 Hz increments at 120 positions on a sphere of radius kr at each frequency and for 10 values of kr. Thus, for each kr and each frequency, a set of 120 spatial points is calculated. From an experimental point of view, this procedure would be extremely time consuming to implement.

The situation can be improved somewhat by choosing the 120 spatial positions on spheres of constant radius r as opposed to radius of constant kr. As mentioned previously, it takes approximately 4 hours to
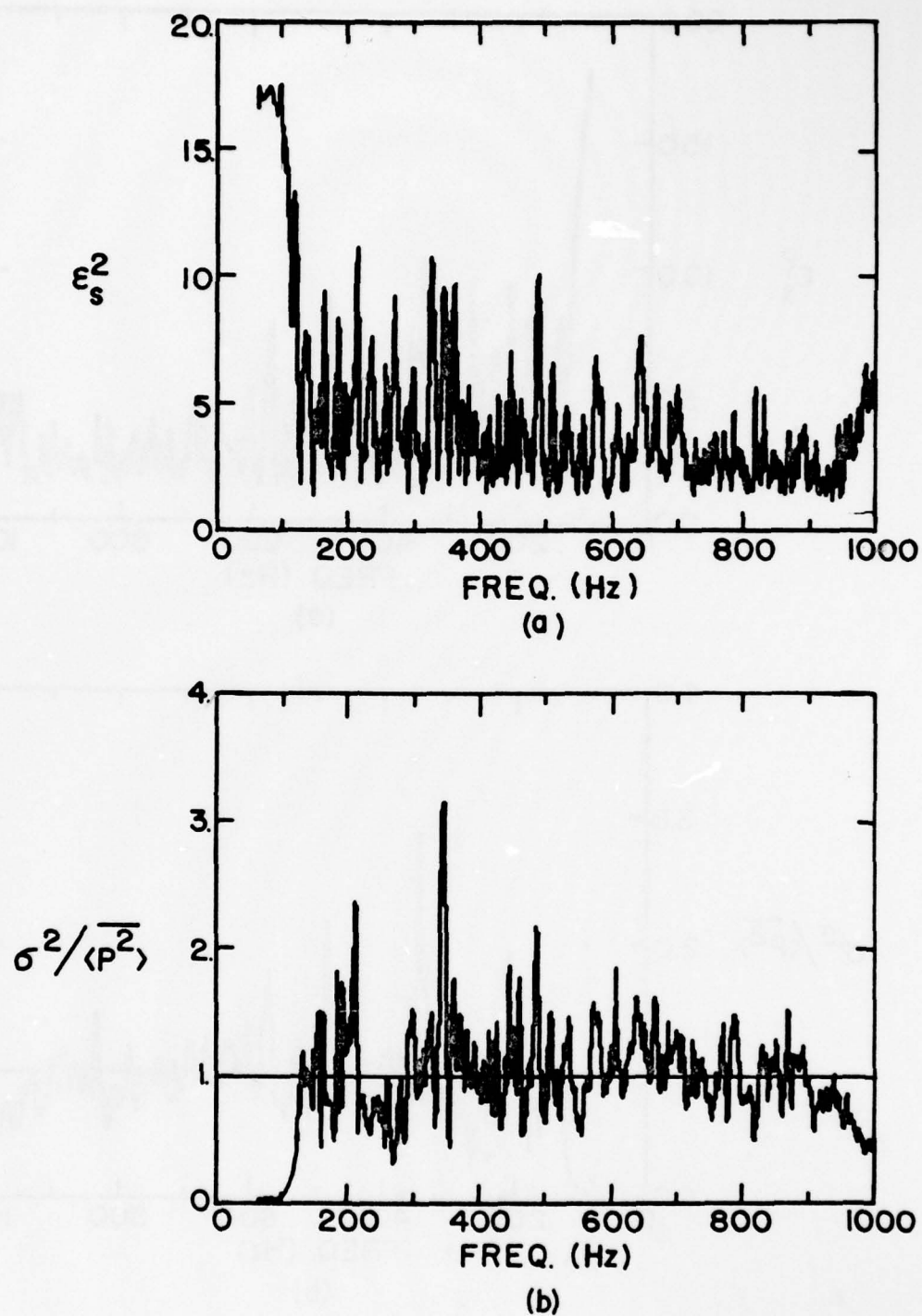
Figure 5.20. (a) Standard error of estimate ϵ_s^2 and (b) the normalized spatial variance $\sigma^2/\overline{\langle p^2 \rangle}$ for the experimental configuration given in Figure 5.19 but with absorption on one wall.
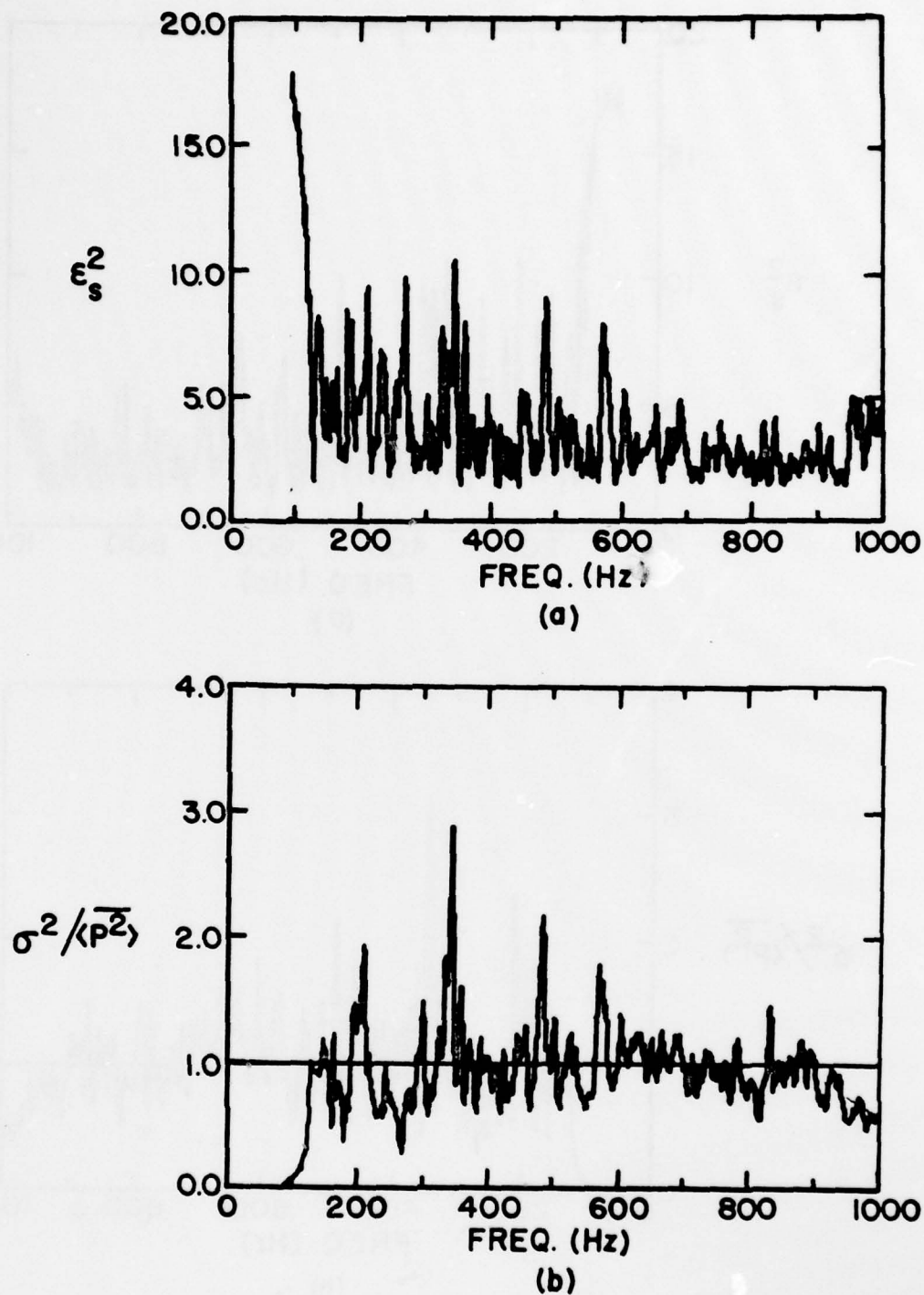
Figure 5.21. (a) The standard error of estimate ϵ_s^2 and (b) the normalized spatial variance $\sigma^2/\langle\overline{p^2}\rangle$ for the experimental configuration given in Figure 5.19 but with absorption on two walls.
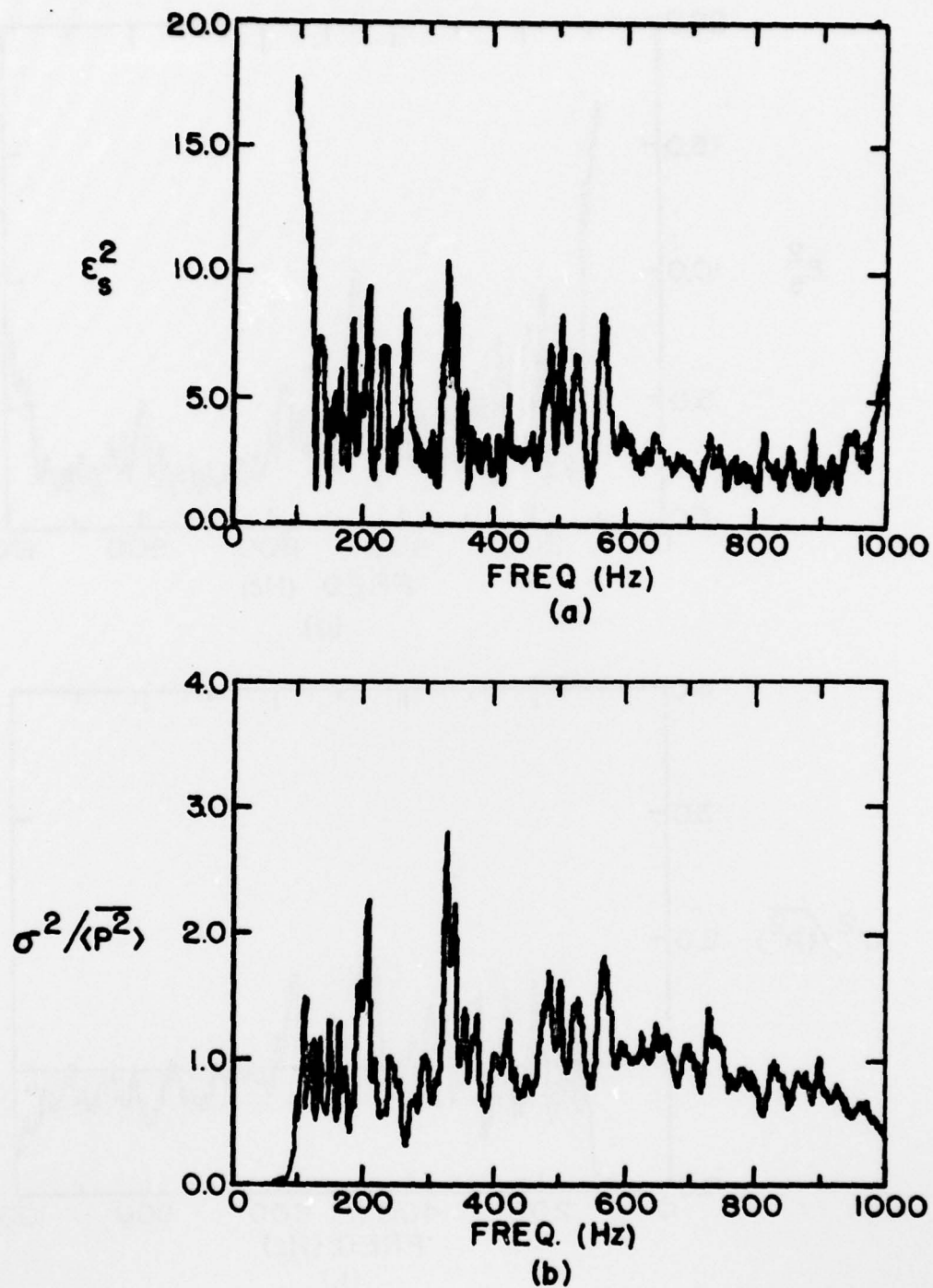
Figure 5.22. (a) The standard error of estimate ϵ_s^2 and (b) the normalized spatial variance $\sigma^2/\langle\overline{p^2}\rangle$ for the experimental configuration given in Figure 5.19 but with absorption on three walls.
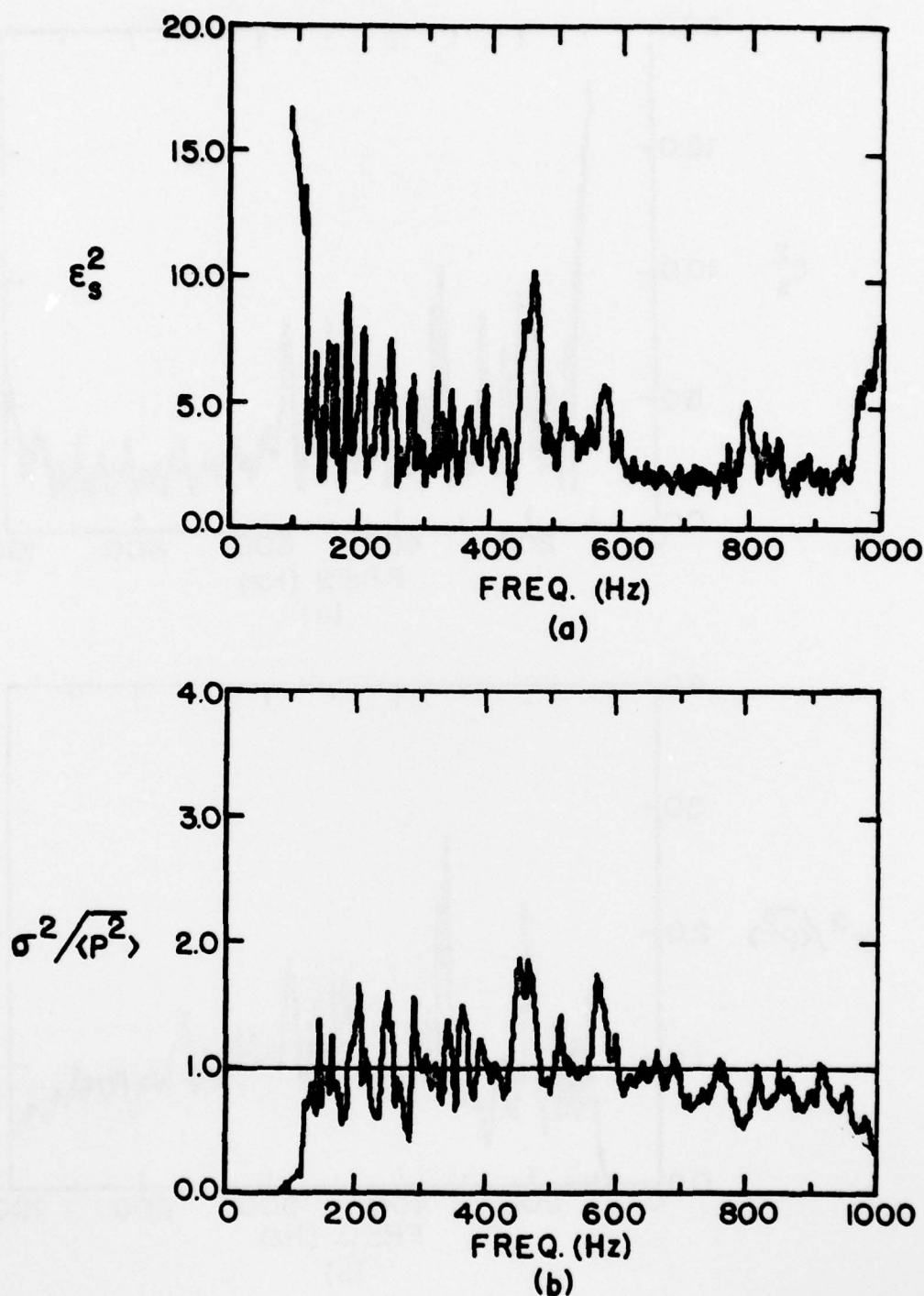
Figure 5.23. (a) The standard error of estimate ε_s^2 and (b) the

normalized spatial variance $\sigma^2/\overline{<p^2>}$ for the experimental configuration given in Figure 5.19 but with absorption on four walls.
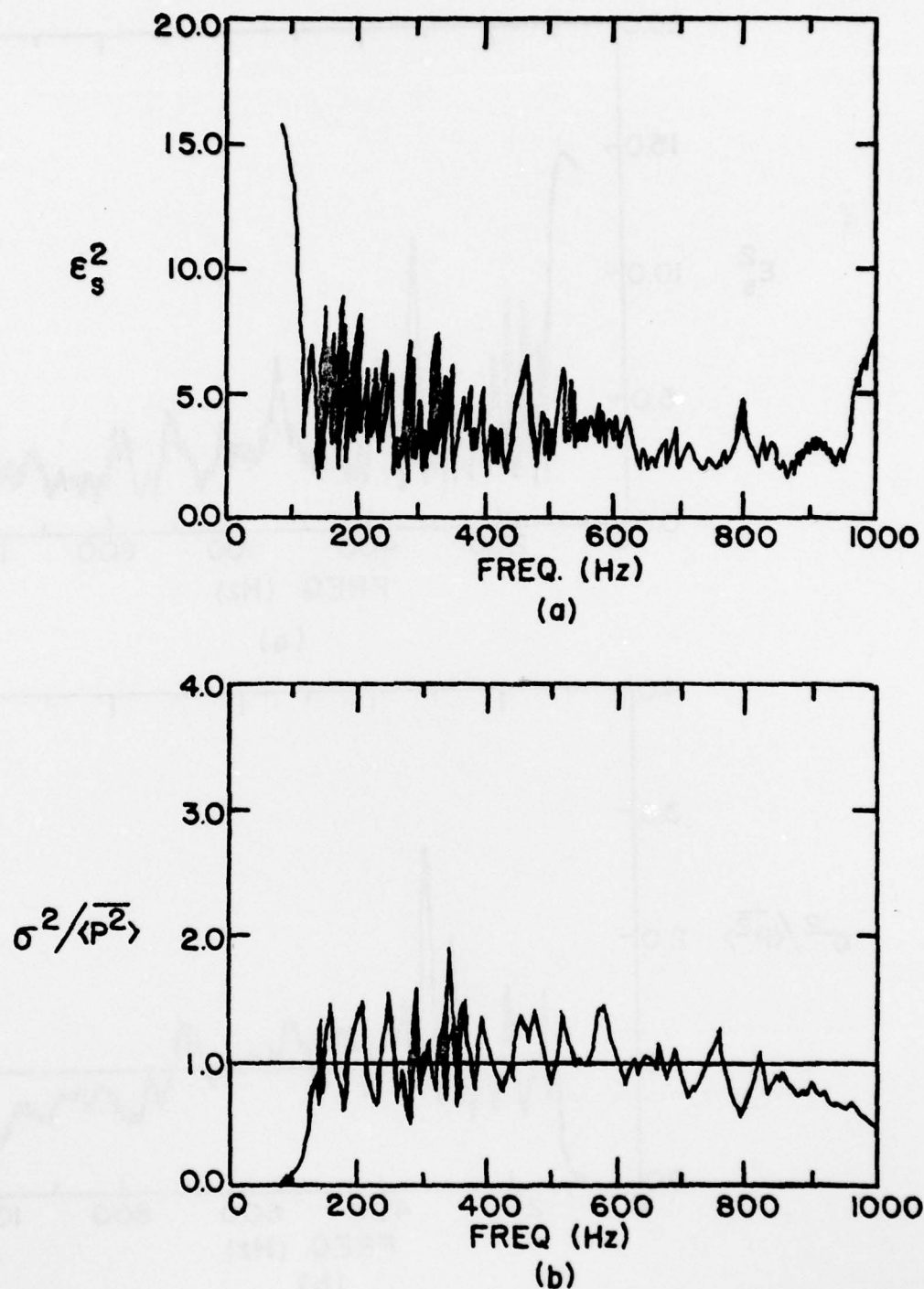
Figure 5.24. (a) The standard error of estimate ε_s^2 and (b) the normalized spatial variance $\sigma^2/\langle\overline{p^2}\rangle$ for the experimental configuration given in Figure 5.19 but with absorption on five walls.
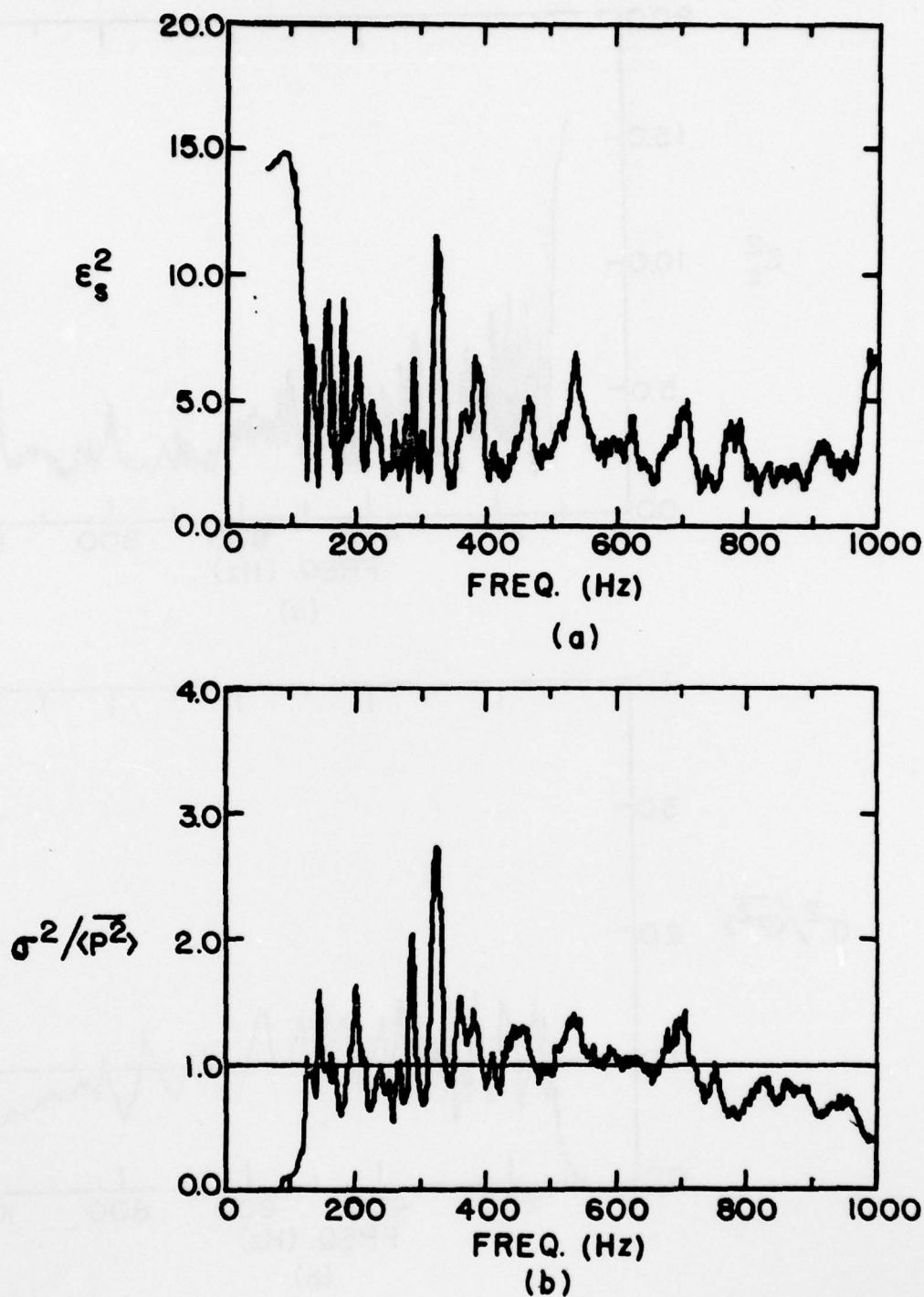
Figure 5.25. (a) The standard error of estimate ε_s^2 and (b) the normalized spatial variance $\sigma^2/\langle \overline{p^2} \rangle$ for the experimental configuration given in Figure 5.19 but with absorption on six walls.
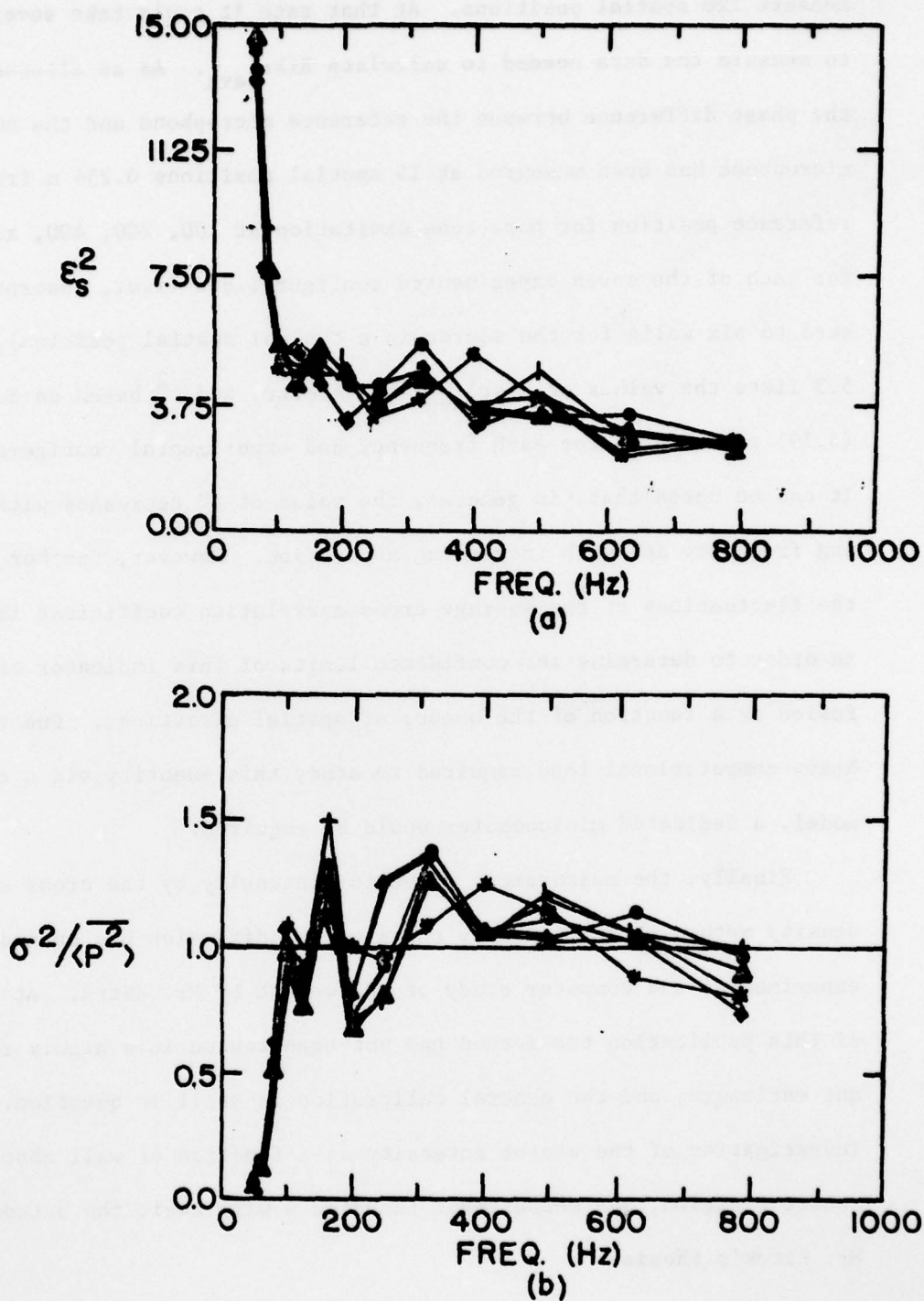
Figure 5.26. The 1/3-octave average of (a) ε_s^2 and (b) $\sigma^2/\langle \overline{p^2} \rangle$ for absorption on zero through six walls.

measure 120 spatial positions. At that rate it could take several days to measure the data needed to calculate $R(kr)_{avg}$. As an alternative, the phase difference between the reference microphone and the moving microphone has been measured at 15 spatial positions 0.254 m from the reference position for pure-tone excitation at 100, 200, 400, and 800 Hz for each of the seven experimented configurations (i.e., absorption on zero to six walls for the source in a typical spatial position). Table 5.3 lists the values of $R(kr)_{avg}$, $\sin(kr)/kr$, and ε_r^2 based on Equation (3.19) with N = 15 for each frequency and experimental configuration. It can be noted that, in general, the value of ε_r^2 decreases with increasing frequency and with increasing absorption. However, further study of the fluctuations of the average cross correlation coefficient is required in order to determine the confidence limits of this indicator of diffusion as a function of the number of spatial directions. Due to the heavy computational load required to study this quantity via a computer model, a dedicated minicomputer would be required.

Finally, the measurement of vector intensity by the cross spectral density method as initiated by the study of diffusion has opened an experimental and computer study of the method by Mr. Kitek. At the time of this publication the method has not been tested in a highly reverberant enclosure, and the general calibration is still in question. Further investigation of the vector intensity as a function of wall absorption, source position, and measurement techniques will await the outcome of Mr. Kitek's thesis.

5.4 Sound Field with Feedback

As described in Section 4.7, the computer implementation of the normal mode model of the sound field with feedback has shown that,

Table 5.3. The experimentally measured spatially averaged cross correlation coefficient $R(kr)_{avg}$ and the standard error of estimate ϵ_r^2 for the deviation of the measured value of sin(kr)/kr behavior at 100, 200, 400, and 800 Hz for absorption on zero to six walls of the model enclosure.

Number of Walls Covered	Frequency (Hz)	kr	$R(kr)_{avg}$	$R(kr)_T$	ϵ_r^2
0	100	0.553	0.419	0.950	0.282
	200	1.106	0.529	0.808	0.077
	400	2.213	0.301	0.362	0.004
	800	4.423	−0.047	−0.217	0.029
	1000	5.523	−0.112	−0.123	0.0001
1	100	0.553	0.417	0.950	0.283
	200	1.106	0.832	0.808	0.0006
	400	2.213	0.370	0.362	0.0001
	800	4.423	−0.257	−0.217	0.0016
	1000	5.523	0.129	−0.123	0.064
2	100	0.553	0.458	0.950	0.242
	200	1.106	0.879	0.808	0.005
	400	2.213	0.337	0.362	0.0006
	800	4.423	−0.240	−0.217	0.0005
	1000	5.523	−0.099	−0.123	0.0006
3	100	0.553	0.510	0.950	0.1938
	200	1.106	0.889	0.808	0.007
	400	2.213	0.339	0.362	0.0006
	800	4.423	−0.195	−0.217	0.0005
	1000	5.523	−0.189	−0.123	0.004
4	100	0.553	0.559	0.950	0.153
	200	1.106	0.889	0.808	0.006
	400	2.213	0.340	0.362	0.0005
	800	4.423	−0.214	−0.217	0.0000
	1000	5.523	−0.240	−0.123	0.014
5	100	0.553	0.645	0.950	0.093
	200	1.106	0.883	0.808	0.006
	400	2.213	0.330	0.362	0.001
	800	4.432	−0.205	−0.217	0.0001
	1000	5.523	−0.272	−0.123	0.022

Number of Walls Covered	Frequency (Hz)	kr	$R(kr)_{avg}$	$R(kr)_T$	ϵ_r^2
	100	0.553	0.703	0.950	0.061
	200	1.106	0.877	0.808	0.005
6	400	2.213	0.320	0.362	0.002
	800	4.432	−0.191	−0.217	0.0006
	1000	5.523	−0.291	−0.123	0.028

although the various indicators of diffusion have been affected by the addition of a particular feedback function, the effects are not statistically significant. In the experimental implementation of the FIR filter designed for multiple peaks, the fluctuation of temperature has made conditions worse.

The experimental procedures for implementation of a given feedback function is as follows:

(1) Measure the magnitude and phase of the open loop response with FIR filter in the all pass mode.

(2) Design the desired filter based on the open loop response and allowable gains.

(3) Implement the FIR filters in the closed loop response at the gain for which the loop is stable.

(4) Measure the pressure at 120 spatial locations and store this data for later analysis.

Two problems have been encountered in the implementation of a given feedback function. The first is that the allowable gain in the closed loop response has to be 4 to 5 dB lower than that predicted by the computer model, and, second, to maintain stability over the period of 4 hours required to measure the spatial data, the open loop response changes as the temperature in the enclosure changes. Although the filter is designed with a gain margin of 20 dB, only a gain of 13 dB (ref input) could be achieved without instability or "howl back" occurring. This reduction in gain further reduces the effectiveness of the addition of feedback.

The three stepping motors located in the interior of the enclosure generate a great deal of heat. Over a 1 hour period, the temperature

in the air tight enclosure has been measured to change 1° or 2° celsius. This change in temperature causes the amplitude and phase of the open loop response to shift from stable to unstable, as shown in Figure 5.27 which plots the open loop response for the optimum FIR filter at two temperatures. Due to the steep phase lag of the FIR filter, the stability of the feedback loop is very sensitive to any changes in phase.

Finally, by opening and closing the enclosure door every 20 minutes, the temperature in the interior of the enclosure can be satisfactorily controlled. The 1/3-octave average of the normalized spatial variance and ε_s^2 of the sound field with and without feedback for the enclosure with no absorption on the walls and the source in a typical spatial position are plotted in Figure 5.28. The feedback functions as given in Figure 4.22 have been shown to be the optimum realizable function considered in this study based on the design conditions and stability restrictions. As predicted, the effects of the addition of this feedback are not statistically significant.

5.5 Summary

An experimental model enclosure with a three-dimensional scanning system has been built for this project to experimentally measure the low frequency characteristics of the sound field and to measure the effects of the implementation of non-inline digital electronic feedback. The study has been made possible by the interfacing of a dual channel analyzer via a microprocessor to a minicomputer for the storage and later analysis of data.

The sound field in the experimental enclosure has been sampled in a grid of 120 positions with a minimum separation of 0.152 m for several
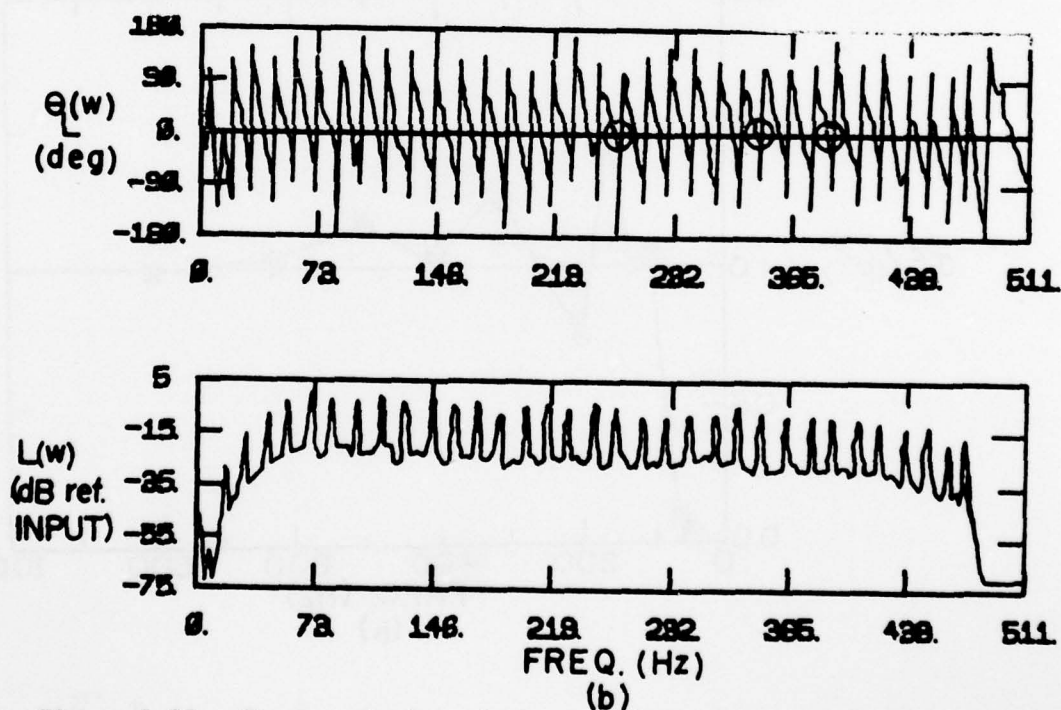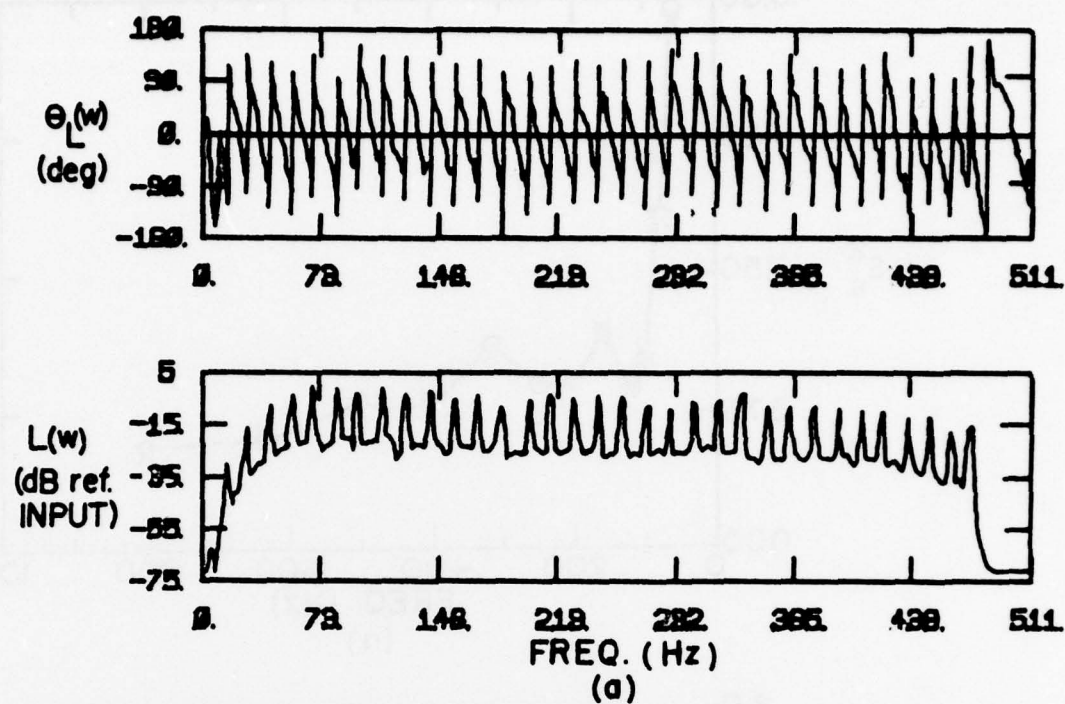
Figure 5.27. The magnitude and phase of the open loop response for (a) a stable filter with T 24.7°C and (b) an unstable filter for T 28.3°C with the circles indicating the frequencies that violate the stability criteria.
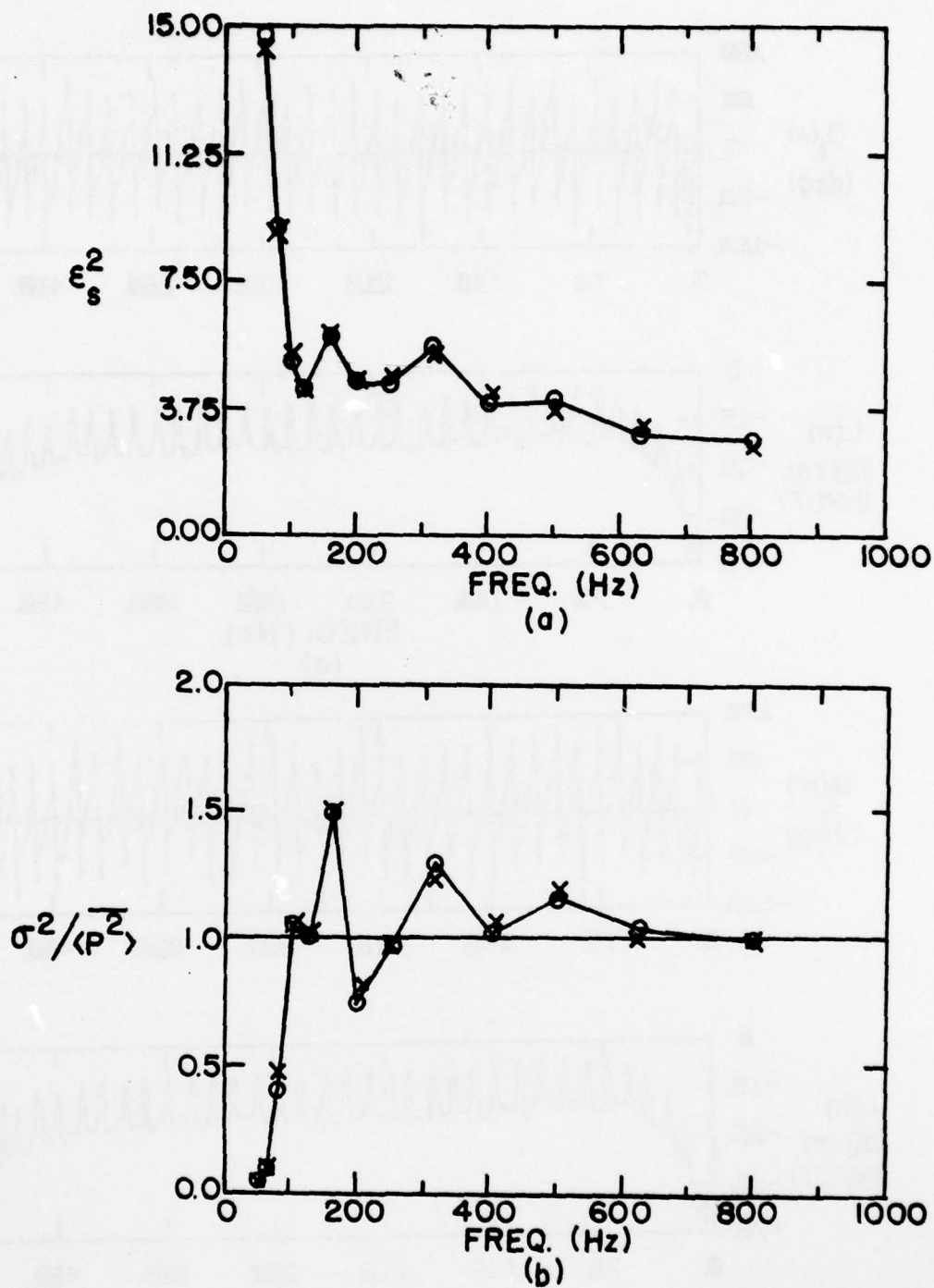
Figure 5.28. The 1/3-octave average of (a) ε_s^2 and (b) $\sigma^2/\langle\overline{p^2}\rangle$ based on experimental data with (X) and without (0) feedback.

experimental configurations. The normalized spatial variance and the standard error of estimate for the variations of the measured cumulative distribution function from the exponential distribution have shown results similar to those predicted by the normal mode model. The results show that, for a source in a typical spatial position in the interior of the enclosure, the sound field can be considered diffuse to a much lower frequency than predicted by Schroeder, particularly when 1/3-octave averages are considered.

The measurement of the average cross correlation coefficient, as it is calculated from the computer model at 120 locations for each kr, is impractical to measure experimentally in the present configuration. Instead, the average cross correlation coefficient has been measured at four discrete frequencies for five values of r and at 15 spatial positions. Again as predicted by the computer model for the enclosure with no additional absorption, there is little fluctuation of ϵ_r^2 with frequency. As additional absorption is added, the values of ϵ_s^2 decrease. Due to the difficulty of the experimental measurement and the computation load on a computer, the distribution that determines the confidence limits for ϵ_r^2 is not known, and the significance of the change in ϵ_r^2 with added absorption is not known. To carry out this study, a dedicated minicomputer is required.

The implementation of digital electronic feedback has been further complicated by the effects of the changing temperature. As predicted by the computer model, the effects of the addition of feedback on diffusion as indicated by the changes in $\sigma^2/\overline{<p^2>}$ and ϵ_s^2 are not statistically significant.

MICROCOPY RESOLUTION TEST CHART

NATIONAL BUREAU OF STANDARDS-1963-A

CHAPTER VI

CONCLUSIONS AND RECOMMENDATIONS FOR FURTHER STUDY

6.1 Summary and Conclusion

The aim of this study has been to investigate the characteristics
of the low frequency region of the sound field in reverberant enclosures
and to experimentally implement digital electronic feedback in an attempt
to beneficially modify the characteristics of the field. The use of a
reverberant enclosure for the measurement of sound power of a source,
sound transmission loss of a barrier, or sound absorption of material is
based on the assumption that the sound field is diffuse and the charac-
teristics that describe the sound field approach well-defined statistical
properties.

The study can be divided into three phases which include:

(1) the theoretical and computer model study of the charac-
teristics of the sound field from low to high frequency,

(2) the theoretical and computer model study of the
characteristics of digital electronic feedback and the
effects of feedback as predicted by the computer model,
and

(3) the experimental measurement of the characteristics of
the sound field in a model enclosure with and without
digital electronic feedback.

In Phase I the classical ray-acoustic model of the sound field has
been used to describe several measurable characteristics of the diffuse

experimental configurations. The normalized spatial variance and the standard error of estimate for the variations of the measured cumulative distribution function from the exponential distribution have shown results similar to those predicted by the normal mode model. The results show that, for a source in a typical spatial position in the interior of the enclosure, the sound field can be considered diffuse to a much lower frequency than predicted by Schroeder, particularly when 1/3-octave averages are considered.

The measurement of the average cross correlation coefficient, as it is calculated from the computer model at 120 locations for each kr, is impractical to measure experimentally in the present configuration. Instead, the average cross correlation coefficient has been measured at four discrete frequencies for five values of r and at 15 spatial positions. Again as predicted by the computer model for the enclosure with no additional absorption, there is little fluctuation of ϵ_r^2 with frequency. As additional absorption is added, the values of ϵ_s^2 decrease. Due to the difficulty of the experimental measurement and the computation load on a computer, the distribution that determines the confidence limits for ϵ_r^2 is not known, and the significance of the change in ϵ_r^2 with added absorption is not known. To carry out this study, a dedicated minicomputer is required.
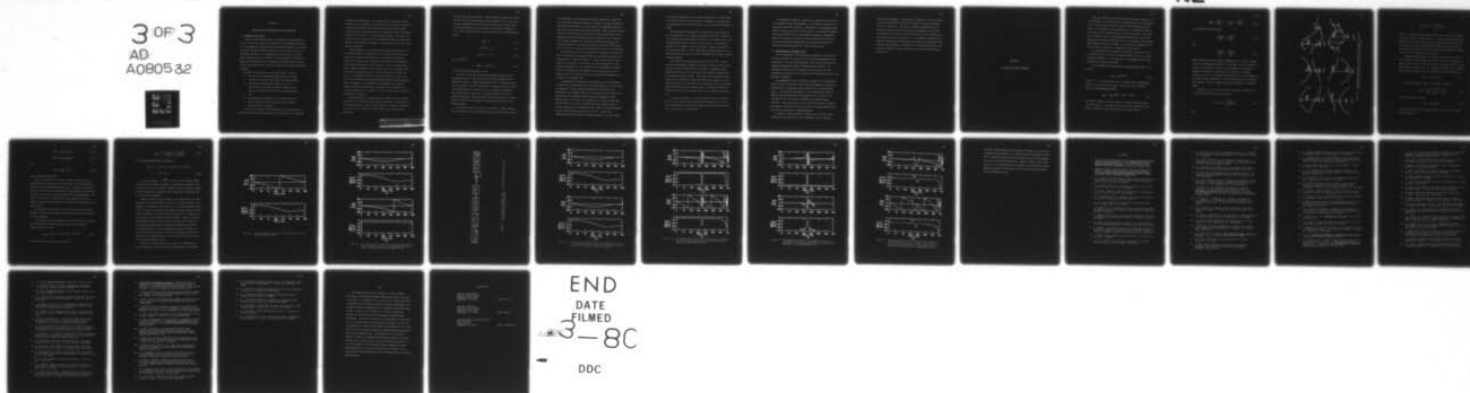
The implementation of digital electronic feedback has been further complicated by the effects of the changing temperature. As predicted by the computer model, the effects of the addition of feedback on diffusion as indicated by the changes in $\sigma^2/\overline{<p^2>}$ and ϵ_s^2 are not statistically significant.

sound field at high frequencies. These characteristics include the spatial mean $\overline{<p^2>}$ and the normalized spatial variance $\sigma^2/\overline{<p^2>}$ of the time-averaged, squared pressure; the cumulative distribution function CDF; the cross correlation coefficient R(kr); and the vector intensity $\vec{I}$. For a diffuse sound field these characteristics have the following properties:

$$\overline{<p^2>} \propto W \quad ; \tag{6.1}$$

$$\sigma^2/\overline{<p^2>} = 1.0 \quad ; \tag{6.2}$$

$$CDF(x) = 1 - e^{-x} \quad ; \tag{6.3}$$

for $x = \overline{p^2}/\overline{<p^2>}$,

$$R(kr) = \sin(kr)/kr \quad ; \tag{6.4}$$

and $\vec{I}$ is uniformly distributed in space.

In order to study the frequency-by-frequency transition of the characteristic of the sound field from low to high frequency (low to high modal overlap), a computer implementation of the normal mode model has been employed. Based on a theoretical investigation of the ratio of sound power radiated by a point source in a reverberant enclosure to that radiated in free space, the two unknown factors in the use of reverberant enclosure have been studied; these factors are the relative degree of diffusion and the manner of estimating the spatial mean of squared pressure.

This study has shown that, for a large number of spatial samples, $\overline{<p^2>}$ is proportional to the sound power W even at low frequency and that

the sound field can be considered sufficiently diffuse at frequencies much lower than previously predicted. In addition, two new criteria for evaluating the diffusion of the sound field in a reverberant enclosure excited by a pure-tone source have been studied. These include the standard error of estimate ϵ_s^2 for the variation of the measured CDF from the exponential CDF and the standard error of estimate ϵ_r^2 for the variation of the spatial averaged cross correlation coefficient $R(kr)_{avg}$ from $\sin(kr)/kr$ behavior. The study also focused on the second order statistics of the error encountered in the measurement of ϵ_s^2 at low frequencies.

The theoretical study of the diffusion in reverberant enclosures in Phase I has defined the frequency range for the theoretical study of the implementation of feedback in Phase II. Based on the promising results reported by Lilly (43), the fact that the lack of diffusion is a low frequency phenomenon, and the flexibility of a programmable FIR digital filter for implementation of feedback, the study has focused on the characteristics of the FIR filter and the necessary requirements for the stability of the feedback loop.

A programmable FIR filter has been purchased, and its characteristics have been incorporated into the normal mode model of the sound field with feedback. Several computer designed filter shapes have been implemented in the computer study and all designs have been based on the discrete Hilbert transform relations between the magnitude and the minimum phase of the filter. The properties of a linear all pass phase lag have been used to design an optimum FIR filter which consists of multiple peaks centered at frequencies 180° removed from the frequencies at which instabilities are most likely to occur. Despite the sophistication and flexibility of the design feature of the FIR filter,

the computer implementation of the normal mode model of the sound field with feedback has shown that the effects of feedback, as determined by the various quantities studied in Phase I, are not statistically significant.

The experimental implementation of feedback in a model enclosure and the measurement of the various indicators of diffusion in Phase III of this study have substantiated the results of the computer study. The measurement and storage of spatial pressure data at a large number of positions in the model enclosure have required computer interfacing to the measurement system. A three-dimensional scanning system and a dual channel analyzer have made the accurate measurement of pressure magnitude and phase possible.

The frequency-by-frequency variations of ϵ_s^2 , $\sigma^2/\overline{<p^2>}$, and CDF have been experimentally measured in the model enclosure for two source positions, seven different amounts of absorption (covering no walls through all walls), and for digital electronic feedback implementation of an optimum FIR filter design. The results of the experimental phase indicate that, although the normal mode model cannot predict the exact transfer function in the enclosure, on the average, theory and experiment agree particularly when the computer model is modified to include the frequency fluctuation of wall absorption, source strength, and temperature.

In general, the design of a stable feedback function is nontrivial and, due to the stability requirement and characteristics of the FIR filter considered in this study, no significant effect on the diffusion of the sound field has been observed.

The experimental apparatus, though fairly sophisticated, would have to be improved to make the measurement of the spatially averaged cross correlation coefficient practical. Nevertheless, the experimental measurement of $R(kr)_{avg}$ for pure-tone excitation at a few discrete frequencies indicates that there is an underlying fundamental correspondence between the statistical properties of the sound field excited by pure tone and then spatially averaged and those properties measured at a single position and averaged over a narrow frequency band.

6.2 Recommendation for Further Study

With the upgrading of the experimental apparatus to include high speed data transfer and computer control of the three-dimensional scanning system, a more detailed experimental study of the relation between spatial averaging and frequency averaging can be considered. The fundamental properties of the magnitude and particularly the phase distribution of pressure for the standing wave field excited by pure tone should be considered.

The measurement of vector intensity by means of the cross spectral density function between two closely spaced microphones has intriguing possibilities as a measurement tool, particularly in semireverberant spaces. The near-field measurement of $\vec{I}$ for simple sources could be studied both theoretically and experimentally as a function of the diffusion of the sound field in reverberant and semireverberant enclosures. With the addition of color graphics displays, the spatial and frequency fluctuation of source and sound field characteristics can be studied for enclosures of other geometries.

In regard to digital electronic feedback and its effect on the diffusion of the sound field at low frequencies, several different

schemes may be attempted. The problem of instability at certain frequencies may be eliminated by slowly and continually varying the sampling rate of the FIR filter. This would, in effect, constantly shift the frequency location of the multiple peaks as considered in this study. The expansion of the study to include multiple sources for a single feedback loop may prove to be beneficial. It is strongly recommended that a computer study using the normal mode model precede any experimental study with particular attention to be paid to the second order statistics that indicate the degree of change required for any significant improvement in diffusion.

APPENDIX A

THE DISCRETE HILBERT TRANSFORM

With the recognition in the past 20 years of digital signal processing techniques, the discrete Hilbert transform (DHT) and its implementation by various discrete Fourier transform (DFT) techniques have been shown to be an important data processing tool. (See Reference (16) for an extensive list of application areas of the DFT and DHT.) This appendix is intended to give a brief mathematical background to the Hilbert transform and its digital implementation by DFT techniques and to present some examples of FIR filter designs. For an in-depth development of the discrete Hilbert transform, see Oppenheim and Schafer (60).

As a consequence of the properties of analytic functions, the real and imaginary parts of a class of functions denoted L^2 (61) are related by Hilbert transforms. If the real part or the imaginary part is known, the function is completely defined.

If it is assumed that any measurable transform function H(S) can be written,

$$H(S) = A(S)e^{i\phi(S)} \quad , \tag{A.1}$$

where $S = \sigma + i\omega$, then the phase can be separated into a minimum phase, $\phi_m(S)$, and an all pass phase, $\theta_{Ap}(S)$, where $\phi_m(S) = $ DHT $(\ln(A(S)))$. Thus, for a minimum phase network,

$$H_m(S) = A(S)e^{i\phi_m(S)} = e^{a(S) + i\phi_m(S)} \quad , \tag{A.2}$$

where $a(S) = \ln(A(S))$, and there exists a unique relationship between the a(S) and $\phi_m(S)$. A heuristic description of the relationship can be given by applying the Cauchy-Reimann equations, which yields

$$\frac{\partial a(S)}{\partial \sigma} = \frac{\partial \phi_m(S)}{\partial \omega} \quad , \quad \frac{\partial a(S)}{\partial \omega} = - \frac{\partial \phi_m(S)}{\partial \sigma} \qquad (A.3)$$

and, taking further derivatives,

$$\frac{\partial^2 a(S)}{\partial \omega^2} = - \frac{\partial^2 a(S)}{\partial \sigma^2} \qquad (A.4)$$

and

$$\frac{\partial^2 \phi_m(S)}{\partial \omega^2} = - \frac{\partial^2 \phi_m(S)}{\partial \sigma^2} \quad . \qquad (A.5)$$

Heyser (34) has shown that, based on Equations (A.3) to (A.5), a simple rule for a minimum phase network can be observed: at a local maximum or minimum in the transform function, a local maximum in the amplitude response corresponds to a local point of inflection in the phase response, and, due to the symmetry of Equation (A.3), a local maximum in the phase response corresponds to a local inflection point in the amplitude response. Figure A.1 reproduces these conclusions in a graphical manner.

In general, it can be shown (35) that the Hilbert transform relationship between $a(S)$ and $\phi_m(S)$ is given by

$$a(\omega) = \frac{1}{\pi} \text{ P.V.} \int_{-\infty}^{\infty} \frac{\phi_m(x)}{\omega_\alpha - x} dx \qquad (A.6)$$

and
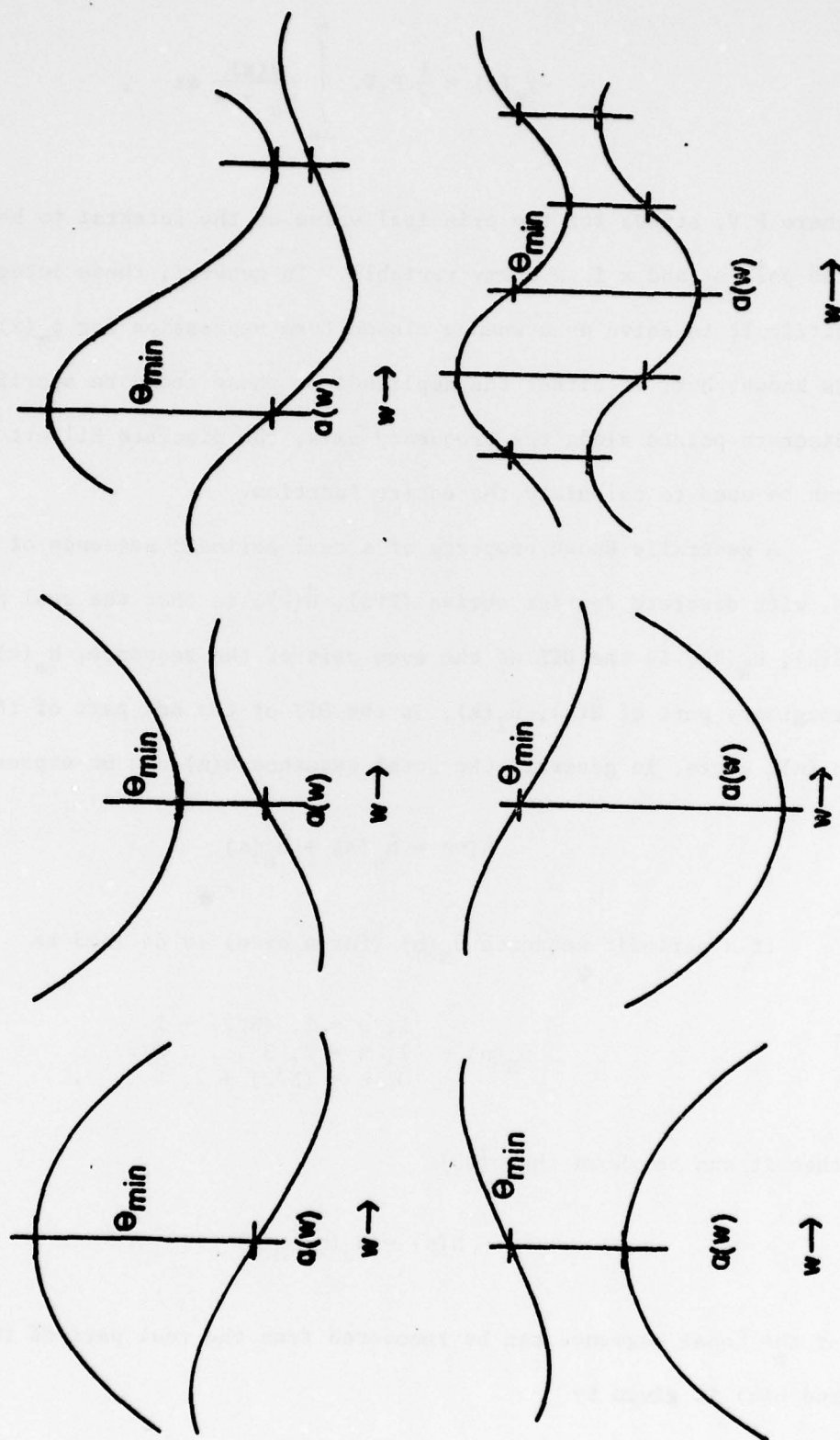
Figure A.1. Illustration of the effect of the Hilbert transform on maxima, minima, and inflection points of $a(w) = \ln|H|$ and θ_{min}.

$$-\phi_m(\omega) = \frac{1}{\pi} \text{ P.V.} \int_{-\infty}^{\infty} \frac{a(x)}{\omega_\alpha - x} \, dx \quad,$$

where P.V. stands for the principal value of the integral to be taken at the pole ω_α and x is a dummy variable. In general, these integrals are difficult to solve even when a closed form expression for $\phi_m(x)$ or $a(x)$ is known, but, if either the amplitude or phase could be specified at discrete points along the frequency axis, the discrete Hilbert transform can be used to calculate the entire function.

A generally known property of a real periodic sequence of period, N, with discrete Fourier series (DFS), $\tilde{H}(k)$, is that the real part of $\tilde{H}(k)$, $\tilde{H}_R(k)$, is the DFS of the even part of the sequence, $h_e(n)$, and the imaginary part of $\tilde{H}(k)$, $\tilde{H}_I(k)$, is the DFS of the odd part of the sequence $h_0(n)$, where, in general, the total sequence h(n) can be expressed as

$$\tilde{h}(n) = \tilde{h}_e(n) + \tilde{h}_0(n) \quad. \tag{A.7}$$

If a periodic sequence $\tilde{\mu}_N(n)$ (for n even) is defined as

$$\tilde{\mu}_N(n) = \begin{cases} 1, & n = 1, \ (N/2) + 1 \\ 2, & n = 2, \ 3 \ . \ . \ . \ N/2 \\ 0, & n = (N/2) + 2, \ N \end{cases} \tag{A.8}$$

then it can be shown that (60)

$$\tilde{h}(n) = \tilde{h}_e(n)\tilde{\mu}_N(n) \quad, \tag{A.9}$$

or the total sequence can be recovered from the real part of the $\tilde{H}(k)$, and H(k) is given by

$$\tilde{H}(k) = \tilde{H}_R(k) + \tilde{H}_I(k) \quad , \tag{A.10}$$

$$\tilde{H}(k) = DFT\big(h_e(n)\tilde{\mu}_N(n)\big) \quad , \tag{A.11}$$

and

$$\tilde{H}(k) = \tilde{H}_R(k) * \tilde{\mu}_N(k) \quad , \tag{A.12}$$

where * indicates convolution.

Thus, it is possible to calculate a phase function from the $\log_e$ magnitude by setting the real part of $\tilde{H}(k)$ equal to the log magnitude, taking the inverse DFT, multiplying by $\tilde{\mu}_N(n)$ and taking the forward DFT with the real part of the result being the $\log_e$ magnitude and the imaginary part of the result being an approximation of the minimum phase. The product of the inverse transform of the $\log_e$ magnitude and $\tilde{\mu}_N(n)$ is called the cepstrum and has several useful properties (see Chapter 10 in Reference (60)).

To illustrate this procedure, the next section will give several examples of the FIR filter designs using the DFT to calculate the DHT of the $\log_e$ (magnitude).

To illustrate the design procedures for a known function, a minimum phase finite-duration impulse response, which has the following z-transform system function,

$$H_{min}(z) = \frac{1}{R^2} (1 - re^{i\theta}z^{-1})^2(1 - re^{-i\theta}z^{-1})^2 \quad , \tag{A.13}$$

is multiplied by an all pass function given by

$$H_{Ap}(z) = \frac{z^{-1} - re^{-i\theta}}{1 - re^{i\theta}z^{-1}} \frac{z^{-1} - re^{i\theta}}{1 - re^{-i\theta}z^{-1}} \quad . \tag{A.14}$$

The resulting nonminimum phase function is

$$H(z) = (1 - re^{i\theta}z^{-1})(1 - re^{i\theta}z^{-1})(1 - r^{-1}e^{i\theta}z^{-1})$$

$$(1 - r^{-1}e^{-i\theta}z^{-1}) \quad . \tag{A.15}$$

In these equations, $z = e^{i(\frac{2\pi}{N}k)}$, where k is the frequency sample and N is the total number of samples. The magnitude and phase of each of the three functions are shown in Figures A.2 and A.3, where the amplitude is normalized to a maximum of unity (0 dB) and the frequency axis is divided into 256 samples.

Figure A.4 shows the block diagram of this program logic for implementation of the discrete Hilbert transform. In order to obtain a real sequence, the real part of the function to be inverse transformed (IDFT), $x(e^{i\omega})$ in Figure A.4, must have even symmetry and must therefore be band limited; otherwise, the IDFT process will set the N/2 + 1 term equal to zero, which in turn produces the Gibbs phenomenon. Figure A.5(a) shows the sampled magnitude of H(z) as given by Equation (A.2), and Figure A.5(b) shows the minimum phase calculated by the DHT process and from the sampled magnitude of the nonminimum phase function in Figure A.2. For the large number of samples (N - 1024), the minimum phase and that calculated by the DHT$(\ln|H|)$ are very close, and the only difference is due to the band limiting process.

Figures A.6 through A.8 show three examples of the DHT process where the amplitude is specified and the minimum phase is calculated.
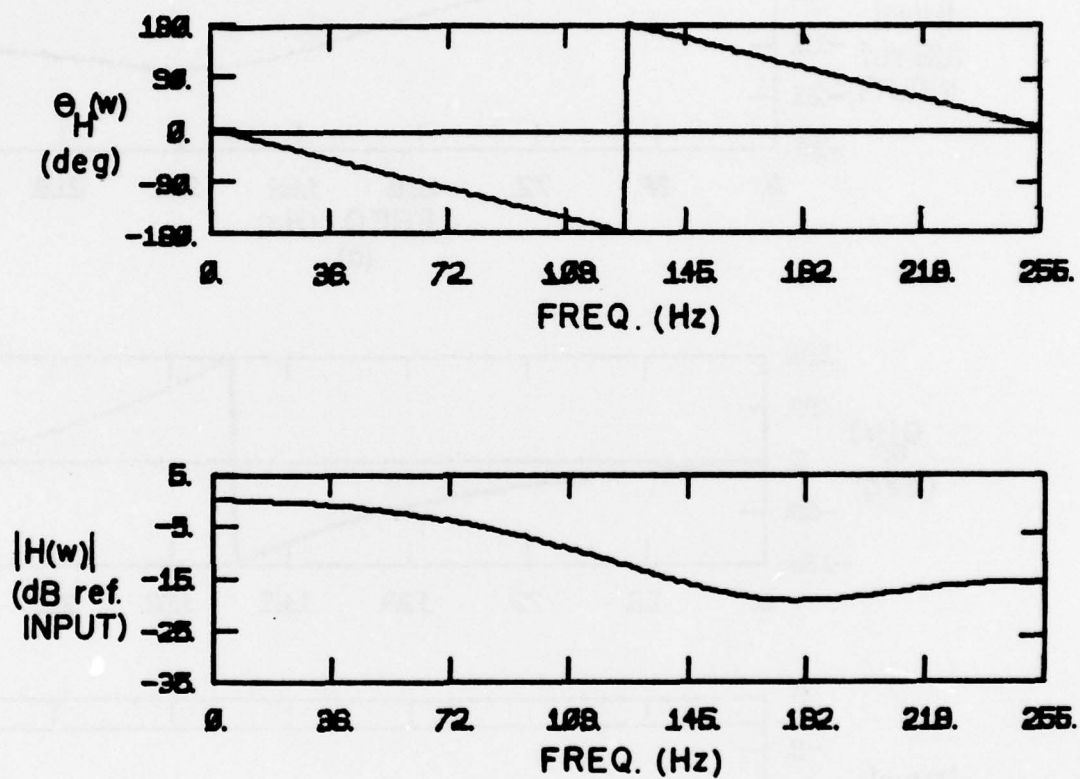
Figure A.2. The magnitude and phase of the nonminimum phase function given by Equation (A.15).
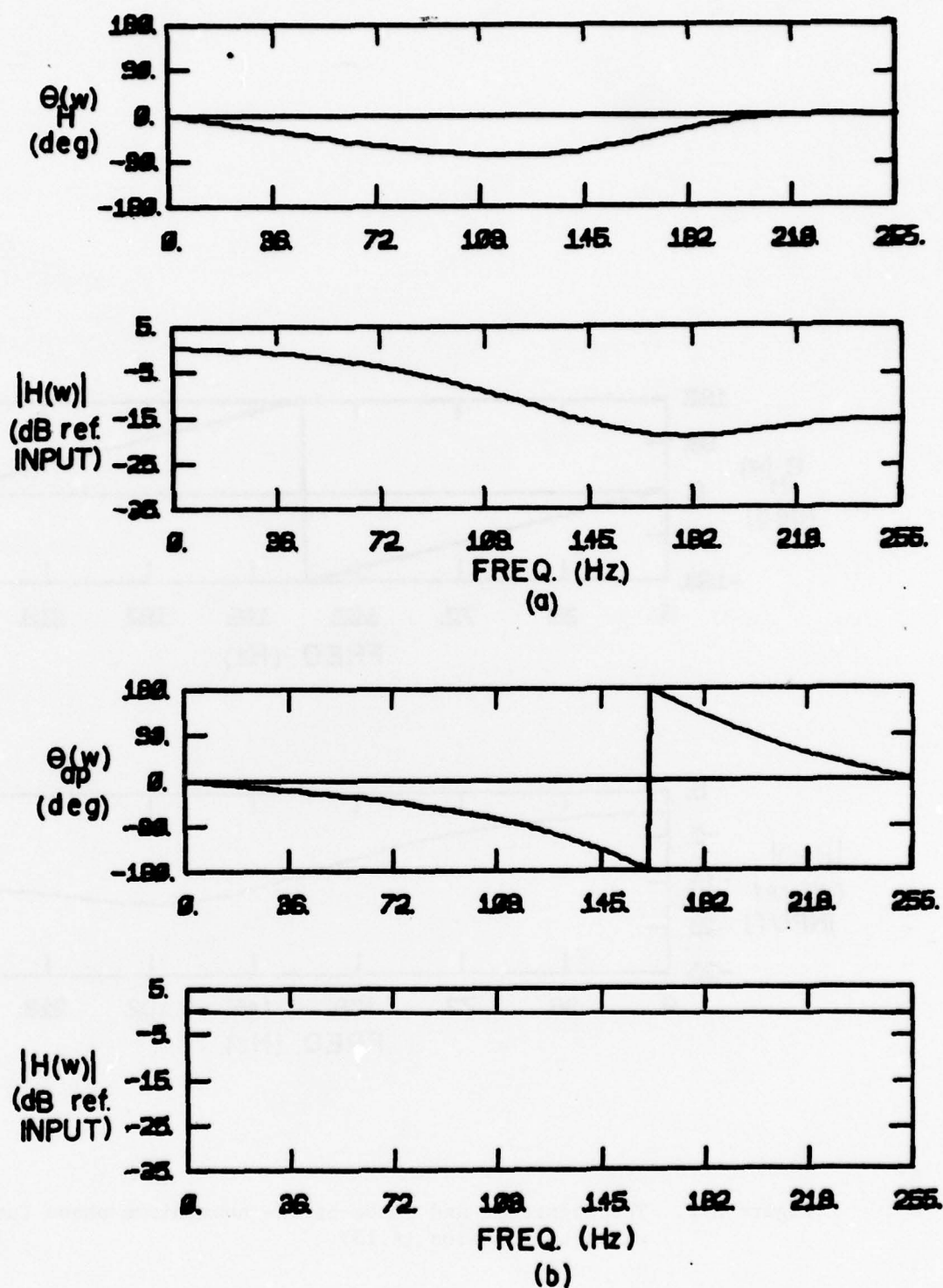
Figure A.3. (a) The magnitude and phase of the minimum phase function given by Equation (A.13); (b) The magnitude and phase of the all pass function given by Equation (A.14).

SAMPLE OR SPECIFY LN|H|

SET X(e^{jω}) = LN|H| + j(0.0)

SET SYMMETRY FOR REAL DFT

INVERSE DFT

c(n)

⊗

u(n)

FORWARD DFT

RE(X)=LN|H| IM(X) = θ_{min}
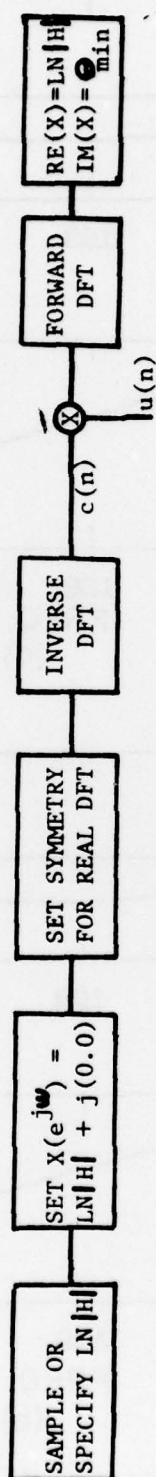
Figure A.4. Block diagram of program logic for calculating the minimum phase from the $\log_e$ of the magnitude.
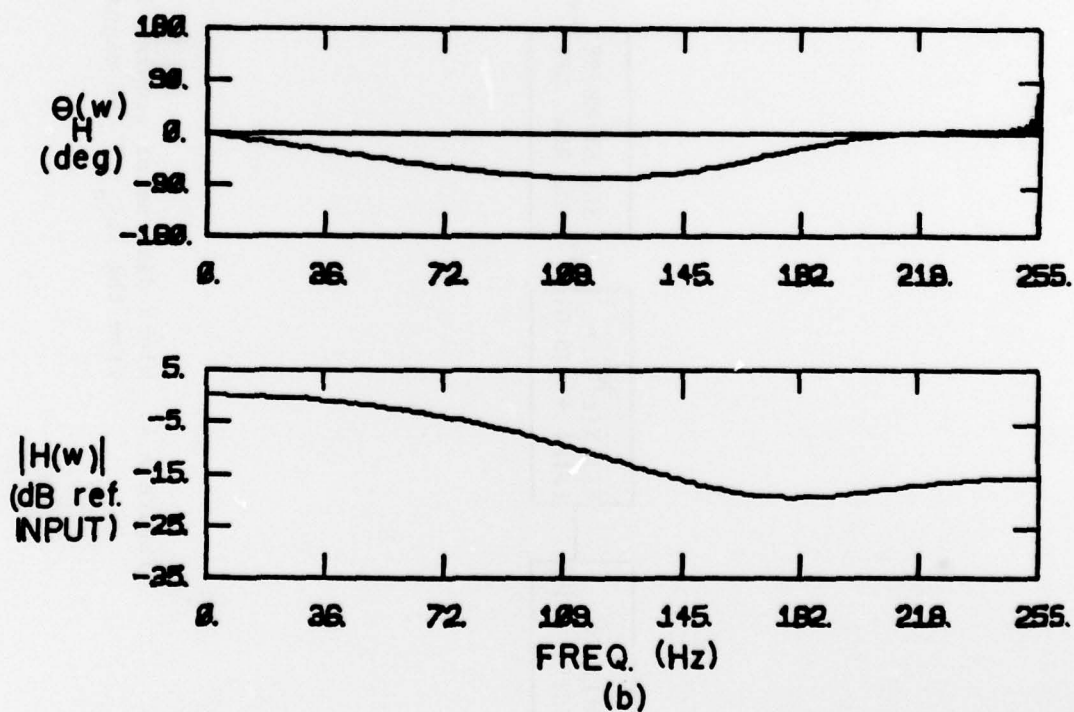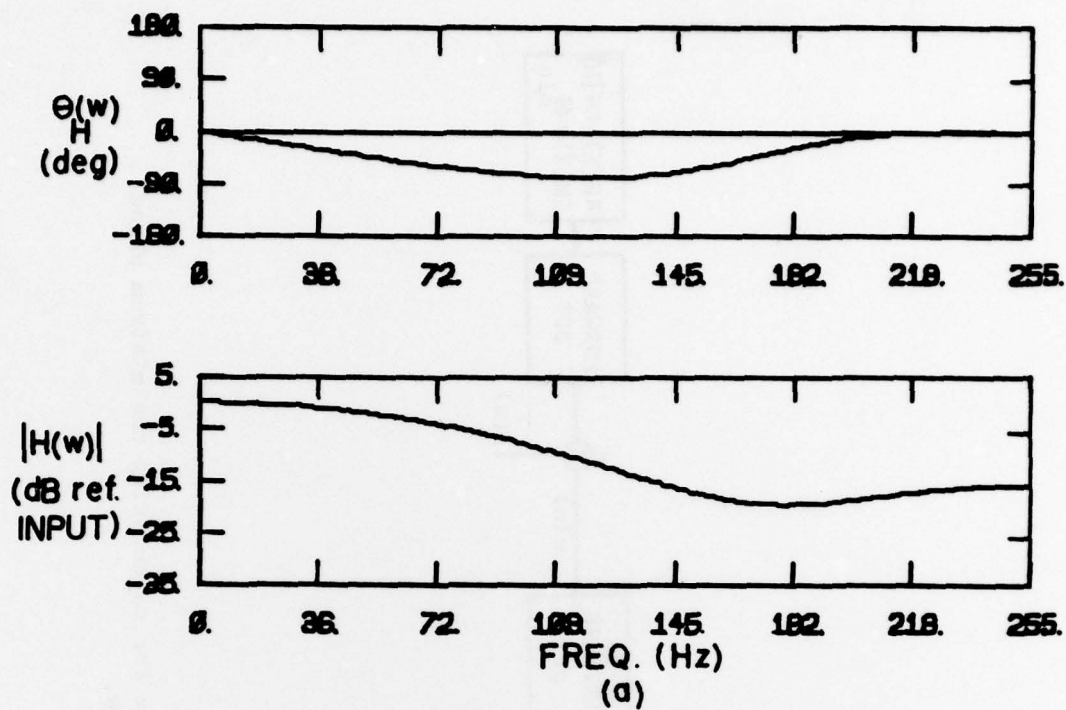
Figure A.5. The magnitude and phase of (a) the minimum phase function given by Equation (A.13) and (b) the minimum phase function calculated by the Discrete Hilbert Transform.
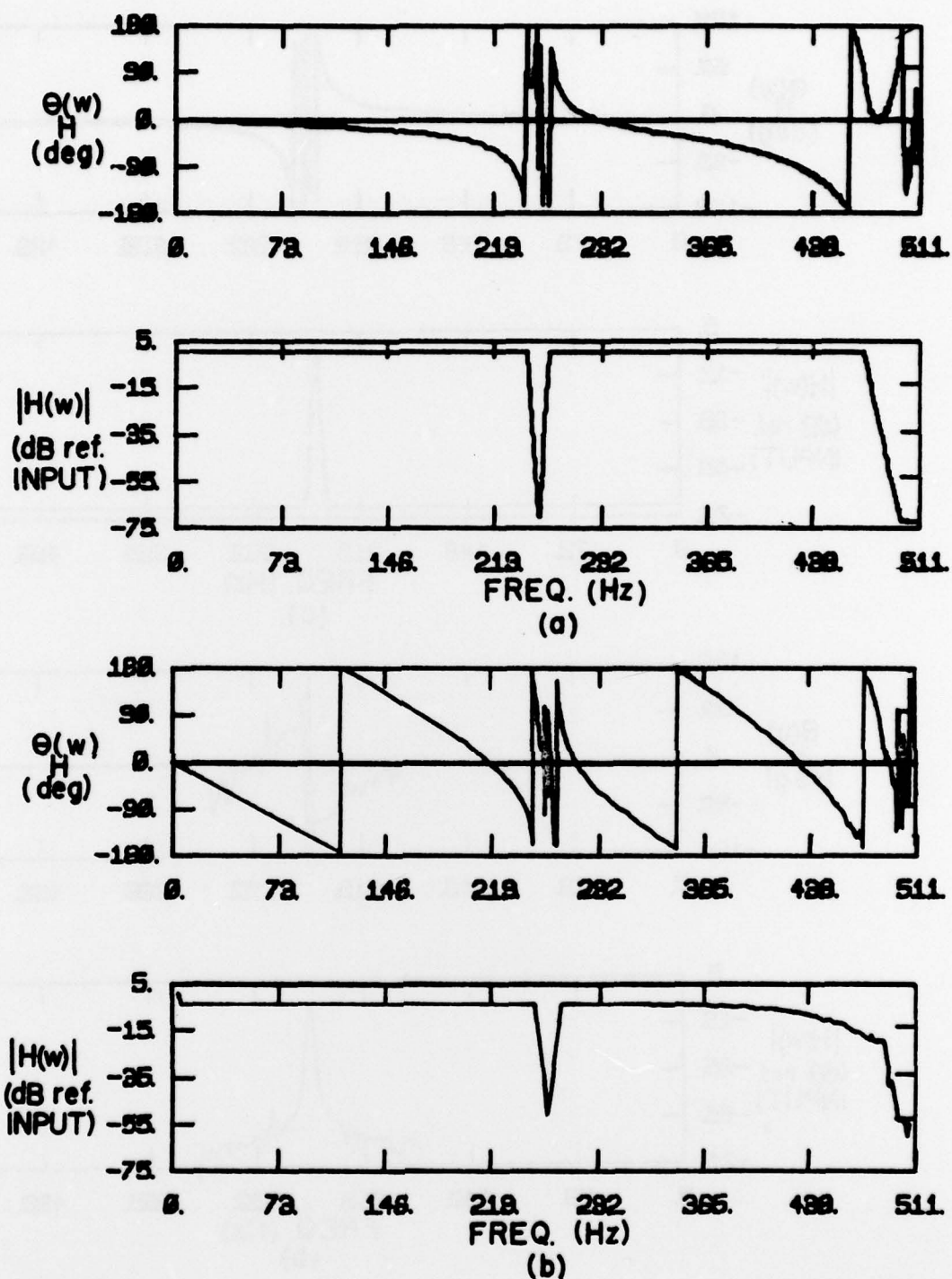
Figure A.6. The magnitude and phase of a notch filter (a) as specified using the computer model and (b) as measured when implemented on the programmable filter.
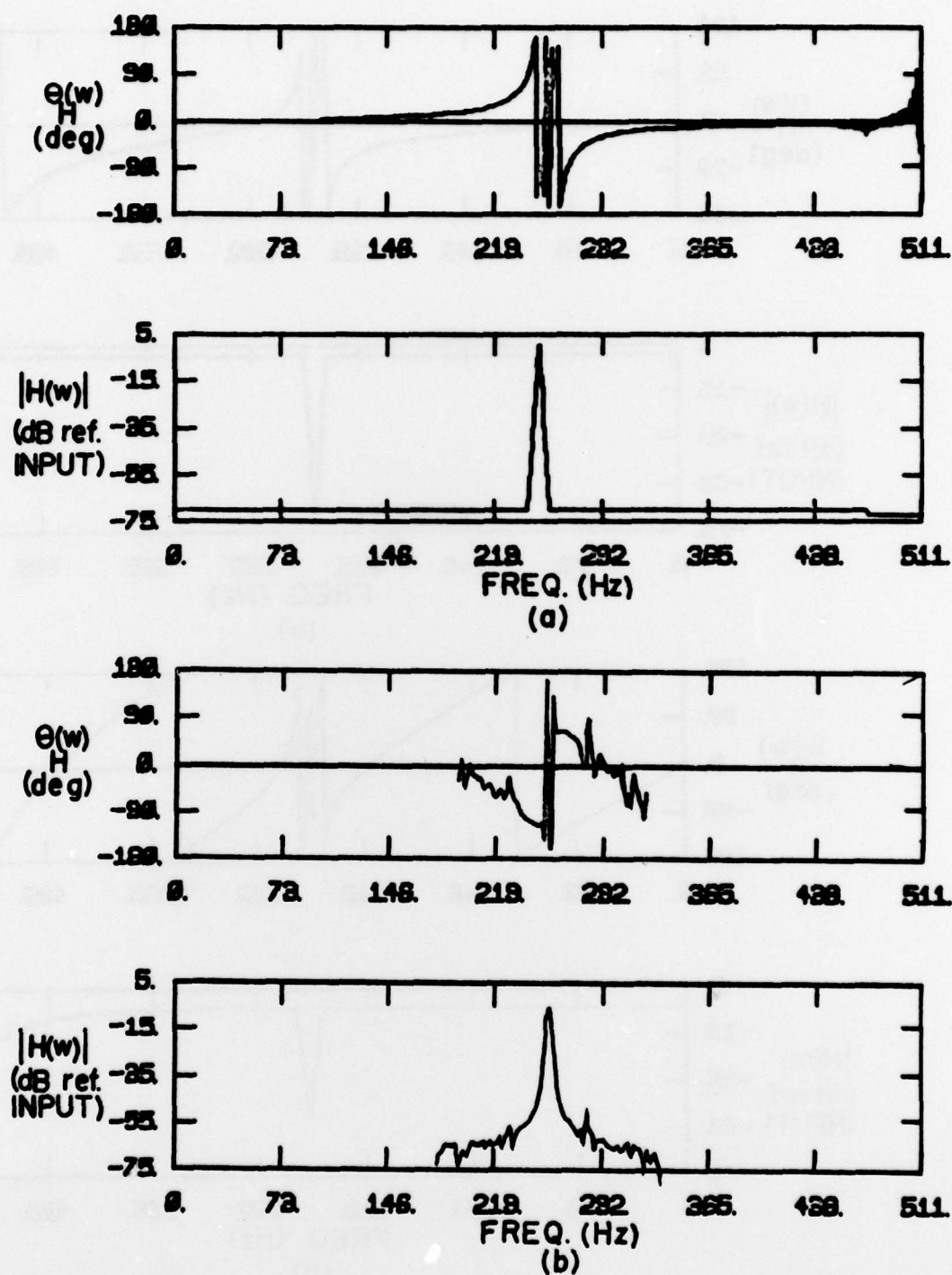
Figure A.7.   The magnitude and phase of a narrowband filter (a) as specified on the computer model and (b) as measured when implemented on the programmable filter.
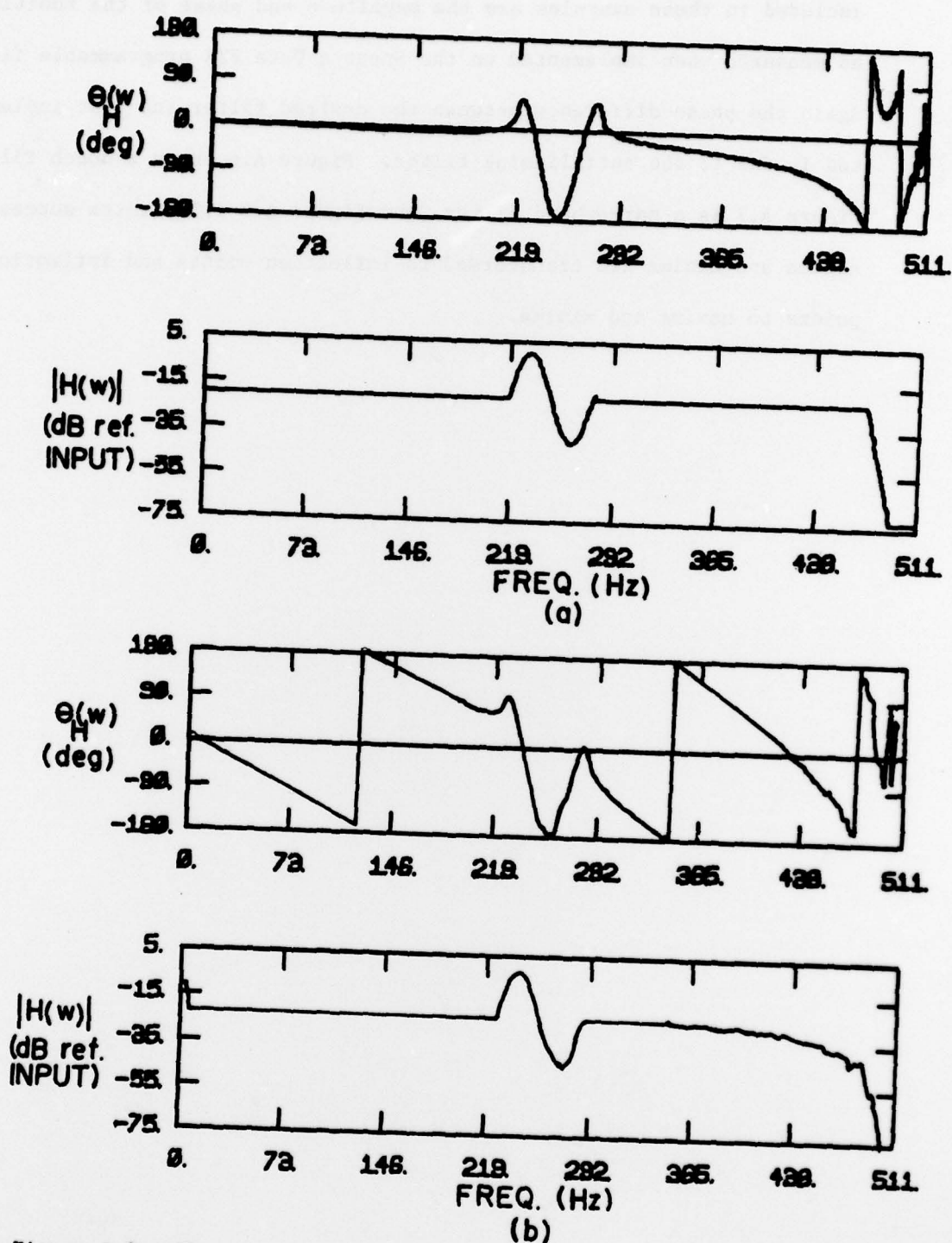
Figure A.8. The magnitude and phase of a filter design to illustrate the transformation of maxima, minima, and inflection points (a) as specified on the computer model and (b) as measured when implemented on the programmable filter.

Included in these examples are the magnitude and phase of the functions as measured when implemented on the Spectra Data FIR programmable filter. Again the phase difference between the desired filter and that implemented is due to the antialiasing filter. Figure A.6 shows a notch filter, Figure A.7 is a narrowband filter, and Figure A.8 illustrates successive maxima and minima are transformed to inflection points and inflection points to maxima and minima.

BIBLIOGRAPHY

1. American National Standards Institute, <u>American National Standards Methods for the Determination of Sound Power Levels of Small Sources in Reverberation Rooms</u>: SI.21-1972 (American National Standards Institute, 1430 Broadway, New York, NY 10018, 1972).

2. American Society of Heating, Refrigeration and Air-Conditioning Engineers, <u>ASHRAE Standard Methods for Sound Rating Heating, Refrigeration and Air-Conditioning Equipment</u>: 36-1972 (ASHRAE, Inc., East 47th St., New York, NY 10017, 1972).

3. H. G. Andres, "A law describing the random spatial variation of the sound field in rooms and its application to sound power measurements," Acustica <u>16</u>, 278 - 281 (1965).

4. H. S. Antman, "Extension to the theory of howlback in reverberant rooms," J. Acoust. Soc. Am. <u>39</u>, 399 (1966).

5. P. K. Baade, "Equipment sound power measurements in reverberation rooms," J. Sound Vib. <u>16</u>, 131 - 135 (1971).

6. C. G. Balachandran and D. W. Robinson, "Diffusion of the decaying sound field," Acustica <u>19</u>, 245 - 257 (1967).

7. G. C. J. Bart, "Spatial cross correlation in anisotropic sound fields," Acustica <u>28</u>, 45 - 49 (1973).

8. W. K. Blake and R. V. Waterhouse, "The use of cross-spectral density measurements in partially reverberant sound fields," J. Sound Vib. <u>54</u>, 589 - 599 (1977).

9. K. Bodlund, "A new quantity for comparitive measurements concerning the diffusion of stationary sound fields," J. Sound Vib. <u>44</u>, 191 - 207 (1976).

10. K. Bodlund, "Statistical characteristics of some standard reverberant sound field measurements," J. Sound Vib. <u>45</u>, 539 - 557 (1976).

11. K. Bodlund, "A normal-mode analysis of the sound power injection in reverberant chambers at low frequencies and the effect of source response averaging techniques," J. Sound Vib. <u>55</u>, 563 - 590 (1977).

12. R. H. Bolt, "Normal frequency spacing statistics," J. Acoust. Soc. Am. <u>19</u>, 71 - 90 (1947).

13. R. H. Bolt and R. W. Roop, "Frequency response fluctuations in rooms," J. Acoust. Soc. Am. <u>22</u>, 280 - 289 (1950).

14. C. P. Boner and C. R. Boner, "Minimizing feedback in sound systems and room ring modes with passive networks," J. Acoust. Soc. Am. 37, 131 - 135 (1965).

15. M. J. Brien, "Sound fields in a reverberation chamber with one oscillating wall," M.S. Thesis in Acoustics, The Pennsylvania State University, University Park, PA (1978).

16. D. G. Childers, D. P. Shinner, and R. C. Kemerant, "The cepstrum: a guide to processing," Proc. IEEE 65 (10), 1428 - 1443 (1977).

17. W. T. Chu, "Pure tone measurements in a reverberation room," presented at the 96th Meeting of the Acoust. Soc. Am., Honolulu, HI, 1978 (unpublished).

18. W. T. Chu, "Computer studies of reverberant sound fields in rectangular rooms -- eigenmode model," presented at the 97th Meeting of the Acoust. Soc. Am., Cambridge, MA, 1979 (unpublished).

19. J. Chung and J. Pope, "Practical measurements of acoustical intensity -- the two microphone cross spectral method," in Proceedings of Internoise 78, edited by William W. Lang (Noise Control Foundation, P. O. Box 3469, Arlington Branch, Poughkeepsie, NY 12603, 1978).

20. R. K. Cook, R. V. Waterhouse, R. D. Berendt, S. Edelman, and M. C. Thompson, Jr., "Measurement of correlation coefficients in reverberant sound fields," J. Acoust. Soc. Am. 27, 1072 - 1077 (1955).

21. B. F. Cron and C. H. Sherman, "Spatial correlation functions for various noise models, "J. Acoust. Soc. Am. 34 (11), 1732 - 1736 (1968).

22. G. J. Curtis, "An analysis of the regenerative reverberation effects of acoustic feedback in rooms," Acustica 20, 119 - 133 (1968).

23. G. J. Curtis, "The regenerative reverberation effects of acoustic feedback in rooms," Acustica 20, 134 - 148 (1968).

24. P. Dammig and G. Venzke, "Measurement of diffuseness in reverberation chambers with absorbing material," J. Acoust. Soc. Am. 33, 1687 - 1689 (1961).

25. J. J. D'Azzo and C. H. Houpis, Feedback Control System Analysis and Synthesis, 2nd ed. (McGraw-Hill, Inc., New York, 1966).

26. P. E. Doak, "Fluctuations of sound pressure level in rooms," Acustica 9, 1 - 9 (1959).

27. G. Dodd, "Assisted resonances and room acoustics in small auditoria," Ph.D. Thesis, The University of Southampton, Southampton, England (1972).

28. C. E. Ebbing, "Experimental evaluation of moving sound diffuser for reverberation rooms," J. Sound Vib. 16, 99 - 118 (1971).

29. C. E. Ebbing and G. C. Maling, "Reverberation room qualification for determination of sound power of sources of discrete-frequency sound," J. Acoust. Soc. Am. 54, 935 - 949 (1973).

30. C. Eckart, "The theory of noise in continuous media," J. Acoust. Soc. Am. 25, 195 - 199 (1953).

31. F. J. Fay, "Measurement of acoustic intensity using the cross-spectral density of two microphone signals," J. Acoust. Soc. Am. 62, 1057 - 1059 (1977).

32. R. W. Guelke and A. D. Broadhurst, "Reverberation time control by direct feedback," Acustica 24, 33 - 41 (1971).

33. H. D. Helms, "Nonrecursive digital filters: design method for achieving specification in the frequency response," IEEE Transactions on Audio and Electroacoustics 16 (3), 336 - 342 (1969).

34. R. C. Heyser, "Loudspeaker phase characteristics and time delay distortion: Part 1," J. Audio Eng. Soc. 17 (1), 30 - 41 (1969).

35. R. C. Heyser, "Concepts in the frequency and time domain responses of loudspeakers," Proc. IRE., 67 - 76 (1976).

36. Y. Hwang, "Acoustic modulations by time harmonic boundary motion," Ph.D. Thesis in Acoustics, The Pennsylvania State University, University Park, PA (1975).

37. M. H. Jones and F. Fowweather, "Reverberation reinforcement - an electroacoustical system for increasing the reverberation time of an auditorium," Acustica 20, 134 - 148 (1968).

38. L. Kinsler and A. Frey, Fundamentals of Acoustics, 2nd ed. (Wiley, New York, 1962).

39. C. W. Kosten, "International comparison measurements in the reverberation room," Acustica 10, 400 - 407 (1960).

40. M. Koyasu and M. Yamashita, "Evaluation of the degree of diffusion in reverberation rooms by cross correlation techniques," J. Acoust. Soc. Japan 26, 132 - 142 (1971).

41. B. C. Kuo, Analysis and Synthesis of Sampled-Data Control Systems, (Prentice-Hall, Englewood Cliffs, NJ, 1963).

42. H. P. Lamhick and W. A. Stakel, "A sound intensity meter and its application in car acoustics," in Proceedings of Internoise 77, edited by Eric J. Rathe (Noise Control Foundation, P. O. Box 3469, Arlington Branch, Poughkeepsie, NY 12603, 1977).

43. J. G. Lilly, "Electroacoustic feedback in rectangular reverberation chambers," M.S. Thesis in Acoustics, The Pennsylvania State University, University Park, PA (1975).

44. M. M. Louden, "Dimension-ratios of rectangular rooms with good distribution of eigentones," Acustica $\underline{24}$, 101 – 104 (1971).

45. D. Lubman, "Distribution of reverberant sound in large rooms," J. Acoust. Soc. Am. $\underline{39}$, 1266(A) (1966).

46. D. Lubman, "Fluctuation of sound with position in a reverberant room," J. Acoust. Soc. Am. $\underline{44}$, 1491 – 1502 (1968).

47. D. Lubman, "Spatial averaging in a diffuse sound field," J. Acoust. Soc. Am. $\underline{46}$, 532 – 534 (1969).

48. D. Lubman, "Spatial averaging in sound power measurements," J. Sound Vib. $\underline{16}$, 43 – 48 (1971).

49. D. Lubman, "Effectiveness of continuous spatial averaging in a diffuse sound field," J. Acoust. Soc. Am. $\underline{53}$, 650 – 659 (1973).

50. D. Lubman, "Precision of reverberant sound power measurements," J. Acoust. Soc. Am. $\underline{56}$, 523 – 534 (1974).

51. D. Lubman, "Transversing microphone spectroscopy as a means of assessing diffusion," J. Acoust. Soc. Am. $\underline{56}$, 1302 – 1304 (1974).

52. R. H. Lyon, "Statistical analysis of power injection and response in structures and rooms," J. Acoust. Soc. Am. $\underline{45}$, 545 – 565 (1969).

53. G. C. Maling, Jr., "Calculation of acoustic power radiated by a monopole in a reverberation chamber," J. Acoust. Soc. Am. $\underline{42}$, 859 – 865 (1967).

54. G. C. Maling, Jr., "Guidelines for measurement of the average sound power radiated by discrete – frequency sources in a reverberation room," J. Acoust. Soc. Am. $\underline{53}$, 1064 – 1069 (1973).

55. G. C. Maling, Jr., and K. S. Nordby, "Reverberation chamber determination of the acoustic power of pure-tone source," IBM J. of Res. and Dev., $\underline{11}$, 492 – 501 (1967).

56. G. Mange, "Effect of source position on the sound power radiation in reverberation chambers," M.S. Thesis in Acoustics, The Pennsylvania State University, University Park, PA (1976).

57. L. N. Mishin, "A method for increasing the stability of sound amplification systems," Sov. Phy. Acoust. $\underline{4}$ (1), 64 – 71 (1958).

58. C. T. Morrow, "Point-to-point correlation of sound pressure in reverberation chambers," J. Sound Vib. $\underline{16}$, 1629 – 1642 (1971).

59. P. M. Morse, Vibration and Sound, (McGraw-Hill, New York, 1936).

60. A. V. Oppenheim and R. W. Schafer, Digital Signal Processing, (Prentice-Hall, Englewood Cliffs, NJ, 1975).

61. C. H. Page, Physical Mathematics, (D. Van Nostrand Company, Sons., Princeton, NJ, 1955).

62. A. G. Piersol, "Use of coherence and phase data between two receivers in evaluation of noise environments," J. Sound Vib. 56, 215 - 228 (1978).

63. L. R. Rabiner, B. Gold, and C. A. McGonegal, "An approach to the approximation problems for nonrecursive digital filters," IEEE Trans. Audio Electro. 18, 83 - 105 (1970).

64. L. R. Rabiner, "Linear program design of finite impulse response (FIR) digital filters," IEEE Trans. Audio Electro. 20, 280 - 288 (1972).

65. K. P. Roy, "Qualification of reverberant chambers for sound power measurements," M.S. Thesis in Architectural Engineering, The Pennsylvania State University, University Park, PA (1973).

66. K. P. Roy, "Experimental investigation of the sound field modulation phenomenon of a rotating diffuser," Ph.D. Thesis in Acoustics, The Pennsylvania State University, University Park, PA (1977).

67. T. D. Scharton, P. E. Rentz, D. Lubman, and P. H. White, "Techniques for improving the low-frequency performance of small reverberation chambers," Bolt, Beranek and Newman, Report 1867.

68. M. R. Schroeder, "Frequency correlation functions of frequency response in rooms," J. Acoust. Soc. Am. 34, 1819 - 1823 (1962).

69. M. R. Schroeder, "Improvement of acoustic-feedback stability of frequency shifting," J. Acoust. Soc. Am. 36, 1718 - 1724 (1964).

70. M. R. Schroeder, "The effects of frequency and space averaging on the transmission responses of multimode media," J. Acoust. Soc. Am. 46, 277 - 283 (1969).

71. T. J. Schultz, "Diffusion in Reverberation Rooms," J. Sound Vib. 16, 17 - 28 (1971).

72. L. W. Sepmeyer, "Computed frequency and angular distribution of normal modes of vibration in rectangular rooms," J. Acoust. Soc. Am. 37, 413 - 423 (1965).

73. W. F. Smith and R. J. Baily, "Investigation of the statistics of sound power injection from low-frequency finite size sources in a reverberation room," J. Acoust. Soc. Am. 54, 950 - 955 (1973).

74. *Sound Fields in Rectangular Enclosures*, computer animated film produced by J. B. Ochs (distributed by the Graduate Program in Acoustics, The Pennsylvania State University, Box 30, State College, PA 16801), 16 mm, color, magnetic or optical sound, 15 min.

75. J. Tichy, "Effect of rotating vanes on the sound field in reverberation chambers," presented at the 80th Meeting of the Acoust. Soc. Am., Houston, TX, 1970 (unpublished).

76. J. Tichy, "Sound field in reverberant chambers at discrete frequencies," presented at the ASHRAE Meeting, Kansas City, KS, 1970 (unpublished).

77. J. Tichy, "The effect of boundary conditions on the statistical properties of the sound field in enclosures," presented at the 81st Meeting of the Acoust. Soc. Am., Washington, DC, 1971 (unpublished).

78. J. Tichy, "The effect of rotating vanes on the sound field in reverberation chambers," J. Acoust. Soc. Am. $\underline{49}$, 89(A) (1971).

79. J. Tichy, "The measurement of sound power in reverberation chambers at discrete frequencies," in *Proceedings of Internoise 72*, (Noise Control Foundation, P. O. Box 3469, Arlington Branch, Poughkeepsie, NY 12603, 1972).

80. J. Tichy, "Application of rotating vanes for sound power measurements in reverberation chambers," American Society of Heating, Refrigeration and Air-Conditioning Engineers (ASHRAE) Research Report RP-103, 1972.

81. J. Tichy and P. K. Baade, "The effect of rotating diffusers and sampling techniques on pressure averaging in reverberation rooms," J. Acoust. Soc. Am. $\underline{56}$, 137 - 143 (1974).

82. J. Tichy, M. Brien, and K. P. Roy, "Sound power measurements in reverberation chambers," National Bureau of Standards Research Report No. 4-9030, 1976.

83. B. J. Tunbridge and R. W. B. Stephens, "The interaction of an acoustic feedback channel with the transient sound field in a rectangular enclosure," Acustica $\underline{31}$, 271 - 280 (1974).

84. U. S. Dept. of Commerce, "Review of reverberant sound power measurement standard and recommendations for further research," U. S. Dept. Commerce/National Bureau of Standards, NBS Technical Note 941.

85. M. S. Warshawsky, "The effect of rotating diffusers on the diffusion in reverberation rooms," M.S. Thesis in Acoustics, The Pennsylvania State University, University Park, PA (1979).

86. R. V. Waterhouse, "Interference patterns in reverberant sound fields," J. Acoust. Soc. Am. $\underline{27}$, 247 - 258 (1955).

87. R. V. Waterhouse, "Output of a sound source in a reverberant chamber and other reflecting environment," J. Acoust. Soc. Am. 30, 4 - 13 (1958).

88. R. V. Waterhouse, "Radiation impedance of a source near reflectors," J. Acoust. Soc. Am. 35, 1144 - 1151 (1963).

89. R. V. Waterhouse, "Theory of howlback in reverberant rooms," J. Acoust. Soc. Am. 37, 921 - 923 (1965).

90. R. V. Waterhouse, "Statistical properties of reverberant sound fields," J. Acoust. Soc. Am. 43, 1436 - 1444 (1968).

91. R. V. Waterhouse, "Power output of a point source exciting a single cartesian mode," J. Acoust. Soc. Am. 49, 9 - 16 (1971).

92. R. V. Waterhouse, "Sound diffusion in enclosures," J. Acoust. Soc. Am. 56, 702 (1974).

93. R. V. Waterhouse and R. Cook, "Diffuse sound fields: eigenmode and free-wave models," J. Acoust. Soc. Am. 59, 516 - 581 (1976).

VITA

John Baptist Ochs was born on February 21, 1949, in Summit,
New Jersey. He graduated from Summit High School, Summit, New Jersey,
in June 1967. In December 1972, he received a B.S. degree with honors
in Mathematics from Villanova University, Villanova, Pennsylvania, and
received an honorary membership in the Pi Mu Epsilon Mathematics Honor
Society. In May 1975, he received a M.S. degree in Engineering
Acoustics at The Pennsylvania State University, University Park,
Pennsylvania. The Master's thesis was an investigation of plate vibra-
tion for various boundary conditions and mass loadings. From May 1975
to September 1979, he has been studying the characteristics of the sound
fields and various signal processing and computer graphics techniques to
measure these characteristics. Since August 1979, he has been an
Assistant Professor of Mechanical Engineering and Mechanics at Lehigh
University and a member of their Computer Aided Design Laboratory. He
is an active member of the Acoustical Society of America, the Audio
Engineering Society, the Special Interest Group on Graphics of the
Association for Computing Machinery, and the Phi Kappa Phi and Sigma Chi
Honor Societies.

DISTRIBUTION